A COMPREHENSIVE STUDY OF SUPERNOVAE MODELING

by

Chengdong Li

BS, University of Science and Technology of China, 2006

MS, University of Pittsburgh, 2007

Submitted to the Graduate Faculty of

the Dietrich School of Arts and Sciences in partial fulfillment

of the requirements for the degree of

Doctor of Philosophy

University of Pittsburgh

2013

UNIVERSITY OF PITTSBURGH

PHYSICS AND ASTRONOMY DEPARTMENT

This dissertation was presented

by

Chengdong Li

It was defended on

January 22nd 2013

and approved by

John Hillier, Professor, Department of Physics and Astronomy

Rupert Croft, Associate Professor, Department of Physics

Steven Dytman, Professor, Department of Physics and Astronomy

Michael Wood-Vasey, Assistant Professor, Department of Physics and Astronomy

Andrew Zentner, Associate Professor, Department of Physics and Astronomy

Dissertation Director: John Hillier, Professor, Department of Physics and Astronomy

A COMPREHENSIVE STUDY OF SUPERNOVAE MODELING

Chengdong Li, PhD

University of Pittsburgh, 2013

The evolution of massive stars, as well as their endpoints as supernovae (SNe), is important both in astrophysics and cosmology. While tremendous progress towards an understanding of SNe has been made, there are still many unanswered questions. The goal of this thesis is to study the evolution of massive stars, both before and after explosion. In the case of SNe, we synthesize supernova light curves and spectra by relaxing two assumptions made in previous investigations with the the radiative transfer code CMFGEN, and explore the effects of these two assumptions. Previous studies with CMFGEN assumed γ-rays from radioactive decay deposit all energy into heating. However, some of the energy excites and ionizes the medium. A new solver is developed to include these non-thermal excitation and ionization processes. Non-thermal excitation and ionization are crucial for forming some lines, especially Hα in the nebular phase. To investigate non-thermal effects, a comparison is made between models with, and without, the non-thermal solver. Benchmarking the solver is done by comparing the non-thermal models with observations of SN 1987A. Satisfactory agreement is achieved and possible problems are discussed. With the new solver, future studies will shed light on the mixing of material between layers of different composition in supernova explosions and put further constraints on supernova explosion models.

Hubble expansion is a good approximation for most types of SNe, except Type II-P. Red supergiants are widely accepted to be the progenitors of Type II-P SNe and they have radii of hundreds to thousands of times larger than that of the Sun. Type II-P SNe "memorize" their large radii at the time of explosion for several weeks and material is still being accelerated. A time-dependent fully relativistic solver is developed to handle such cases.

TABLE OF CONTENTS

PREFACE xxiii

1.0 INTRODUCTION 1

1.1 EVOLUTION OF MASSIVE STARS 1

1.1.1 Stellar evolution 1

1.1.2 Massive stars 3

1.2 CLASSIFICATION OF SUPERNOVAE 5

1.3 THE IMPORTANCE OF CORE-COLLAPSE SUPERNOVAE 11

1.4 THE PROBLEMS OF CORE-COLLAPSE SUPERNOVAE 15

1.4.1 Progenitor problems 15

1.4.2 Explosion problems 19

1.4.3 Mixing problems 21

1.5 ASYMMETRY OF CORE-COLLAPSE SUPERNOVAE 24

1.6 OUTLINE OF THE THESIS 25

2.0 RADIATION TRANSPORT THEORY 27

2.1 THE RADIATIVE TRANSFER EQUATION 27

2.1.1 The specific intensity 27

2.1.2 The radiative transfer equation 27

2.1.3 Sources of opacity and emissivity 29

2.2 MOMENTS OF THE TRANSFER EQUATION 29

2.2.1 Moments of the radiation field 29

2.2.2 Scattering problem 30

2.2.3 Moments of the transfer equation 31

2.2.4 The boundary conditions . . . 32
2.3 THE STATISTICAL AND RADIATIVE EQUILIBRIUM EQUATIONS . . 32
2.3.1 LTE VS Non-LTE . . . 32
2.3.2 The statistical equilibrium equations . . . 33
2.3.3 The radiative equilibrium equation . . . 34
2.4 THE RADIATIVE TRANSFER CODE CMFGEN . . . 34
2.4.1 Super levels . . . 36
2.4.2 The elimination scheme . . . 36
2.4.3 Fully Non-LTE . . . 37
2.4.4 Time-dependence . . . 38
2.4.5 Link to a hydrodynamical model . . . 42
3.0 PART I. NONTHERMAL EXCITATION AND IONIZATION IN SUPERNOVAE . . . 43
3.1 WHY WITH NON-THERMAL EXCITATION AND IONIZATION . . . 43
3.2 THE NON-THERMAL SOLVER . . . 44
3.2.1 The Spencer-Fano Equation . . . 44
3.2.2 Ionization cross sections . . . 47
3.2.3 Excitation cross sections . . . 49
3.3 The hydrodynamical input . . . 52
3.4 The non-thermal model . . . 53
3.4.1 The degradation spectrum . . . 54
3.4.2 Number density of non-thermal electrons . . . 55
3.4.3 Energy fraction of the three channels . . . 56
3.4.4 Excitation and ionization . . . 57
3.5 Non-thermal vs thermal models . . . 59
3.5.1 Comparison of the temperature structure . . . 59
3.5.2 Controlling processes for H I and He I lines . . . 60
3.5.3 Comparison of optical and IR spectra . . . 66
3.5.4 Comparison of the spectral evolution . . . 68
3.6 The influence of Fe I . . . 70

3.7 Comparison with the observations . . . 72
3.7.1 The synthetic and observed light curves . . . 72
3.7.2 Spectral comparison . . . 75
3.7.3 Comparison of the spectral evolution . . . 77
3.8 UNCERTAINTIES . . . 77
3.8.1 Impact excitation and ionization cross sections . . . 77
3.8.2 E_{max} for high energy electrons . . . 81
3.8.3 The time-dependence effects on non-thermal processes . . . 81
3.9 DISCUSSION . . . 82
3.10 CONCLUSION . . . 84
4.0 PART II. FULLY RELATIVISTIC RADIATIVE TRANSFER . . . 87
4.1 DEVIATION FROM HUBBLE EXPANSION . . . 87
4.2 TRANSFER EQUATIONS IN THE FULLY RELATIVISTIC FORM . . . 88
4.3 INITIAL SETUP . . . 92
4.4 TESTING . . . 93
4.4.1 Solution to homologous models . . . 93
4.4.2 Departure coefficients . . . 95
4.4.3 Ejecta temperature . . . 97
4.4.4 Global energy constraint . . . 100
4.5 MODEL EVOLUTION . . . 101
4.6 LIGHT CURVES AND SPECTRAL EVOLUTION . . . 105
4.6.1 Bolometric and multi-band light curves . . . 105
4.6.2 Spectral evolution . . . 106
4.7 DISCUSSION . . . 106
4.7.1 Bias of distance measurements . . . 106
4.8 CONCLUSIONS . . . 108
5.0 PART III. ETA CARINAE . . . 110
5.1 INTRODUCTION . . . 110
5.2 OPTICAL MAPPING OF THE HOMUNCULUS . . . 113
5.3 THE POSITIONAL APPEARANCES OF HYDROGEN PROFILES . . . 115

5.4 THE EQUIVALENT WIDTH MAP OF Hα . . . 117
5.4.1 Calculation of EW and uncertainty . . . 118
5.4.2 Positional variation of the EW map . . . 120
5.4.3 The Equatorial disk and NW lobe . . . 121
5.4.4 SE lobe . . . 124
5.4.5 Core region . . . 124
5.4.6 The EW "sword" . . . 125
5.4.7 The pixel-to-pixel variation . . . 126
5.4.8 Interpretation of the EW map . . . 128
5.4.8.1 The NW lobe . . . 128
5.4.8.2 The SE lobe . . . 131
5.4.8.3 Pixel-to-pixel variations . . . 133
5.5 Absorption constraints on the wind structure . . . 134
5.5.1 P Cygni absorption in the SE lobe . . . 134
5.5.2 Abnormality of the P Cygni absorption . . . 136
5.6 Optical depth of the Homunculus . . . 141
5.7 CONCLUSION . . . 146
6.0 PART IV. FUNDAMENTAL PARAMETERS AND THE EUV FLUX OF ϵ CANIS MAJORIS . . . 149
6.1 INTRODUCTION . . . 149
6.2 OBSERVATIONAL DATA . . . 151
6.3 MODELS . . . 154
6.4 RESULTS . . . 155
6.4.1 Balmer line wings fitting . . . 155
6.4.2 Balmer jump . . . 156
6.4.3 Equivalent widths of silicon lines . . . 159
6.4.4 Spectral energy distribution . . . 161
6.5 DISCUSSION . . . 167
6.5.1 Continuum determination of echelle spectra . . . 167
6.5.2 Microturbulence . . . 168

6.5.3 Mass loss . . . 168
6.5.4 Reddening . . . 170
6.5.5 Other possibilities . . . 171
6.6 CONCLUSIONS . . . 172
7.0 CONCLUSIONS OF THE THESIS . . . 174
7.1 NON-THERMAL PROCESSES IN SUPERNOVAE . . . 174
7.2 Fully relativistic radiative transfer of SNe . . . 175
7.3 The wind geometry of η Carinae . . . 176
7.4 The physical parameters of ϵ Canis Majoris . . . 177
APPENDIX A. ABBREVIATION SUMMARY . . . 178
APPENDIX B. STRATEGY TO SOLVE THE MOMENT EQUATIONS . 180
BIBLIOGRAPHY . . . 183

LIST OF TABLES

1.1 Deaths of massive stars 17

3.2 Combinations of species to scale the cross sections 79

4.3 Start and end times for the simulations 103

6.4 Previous parameter determinations for ϵ CMa 151

6.5 Stellar parameters for ϵ CMa 152

6.6 JHK$_s$ photometry of 2MASS All Sky Catalog of Point Sources for ϵ CMa . . 153

6.7 Element abundances used in model calculations 155

6.8 $T_{\rm eff}$ and $\log g$ combinations that give the best fits to the wings of the Hα profile. 159

LIST OF FIGURES

1.1 Classification of supernovae. 6

1.2 Spectral features of different types of SNe at early time. t and τ denote the time after B-band maximum and the time after core collapse, respectively. This figure is taken from Filippenko [116]. 7

1.3 Light curves of various types of SNe. This figure is taken from Filippenko [116]. Type Ia are powered by radioactive decay for most of the evolution – even pre-maximum. Type IIP are powered by shock and recombination energy until they become thin. Type Ibc also tend to be powered by nuclear decay. While Type II-P SNe are characterized by a plateau phase after maximum, Type II-L SNe display a linear light curve at the tail. Light curves of Type Ib/c SNe resemble those of Type Ia SNe, but have a variety of decline rates. SN 1987A (Type IIp) exhibit a slow rise to maximum. 8

1.4 Pie charts of fractions for supernova types from the Lick Observatory Supernova Search (LOSS). The left panel shows the fractions of the three broad types of supernovae, while the right panel shows the fractions of subtypes of core-collapse supernovae. The data is taken from Li et al. [242]. 16

1.5 The progenitor-supernova map, showing the connections between the progenitor star and the supernova type. The events are served as evidences, or possible evidences (relations with question mark), are written in the box connecting the progenitor and the supernova type. This figure is taken from Gal-Yam et al. [126]. 18

2.6 Departure coefficients of H I, O I and Fe II for a Type II-P supernova model with progenitor mass of 15 $M_\odot$ at two different epochs [90]. 38

2.7 The match between the observation of SN 1999em (black) and the synthetic spectra of CMFGEN models (red). Left panel: the observation is compared to the time-dependent model. Right panel: the observation is compared to the stationary model. Failure of production of the Hα strength in the stationary model is no longer seen in the time-dependent model [88]. 41

3.8 Comparison of the ionization cross sections of H I. The ionization cross sections are in unit of πa^2, where a is the Bohr radius. Several theoretical methods and a set of experimental data (green) are shown to compare with the prediction of the Arnaud and Rothenflug method. BEB Direct (magenta) and BEQ (red) models are from Kim and Rudd [202], while the shah87 (green), gryz65 (yellow), younger81 (cyan) and Johnson (blue) are from Shah et al. [330], Gryziński [145], S.M. and Younger [335] and Johnson [195], respectively. The BEB Direct, BEQ, shah87, gryz65 and younger81 results are obtained from National Institute of Standard and Technology (NIST). The Johnson's curve is computed by the formula in Johnson [195]. 48

3.9 The tabulated gaunt factor (stars) for neutral atoms as a function of $x = \sqrt{\frac{mv^2}{2\Delta E}}$ given in van Regemorter [385]. The second order (solid) and the third order (dashed) polynomial fit are also shown. 50

3.10 Same as Fig. 3.8, but now shows the comparison of excitation cross sections for transition from state 1s to 2p. The BE-scaled, cccweb01, grafe01 and Johnson models are from Stone et al. [356], Bray and Ralchenko [33], Grafe et al. [134] and Johnson [195], respectively. The results of the BE-scaled, cccweb01 and grafe01 come from the NIST. 51

3.11 Illustration of the elemental mass fractions on a logarithmic scale as a function of velocity at day 127. We plot hydrogen (black), helium (red), carbon (green), oxygen (blue) and ^{56}Co (magenta) – five important elements in the model. . 53

3.12 The degradation spectra at a model velocity of $\sim 1000\,\mathrm{km\,s^{-1}}$ computed using different numbers of energy bins: 100 (black), 1000 (red), 10 000 (blue). . . . 55

3.13 Comparison of the number density of the non-thermal electron (solid) and the thermal electron (dashed). 56
3.14 The fractional energy that goes into heating δE_h(red), ionization δE_i (blue) and excitation δE_e (green) in model D127_NT, as a function of velocity. The ejecta ionization fraction X_e, which is defined as the ratio of number of ions to number of atoms, is also shown (black). 57
3.15 The largest 5 (summation over all depths) fractional energies taken away from the non-thermal electrons by species in the excitation (top) and ionization (bottom) channel (solid lines). The fractions of species abundances are over-plotted for comparison. Importantly, the highest ionization stage of each element is excluded in the calculations of fractional abundances. (see the text for details). 58
3.16 Comparison of temperature structure between model D127_NT (solid) and model D127 (dashed). 60
3.17 Logarithmic species fractions of different ionization stages for hydrogen (top) and helium (bottom). Comparison is made between model D127_NT (solid lines) and D127 (dashed lines). 61
3.18 Upper panel: The D127 model spectrum (black) and the model spectra computed by including only bound-bound transitions of He I (red) and H I (blue) at optical band. Lower panel: Same as the upper panel, but for the D127_NT model. 62
3.19 Illustration of model spectrum (solid) and model spectrum computed by including only bound-bound transitions of He I (dashed) for model D127 (top panel) and D127_NT (bottom panel) between 1.9 and 2.2 μm. 63
3.20 Top: Normalized rates for different processes that populate and depopulate the 1s 2p ^{1}P^o state of He I. Only processes with a fractional rate $\geq 5\%$ at more than one depth are shown. Bottom: Same as the top panel, but for the case of 1s 2p ^{3}P^o state of He I. 64
3.21 Normalized rates for H I (top) and He I (bottom), including all processes allowed in the modeling. 65

3.22 Comparison of optical and IR spectra between model D127_NT and D127. . . 67

3.23 Comparison of the Hα profile between models D127_NT (solid) and D127 (dashed). 68

3.24 Left panel: montage of synthetic optical spectra for the thermal sequence. The days since breakout are labeled below each spectra. Right panel: montage of synthetic spectra at the same epochs shown in the left panel for the non-thermal sequence. The synthetic spectra are reddened with E(B-V) = 0.15 and scaled for a distance of 50 kpc. The most prominent difference between the spectra of the two sequences is the evolution of Hα – its strength persist at all times in the non-thermal sequence but it almost disappears at late times in the thermal sequence. 69

3.25 Comparison of optical spectral between model D127_NT and the model with Fe I (hereafter model D127_NT_FeI). 70

3.26 Comparison of the observed (black stars, Suntzeff and Bouchet 1990) bolometric light curve of SN 1987A to the theoretical bolometric light curves of the thermal (red) and non-thermal (blue) sequences, with symbols referring to the computed epochs of models. The observational bolometric light curve is constructed by using ultraviolet, optical and infrared photometry. A light curve resulting from the conversion of energy from the radioactive decay of 0.084 $M_\odot$ (green) is also shown for reference. 71

3.27 Comparison of the V-, R-, and I-band light curves of SN 1987A to the corresponding synthetic light curves. The observed V, R, and I magnitudes are shown in stars, and the synthetic V, R, and I magnitudes from the non-thermal sequence are plotted in squares connected by dashed-dotted lines. A scaling is applied to the R and I band magnitudes, both observed and synthetic, to optimize visualization. The synthetic photometry is computed by convolving the synthetic spectra with the Landolt filter bandpasses [225]. We applied a reddening of E(B-V)=0.15 and adopted a distance of 50 kpc. 73

3.28 Comparison between observed spectrum of SN 1987A and the model spectra at day 127. A scaling is applied to the observed spectrum to correct for the difference between the spectroscopic (4.30) and the photometric (4.37) V-magnitude. The three model spectra are scaled by 0.07/0.084 according to the ^{56}Ni mass in SN 1987A and in the model. 74

3.29 Same as Fig. 3.28, but it now shows the comparison of the Hα profile in the velocity space between observation (solid) and model D127_NT (dashed). . . 75

3.30 Left panel: montage of observed optical spectra of SN 1987A. The days since breakout are shown below each spectra. Right panel: montage of synthetic spectra of the non-thermal sequence. Each observed spectrum on the left is compared to a synthetic spectrum at roughly the same time since explosion. The synthetic spectra are reddened with E(B-V) = 0.15 and scaled for a distance of 50 kpc. 76

3.31 Comparison of the energy fractions of the three γ-ray decay channels in models in which we have artificially scaled the excitation or ionization cross sections. The model used for testing is the one at day 127 without including Fe I. Left: The 3 test cases of scaling the impact excitation cross sections. The scaling conditions are denoted in the figure. Different colors are fractions of different channels. The solid lines shows the fractions of the original model. The dotted lines, the dashed lines and the dashed-dotted lines represent the EH5 model, the EM5 model and the EA5 model, respectively. Right: The same as the left, but it shows the 3 cases of scaling the impact ionization cross sections. The dotted lines, the dashed lines and the dashed-dotted lines show the channel fractions of the IH5, IM5 and IA5 model, respectively. 78

4.32 The ejecta properties of the adjusted models (black solid), which are used as initial models for CMFGEN, and of the original hydrodynamical models (red dashed) from V1D. The hydrodynamical model has a progenitor mass of 11 $M_\odot$, 15 $M_\odot$, and 20 $M_\odot$ from the top to bottom. 94

4.33 Comparison of the temperature structure (left) and the spectra (right) between two identical and homologous models computed by the Hubble solver (red) and the fully-relativistic solver (blue). The red curves are overlapped by the blue curves in both plots, indicating identical solutions for the two solvers. 95

4.34 Left column: variation of the departure coefficients of H I (top), O I (middle), and Fe II levels versus Rosseland optical depth for model s20_v1d at 3.94 d after shock breakout. Right column: same as left, but for the model s20_v1d at 21.9 d after shock breakout. Non-LTE level populations computed by the fully-relativistic solver match closely their LTE counterpart in regions where the Rosseland mean optical depth $\tau_{\rm Rosseland} \gtrsim 10$. Departure from LTE is prevalently seen above $\tau_{\rm Rosseland} \approx 10$. 96

4.35 The quantity $T_n(\frac{V_n}{V_0})^{1/3}$ as a function of ejecta velocity for sequence s11_v1d (left) and s15_v1d (right). The time since breakout is differentiated by a color coding. For pure adiabatic expansion, $T_n(\frac{V_n}{V_0})^{1/3}$ represents the initial temperature of the ejecta, and thus these curves would lie on top of each other. 97

4.36 Model temperature evolution for the s11 sequence from 1.2 to 15.75d since explosion, which is encoded in color. 99

4.37 Top: Global energy constraint for a model in simulations based on s11_v1d. The left panel show the "conserved luminosity" (red; $r^2_{\rm max}H(r_{\rm max})$), the depth-dependent luminosity (blue; $r^2H(r)$), the $D(r^4J)/(cr^2Dt)+\beta\sigma r(J+K)$ term (green; $-\int_r^{r_{\rm max}}\left[\frac{1}{cr^2}\frac{D(r^4J)}{Dt}+\beta\sigma r(J+K)\right]dr$), and the radioactive decay term (magenta; $\frac{De_{\rm decay}}{Dt}$) in Eq. 4.20 as a function of ejecta velocity. Bottom: same as top, but for a model in simulations based on s20_v1d. 102

4.38 Evolution of photospheric velocity V_4 (black; $V_4 = V_{\rm phot}/10^4\,{\rm km\,s^{-1}}$), photospheric radius R_{15} (red; $R_{15} = R_{\rm phot}/10^{15}\,{\rm cm}$), and photospheric temperature T_4 (blue; $T_4 = T_{\rm phot}/10^4\,{\rm K}$) for the simulations based on model s20_v1d. . . . 103

4.39 Evolution of the ejecta gas temperature from 4 to 134 d since shock breakout in the simulations based on model s20_v1d. Stars give the position of the photosphere. A color coding is used to differentiate the epochs. 104

4.40 Top: bolometric light curve for the simulations based on model s20_v1d. Bottom: UBVRI light curves for simulations based model s20_v1d. 105

4.41 Spectral evolution for simulations based on model s20_v1d. Early spectra are blue and emission lines are rather weak. Hα (6563 Å) and Ca II triplet (around 8600 Å) are quite broad at early times, but Ca II triplet does not develop until 6d. The line-blanketing effect (mainly below 5000 Å) becomes prominent after 14d. The continuum fades gradually from 110d and the ejecta enters its nebular phase. 107

5.42 This figure is the HST/WFPC2 image obtained in 1995. The lines show the positions of the slits in different observations. The three vertical slits are the central three slits of the mapping observation in 2000. There are 49 observations with different offsets from the central source, covering the whole Homunculus. The other 4 lines (almost horizontal) show the slit positions and slit orientation in the December 2002 observations, which provide good information to explore the variation in SE lobe near periastron passage, just before the start of the low ionization state. 114

5.43 An illustration of the typical variation in Hα profiles along the slit offset by 0.75″ from the central slit with their positions shown on the left of the profiles. As we move up along the slit, the absorption component gets smaller and perhaps disappear around 5″. A reflection component from the rear of the NW lobe gives rise to a second broad component at $v \sim 1200\,\mathrm{km\,s^{-1}}$. 116

5.44 Illustration of the Hα and [N II] blend in the core of the Homunculus (left panel). The profiles are complex blend of scattered and intrinsic emission. The right panel shows the location of the regions sampled in the left panel. Note that η Carinae is at the position in the bottom left corner. 117

5.45 The EW map and the uncertainty map. The color bars show the range for each map. The coordinates are in unit of arcseconds, with the origin on the central source. The dark vertical stripe in the left image contains corrupted data, while the red-cross is due to the diffraction spikes originating from the HST secondary mirror support structure. 119

5.46 Illustration of Hα profiles from the central (red) and the right (blue) stripes at low (left panel) and high (right panel) latitudes in the NW lobe, with the coordinates shown in the square brackets. The dashed lines indicate the locations of [N II] 6548 Å, Hα 6562.8 Å and [N II] 6584 Å lines with a systematic velocity shift of 180 km s^{-1} (left panel) and 300 km s^{-1} (right panel) with respect to the rest wavelength of Hα. 122

5.47 Profile comparison of SE lobe between two data sets described in § 5.2. The map on the right in each plot is an EW map, using histogram equalization as an image processing method to increases the local contrast. The black profiles belongs to the 2000 data set recorded at PA = -35°, and the red profiles come from the 2002 data set recorded at PA= -115°. The red line in the right map of each panel shows the slit in the 2002 observation and the green square marks the position that we are looking at. As one can see, this second observation covers part of the "EW sword" and the "hole". 123

5.48 Left panel: radio emission extracted from Duncan and White [97]. The image is taken in March 2000, which is the same period as the optical spectroscopic observation. Since the slit has a non-zero orientation in our data sets, we have rotated the image 35° clockwise to facilitate comparison with our EW map. Right panel: central part of the EW map in greyscale. 125

5.49 Illustration of Hα profiles at the "EW sword" (red) and nearby regions (blue and green). The dashed lines indicate the locations of [N II] 6548 Å, Hα 6562.8 Å and [N II] 6584 Å lines with a systematic velocity shift of 150 km s^{-1} (left panel) and 205 km s^{-1} (right panel) to the rest wavelength of Hα. 126

5.50 Illustration of Hα emission images at various wavelengths. The central stripe is due to CCD bleeding effect mentioned previously. Diffraction spikes can also be seen in some of images. The "hole" and the "paddle" are discernible in the images. Note that the fluxes in the EW "sword" region are slightly smaller than its surroundings in the images with wavelengths of 6525 Å, 6553 Å, 6609 Å, 6664 Å, and 6720 Å. 127

5.51 Top two panels: illustration of pixel-to-pixel variation – four nearby continuum-normalized profiles are plotted with the spatial coordinates indicated in the square bracket and the EW and uncertainty indicated after the colon. The subpanel focuses on the normalization of the four profiles. Bottom pair of panels: same as upper panel but shows another example of small scale variations. A careful study of the plots at higher resolutions show that the profiles also differ in shape. For example, in the lower panel the green profile is significantly broader on the long wavelength side than the black profile. Such a variation cannot be due to an error in the normalization of the continuum. 129

5.52 Comparison of a Hα profile in the NW lobe (dashed profile; coordinates indicated in the square brackets) with that of the central source (solid profile). The continua have been rectified to unity, and the two profiles have been shifted so that they are aligned. The Hα profile of the central source is much stronger that that of the lobe. The later shows strong "nebular" absorption. 130

5.53 The EW map overlapped by a 3D axisymmetric model using the geometry of the Homunculus obtained by [337]. The model is tilted 41° according to the results in Davidson et al. [82]. It is also rotated 13° clockwise to align with the polar axis of the Homunculus. Obviously, the SE lobe is not perfectly axisymmetric. 132

5.54 Comparison of Hα line profiles from four spatially distinct locations in the SE lobe. The four profiles have been normalized to unity continuum and shifted in wavelength to allow convenient comparison. The bottom left panel shows the same profiles as the upper left panel, but focuses on the absorption component. The right panel indicates the positions of the four profiles with corresponding colors. Note the striking similarity in the absorption component for the 45° pair (red and blue), and for the polar pair (green and magenta). 135

5.55 A map of velocity at the minimum of the absorption component with respect to the centroid of the Hα profile in the SE lobe. 136

5.56 Illustration of optical depth maps of SE lobe with g of 0.3 (left), 0.5 (middle) and 0.8 (right) in the phase function. The color contours correspond to levels of 0.005 (black), 0.02 (red), 0.05 (blue), 0.1 (green), and 0.2 (magenta). . . . 137

5.57 Top: Comparison of a Hα profile in SW lobe (black) with those of the P Cyngi stars HDE 316285 (red) and P Cygni (blue). Notice how shallow the absorption component of Eta Car is compared with that of the other 2 stars. Bottom: same as top panel, but shows the comparison of Hβ profiles. 137

5.58 2D radiative transfer simulation of Hα profile from pole-on (red) and 45 degree (blue) views based on scaled 1D models. The velocity is assumed to scale like $1 + 0.3\cos^4\theta$. At 90 degree, $V_\infty = 650$, while at 45 degree, $V_\infty = \sim 540\,\mathrm{km\,s^{-1}}$. 138

6.59 Fitting the wings of Hα. The x-axis for all plots is wavelength in unit of Å. The models have a microturbulence of 10 $\mathrm{km\,s^{-1}}$. The synthetic spectra have a resolution of 0.2 Å, similar to the observations. Also, a rotational velocity $v \sin i = 25\ \mathrm{km\,s^{-1}}$ has been applied to the model spectra. Models in the same panel have the same temperature, and the temperatures in the plot from top to bottom and from left to right are 20500, 21000, 21500, 22000, 22500, 23000, 23500, and 24000 K, respectively. 157

6.60 Same as Figure 6.59, but illustrate the fit to Hβ. 158

6.61 The Balmer jump comparison of the NGSL spectrum and synthetic spectra with $T_{\rm eff} = 22000$ (top), 23000 (middle), and 23500 K (bottom). All synthetic spectra have been scaled to fit the discontinuity at 3646 Å. 160

6.62 The best EW fitting models (symbols) for $\xi = 10\ \mathrm{km\,s^{-1}}$ (left panel) and $\xi = 15\ \mathrm{km\,s^{-1}}$ (right panel). The lines are the least square fits to the dots with corresponding colors. Note that the fitting lines for Si III 4568 (blue) and 4575 Å (green) are overlapped in the top panel, and the fitting lines for Si III 4553 (red), 4568 (blue) and 4575 Å (green) are overlapped in the bottom panel. The models with the best Hβ wing profile fitting (black) are also shown for assistance. 162

6.63 Comparison of spectral energy distribution for models T235g33M1em8 (black solid) and T220g32M1em8 (black dashed) with observations. The synthetic spectra have been scaled by a distance of 124 pc. The EUV spectrum (red) has been corrected for interstellar neutral hydrogen with column density of 1×10^{18} cm^{-2}. The IUE (blue) and NGSL (green) spectra have been smoothed to a resolution of 5 Å. Other photometric measurements are also indicated in the figure. While there is broad agreement between the model and observations, a significant discrepancy can be seen in the UV range(around 2000 Å). 163

6.64 Top: comparison of synthetic and observed spectra in the UV band. The plot shows the quantity $\lambda^3 F_\lambda$ to facilitate comparison. Synthetic spectra for model T235g33M1em8 (black solid) and T220g33M1em8 (black dotted), and observed IUE (blue) and STIS NGSL (green) spectra are illustrated. The UV photometry from S2/68 (magenta) observation is also shown. Bottom: same as the top, but a reddening of $E(B-V) = 0.032$ is applied to the synthetic spectra. All spectra have a resolution of 5 Å. 164

6.65 Same as the Figure 6.65, but a reddening of E(B-V)=0.032 has been applied to the synthetic spectra. With a non-zero reddening there is a much better agreement between model and observations in the UV range. 165

6.66 Spectral comparison at UV band around 2200 Å. Synthetic spectra of models T235g33M1em8 with reddening of E(B-V) = 0.032 (black) and without reddening (red), and of model T220g32M1em8 without reddening (green) are compared with STIS/NGSL observations. All synthetic spectra have been scaled to fit the observations around 3500 Å. Notice how the reddened model matches the observations much better over the relatively line-free region extending from 2100 Å to 3000 Å. 166

6.67 Comparison of EUV spectra with different mass loss rates. The EUVE observation is provided for reference (black). All models have been normalized in the optical. While models with this temperature and gravity match optical diagnostics they provide a poor fit to EUV observations, even after allowing for significant mass-loss by a stellar wind. 169

6.68 Illustration of Hα profiles for models with the same $T_{\rm eff} = 23500\,{\rm K}$ and $\log g = 3.3$, but with different ass loss rates. The mass lost rates are indicated in the plot. Notice that, some parts of the Hα wings in the $\dot{M} = 2 \times 10^{-8}\,{\rm M}_{\odot}\,{\rm yr}^{-1}$ model (blue) are above the continuum. 170

PREFACE

Foremost, I would like to express my sincere gratitude to my supervisor Prof. John Hillier for the continuous support of my Ph.D study and research, for his patience, motivation, enthusiasm, and immense knowledge. I also thank him for providing me all possible opportunities to broaden my knowledge of different areas in astrophysics and cosmology.

I am also indebted to my committee members Prof. Michael Wood-Vasey, Prof. Andrew Zentner, Prof. Steve Dytman, and Prof. Rupert Croft, for their insightful comments, and hard questions.

My endless thanks to Dr. Luc Dessart for his useful and helpful comments on the project of non-thermal processes in supernovae, as well as the provision of hydrodynamical models in the fully-relativistic transfer study. My sincere thanks also goes to Prof. Mairan Teodoro for his great patience in answering my questions and providing perceptive suggestions.

I would like to thank my parents for supporting me spiritually throughout my life. Last but not the least, I would like to thank my wife for her understanding and continuous support.

1.0 INTRODUCTION

1.1 EVOLUTION OF MASSIVE STARS

1.1.1 Stellar evolution

Stars are the most important constituent of galaxies. They vary greatly in mass, brightness, size, temperature, and color, of which mass is the most important property. In 1924, Arthur Eddington discovered the Mass-Luminosity Relationship $L \propto M^{\alpha}$, with $\alpha \sim 3.5$ for main-sequence (MS) stars between $2\,\mathrm{M}_{\odot} < \mathrm{M} < 20\,\mathrm{M}_{\odot}$. As the lifetime of a star, t, is expected to be $\propto M/L$, we have $t \propto 1/M^{\alpha-1}$ with the Mass-Luminosity Relationship, which indicates more massive stars live shorter lives.

All stars spend about 90% of their lives as MS stars, during which their released energy is produced by nuclear fusion of hydrogen into helium in the dense core. During the MS phase, the stars are in hydrostatic equilibrium and the inward gravitational force is balanced by the outward thermal pressure. When hydrogen is exhausted at the core, stars leave their MS phase and evolve to the post MS phases, which differ dramatically for stars with different masses.

Stars with masses $0.4\,\mathrm{M}_{\odot} < M < 8\,\mathrm{M}_{\odot}$[1] undergo core contraction after hydrogen is depleted at the core, while the hydrogen shell continues to burn. Energy released by gravitational collapse heats up the helium core and hydrogen shell, increasing the nuclear reaction rates and thus the output energy, which causes the star to expand significantly to become a red giant and the star ascends the red giant branch (RGB). When the temperature and pressure in the core become sufficient to ignite helium, the helium core is electron-degenerate

[1] Stars with masses less than about $0.4\,\mathrm{M}_{\odot}$ can lives longer than the age of the universe.

for stars with mass $M < 2\,M_\odot$, which prevents core expansion as helium fuses. This results in a rapid increase in the helium fusion rate, which is termed the helium flash, and a continuous increase in the temperature. Stars with $M > 2\,M_\odot$ are spared the helium flash, since helium ignites before the core becomes degenerate. As the star burns helium in the core and hydrogen in the shell, it evolves on a stage called the horizontal branch. Helium finally is exhausted in the core, the core contracts further and becomes degenerate. At this stage, helium shell burning occurs under the hydrogen shell burning. This evolutionary track on the Hertzsprung-Russell (H-R) diagram is called the asymptotic giant branch (AGB). After AGB, the star ejects its outer layers, leading to the formation of planetary nebula. All stars with $M < 8\,M_\odot$ develop electron-degenerate cores and lose their envelopes, and finally become CO[2] white dwarfs (WDs).

The post MS evolution of stars more massive than $8\,M_\odot$ is complicated and may involve many phases like red supergiant (RSG), blue supergiant (BSG), Wolf-Rayet (W-R) star, and luminous blue variable (LBV). Despite the paramount role of mass in stellar evolution, many other factors can also have a substantial influence on the evolutionary path of massive stars, e.g., mass loss via a stellar wind, rotation, chemical composition, magnetic field, and whether the star is a binary or not.

There are mainly three broad classes of stellar winds – radiative, coronal, and hybrid [46]. In the coronal model for cool stars, the wind is thermally or pressure driven – the outward force counteracting the gravitational force comes from the gas pressure gradient induced by high temperature at the corona. Such a wind hardly influences the evolution of the star, although it can lead to a spin down of the star by transferring angular momentum from the star to wind. For hot stars (OB types), the wind is driven by radiation pressure and is able to carry away up to a few tens of solar masses over the stars lifetime, and this substantially affects their evolution. By losing mass through winds, these stars also change their envelope compositions by exposing deeper layers. A hybrid model is a combination of the previous two models and was proposed by Hearn [159] to explain the X-ray in OB stars [48, 47].

Rotation also plays an important role in stellar evolution by inducing internal mixing [252, 160], particularly for OB stars which are rapid rotators (stars like the Sun spin much

[2]CO: carbon-oxygen

more slowly). On one hand, material from inner is dredged up to the envelope and thus the metal content of the stellar surface is changed. In stars more massive than about $1.3\,M_\odot$, the CNO-cycle, in which carbon, nitrogen, and oxygen act as catalysts to convert hydrogen to helium, is the dominant energy source during the MS phase. However, nitrogen is enriched during CNO burning because the reaction converting nitrogen to oxygen is the slowest one in the cycle. Because of mixing, CNO-processed material with enrichment of helium and nitrogen and depletion of carbon and oxygen is observed [163]. On the other hand, outer hydrogen-rich material is dredged down to the core, which provides more fuel for core burning and lengthens the lifetime of the stars. Rapid rotation can also cause latitude-dependent temperature [389, 253] and mass loss profiles [122, 302, 223].

Binarity is another important factor in stellar evolution. A star in a binary system can accrete mass from or transfer mass to its companion via Roche lobe overflow, which changes the fates of both stars. For example, in a canonical view, Type Ib/Ic supernovae (SNe), which exhibit no hydrogen or helium lines in their spectra, come from stars with MS mass above $25\,M_\odot$ [336], since this is the minimum mass required for the stellar wind to peel of most of its hydrogen envelope, and perhaps helium envelope, so that it becomes a W-R star. However, it is also possible for less massive stars to peel their hydrogen and helium layers in a binary system.

LBVs, which are very bright, blue, and unstable stars, can also lose mass by means of a great eruption [182]. η Carinae, Pistol Star, P Cygni, and S Doradus are well observed examples of LBVs. During the outburst, LBVs can eject tens of solar masses of material [209, 182, 224].

1.1.2 Massive stars

Massive stars, which are considered to be main sequence stars with masses greater than $\sim 8\,M_\odot$, are of great importance in various areas. These stars are hot and possess strong radiation, which can initially photo-dissociate interstellar molecular gas and produce a photo-dissociation region with mostly atomic and partially ionized gas. The Lyman continuum photons can further ionize the H I gas and create a H II region, which is an indicator of

star formation. Massive stars also lose significant amount of mass during their evolution by stellar winds, enriching the surrounding medium with nuclear processed material.

Massive stars are also able to undergo core-collapse at the endpoint of their evolution and explode as SNe. SN explosions are the main factories for heavy elements. They can also trigger star formation by compressing nearby gas. SNe themselves are ideal laboratories to study exotic physics.

Despite their profound impacts, the evolution of these stars is not well understood. The general evolutionary picture for stars with initial mass greater than $\sim 25\,M_\odot$ is summarized by Crowther [68] as following,

$M > 75\,M_\odot$

O $\rightarrow$ WN(H rich) $\rightarrow$ LBV $\rightarrow$ WN(H poor) $\rightarrow$ WC $\rightarrow$ SNIc

$40\,M_\odot \leq M \leq 75\,M_\odot$

O $\rightarrow$ LBV $\rightarrow$ WN(H poor) $\rightarrow$ WC $\rightarrow$ SNIc,

$25\,M_\odot \leq M \leq 40\,M_\odot$

O $\rightarrow$ LBV/RSG $\rightarrow$ WN(H poor) $\rightarrow$ SNIb.

where WNs or WCs are W-R stars that exhibit strong helium and nitrogen, or helium and carbon emission lines. Observationally, there is an absence of RSGs with luminosity greater than $6 \times 10^5\,L_\odot$, known as the Humphreys-Davidson limit [181]. Stars begin their LBV phase as they evolve towards the red. However, the LBV phase is very poorly understood. It may be that stars above $\sim 25\,M_\odot$ all evolve through the LBV phase, or in some cases the LBV phase is totally circumvented. In a classic view, a LBV is only thought to be a transition stage between core-hydrogen burning and core-helium burning in massive star evolution. One of the characteristics of LBVs is their eruptive nature. During their great eruptions, which are called SN impostors, LBVs can eject 10-20 $M_\odot$ material. It is still unknown how the outburst happens. Nearby LBVs, like η Carinae, allow us to explore the nature of LBVs in great detail [77, 186, 337, 365].

Massive stars end their lives through violent explosions as SNe, leaving neutron stars or black holes as their remnants. Depending on the evolution and the progenitor of a star, SNe from massive stars can be categorized into a variety of classes.

1.2 CLASSIFICATION OF SUPERNOVAE

SNe are spectacular events in the sky. The first recorded supernova is SN 185 and was observed by Chinese astronomers in 185 AD. Other pre-telescope examples include SN 1006 – the brightest recorded SN, SN 1054 – the SN that created the Crab Nebula, SN 1572 – Tycho's SN, and SN 1604 – Kepler's SN. Serious and systematic studies on SNe did not begin until 1880s, when the German astronomer Hartwig discovered a super luminous nova, later named the supernova "S Andromedae". The term "supernova" was introduced by Baade and Zwicky [15] and the first classification of SNe was given by Minkowski [273]. As more and more spectral information obtained, four principal spectroscopic types have been recognized – Type Ia, Type Ib, Type Ic and Type II SNe (see Figure 1.1).

Type II SNe show hydrogen lines in their spectra, while Type I SNe do not. Type Ia SNe have a strong Si feature around 6355 Å at maximum brightness (see Figure 1.2), which distinguishes this Type from Type Ib and Ic. Type Ib SNe are characterized by the presence of optical He I lines, while Type Ic SNe show no He lines. With the help of photometry, Type II SNe are further classified into Type II-P and Type II-L (see Figure 1.3). Type II-P SNe show a plateau phase in the light curve. After the plateau phase, there is a significant drop in the brightness. Type II-L SNe show a linear decrease in the light curve. Besides these two subclasses of Type II SNe, three other special types II SNe exist, which are Type IIn, Type IIp and Type IIb. The presence of narrow H emission lines defines Type IIn SNe. The letter "p" for Type IIp SNe represents "peculiar" – SN 1987A is the most famous member of this class. The light curve of SN 1987A are shown in Figure 1.3. Early spectra of Type IIb SNe show the presence of weak H lines, which makes the SNe Type II ones. However, H lines disappear at late times and their spectra resemble those of Type Ib SNe.

The spectroscopy and photometry of SNe convey lots of information, helping to uncover the underlying physics. We are now aware that SNe can be physically classified into two broad categories: thermonuclear SNe (Type Ia) and core-collapse SNe (Type Ib/Ic and Type II; see Figure 1.1).

A Type Ia SN is thermonuclear runaway of a White Dwarf (WD) when it gains material from a companion and reaches the maximum mass that can be supported by the electronic

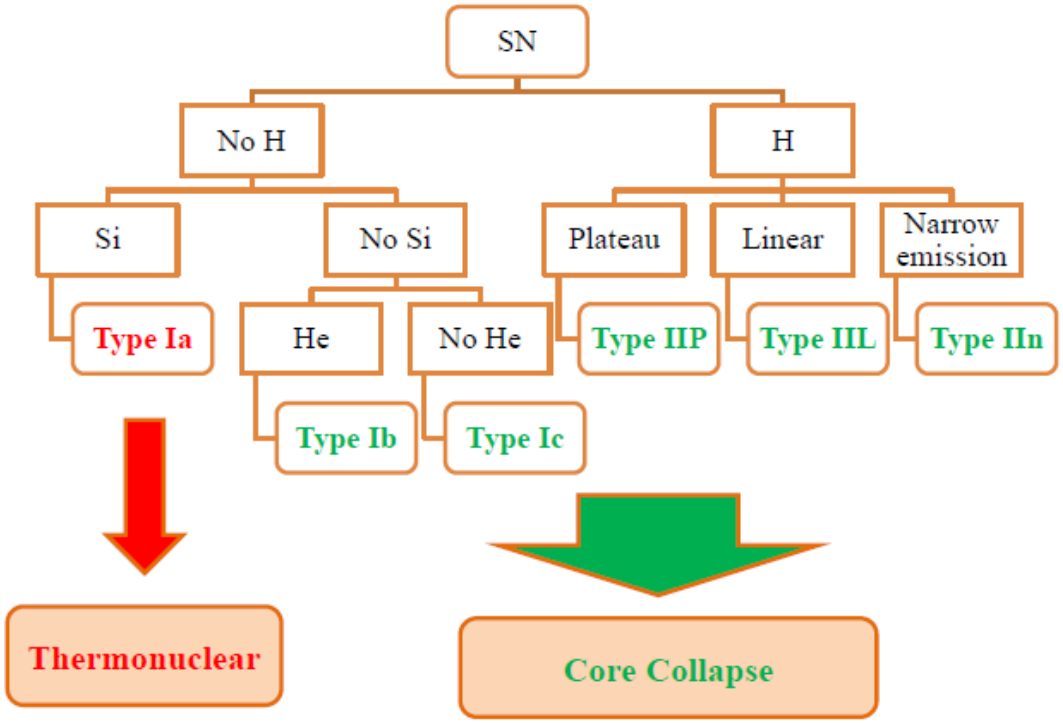

Figure 1.1: Classification of supernovae.

degenerate pressure, which is called the Chandrasekhar mass, around 1.38 $M_{\odot}$. Depending on the companion, the White Dwarf can reach this limit through 2 channels: the single degenerate scenario [SDS; 404, 286] and the double degenerate scenario [DDS; 184, 399]. In the SDS, the WD accretes matter from a companion that could be a RSG, a slightly evolved main sequence star [a subgiant; 288, 243, 198, 151, 227], or a helium star [244, 152, 417, 391, 246]. In the DDS, two WDs lose energy through gravitational wave radiation, and merge to exceed the Chandrasekhar mass. The early detection of Type Ia SN 2011fe in the Pinwheel Galaxy (M101) at a distance of 6.4 Mpc revealed rich information on the nature of its progenitor [291]. The inferred upper limit for the radius of the progenitor star, $R_0 < 0.1R_{\odot}$, and the strong spectral features of carbon and high-velocity oxygen observed at early time strongly indicated a carbon-oxygen WD for its progenitor [291]. Li et al. [241]

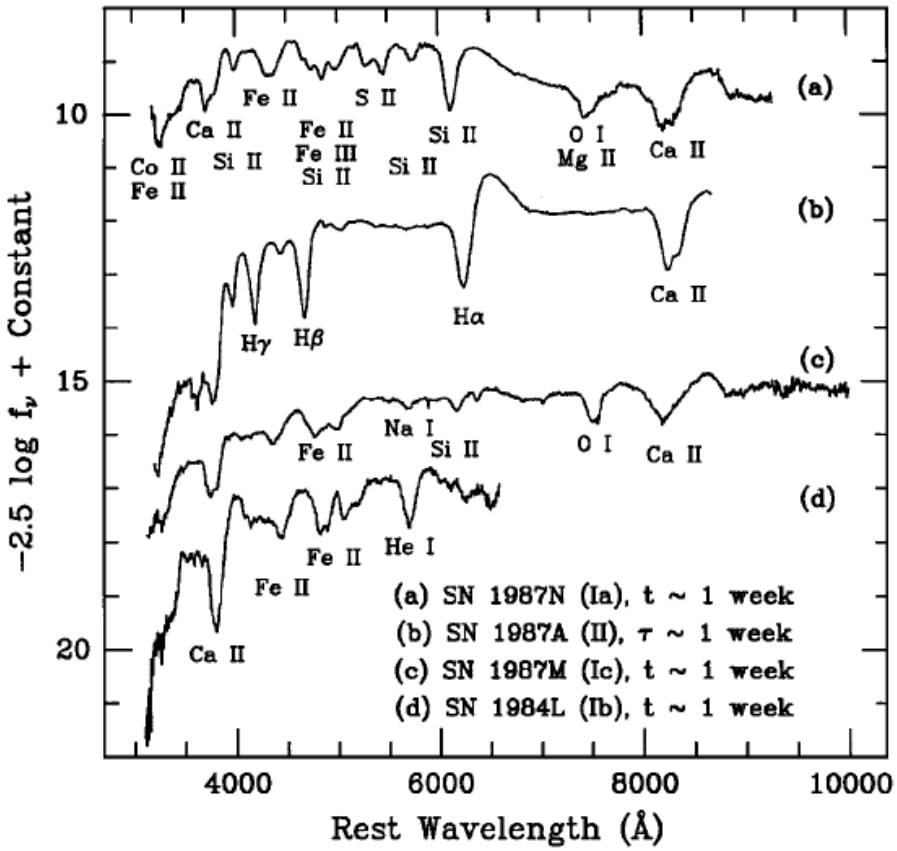

Figure 1.2: Spectral features of different types of SNe at early time. t and τ denote the time after B-band maximum and the time after core collapse, respectively. This figure is taken from Filippenko [116].

ruled out luminous red-giants and almost all helium stars as the mass-donating companion for SN 2011fe.

In the above two channels, carbon is ignited when the WD reaches or exceeds the Chandrasekhar mass. However, sub-Chandrasekhar model are also considered as a viable channel [287, 413, 412], in which helium ignition that happens at the shell of the WD triggers the carbon ignition at the core, disrupting the WD. This channel has been suggested to account for the observed Type Ia SNe rate [419, 383, 16], since there are not sufficient explosions from both Chandrasekhar and super-Chandrasekhar channels.

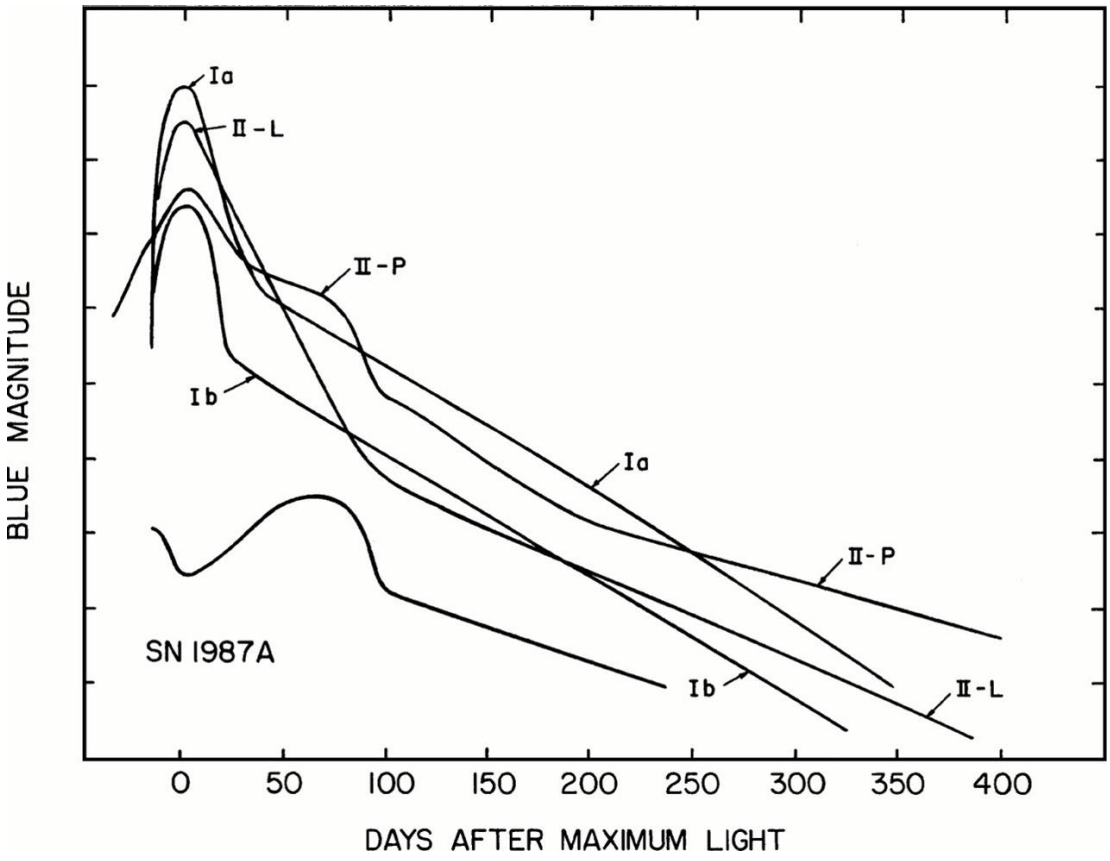

Figure 1.3: Light curves of various types of SNe. This figure is taken from Filippenko [116]. Type Ia are powered by radioactive decay for most of the evolution – even pre-maximum. Type IIP are powered by shock and recombination energy until they become thin. Type Ibc also tend to be powered by nuclear decay. While Type II-P SNe are characterized by a plateau phase after maximum, Type II-L SNe display a linear light curve at the tail. Light curves of Type Ib/c SNe resemble those of Type Ia SNe, but have a variety of decline rates. SN 1987A (Type IIp) exhibit a slow rise to maximum.

Since this thesis is concerned with core-collapse SNe (CCSNe), emphasis will be put on this physical type, particularly Type II-P. CCSNe are violent deaths of massive stars, which have main sequence masses $\geq 8\,M_{\odot}$ and they are able to burn elements heavier than helium during their evolution. Different spectroscopic types reflect the fundamental difference among their progenitors. The plateau phase of Type II-P SNe indicates a extensive hydro-

gen envelope ($\sim 10\ M_\odot$) of the progenitor [135, 51, 111]. Initially, the shockwave propagates through the envelope and heat the material up to very high temperature [$\gg 10^5$ K; 207], causing ionization of all hydrogen and acceleration of the ejecta. As the ejecta expands and cools to $\sim$6000 K, hydrogen starts to recombine, forming the so-called recombination wave. When the recombination wave moves inward, recombination energy, and energy deposited by the shock is released, which balances the expansion and maintains a roughly constant temperature and luminosity during the plateau phase [e.g. 135, 377, 90]. As the photosphere recedes into the helium core, and all hydrogen has recombined, there is a sudden drop in the luminosity. The tail of the light curve is then powered by the radioactive decay from iron group elements [see 229, and references therein].

While Type II-P SNe posses an extensive hydrogen envelope, Type II-L, Type IIb, Type Ib/c show various degrees of stripped hydrogen envelope. Type II-L SNe show hydrogen lines but no plateau phase, which means the hydrogen envelop is relatively smaller than that of Type II-P (about 1-2 $M_\odot$). A Type IIb supernova only shows hydrogen lines at very early time and then the spectra resembles that of a Type Ib supernova, implying very little hydrogen left before the explosion. The absence of hydrogen lines and presence of helium lines in a Type Ib SN reveal that the progenitor has lost the whole hydrogen envelop – even a small amount of hydrogen in the envelope would be detected in pre-maximum spectra [93]. Type Ic SNe show neither hydrogen nor helium lines and might have lost most of their helium. Therefore, in the single-star scenario, the SNe progenitor from not stripped to more stripped follow the sequence: II-P $\rightarrow$ II-L $\rightarrow$ IIb $\rightarrow$ Ib $\rightarrow$ Ic[3]. Since more massive stars have stronger winds and they tend to lose their envelop more easily, the main sequence mass of the progenitor mass from less massive to more massive follow the same sequence above. However, supernova types are not distinct. Some SNe might sit between the definition of the above types, and resemble one type at one time and another time at another time.

Introduced by Schlegel [326], Type IIn SNe are quite different in that they exhibit narrow hydrogen emission lines – an indication of a strong interaction between the SN and some slow moving material, which is the immediate dense circumstellar material (CSM) ejected

[3]There are both observational and theoretical constraints supporting the binary-star progenitor scenario [see 123, and references therein].

by the progenitor right before the explosion [346]. Such dense CSM requires LBV-like giant eruptions and mass ejections within decades before explosions, which is the reason why Type IIn SNe have been frequently associated with LBVs [212, 126, 301, 338]. However, there are two aspects to the problem of an LBV progenitor. One is that a LBV is not expected to explode as a SN, and the other is that observed LBVs generally do not explode in decades after great eruptions. The former is due to that the stars are still core H or core He burning, while the latter requirement arises because the ejecta must be sufficiently dense to decelerate the SN expansion and to convert kinetic energy to thermal energy, producing the remarkably high luminosity of Type IIn SN. Other mechanisms have also been proposed to explain Type IIn SNe, for example pair-instability[4] [e.g. SN 2007bi, 127] and pulsational pair-instability [e.g. SN 2006gy, 414]. η Carinae is a well-observed case and it is expected to explode as a Type IIn SN in the near future [see the review by 77]. It underwent occasional outbursts and may explode at anytime. Intense attention has been paid on it. We will present our study on η Carinae in part III of this thesis.

Type IIn SNe are rare and an inhomogeneous class. Individual Type IIn SN has attracted great interest in the SN community. Some notable examples in this category include: SN 1988Z [355, 372, 382, 55, 108, 8, 407, 328], SN 1994W [371, 351, 327, 57, 92], SN 1998S [31, 113, 131, 233, 245, 7, 53, 114, 231, 56, 311, 312, 121, 313], SN 2005gl [126, 125, 100], SN 2006gy [345, 293, 342, 347, 3, 199, 272, 348]. SN 2005gl is the only case that we found a valid possibility for a LBV-like progenitor, while SN 2006gy is the most luminous SN that has been ever observed. Properties of the above Type IIn SNe show substantial differences. SN 1988Z showed a slow decline rate in its light curve, while SN 1998S exhibited a fast decline rate. SN 1994W showed a plateau phase after maximum, while others fade gradually after the peak. Briefly speaking, Type IIn SNe show a wide range of maximum magnitudes and a variety of light curve shapes.

Type IIp SNe are also different. These SNe have peculiar properties, differentiating them from normal Type II SNe. SN 1987A is the most famous in this category. SN 1987A exploded in the Large Magellanic Cloud, only $\sim$ 50 kpc away, which provided an excellent

[4]The collisions between energetic γ-rays and atomic nuclei result in the creation of electron and positron pairs, which reduces the thermal pressure and leads to a partial collapse of the core.

opportunity to study it in great detail. Its progenitor, a BSG, had been directly detected [133]. However, there is still a lot of debate on why an evolved star should explode as a BSG, rather than as a RSG. A companion star in a binary system is thought to play an important role [107, 196, 309, 84, 19]. The light curve of SN 1987A rises slowly to an optical peak before the nebular epoch. SN 1998A is a similar member of this group, with its light curve resembling that of SN 1987A. Pastorello et al. [300] showed that the progenitor of SN 1998A is also a BSG. SN 2000cb, as noted by Kleiser et al. [208], is another Type IIp SN with peculiar properties. Its light curve shape resembles that of SN 1987A , but its spectra resemble those of normal SNe. While normal Type II SNe have relative homogeneous properties, Type IIp SNe have diverse properties in both photometry and spectroscopy. SNe from BSGs are generally less luminous than SNe from RSGs due to the smaller size of the progenitor at the time of explosion.

1.3 THE IMPORTANCE OF CORE-COLLAPSE SUPERNOVAE

CCSNe play an important role in enriching the environment with metal. A CCSN ejects several solar masses material into the interstellar medium (ISM). Half of the material is unprocessed, and the other half is in the form of helium and heavy elements. Most of the processed material are α elements, like ^{4}He, ^{12}C, ^{16}O, ^{20}Ne, etc. A typical CCSN can produce 0.07-0.15 $M_{\odot}$ of Nickel, which is the energy source for the tail of its light curve. CCSNe also provide the most promising way to produce half of the isotopes heavier than the iron-group elements through the r-process[5] [409].

The shock wave induced by the CCSNe explosions can trigger the nearby star formation. The material ejected by the explosion gains large kinetic energy and moves at a very high speed. If there is a molecular cloud nearby, the fast moving material would compress it. Once the gravity kicks in, new stars form.

CCSNe are also potentially efficient dust producers, though this is still debated [276, 99,

[5]Rapid neutron capture process, in which neutron flux is so high that neutron captures occur faster than β decay.

290, 211, 101]. Dust is an important issue to understand the nearby and distant universe. It has long been recognized that ISM is extremely inefficient in forming dust due to longer time scale of dust formation than that of destruction [370]. Low mass stars cannot explain the dust in the early universe when the age of the universe is smaller than the evolutionary time of low mass stars. CCSNe naturally become the suitable sites for producing the dust, although this is still a open question. The average mass of newly formed dust per CCSN is 10^{-4}-$10^{-3}\,M_\odot$ from observations [105, 266], while calculations show a demand for $1\,M_\odot$. However, simulations have no difficulty in producing such a large amount of dust [290]. Answering the question whether CCSNe can be responsible for dust production requires more observational and theoretical studies of such objects.

CCSNe themselves are of great interest in extreme physics. All four known fundamental forces are involved in the violent explosion. Nuclear and neutrino physics are required to determine to the equation of state (EOS) and the nucleosynthesis. The dynamics of the explosion demands the treatment of magneto-hydrodynamics (MHD) and plasma physics. Neutrino transport is also found to be crucial. General relativity is inevitably involved, since the explosion itself is induced by gravitational collapse of an object only a few times larger than the Schwarzschild radius. Therefore, CCSNe provide an excellent testbed to verify our understanding of extreme physics [190].

Type II SNe have also been used to measure cosmological distances. Type II-P SNe are the most common type of SNe in the universe [255, 43, 336]. There are two methods of measuring the distance using Type II SNe in the literature. Both are primary distance indicators – they do not require calibration. One of them is the expanding photosphere method (EPM) proposed by Kirshner and Kwan [204], and the other is the spectral-fitting expanding atmosphere method (SEAM) [20, 21].

The EPM assumes that a Type II SN radiates as a blackbody up to a dilution factor ξ (also called correction factor), i.e.,

$$f_\nu^{\rm obs} = \xi^2\theta^2\pi B_\nu(T) = \xi^2\left(\frac{R_{\rm phot}}{D}\right)^2\pi B_\nu(T) \tag{1.1}$$

where the $f_\nu^{\rm obs}$ is the observed flux, $R_{\rm phot}$ is the radius of the photosphere, D is the distance to the supernova, $\theta = R_{\rm phot}/D$ is the photospheric angular size, and T is the temperature

where photons are thermalized and in practice it is replaced by the color temperature T_c (see below for derivation of T_c). If reddening is applied, the observed flux will be replaced by the de-reddened observed flux $f_\nu^{\rm obs} = 10^{0.4A_\nu} f_\nu^{\rm obs}$. Assuming a simple explosion, $R_{\rm phot}$ is given by

$$R_{\rm phot} = v_{\rm phot}(t - t_0) + R_0 \tag{1.2}$$

where $v_{\rm phot}$ is the velocity of the photosphere and can be measured by the P Cygni profile of some lines, for example Fe II, t_0 is the time of explosion, and R_0 is the initial radius at the onset of the explosion. As the ejecta expands substantially and "forgets" its initial radius, R_0 becomes negligible and the ejecta approaches homologous expansion[6]. However, t_0 must be accurately determined. Therefore, the photospheric angular size θ and the expansion velocity $v_{\rm phot}$ at more than two epochs, t_1 and t_2, are required. Then, the distance can be obtained by

$$D = \frac{t_2 - t_1}{\theta_2/v_2 - \theta_1/v_1} \tag{1.3}$$

While the color temperature T_c is obtained by matching the slope of the corresponding blackbody to a set of observed magnitudes, the difficult part of EPM lies in the determinations of correction factor ξ. With ξ and T_c obtained by fitting the synthetic and observed photometry, the angular size can be acquired from Eq. 1.1. The EPM has been successfully applied to measure distance to SN 1987A [102], but the application to SN 1999em fail to give a result consistent with that from Cepheid variable stars [235], which gives the best distance measurements to over 30 galaxies within 23 Mpc [236]. Recently, [86, 87] revisited the EPM and found their correction factors are systematically higher than the ones of Hamuy et al. [155], which provides a good consistency to the measurement from Cepheids.

The physics behind the correction factor ξ includes several aspects. Firstly, the blackbody temperature T in Eq. 1.1 corresponds to the layer where photons are thermalized ($R_{\rm th}$), rather than the layer from where photons escape ($R_{\rm phot}$), due to strong contribution of the electron-scattering opacity to the total opacity, which introduces a global flux dilution.

[6] $R_{\rm phot} = v_{\rm phot}(t - t_0)$. Depending on the size of the progenitor, the time required for SN ejecta to become homologous varies from 1 day to several weeks.

Secondly, because of the finite extent of the photosphere, $R_{\rm th}$ varies with wavelength, with larger $R_{\rm th}$ seen in longer wavelengths, which corresponds to lower thermal temperature and weaker dilution. As a result, the emergent flux distribution resembles more a Planck function with a cooler temperature. This is sometimes called the "sphericity" effect. Finally, the correction factor accounts for line blanketing in the SN atmosphere.

The idea of the SEAM is quite similar to EPM, but avoids the dilution factor and the color temperature, and instead fits the synthetic spectrum to the observed spectra directly. Physical quantities are derived from fitting and the radius is determined by assuming a Hubble flow $R = vt$. Dilution factors are no longer needed, but all information of spectral energy distribution (SED) is required. This method has been applied to several SNe, and gives good results [20].

Both EPM and SEAM have their own advantages and disadvantages. The advantage of EPM is that it relies primarily on photometry, which is easily obtained. Spectra are only required to determine $v_{\rm phot}$, and these need not have high signal-to-noise ratio (S/N). However, good quality spectra and all information of the observed SED are required in SEAM to reproduce the an overall fit. The disadvantage of EPM is that it depends sensitively on the derivation of correction factor ξ, which is sensitive to isolated features in the spectra. SEAM does not assume a blackbody and hence avoids the use of correction factors.

In spite of their lower luminosity than Type Ia SNe, Type II-P SNe potentially suffer less evolutionary problems as distance indicators. The cosmic evolution of Type Ia SNe with metallicity is poorly understood [176, 322, 230, 118, 34, 104] and this introduces uncertainties into their calibration. The plateau phase of Type II-P SNe is largely determined by the extensive hydrogen envelope, which is hardly affected by the metallicity. As the massive stars trace the star formation, we also expect plenty of Type II SNe at high redshift. Type II SNe also provide an alternative approach to compliment Type Ia SNe, since they should have very different systematic uncertainties.

1.4 THE PROBLEMS OF CORE-COLLAPSE SUPERNOVAE

After several decades of theoretical and observational studies of CCSNe, there are still lots unsolved problems. In this section, several major problems are discussed. 1) What are the progenitors for different types of SNe? It is widely accepted that CCSNe are explosions of massive stars, while the mass range of each type is quite open and hotly debated. 2) What are the explosion mechanisms? Various theories have been suggested to disrupt the bulk of material [see 190, see Sec. 1.4.2], but simulations can only explode low mass models and no robust explosion has been achieved yet. 3) What is the scale of mixing and what causes the mixing? In this thesis, the primary gaol is to improve the tools and techniques so that we can better synthesize the spectra of CCSNe and place strong constraints to their progenitor systems and to provide useful constraints on explosion models.

1.4.1 Progenitor problems

The relative frequency of SN types have been reported by several studies [42, 381, 314, 336, 242]. Different studies have different volume size. The sample of Cappellaro et al. [42] contains SNe out to 100 Mpc, while the study of van den Bergh et al. [381] reaches a distance out to 140 Mpc. These studies contain different samples from different surveys and the surveys may be biased (e.g., only large galaxies searched).

Cappellaro et al. [42] used a combined sample from various surveys. Figure 1.4 shows the latest statistics on SN rates from the volume-limited Lick Observatory SN Search [LOSS; 242]. The left panel shows the relative frequency of all SNe. Type Ia SNe take up 24 percent of all SNe, while the rest of SNe, CCSNe, takes up 76 percent. CCSNe are about 3 times more than likely Type Ia SNe. The right panel shows the relative frequency of different types of CCSNe, with Type II-P being the most frequent, about half of all CCSNe.

Our understanding of the fate of massive stars in the single star scenario is summarized in Table 1.1[7] [289]. Stars with main sequence masses below 8 $M_\odot$ do not undergo core collapse. Explosion mechanisms for stars above 8 $M_\odot$ are supposed to depend on the star's main

[7] rotation and mass loss introduce uncertainties into these scenarios.

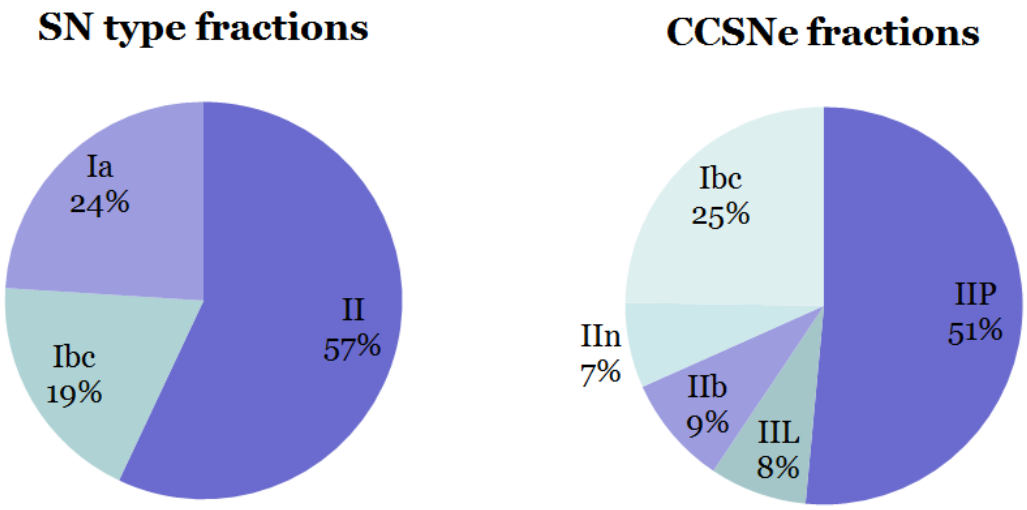

Figure 1.4: Pie charts of fractions for supernova types from the Lick Observatory Supernova Search (LOSS). The left panel shows the fractions of the three broad types of supernovae, while the right panel shows the fractions of subtypes of core-collapse supernovae. The data is taken from Li et al. [242].

sequence mass. Main sequence stars with mass 8-10 $M_\odot$ do not form an iron core. Instead, they have an O+Ne+Mg core before they undergo collapse induced by electron capture[8]. The explosions of these objects are expected to be very weak. 10-90 $M_\odot$ stars are capable of forming a Fe core. When the Fe core reaches the Chandrasekhar limit, it undergoes collapse to a neutron star (NS) or a black hole (BH). Stars with MS masses of 90-140 $M_\odot$ first undergo pulsational pair instability, and finally their Fe core undergo collapse. Higher mass stars are beyond the scope of this thesis, which is only listed in the table for reference.

The most promising means of constraining the SNe progenitor relies on direct detection of their progenitors. Direct detection requires a deep pre-explosion image, which shows the progenitor candidate at the position of the SN site. After the SN explodes and fades out, another image is required to ensure that the progenitor is no longer present. The

[8]A process in which a proton-rich nuclide absorbs an inner atomic electron and changes a nuclear proton to a neutron, and simultaneously emits a neutrino.

Table 1.1: Deaths of massive stars

MS mass	Supernova mechanism
8-10 $M_\odot$	No Fe core, O+Ne+Mg core collapse due to electron capture.
10-90 $M_\odot$	Fe core collapse to a NS or a BH.
90-140 $M_\odot$	Pulsational pair instability, eventually Fe core collapse.
140-300 $M_\odot$	Pair instability supernova.
$\geq$300 $M_\odot$	Direct core collapse to BH or form a GRB.

first detected case was SN 1987A, which had a BSG progenitor. This discovery significantly challenged our understanding that BSGs could not be SN progenitors [164, 11]. Besides SN 1987A, only a handful of progenitors of Type II-P SNe have been directly detected (see Figure 1.5). SN 2003gd, SN 2004A, SN 2005cs and SN 2008bk are all Type II-P SNe and are confirmed to have RSG progenitors. The pre-explosion image of Type IIn SN 2005gl suggests a LBV progenitor, but the possibility that the "candidate" is not a point source and is not resolved cannot be ruled out currently. Future observations will shed light on it. Other detections show more uncertainties.

A recent study on constraining the progenitor mass of Type II-P SNe by Smartt et al. [336] reveals a serious progenitor problem. They derived a lower limit of $m_{min} = 8.5^{+1}_{-1.5}\,M_\odot$ for Type II-P SNe progenitors, which is consistent with theoretical estimates for the maximum mass of a white dwarf progenitor. However, the upper limit given by Smartt et al. [336], $m_{max} = 16.5 \pm 1.5\,M_\odot$, shows inconsistency to the RSG mass in Local Group galaxies. We have observed RSGs in the Local Group with masses up to 25-30 $M_\odot$ [336]. The probability of missing detecting these progenitors is as low as 0.018 or of 2.4σ significance [336]. Moreover, more massive stars are brighter and should be easier to detect. Underestimation of the progenitor masses due to dust extinction has been ruled out. The possibility that all the more massive RSGs ($\geq 17\,M_\odot$) produce other types of SN also seems unlikely. This is called the "red supergiant problem". Even if only 8-17 $M_\odot$ stars produce Type II-P SNe, they still

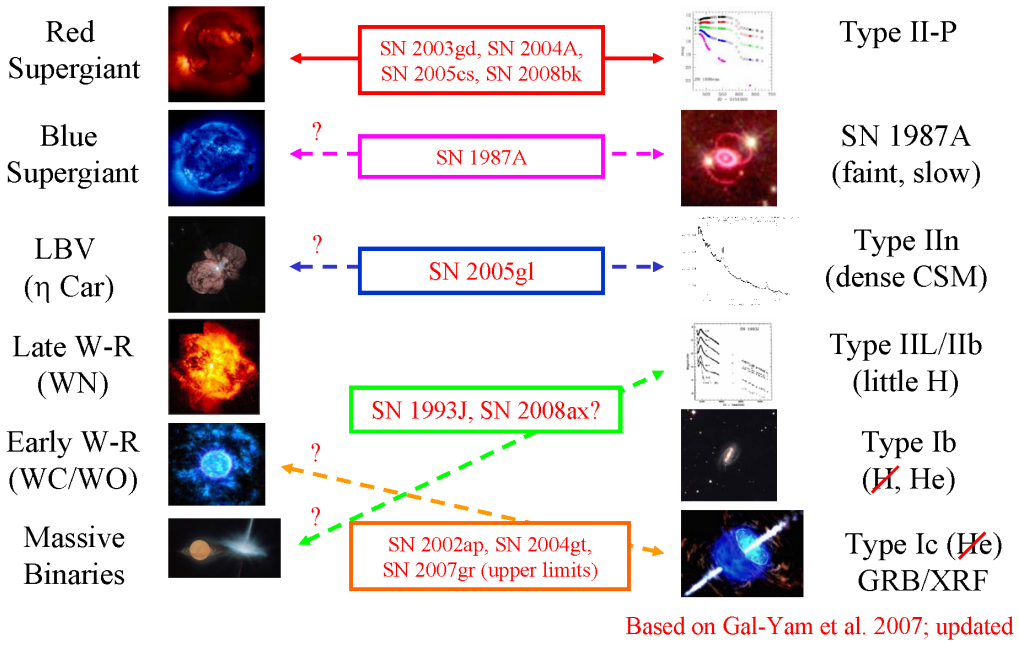

Figure 1.5: The progenitor-supernova map, showing the connections between the progenitor star and the supernova type. The events are served as evidences, or possible evidences (relations with question mark), are written in the box connecting the progenitor and the supernova type. This figure is taken from Gal-Yam et al. [126].

produce more Type II-P SNe than we observe [349].

The connection between Wolf-Rayet (WR) stars and Type Ib/c SNe has also been questioned. Simulations of Type Ib SN light curves indicate a low ejecta mass [106, 93], which corresponding to a MS mass inconsistent with the lower mass limit of WR stars in single star evolution models [161]. Observations also show discrepancies in the Type Ib/c SNe rate, if only stars above 34 $M_\odot$ produce them [349].

To solve the RSG problem, Smartt et al. [336] speculate that higher mass stars may directly collapse to BH. Surveys are underway to search for such events [210, 284]. The

observed fractions of different types of SNe can be explained by including binary channel in stellar evolution. Mass-transfer in binary systems can also explain the low ejecta mass of Type Ib/c SNe [93].

1.4.2 Explosion problems

Modeling the CCSNe explosion is a great challenge and involves sophisticated physics from various fields. The first 1D model was made by Colgate and White [63]. The explosion mechanism of CCSNe has been a mystery for about 50 years. In the canonical view, the iron core undergoes collapse once it reaches the Chandrasekhar mass. The inner part of core is turned into neutrons due to compression. The outer falling part is bounced by the inner compact core, which creates a shock propagating outward. The explosion is considered as successful if the shock reaches the core surface. However, most of the sophisticated simulations show an inability of the shock to reach the core surface with the initial shock energy [408, 281, 369, 35, 357, 36]. The shock loses energy to dissociation of the infalling nuclei and emission of neutrinos, and stalls in the outer iron core. Three possible mechanisms have been proposed to revive the shock to obtain a delayed explosion: the neutrino heating mechanism [32, 25], the magnetorotational mechanism [264, 4, 213, 292, 40] and the acoustic mechanism [38, 39].

The typical explosion energy for a core-collapse supernova is $\sim 10^{51}$ erg (1 Bethe or 1 B). However, the gravitational energy release by the core collapse is $\sim 10^{53}$ erg, two orders of magnitude greater than the explosion energy. This tremendous amount of energy is mostly carried away by the neutrinos. Even if the neutrinos deposit only 1% of their energy, it is possible to rejuvenate the shock and trigger a successful explosion. However, the neutrinos only interact with matter through week interaction, and hence neutrino deposition is very difficult and inefficient. With state-of-the-art neutrino transport solver included in 1D simulations, explosions have been seen for progenitor masses of 8-10 $M_\odot$ [206].

The failure in 1D simulations is thought to be a dimensional issue since physical processes cannot be handled in the spherically symmetric geometry. Multi-dimensional simulations have explored the effects of convection, rotation, anisotropic neutrino emission, all of which

may help to revive the shock in the neutrino heating scenario. However, it turns out that none of them gives sufficient support for a explosion [e.g. 333, 189, 416]. Recently, the standing accretion shock instability (SASI), which is the growth of turbulence behind the shock and the growth in the asymmetry of the initially spherical shock due to nonspherical perturbations to the spherical accretion shock, has gained lots of attention [28, 325]. More realistic simulations in future will tell whether SASI can give sufficient boost to the shock.

Magnetic fields have also been proposed to play an important role in the explosion mechanisms [219, 26]. In order for magnetic field to have a comparable influence as matter pressure and to have an effect on the dynamics, the magnetic field should be stronger than 10^{16} G. Duncan and Thompson [98] showed that magnetic fields in neutron stars could be up to $10^{14} - 10^{15}$ G. Such strongly magnetized neutron stars are called magnetars, and some magnetars are born with very high magnetic fields (e.g. SGR 1806-20). Starting with a rapidly rotating and strongly magnetized core, Sawai et al. [323] showed that jet-like prompt explosions can be produced. Wheeler et al. [403] also found strong axial jets driven by a strong toroidal magnetic field are possible with the aid of very rapid rotation. However, what happens to much weaker fields before collapse is unknown. It is believed that the magneto-rotational instability (MRI) is the key to the question. Akiyama et al. [4] showed that it was possible for MRI to amplify the magnetic field exponentially. In brief, the simulations on this subject are still very immature and it is still too early to draw any conclusion.

Another mechanism is the acoustic mechanism proposed by Burrows et al. [38], in which sound waves deposit energy into the outer mantle. In this scenario, the anisotropic accretion of material on the core induces strong g-mode oscillations[9]. The released gravitational energy from falling material is converted to sound by rapid rotation, and then is transported to the shock. However, this phenomenon is only seen by one group [38, 41]. Confirmation and adequate exploration is required in future studies.

[9]Low frequency density waves which have gravity as their restoring force. Due to adiabatic expansion and small temperature gradient, material moving upward is cooler and denser than its surroundings and hence is pulled back to its original position.

1.4.3 Mixing problems

For massive stars, the temperature is high enough to ignite carbon at the end of the helium burning stage. Successive nuclear fusions continue to build up a layered structure with heavier atomic nuclei in the inner shells until an inert iron core is formed. During SN explosions, the bounce shock moves outward and causes explosive nucleosynthesis of the inner material. As the shock temperature declines, explosive nucleosynthesis finally ceases in the middle layers. Without mixing, the outer layers produced before the explosion are simply ejected, and intermediate mass elements[10] and iron-group elements are abundant in the middle and inner layers, respectively.

The issue of mixing has been extensively studied both theoretically and observationally since the discovery of strong large-scale mixing in SN 1987A [e.g. 11, 260]. SN 1987A, as the closest supernova observed by modern telescopes and one of the best observed supernovae, provides an excellent opportunity to understand this large-scale mixing. Light curve of modeling using evolutionary presupernova models indicated strong ^{56}Ni mixing up to $\sim 4000\,\mathrm{km\,s^{-1}}$ [410, 331, 27], while modeling based on non-evolutionary models, which was constructed by comparison between observations and hydrodynamic models, required moderate ^{56}Ni mixing up to $\sim 2000\,\mathrm{km\,s^{-1}}$ [375]. More sophisticated modeling by Utrobin [376] also necessitated outward mixing of ^{56}Ni to $\leq 2500\,\mathrm{km\,s^{-1}}$. Besides outward mixing of ^{56}Ni, the modeling also argued for inward mixing of hydrogen to fit the broad peak of the bolometric light curve.

Line profiles of different species contain rich information on the degree of mixing. Haas et al. [150] presented observations of the 17.94 and 25.99 μm [Fe II] lines at 410 day and found the wings of the profiles extended to velocities $\geq 3000\,\mathrm{km\,s^{-1}}$. The inner boundary of the hydrogen envelope expanded with a velocity $\sim 2100\,\mathrm{km\,s^{-1}}$ [410], which indicated a certain amount of iron was mixed out to the hydrogen envelope. Colgan et al. [62] also presented these two lines at 640 day, with an additional iron group line [Ni I] 6.6 μm. They also concluded that the iron group elements were significantly mixed outward. The narrow peak of the Hα profile observed by Phillips et al. [306] at 498 day implied H has been mixed

[10] From oxygen to calcium.

down to very low velocities, otherwise the profile would have had a flat top. Kozma and Fransson [216] modeled the Hα emission at $\sim$ 800 day and found the minimum velocity of hydrogen is $\leq 700\,\mathrm{km\,s^{-1}}$.

Many multi-dimensional hydrodynamic simulations have been performed to try to reproduce the mixing signature in SN 1987A. Mixing is a multi-dimensional effect and cannot be simulated in 1D spherical models. Rayleigh-Taylor instability[11] (RTI) is believed to be responsible for the large-scale mixing. Kifonidis et al. [200] studied the mixing issue in a $15\,\mathrm{M_\odot}$ BSG model in 2D, which resembles the case of SN 1987A. The perturbation seeds of RTI in their work was induced by neutrino-driven convection, differing from those in previous studies, which used artificial perturbations. Their results showed strong mixing at the Si/O and (C+O)/He interfaces. However, the mixing at the He/H interface is very week, which disagreed with the observations of SN 1987A. They also failed to reproduce the high velocity ^{56}Ni clump due to the deceleration by a dense helium shell below the He/H interface. It was later found by Kifonidis et al. [201] that the Richtmyer-Meshkov instability[12] (RMI), induced by a significantly deformed shock, could explain the strong mixing at the He/H interface and the large-scale global anisotropy of the inner ejecta. Hammer et al. [153] presented the first 3D simulation based on a successful explosion model [325] and found that the presence of strong mixing and high velocity metal-rich clumps in the absence of the RMI. The RTI in their 3D models grew about 30% faster than that in 2D models. Joggerst et al. [193] confirmed a faster grow rate of RTI in 3D models.

There have been very few mixing studies based on red supergiant progenitors. SN 1999em is one of the best observed Type II-P SNe. Elmhamdi et al. [105] carried out observations of this event from several days after explosion to day 642. Their late-time spectra showed a centrally peaked Ha profile. This is somehow similar to the case of SN 1987A discussed above and indicates a strong mixing of hydrogen down to very low velocities. The simulations of Herant and Woosley [162] showed the formation of a reverse shock when the explosion shock reaches the extensive hydrogen envelope. RT instabilities develop between the two shocks

[11] An instability occurs at the interface of two fluids with different densities when the lighter fluid is pushing the heavier one.

[12] An instability occurs when the interface of two fluids with different densities is impulsively accelerated, e.g. by the passage of a shock wave.

and mix hydrogen downward to the core region. Shigeyama et al. [332] found that the H/He, He/(C+O) and O/(Si+Ni) interfaces were unstable in their models with different progenitor masses. The ^{56}Ni mixing in these models is relatively weak, with moderate mixing for less massive star models ($\sim 13\,M_\odot$) and very little in more massive star ones ($\sim 20\,M_\odot$).

Type II-L/b SNe have less massive hydrogen envelope than Type II-P SNe. In examining the late-time spectra of SN 1993J, Houck and Fransson [177] found that iron group elements were mixed outward to velocities of $\geq 3000\,\mathrm{km\,s^{-1}}$ and Oxygen was mixed inward to $\sim 1000\,$kms by fitting corresponding line profiles. They determined that hydrogen was confined to velocities between 8500 and 10,000 $\mathrm{km\,s^{-1}}$, implying a week, if any, downward mixing of hydrogen. Significant mixing of the helium core is seen in the simulations of Iwamoto et al. [187]. The RT instabilities develop at the He/(C+O) interface, but the instability at the H/He interface is fairly weak, consistent with the observations of SN 1993J.

Large-scale mixing has also been inferred in Type Ib SN 1985F [117], but the material is possibly not mixed thoroughly based on the dissimilarity between the Mg I] and [O I] profiles. Fransson and Chevalier [119] modeled the emission lines of this event and found a significant mixing is required to reproduce the not-flat-topped profiles of Mg I] and [O I]. The simulation work of Kifonidis et al. [200] show reasonably good agreement to the observations. High velocities ^{56}Ni clumps were observed in the model and the degree of mixing is consistent with the one used in Woosley and Eastman [411] to reproduce the spectrum of SN 1984L.

Last but not least, supernova remnant (SNR) observations also revealed large-scale mixing in SNe. Chandra observations of Cassiopeia A (Cas A), a Type IIb SN proved by scattered light [217], clearly showed some Fe-rich material lie above Si-rich material [180, 183], a strong indication that macroscopic mixing happened either during or after the explosion.

In summary, mixing is essentially a 3D effect. However, 3D simulation on mixing problems is still in its infancy. Comprehensive understanding and final conclusions need to await extensive and realistic 3D studies. Due to unsuccessful explosions of theoretical models, the initial models for studying mixing are mostly unrealistic. The seeds for the perturbation are also suspicious. Most of the studies assume artificial perturbations, some other studies use perturbation induced by neutrino heating convection. The results on studying mixing are encouraging, but many problems remain to be solved to fully understand the observations.

Observational constraints for mixing depend mostly on the late-time line profiles of various species. Current modelings on these line profiles are based on various simplification, e.g. ignorance of line transfer or time-dependence, starting from nebular phase. CMFGEN has the advantage to consistently model the SNe ejecta through both the nebular and photospheric phases, although at the cost of expensive computation. The time-dependent fully Non-LTE radiative transport in this thesis will give deep insight to this problem.

1.5 ASYMMETRY OF CORE-COLLAPSE SUPERNOVAE

There has been increasing evidence that the ejections of some SNe material show slight or significant departure from spherical symmetry. The observations of SN 1987A were the first clue that indicated a strong asymmetry in a SN. Both X-ray and γ-ray were detected much earlier than predicted in spherically symmetric models [95, 359, 259]. Pulsars are observed to have high velocities, which requires a deviation from spherical symmetry for CCSNe [249]. The SNR Cas A observations, which showed many high velocity ejecta knots, also suggested significantly non-spherical symmetry [115, 183]. With light echoes, Rest et al. [320] were able to directly confirm the asymmetry of the Cas A SN.

Polarization studies also reveal lots of information about the asymmetry of CCSNe [see the review by 392]. Polarization is believed to be produced by electron scattering. If a SN shows intrinsic linear polarization it must be aspherical. The polarization work of Jeffery [191] and Wang et al. [394] showed that SN 1987A displayed an axisymmetric outflow although with some departure from axisymmetry. Polarization of normal Type II-P SN 1999em and SN 2004dj have also been extensively studied [234, 393, 237, 58, 54]. Their results showed broad consistency with a bipolar jet-like flow for Type II-P SNe. Leonard and Filippenko [232] argued that the temporally increasing polarization in Type II-P SNe is caused by the gradually exposed core of the SNe, while Dessart and Hillier [91] showed that the lower polarization at early times does not necessarily indicate less degree of asymmetry. Another observational finding is that polarization is higher in the nebular phase [see the review by 392, and references therein], which is also seen in the models of Dessart and Hillier [91].

Asymmetry is thought to be more prominent in Type Ib/c SNe. Spectropolarimetry of SN spectra indicates polarization of Type Ib/c SNe is greater than that of normal Type II SNe [232], and hence Type Ib/c SNe are more asymmetric. Moreover, Many Type Ib/c SNe have been associated with gamma ray bursts (GRBs), which are relativistic flows with Lorentz factor γ of at least a few hundreds and last from ten milliseconds to several minutes, e.g. SN 1998bw [GRB 980425; 128], SN 2003dh [GRB 031203; 174, 354]. Collimated effects in GRBs also imply a highly asymmetric explosion in the associated SNe.

1.6 OUTLINE OF THE THESIS

This thesis aims to study various aspects in the evolution of massive stars. In Chapter 2, I summarize the basic knowledge of radiative transfer theory and important techniques and methods in the radiative transfer code CMFGEN [169].

In Chapter 3, I present the implementation of non-thermal excitation and ionization into CMFGEN and comprehensively explore the effects brought by non-thermal processes in modeling SNe. I also compare synthetic light curves and spectra with those of SN 1987A at nebular epochs, when the non-thermal processes are prominent. Discussion on potential uncertainties of the new solver and on discrepancies in the model is also presented.

The study on a new solver for relaxing the Hubble expansion assumption in simulating SNe is put in Chapter 4. The new solver takes into account all relativistic terms in the radiative transfer equations, which can handle a non-Hubble flow when modeling early time evolution of Type II-P SNe. Uncertainties introduced by the assumption of homologous expansion are also discussed.

Chapter 5 presents the work on constraining physical properties of the LBV η Carinae. The non-spherical wind of η Carinae is constrained by the equivalent width and the absorption component of Hα. I also discuss the properties of the Homunculus nebula ejected by the η Carinae.

Chapter 6 focuses on determining the fundamental parameters and reproducing the extreme ultraviolet (EUV) spectra of a type B2 II star – ϵ Canis Majoris. I compare my results

with those from previous studies and conclude that there is still no satisfactory spectral energy distribution fit for all wavelengths. Potential problems in the analysis are discussed.

2.0 RADIATION TRANSPORT THEORY

Many concepts and equations of this chapter are based on Mihalas [267] and Mihalas and Mihalas [268].

2.1 THE RADIATIVE TRANSFER EQUATION

2.1.1 The specific intensity

The specific intensity I_ν represents the amount of energy passing through an area of dA at location $\vec{r}$ into a solid angle $d\Omega$ about the direction $\vec{n}$ in the time dt at the frequency interval ν to $\nu + d\nu$. It is defined by

$$I_\nu(\vec{r}, \vec{n}, t) = \frac{dE}{(dA \cos\theta) d\Omega dt d\nu} \tag{2.1}$$

where dE is the amount of energy. θ is the angle between the normal of the area dA and the direction $\vec{n}$ of the solid angle $d\Omega$. The specific intensity is a fundamental quantity that almost completely describes the radiation field. The only information missing is the polarization of the radiation field.

2.1.2 The radiative transfer equation

The Radiative Transfer Equation (RTE) simply describes the change of the radiation field due to attenuation and strengthening by the absorption, emission and scattering processes

when propagating through a medium. The coordinate free form of the RTE is

$$\frac{1}{c}\frac{\partial I_\nu}{\partial t} + \vec{n}\cdot\nabla I = \eta_\nu - \chi_\nu I_\nu \tag{2.2}$$

where η_ν is the emission coefficient (emissivity) and χ_ν is the absorption coefficient (opacity), or the extinction coefficient. The absorption coefficient takes into account the contributions from pure absorption and scattering processes ($\chi_\nu = \kappa_\nu + \sigma_\nu$, where κ_ν is the pure absorption coefficient and σ_ν is the scattering coefficient, including coherent, non-coherent, isotropic continuum scattering such as Thomson scattering or Rayleigh scattering), and the emission coefficient includes the contributions from thermal emission and scattering processes ($\eta_\nu = \kappa_\nu B_\nu + \sigma_\nu J_\nu$, where B_ν is the Planck function and J_ν is the mean intensity of the radiation field and will be introduced in Sec. 2.2.1).

For outflows, e.g., stellar wind and supernovae, it is more convenient to solve the RTE in the comoving frame. The advantages can be viewed from several aspects. First, in the relativistic sense, microscopic descriptions of material properties by thermodynamics and statistical mechanics apply in the Lagrangian frame of the ejecta, which is identical to the comoving frame. Second, radiation-matter interaction is greatly simplified in the comoving frame [e.g. partial redistribution by scattering; 269]. Third, the material properties are isotropic in the comoving frame (e.g. extinction and emission coefficients). Therefore, the comoving frame is a natural and advantageous frame to work in.

In modeling SNe, the assumption of homologous expansion is commonly made. Under such assumption, the comoving frame RTE in spherical coordinates, to the first order in v/c, is

$$\frac{1}{c}\frac{\partial I_\nu}{\partial t} + \frac{\mu c + v}{c}\frac{\partial I_\nu}{\partial r} + \frac{1-\mu^2}{r}\frac{\partial I_\nu}{\partial \mu} - \frac{v\nu}{rc}\frac{\partial I_\nu}{\partial \nu} + \frac{3v}{rc}I_\nu = \eta_\nu - \chi_\nu I_\nu \tag{2.3}$$

where v is the expansion velocity. Here $\mu = \cos\theta$ and θ is angle between the direction of a considered light ray and the radial direction.

2.1.3 Sources of opacity and emissivity

Sources of opacity and emissivity come from various processes, including free-free, bound-free, bound-bound, dielectronic recombination, scattering, and collisional processes.

The free-free transition is emission or absorption of radiation due to collisions between two free particles. The free-free emission is also known as Bremsstrahlung. This usually happens between a free electron and an ionized atom. Since the free-free transition is a collisional process, it is always in Local Thermodynamic Equilibrium (LTE). The free-free emissivity η_ν^{ff} and the free-free opacity χ_ν^{ff} are related by the Kirchhoff-Planck law, i.e. $\eta_\nu^{\text{ff}} = \chi_\nu^{\text{ff}} B_\nu$.

In the bound-free transition, a photon is emitted when a free electron is captured and becomes bound to an atom or a photon is absorbed when a bound electron is ejected and becomes free. The former is a recombination process, while the latter is a photoionization process.

When an electron moves from one bound state to another bound state, it is called a bound-bound transition. The bound-bound transitions produce the spectral lines, while the bound-free and free-free transitions produce the continuum. Since a photon can be emitted in the same transition in which it is absorbed, bound-bound processes are a mix of true absorption and scattering.

Other processes, for instance the dielectronic recombination, electron and Rayleigh scattering, and collisional processes, can also contribute to the opacity χ_ν and emissivity η_ν in the RTE.

2.2 MOMENTS OF THE TRANSFER EQUATION

2.2.1 Moments of the radiation field

Moments of the radiation field are useful in radiative transfer theory. Moments of the radiation field are involved in the rate equations (see Sec. 2.3.2) and the energy balance equations (see Sec. 2.3.3). Moreover, it is easier to solve the transfer equation for the zeroth

moment of the radiation field rather than the specific intensity. The moments of the radiation field in spherical (or planar) geometry are defined as follows:

$$[J_\nu, H_\nu, K_\nu, N_\nu] = \frac{1}{2}\int_{-1}^{1} I_\nu[1, \mu, \mu^2, \mu^3]d\mu \tag{2.4}$$

where $\mu = \cos\theta$, and J_ν, H_ν, K_ν and N_ν are the zeroth, first, second and third moment of the radiation field, respectively.

J_ν is called the mean intensity, and is related to the energy density U_ν by

$$J_\nu = \frac{c}{4\pi}U_\nu \tag{2.5}$$

H_ν is called Eddington flux, and is related to the energy flux F_ν by

$$H_\nu = \frac{1}{4\pi}F_\nu \tag{2.6}$$

K_ν is a pressure-like quantity, and is related to the radiation pressure P_ν by

$$K_\nu = \frac{c}{4\pi}P_\nu \tag{2.7}$$

N_ν is seldom used, but is required in the fully relativistic solver.

The ratio of the second moment to the zeroth moment is defined as the variable Eddington factor f, i.e.

$$f_\nu = K_\nu/J_\nu \tag{2.8}$$

As we shall see in Sec. 2.2.3, the number of radiation field moments is always more than the number of the moment equations by one or more. The Eddington factor is introduced to assist in solving the transfer equation. It measures the anisotropy of the radiation field and has a well-defined value of $0 < f \leq 1$. For cases of isotropic radiation, $f = \frac{1}{3}$.

2.2.2 Scattering problem

The RTE (Eq. 2.3) can be solved if the opacity χ_ν and the emissivity η_ν are known. The complication comes into the problem when we have scattering processes, e.g. Thomson

scattering. Both χ_ν and η_ν can be split into a thermal part and a scattering part, i.e.,

$$\chi_\nu = \kappa_\nu + \sigma_\nu \tag{2.9}$$

and

$$\eta_\nu = \eta_\nu^{\mathrm{t}} + \eta_\nu^{\mathrm{s}} \tag{2.10}$$

In most astrophysical applications it is usual to assume η_ν^{s} depends only on J_ν, and not on I_ν. To explicitly take into account the scattering processes and to solve the RTE, the moments of the transfer equation are introduced.

2.2.3 Moments of the transfer equation

The zeroth moment of the transfer equation is obtained by integrating the RTE over the angle $\mu = \cos\theta$. For supernovae, we integrate Eq. 2.3 to obtain

$$\frac{1}{cr^3}\frac{D(r^3 J_\nu)}{Dt} + \frac{1}{r^2}\frac{\partial(r^2 H_\nu)}{\partial r} - \frac{v\nu}{rc}\frac{\partial J_\nu}{\partial \nu} = \eta_\nu - \chi_\nu J_\nu \tag{2.11}$$

where D/Dt is the Lagrangian derivative. In the case of spherical geometry, we have

$$\frac{D}{Dt} = \frac{\partial}{\partial t} + v\frac{\partial}{\partial r} \tag{2.12}$$

Multiply the RTE (here Eq. 2.3) by μ and then integrate it over the angle μ, we obtain the first moment of the transfer equation in the comoving frame for supernovae.

$$\frac{1}{cr^3}\frac{D(r^3 H_\nu)}{Dt} + \frac{1}{r^2}\frac{\partial(r^2 K_\nu)}{\partial r} + \frac{K_\nu - J_\nu}{r} - \frac{v\nu}{rc}\frac{\partial H_\nu}{\partial \nu} = -\chi_\nu H_\nu \tag{2.13}$$

As higher moments of the transfer equation can be introduced, the number of the quantities (moments of the radiation field) to be solved will be always more than the number of the moment equations. The Eddington factor f_ν defined in Sec. 2.2.1, and which relates to K_ν and J_ν, provides the means to close the system.

2.2.4 The boundary conditions

The radiative transfer problem requires two boundary conditions, one for each side of the area considered. The boundary condition at $\tau = \tau_{\max}$ is required for solving the outgoing rays, while the boundary condition at $\tau = 0$ is required for solving the ingoing ones.

The benefits of solving the moment equations rather than the RTE is that the scattering processes are explicitly taken care of. The boundary conditions in this moment technique are usually specified by Eq. 2.13. At the outer boundary, the incoming flux is assumed to be zero; at the inner boundary, the net outgoing flux can be specified by the diffusion approximation in the case of stellar atmosphere or a zero net flux is adopted in the case of SNe.

2.3 THE STATISTICAL AND RADIATIVE EQUILIBRIUM EQUATIONS

2.3.1 LTE VS Non-LTE

Local thermodynamic equilibrium (LTE) is a local description of the gas, in which thermodynamic properties such as the temperature and pressure can vary in space and time, but they are varying so slowly that for any point in space one can assume thermodynamic equilibrium in some neighborhood around that point. With the assumption of LTE, the state of the gas, e.g., velocity distribution of the electrons, electron distribution in the bound levels, and excitation state in the atoms, can be specified by the temperature T and the total particle density N. The LTE assumption is equivalent to assuming

1. A Maxwell-Boltzmann velocity distribution of electrons and ions.
2. The excitation state is given by the Boltzmann equation.
3. The ionization state is given by the Saha equation.
4. The source function is given by the Planck function at the local temperature.

The LTE assumption is reasonable under the following two conditions:

1. The photon mean free paths are short compared to the length scales over which the gas properties change.
2. The density is so high that collision rates are high enough to establish equilibrium.

Unfortunately, the conditions for LTE are generally not met in the SN ejecta. When LTE breaks down, we have a 'Non-LTE' situation. In the case of Non-LTE, the populations are determined by the rate equations, which are coupled with the radiative transfer equations.

2.3.2 The statistical equilibrium equations

The moments of the transfer equation are solvable if η_ν and χ_ν are known. However, η_ν and χ_ν are generally functions of temperature, electron density and level populations of some species. To build up a realistic model for a supernova, a lot of species and a lot of levels are to be included. The level populations are determined by the statistical equilibrium equations (rate equations), i.e.,

$$\rho \frac{D(n_i/\rho)}{Dt} = \sum_j (n_j R_{ji} - n_i R_{ij}) \tag{2.14}$$

[88] where n_i and n_j are the population density of state i for some species, ρ is the mass density and R_{ij} is the total rate from state i to state j. In the case of homologous expansion, the statistical equilibrium equations can be rewritten as

$$\frac{1}{r^3} \frac{D(r^3 n_i)}{Dt} = \sum_j (n_j R_{ji} - n_i R_{ij}) \tag{2.15}$$

The total rate R_{ij} and R_{ji} need to be computed to solve the population densities. However, R_{ij} and R_{ji} are generally functions of the electron density n_e, temperature and the radiation field. For a bound-bound process we have, for example, $R_{ij} = 4\pi \int (h\nu)^{-1} \alpha_{ij}(\nu) J_\nu d\nu$, where $\alpha_{ij}(\nu)$ is the absorption coefficient. The deep coupling between the moments of the transfer equation and the statistical equilibrium equations requires these equations to be solved simultaneously.

2.3.3 The radiative equilibrium equation

The radiative equilibrium equation is essentially a energy conservation equation, which is

$$\rho\frac{De}{Dt} - \frac{P}{\rho}\frac{D\rho}{Dt} = 4\pi\int d\nu(\chi_\nu J_\nu - \eta_\nu) + \frac{De_{\rm decay}}{Dt} \tag{2.16}$$

[89] where e is the internal energy per unit mass, P is the gas pressure, and $e_{\rm decay}$ is the specific energy from decay of unstable elements. The internal energy e consists of the kinetic energy e_K and the "potential" energy e_I, i.e.,

$$e = e_K + e_I \tag{2.17}$$

The kinetic energy e_K and the potential energy e_I are written as

$$e_K = \frac{3(n+n_e)kT}{2\mu mn} \tag{2.18}$$

and

$$e_I = \sum_i \frac{n_i E_i}{\mu mn} \tag{2.19}$$

[89] where n is the total number density of all particles, k is the Boltzmann constant, μm is the atomic mass, and E_i is the total excitation and ionization energy of state i.

In stellar atmospheres, which are essentially in steady state, the time-dependent terms in the moments of the transfer equation, statistical and radiative equilibrium equations can be neglected.

2.4 THE RADIATIVE TRANSFER CODE CMFGEN

CMFGEN is a sophisticated radiative transfer code developed for modeling the atmosphere of massive stars, such as Wolf-Rayet stars and O stars [169]. The extension of the code to model SNe has been extensively tested [85, 86, 87, 88, 89, 90]. As more and more details are

in need of understanding in SNe, many approximations are no longer good ones. It will be ideal to use CMFGEN and to extend it to carry out more comprehensive studies on SNe.

As mentioned in Sec. 2.3.2, the coupling between the moments of the transfer equations and the statistical equilibrium equations severely complicates the calculations of a radiative transfer problem. Formally the equations to be solved can be written as

$$S_i(\psi_i) = S_i(\psi_i(n_{e,i}, T_i, J_{1i}, ..., J_{mi}, ..., n_{1i}, ..., n_{li}, ...)) = 0 \qquad (i = 1, ..., N_D) \tag{2.20}$$

where S_i is the constraint equation and ψ_i is the vector of variables at depth i, $n_{e,i}$ is the electron density at depth i, T_i is the temperature of the gas, J_{mi} is the mean intensity at frequency ν_m, and n_{li} is the population density of level l. Assuming that the total number of the frequency grid is N_ν $(m = 1, ..., N_\nu)$, the total number of super levels is N_L $(l = 1, ..., N_L)$, and the number of optical depth is N_D $(i = 1, ..., N_D)$, the number of constraints at each optical depth is $N_T = N_\nu + N_L + 2$ and the total number of constraints of the system is $N_C = N_D \times (N_\nu + N_L + 2)$. The system to be solved is a $N_C \times N_C$ matrix, i.e. $S_{N_C \times N_C}$.

Linearization of Eq. 2.20 can be written as,

$$\delta S_i \cdot \delta\psi = -\Delta S_i \tag{2.21}$$

The complete linearization technique [13] starts with an initial guess of the solutions. The whole system is linearized to compute the corrections to the real solutions. New solutions are updated and iterated until the corrections are small enough. This iterative procedure is basically a multi-dimensional Newton-Raphson method. The limitation of the complete linearization technique lies in the size of the matrix $S_{N_C \times N_C}$. The complete linearization method cannot handle a large number of frequency grids or a large amount of levels.

In CMFGEN, super levels are utilized to handle a huge amount of levels. Also, a partial linearization technique is used instead of the complete linearization scheme. The complete linearization scheme considers the changes in the radiation field at all frequencies and at all depths in terms of the changes in populations at all depths [267], while the partial linearization technique in CMFGEN takes into account only the coupling between the radiation field and the populations locally and at adjacent grid points. Moreover, the elimination

scheme used in Mihalas [267] eliminates the populations in the statistical equilibrium equations, while CMFGEN eliminates the radiation field and thus circumvents the limitation of the frequency grid.

2.4.1 Super levels

A super level is a group of levels with similar properties that are grouped as one level. First proposed by [6], super levels have proved useful and powerful in handling numerous levels. In CMFGEN, levels with close energies and similar properties are assigned to a single super level. The population of this super level ${}^{S}n_j$ is the total populations of the levels grouped, i.e. ${}^{S}n_j = \sum_i n_{ij}$, where n_{ij} is the real level population in a full model atom. Only the super levels are used in the statistical equilibrium equations, therefore the total number of the SEE is reduced from N_F to N_S, where N_F and N_S are the number of levels and super levels respectively. Inside a super level, all levels are assumed to be in LTE with respect to each other, i.e., within a super level, all the levels are assumed to have the same departure coefficient.

2.4.2 The elimination scheme

To cover the whole spectrum of a supernova and to resolve important details of the spectrum, a total number of radiation frequencies of $\sim 10^5$ is used in CMFGEN. In the elimination scheme of Mihalas [267], the matrix to be solved is a $N_M \times N_M$ matrix, where $N_M = N_D \times (N_F + 2)$. No matter how small the number of levels is, the enormous number of frequency grids will lead to a overwhelmingly huge matrix. In CMFGEN, the radiative transfer equations are linearized and used to eliminate the radiation field rather than the populations. As a result, the matrix to be solved becomes a $N_G \times N_G$, where $N_G = N_D \times (N_L + 2)$. Moreover the matrix is sparse and has a block tridiagonal or block diagonal shape with each block $N_L \times N_L$. With this elimination scheme, CMFGEN is able to compute the whole SN spectra with fine resolution.

2.4.3 Fully Non-LTE

In LTE, the level populations can be determined by the temperature and the electron density. Thus, the statistical equilibrium equations are unnecessary. This assumption can dramatically simplify the problem. However, the LTE assumption is not a good one in supernovae, especially at late times. Non-LTE calculations are very time-consuming, but the non-LTE situation is the real nature of these events. In Non-LTE, the level populations are determined by the statistical equilibrium equations, which counts the rates leaving and entering a state. The rates from various processes have very different physical origin and are computed individually. CMFGEN includes the following processes: bound-free, bound-bound, dielectronic recombination, inner-shell ionization by X-rays, collisional ionization/recombination, collisional excitation/de-excitation and charge exchange reactions with H and He. Other important processes will be subsequently incorporated into the code to model SNe from first principles.

The degree of deviation from LTE for a state is defined by the departure coefficient, which is the ratio of the real population of the state to the LTE population, i.e. $b = n/n^*$. In principle, n^* is defined in terms of the LTE ion and electron densities. However, we define n^* in terms of the actual ion and electron densities for purpose of convenience. Figure 2.6 shows the departure coefficients of three species in a Type II-P supernova model. At large optical depth (below $\sim \tau = 10$), the LTE condition is recovered (the departure coefficients are unity). However, the departure coefficients illustrate a highly Non-LTE environment in the outer region, even at early times. Conclusions drawn from codes which assumes LTE or partial Non-LTE are suspicious since the LTE assumption obviously breaks down in the region where the spectra form. He I lines in Type Ib/c SNe have been expected to come from the non-thermal excitation of high energy electrons produced in γ-ray deposition [248, 360, 214]. However, Dessart et al. [93] treated all lines in Non-LTE and they showed that He I lines could be reproduced by Non-LTE effects if the helium mass fraction is $\geq 50\%$. The interpretation of the features in supernova spectra relies on realistic models. The fully Non-LTE treatment of all lines in CMFGEN provides a more realistic analysis for supernovae at the cost of computational time.

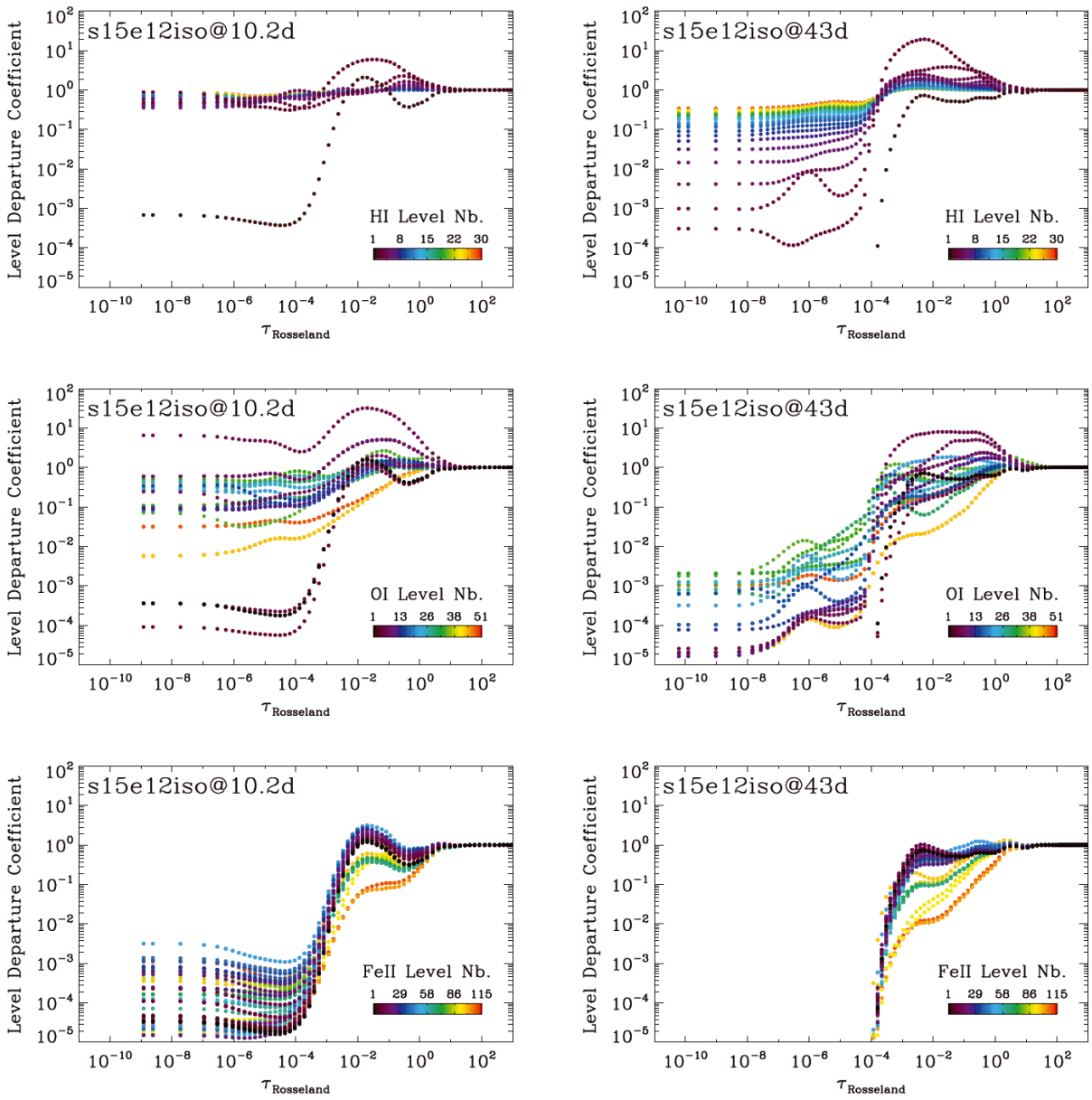

Figure 2.6: Departure coefficients of H I, O I and Fe II for a Type II-P supernova model with progenitor mass of 15 $M_\odot$ at two different epochs [90].

2.4.4 Time-dependence

Time-dependent terms in the radiative transfer equation, statistical and radiative equilibrium equations were once thought to be unimportant in Type II SNe and the SN at a particular

time can be treated as a steady state problem, because the recombination time of hydrogen at the photosphere is supposed to be much less than the SN age. The recombination time-scale for hydrogen can be crudely estimated by the time needed for all ions to recombine in the condition of a fixed electron density, which is

$$t_{\rm rec} = \frac{n({\rm H}+)}{n({\rm H}+)n_e\alpha} = \frac{1}{n_e\alpha} \tag{2.22}$$

[296], where α is the recombination coefficient and $\alpha = \alpha_B = 2.59 \times 10^{-13}\,{\rm cm^3\,s^{-1}}$ at 10 000 K [296]. The adoption of α_B, which is the value for the case that every direct recombination to the ground state is followed by an ionization, is valid in the conditions in SN ejecta. Thus, the recombination time scale is $t_{\rm rec} = \frac{3.86\times10^{12}}{n_e}$ s. Since a typical SN age at photospheric epoch is $t_{\rm age} \sim 10^6 - 10^7$ s, the condition that $t_{\rm rec} \ll t_{\rm age}$ can be fulfilled if $n_e \gg 10^7\,{\rm cm^{-3}}$. However, the comoving density is $\propto 1/t^3$ and hence the recombination time is $\propto t^3$, which means the ratio of recombination time to the flow time scales as t^2. Therefore, the ionization must eventually become frozen, starting from high velocities and spreading to lower velocities.

The above discussion neglects the optical depth effects and the existence of metastable states. When these two factors are taken into account, the effective recombination time-scale can be lengthened significantly due to a small net down rate to the ground state [88]. Take a two-level atom for example, the rate equations for level 1 and 2 are given by

$$\frac{Dn_1}{Dt} = n_2R_{21} - n_1R_{12} \tag{2.23}$$

and

$$\frac{Dn_2}{Dt} = n_en_I\alpha - n_2P_{2I} + n_1R_{12} - n_2R_{21} \tag{2.24}$$

where n_I is the ion population, P_{2I} is the photoionization rate, R_{21} is the total rate from level 2 to 1, and R_{12} the total rate from level 1 to 2. Here detailed balance is assumed for the ground state continuum ($R_{1I} = R_{I1}$). If the optical depth for the transition from level 2 to level 1 is large, which means $n_1R_{12} - n_2R_{21}$ is small, $n_en_I\alpha$ and n_2P_{2I} dominate Eq. 2.24,

which becomes

$$n_2 P_{2I} = n_e n_I \alpha \tag{2.25}$$

The effective recombination time-scale, $t_{\rm eff}$, is given by

$$\begin{aligned} t_{\rm eff} &= \frac{n_I}{(Dn_1/Dt)} = \frac{n_I}{n_2 R_{21} - n_1 R_{12}} \\ &> \frac{n_I}{n_2 R_{21}} = \frac{n_I}{n_e n_I \alpha R_{21}/P_{2I}} \\ &= t_{\rm rec} \frac{P_{2I}}{R_{21}} \end{aligned} \tag{2.26}$$

For He I $2s\,^1S$ state at $T = 10^4\,$K, we find $t_{\rm eff} = 9.2 \times 10^3 t_{\rm rec}$. Although the true situation is much more complicated, the effective time-scale can easily be comparable to the flow time-scale and time-dependent effects can actually operate at very early time.

Also, time-dependent terms are important in the inner region at early time, when it is optically thick. At such depths, the flux scale as $H \sim J/\tau$ and v/c can be order of $1/\tau$. The time-dependent term in Eq. 2.11 is non-negligible, and a substantial amount of energy is transported by the flow, which leads to a lower temperature at depth. Thus time-dependent terms are crucial for explaining the light curves of SNe. Their importance is not so clear if we simply model the outer layers where the spectrum is formed.

It was first realized by Kirshner and Kwan [205] that the time-dependent hydrogen ionization is crucial to maintain the high Hα luminosity at about 1 month in SN 1970g. Clayton et al. [59] and Fransson and Kozma [120] independently showed the ionization is essentially frozen at late epochs of SN 1987A. Utrobin and Chugai [378, 379] showed the time-dependent hydrogen ionization can successfully explain the strong Hα line in SN 1987A at early epochs ($\sim$ 40 days). Sophisticated modeling with time-dependent calculations is carried out by Dessart and Hillier [88] using CMFGEN. They included time-dependent terms in the statistical and radiative equilibrium equations and their time-dependent models show broad consistency with the observations of SN 1999em (see Fig. 2.7).

Full time-dependence, which is the inclusion of all the time-dependent terms in moments of the transfer equation, statistical and radiative equilibrium equations, is implemented into CMFGEN recently [89]. The success of the time-dependent solver in reproducing many

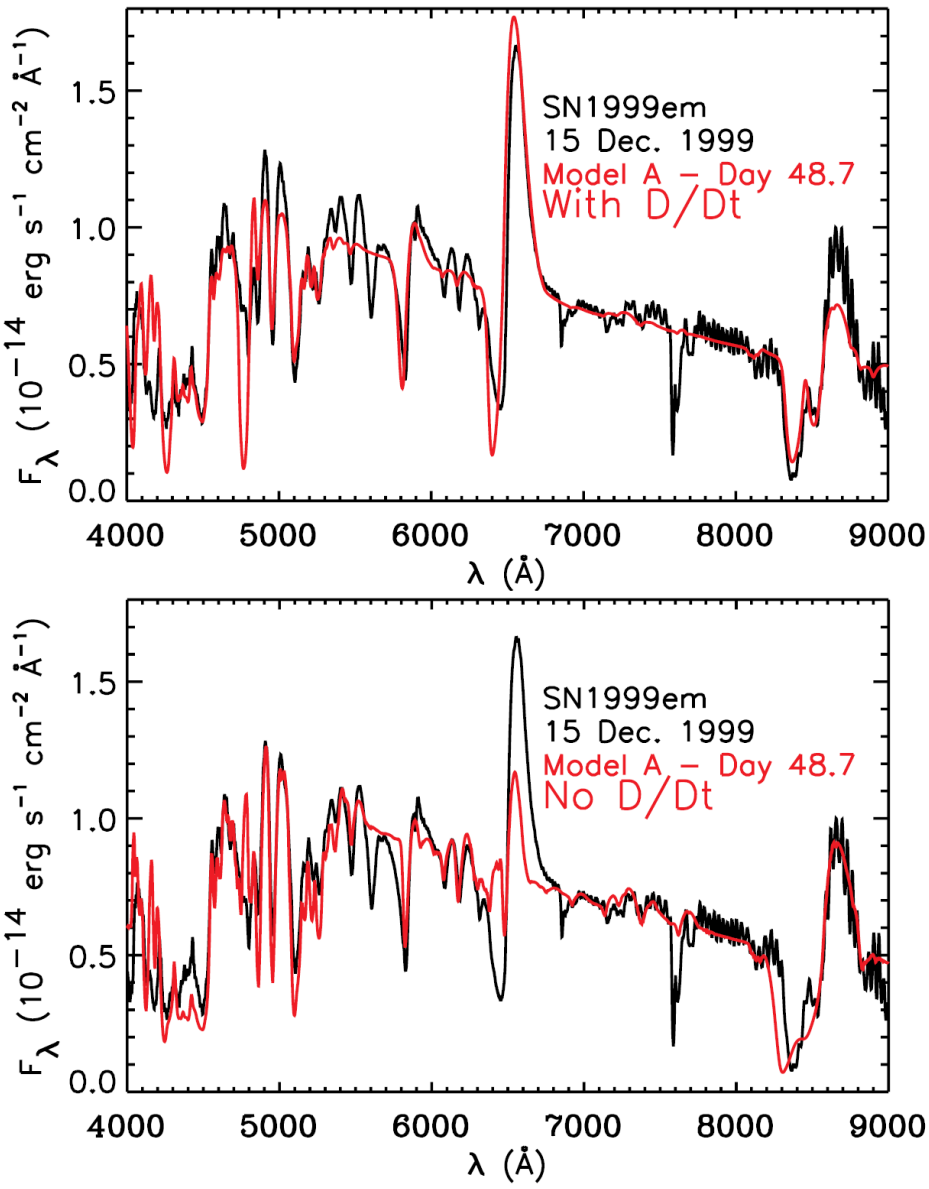

Figure 2.7: The match between the observation of SN 1999em (black) and the synthetic spectra of CMFGEN models (red). Left panel: the observation is compared to the time-dependent model. Right panel: the observation is compared to the stationary model. Failure of production of the Hα strength in the stationary model is no longer seen in the time-dependent model [88].

important features in the supernovae is indeed exciting. However, the time-dependent nature of these events makes detailed modelings extremely time-consuming. An initial model should be set up at early time when the time-dependent effect is minor. Experience suggests an 10% increment in time-step is stable and reasonable. Therefore, a lot of computational time is spent at very early times. The current approach has to start at a relatively late time, when the velocity becomes approximately homogeneous. Thus, the time-dependent information is missing at early stage. One of the goals of this thesis is to explore the time-dependent effects at early time for non-homogeneously expanding ejecta.

2.4.5 Link to a hydrodynamical model

Using a hydrodynamical model as an input is a huge improvement to CMFGEN. Fine tuning models may fit better to the observations, but models with fine tuning parameters are not considered to be robust. Degeneracy in the parameters could falsify the interpretation from these models. The radiation hydrodynamics usually make the LTE assumption throughout the ejecta. Fully Non-LTE calculations, as mentioned in Sec. 2.4.3, are complicated and time-consuming. As a result, a better approach is to use radiation hydrodynamics to simulate the explosion up to the time when acceleration becomes negligible, and then employ the hydrodynamical output as an initial model in a sophisticated radiative transfer code. Another advantage of doing this is that it can provide better constraints to the explosion models. Many aspects from the explosion models are under hot debate, such as nucleosynthesis, ^{56}Ni mass, explosion energy and mixing. With the linkage to the hydrodynamics, radiative transfer codes can also put strong constraints on the radius and the mass of the progenitor.

3.0 PART I. NONTHERMAL EXCITATION AND IONIZATION IN SUPERNOVAE

3.1 WHY WITH NON-THERMAL EXCITATION AND IONIZATION

Supernovae are the main factories for the production of heavy elements. During the explosion, significant amount of radioactive elements are produced, especially ^{56}Ni. A typical Type Ia SN can produce $\sim$ 0.5 - 1.0 $M_\odot$ ^{56}Ni, while a core collapse supernova synthesizes $\sim$ 0.07 - 0.15 $M_\odot$ ^{56}Ni. ^{56}Ni is the main energy source in Type Ia SNe. Core collapse supernovae first release the energy deposited by the shock wave, and finally will be powered by radioactive decay energy. ^{56}Ni decays into ^{56}Co with a half-life of 6.1 days, and ^{56}Co further decays into ^{56}Fe with a half-life of 77 days. Radioactive decay produces γ-rays with energies of $\sim$ 1 MeV. γ-rays can interact with the medium through photoelectric effect, Compton scattering and pair production. The photoelectric effect dominates at the low energy range, while pair production happens at very high energy. For intermediate energies $\sim$ 100 KeV - 10 MeV, Compton scattering is the dominant processes.

In a Compton scatter, a high energy γ photon loses energy to eject an electron and becomes a lower energy γ photon. The ejected fast electrons have energies of $\sim$ 0.1 - 1 MeV and they degrade and deposit their energies into the medium through three channels: excitation, ionization and heating.

At early phases of core collapse supernovae, the excitation and ionization processes induced by the nonthermal electrons are usually thought to be unimportant. There are mainly two reasons. One is that the supernovae are hot and the ionization and excitation processes are dominated by radiation transport, the other is that an implausible amount of ^{56}Ni outward mixing is required for nonthermal processes to have a significant effect.

Mitchell et al. [274] argued for 10^{-4} $M_\odot$ ^{56}Ni to account for the strong Hα at 4 days after explosion, but it was proven to be time-dependent ionization effects [379, 88]. He I lines in Type Ib/Ic Supernovae have also been attributed to nonthermal excitation processes [157, 248, 360, 214, 361, 362, 215, 216]. However, Dessart et al. [93] showed that it is possible to reproduce these lines without nonthermal processes if the He mass fraction is $\geq 50\%$.

As a supernova expands and cools, the "photosphere" (defined as the region where the electron scattering opacity is equal to 2/3) recedes and we look deeper into the supernova. Studying the nebular spectra provides rich information on the explosion mechanism and perhaps uncovers the progenitor. However, nonthermal processes are crucial for line formation at the nebular epoch, making the inclusion of these processes necessary to analyze and interpret the spectra. For example, Dessart and Hillier [90] was unable to reproduce an the strong Hα profile at the end of the photospheric phase due to the absence of Balmer continuum photons. Moreover, Jerkstrand et al. [192] showed that radiative transfer effects are still substantial in SN 1987A at eight years after the explosion. Therefore, sophisticated radiative transfer calculations with nonthermal processes taken into account is necessary at the nebular phase.

3.2 THE NON-THERMAL SOLVER

3.2.1 The Spencer-Fano Equation

The radiative transfer code CMFGEN, which takes into account radioactive decay, previously assumed that all radioactive decay energy is deposited as heat. In reality, fast electrons resulting from Compton scattering between γ-ray and thermal electrons lose energy through three different channels – heating, excitation and ionization. The fractions of energy for the three channels can be computed if the degradation spectrum is known. This can be done by solving the Spencer-Fano equation [352]. Following Kozma and Fransson [214], the Spencer-Fano equation, which balances the number of electrons leaving and entering an

energy interval, can be written as:

$$\begin{aligned}
&\sum_i n_i y(E) \left[\sum_j \sigma_{ij}(E) + \int_I^{(I+E)/2} \sigma_c(E,\epsilon) d\epsilon \right] \\
&\quad - \frac{d}{dE}\left[y(E) L_e(E) \right] = \sum_i n_i \sum_j y(E+E_{ij}) \sigma_{ij}(E+E_{ij}) \\
&\quad + \sum_i n_i \int_I^{\lambda} y(E+\epsilon) \sigma_c(E+\epsilon,\epsilon) d\epsilon \\
&\quad + \sum_i n_i \int_{2E+I}^{E_{\max}} y(E') \sigma_c(E', E+I) dE' + S(E)
\end{aligned} \tag{3.1}$$

where $\lambda = \min(E_{\max} - E, E + I)$, $E_{\max}$ is the maximum energy of non-thermal electrons, and I is the ionization potential. $y(E)dE$ is defined as the flux of non-thermal electrons in the energy interval $(E, E + dE)$. n_i is the number density of a single species, and the sum over i allows for the contribution of different ionization stages and species. $L_e(E)$ is the energy loss of the non-thermal electrons due to Coulomb scattering by the thermal electrons. E_j is the excitation energy, σ_j is the excitation cross section of level j and $\sigma_c(E, \epsilon)$ is the differential ionization cross section for a fast electron with energy E and an energy loss of ϵ. Therefore, the ejected electron has energy $\epsilon - I$. The fast electron is called the primary electron and the ejected electron is called the secondary electron. The secondary electron can further degrade through the three same channels as the primary electron. $S(E)$ is the source term, and we assume all non-thermal electrons are injected at $E_{\max}$. The degradation spectrum $y(E)$ is normalized to $E_{\max}$, so that $y(E)$ is the degradation spectrum for 1 eV energy input. The first and second term on the left side represent the number of electrons leaving the energy interval $(E, E + dE)$ by impact excitation and ionization, respectively. The term with $L_e(E)$ is the number of electrons leaving the energy interval by heating the medium. The first term on the right side is the number of electrons entering the energy interval $(E, E + dE)$ by exciting another ion and losing energy. The second term is the ionization contribution from the primary electrons, and the third term is the ionization contribution from the secondary electrons if applicable.

The Spencer-Fano equation is more conveniently solved numerically using the integral

form [214], i.e.,

$$\begin{aligned}
&\sum_i n_i \sum_j \int_E^{E+E_j} y(E')\sigma_j(E')dE' \\
&+\sum_i n_i \int_E^{E_{\max}} y(E') \int_{E'-E}^{(E'+E)/2} \sigma_c(E',\epsilon)d\epsilon dE' + y(E)L_e(E) \\
&=\sum_i n_i \int_{2E+I}^{E_{\max}} y(E') \int_{E+I}^{(E'+I)/2} \sigma_c(E',\epsilon)d\epsilon dE' + \int_E^{E_{\max}} S(E')dE'
\end{aligned} \tag{3.2}$$

In Eq. 3.1, the integral of the differential ionization cross sections needs to be done numerically. However, only the total ionization cross sections appear in the integral form of the Spencer-Fano equation (Eq. 3.2), and can be computed analytically.

With the solution of the degradation spectrum, the fractional energies entering heating, η_h, excitation of ion i to level j, η_{ij}, and ionization of ion i, η_{ic}, can be computed by

$$\begin{aligned}
\eta_h = &\frac{1}{E_{\rm init}} \int_{E_0}^{E_{\max}} y(E')L_e(E')dE' \\
&+ \frac{1}{E_{\rm init}} E_0 y(E_0)L_e(E_0) + \frac{1}{E_{\rm init}} \int_0^{E_0} N(E')E'dE'
\end{aligned} \tag{3.3}$$

$$\eta_{ij} = \frac{n_{ij}E_{ij}}{E_{\rm init}} \int_{E_{ij}}^{E_{\max}} y(E')\sigma_{ij}(E')dE' \tag{3.4}$$

$$\eta_{ic} = \frac{n_i I_i}{E_{\rm init}} \int_{I_i}^{E_{\max}} y(E')\sigma_{ic}(E')dE' \tag{3.5}$$

where

$$\begin{aligned}
N(E) = \sum_i n_i \Bigg[&\sum_j y(E+E_{ij})\sigma_{ij}(E+E_{ij}) \\
&+ \int_{I_i}^{\lambda_i} y(E+E')\sigma_{ic}(E+E',E')dE' \\
&+ \int_{2E+I_i}^{E_{\max}} y(E')\sigma_{ic}(E',E+I_i)dE' \Bigg] + S(E)
\end{aligned} \tag{3.6}$$

[214]. $E_{\rm init}$ is the mean energy of the initial electrons, and E_0 is the lowest excitation or ionization energy.

To save computational effort, we only take into account the dominant ionization stages when computing the degradation spectrum. The other approximation is the neglect of γ-ray transport. In reality, some γ-rays may escape the SN, while others may deposit their energy at large distances from where they were created. In these calculations we assume, for simplicity, in-situ deposition. While not available at the time of the work in this chapter, a γ-ray transport code was later developed for use with CMFGEN [168].

We previously mentioned that for the source term we assume that all high energy electrons are injected at $E_{\max}$. Although not entirely realistic, this kind of source function generally has little influence on the results. High energy electrons "forget" their initial energies after several scatterings, and the source function is quickly washed out. Alternatively we can assume a bell shape source function near $E_{\max}$. This tends to give a smoother degradation spectrum near $E_{\max}$.

3.2.2 Ionization cross sections

Arnaud and Rothenflug [9] adopted the formula proposed by Younger [418] for calculating the impact ionization cross sections

$$\begin{aligned} Q_i(E) = \frac{1}{uI_i^2}\{A_i\left(1-\frac{1}{u}\right) + B_i\left(1-\frac{1}{u}\right)^2 + \\ + C_i\ln(u) + D_i\frac{\ln(u)}{u}\} \end{aligned} \tag{3.7}$$

where $u = E/I_i$. E is the energy of the impact electron, and I_i is the ionization potential for the element. A_i, B_i, C_i, and D_i are all coefficients. For the meaning of these coefficients, the reader should refer to Arnaud and Rothenflug [9]. In our calculations, we have used the most up-to-date coefficients (Arnaud 2011, private communication).

With the total cross section computed by Eq. 3.7, the differential cross section $\sigma_c(E,\epsilon)$ can be written as,

$$\sigma_c(E,\epsilon) = Q(E)P(E,\epsilon - I) \tag{3.8}$$

where $P(E_p, E_s)$ is the distribution of the secondary electrons for a primary electron energy

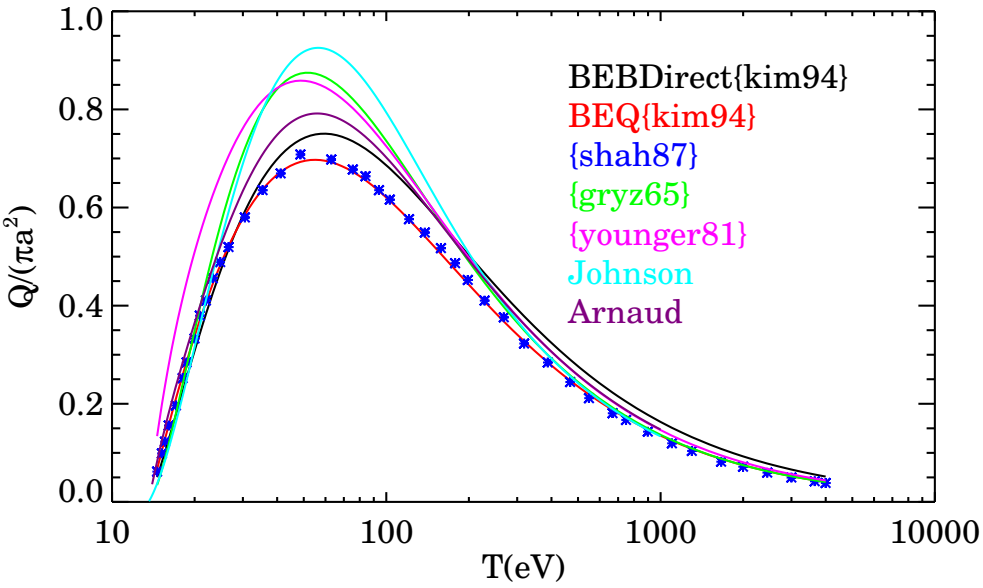

Figure 3.8: Comparison of the ionization cross sections of H I. The ionization cross sections are in unit of πa^2, where a is the Bohr radius. Several theoretical methods and a set of experimental data (green) are shown to compare with the prediction of the Arnaud and Rothenflug method. BEB Direct (magenta) and BEQ (red) models are from Kim and Rudd [202], while the shah87 (green), gryz65 (yellow), younger81 (cyan) and Johnson (blue) are from Shah et al. [330], Gryziński [145], S.M. and Younger [335] and Johnson [195], respectively. The BEB Direct, BEQ, shah87, gryz65 and younger81 results are obtained from National Institute of Standard and Technology (NIST). The Johnson's curve is computed by the formula in Johnson [195].

of E_p. Opal et al. [295] found $P(E_p, E_s)$ could be well described by

$$P(E_p, E_s) = \frac{1}{J \arctan[(E_p - I)/2J]} \frac{1}{[1 + (E_s/J)^2]} \tag{3.9}$$

where J is a parameter that gives a best fit to measurements and varies for different species. We adopt $J = 0.6I$, which is shown to be a reasonable approximation [295]. The secondary distribution function drops quickly so that very few secondary electrons have high energies.

Specifically, for H I with $I = 13.6\,\mathrm{eV}$, 66.7% of secondary electrons are below the ionization potential if $E_p = 1000\,\mathrm{eV}$ and 69.8% in the case of E_p =10 000 eV. Further, the mean energy of the secondary electrons, $\bar{v}_{\mathrm{sec}}$, only varies slowly as the energy of the primary electron E_p increases. For hydrogen, $\bar{v}_{\mathrm{sec}} = 21.53\,\mathrm{eV}$ for $E_p = 1000\,\mathrm{eV}$ and $\bar{v}_{\mathrm{sec}} = 33.36\,\mathrm{eV}$ for E_p =10 000 eV. Secondary electrons with low energies are easily thermalized and deposit energy as heat.

Fig. 3.8 shows the comparison of ionization cross sections of H I among theoretical models and experimental data, where the green dots are the experimental data and the others are theoretical predictions. The BEQ model gives the best fit to the data, but this model only suitable for small atoms. The Arnaud and Rothenflug formula can be applied to all atoms with different coefficients. All the models agree with the data at high energies, while the scatter is large at low energies. However, the uncertainties in the experimental data are large at low energies, which is not shown in the figure. The Arnaud and Rothenflug model still gives reasonable predictions.

3.2.3 Excitation cross sections

The electron impact excitation cross sections are only available for a few species, and only for a few levels. To proceed further, we adopt the Bethe approximation as discussed by van Regemorter [385]. With this approximation, Q_{ij} is given by

$$Q_{ij} = \frac{8\pi}{\sqrt{3}} \frac{1}{k_i^2} \frac{I_H}{E_j - E_i} f_{ij} \bar{g} \pi a_0^2 \tag{3.10}$$

where k_i^2 is the initial electron kinetic energy normalized to hydrogen ionization energy 13.6 eV, I_H is the hydrogen ionization energy, $E_j - E_i$ is the energy difference between the two levels, f_{ij} is the oscillator strength, and a_0 is the Bohr radius. The Gaunt factor $\bar{g}$ for neutral atoms utilizes Table 1 of van Regemorter [385], which is shown in Fig. 3.9. The variable x is defined by $x = \sqrt{\frac{mv^2}{2\Delta E}}$, where $\frac{1}{2}mv^2$ is the kinetic energy of the impact electron and ΔE is the transition energy. For positive ions, $\bar{g}$ has a constant value of 0.2 when $x \leq 1$ and is the same as the $\bar{g}$ for neutral atoms when $x > 1$. We also show the second order and the third order polynomial fit to the tabulated data. Although the third order gives a

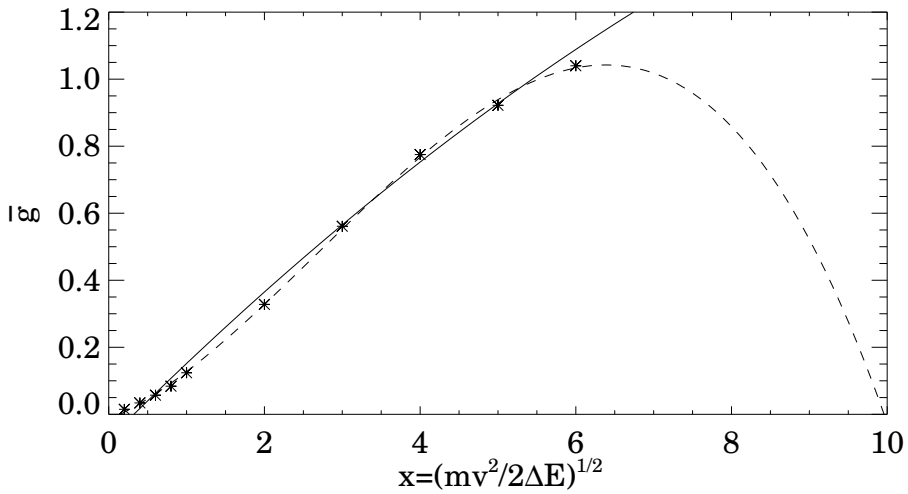

Figure 3.9: The tabulated gaunt factor (stars) for neutral atoms as a function of $x = \sqrt{\frac{mv^2}{2\Delta E}}$ given in van Regemorter [385]. The second order (solid) and the third order (dashed) polynomial fit are also shown.

better fit to the data, it drops rapidly at larger values of x. Thus, we adopt the second order polynomial fit in our calculations. At high energies, the Bethe approximation shows that the collisional excitation cross-section, like the ionization cross-section, scales as $\log E/E$.

Note that the Bethe approximation is only for permitted transitions (electric dipole transitions among states with the same spin). However, impact excitation by non-thermal electrons can occur for all transitions. To make allowance for those forbidden transitions, we use the collision strengths to compute the excitation cross sections, such that

$$Q_{ij} = \frac{1}{k_i^2}\frac{1}{w_i}\Omega_{ij}\pi a_0^2 \tag{3.11}$$

where w_i is the statistical weight of level i and Ω_{ij} is the collision strength. The main difficulty with this approach is that very few collision strengths are available. What we usually have are the thermally averaged effective collision strengths, defined by:

$$\Upsilon_{ij} = \int_0^\infty \Omega_{ij} \exp\left(-\frac{E_j}{kT}\right) d\left(\frac{E_j}{kT}\right) \tag{3.12}$$

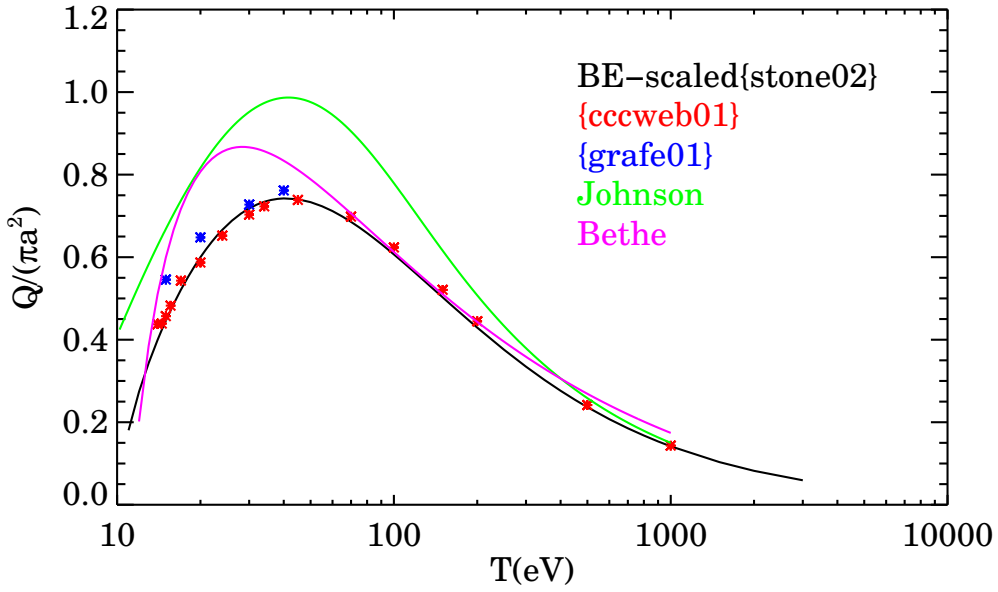

Figure 3.10: Same as Fig. 3.8, but now shows the comparison of excitation cross sections for transition from state 1s to 2p. The BE-scaled, cccweb01, grafe01 and Johnson models are from Stone et al. [356], Bray and Ralchenko [33], Grafe et al. [134] and Johnson [195], respectively. The results of the BE-scaled, cccweb01 and grafe01 come from the NIST.

where E_j is the kinetic energy of the outgoing electron. Fortunately, the thermally averaged effective collision strengths for forbidden transitions are almost constant at high temperatures, and hence we adopt such constant effective collision strengths as the collision strengths for impacting non-thermal electrons at all energies. This approximation is unlikely to have a major influence on the results since at high energies collisions for permitted transitions dominate (see Sec. 3.5.2), while at low energies there are relatively few non-thermal electrons, and collision rates are dominated by thermal electrons. An important distinction from non-thermal ionization is that non-thermal excitation does not produce secondary electrons.

In Fig. 3.10, the comparison of the excitation cross sections is shown. The results are similar to that of the ionization cross sections. The BE-scaled method gives better fit than the Bethe approximation and the Johnson's formula, but only works for small atoms. Bethe

approximation overestimates the excitation cross sections at low energies, but approaches the experimental data at high energies.

The accuracies and the uncertainties of the Arnaud & Rothenflug cross sections and the Bethe approximation will be discussed in Sec. 3.8.1.

3.3 THE HYDRODYNAMICAL INPUT

The hydrodynamical model 'lm18a7Ad' (Woosley 2010, private communication) we use as an initial input is the same as that adopted by Dessart and Hillier [89]. We briefly summarize the main properties of this model below. The hydrodynamical model was produced by the code KEPLER [398], using a progenitor with main-sequence mass of 18 $M_\odot$. The metallicity of the Large Magellanic Cloud (LMC) was adopted, which is $Z = 0.4Z_\odot$. The star is a BSG when the explosion is initiated.

The hydrodynamical model at 0.27 days was employed, since at this time homology is a good approximation in the outer regions. The rest of the ejecta is enforced to be strictly homologous to accommodate CMFGEN, although the innermost part of the ejecta is trimmed since it suffers fallback. Moderate mixing[1] is induced manually to soften the composition gradients. Hydrogen is deficient below 1500 $km\,s^{-1}$, while ^{56}Ni is primarily found below 2000 $km\,s^{-1}$. The total amount of ^{56}Ni in the initial hydrodynamical model is 0.084 $M_\odot$. Although a large set of model atoms are utilized, some potentially important species such as Ti I, Fe I, Sc I and Sc II are missing. The pre-SN steady and explosive nucleosynthesis in the KEPLER model were undertaken with a 13-isotope network which only captures the composition approximately. It also only computes explicitly the abundance of one unstable isotope (^{56}Ni) – numerous intermediate-mass elements (IMEs) and iron-group elements (IGEs) are bundled together. Moreover, the hydrodynamical model is enforced to be homologous, which affects the kinematics of the inner ejecta. With the recent availability of a model atom for Fe I we discuss the influence of Fe I on the spectra in Sec. 3.6.

The models from day 0.27 to day 20.8 have been presented in Dessart and Hillier [89],

[1] Hydrogen is absent below 1500 $km\,s^{-1}$ and the ^{56}Ni mass fraction is sizable only below 1000-2000 $km\,s^{-1}$.

focusing on early evolution at the photospheric phase.

3.4 THE NON-THERMAL MODEL

To study the long-term evolution of our SN model, we evolved the model further in time until day ~ 1000 – well into the nebular phase. After about 40.6 days, the sequence is separated into two branches, a "thermal sequence" with γ-ray deposition into heat exclusively, and a "non-thermal sequence" with non-thermal excitation and ionization.

In this section, we focus on a typical non-thermal model and discuss the properties of non-thermal processes in the model. We select a non-thermal model at day 127 (hereafter model D127_NT) near the beginning of the nebular phase. It is during the nebular phase that non-thermal effects will be the most important. Moreover, complications arising from dust will not be present since dust formation is not thought to happen until day 300 [358, 130].

In Fig. 3.11 we illustrate the elemental mass fractions on a logarithmic scale as a function of velocity at day 127. Hydrogen is an order of magnitude less abundant below velocity 1500 $\mathrm{km\,s^{-1}}$ and this velocity can be taken to indicate the velocity down to which H has been mixed. Rather than ^{56}Ni, we show the mass fraction of ^{56}Co, since at day 127 only a small amount of ^{56}Ni is left, and ^{56}Co decay is the main energy source. The figure shows that ^{56}Co has been mixed out to about 2000 $\mathrm{km\,s^{-1}}$ in the initial model, although trace amounts also exist at higher velocities.

3.4.1 The degradation spectrum

A typical degradation spectrum at velocity ~ 1000 $\mathrm{km\,s^{-1}}$ for the D127_NT model is shown in Fig. 3.12 (red). The sharp rise at high energy is a result of the adopted source function – we inject all fast electrons at $\mathrm{E_{max}}$. The spectrum from $\mathrm{E_{max}} = 1\,\mathrm{keV}$ down to 100 eV shows the slowing down of primary electrons, while the rise at low energy indicates a cumulation of secondary electrons. The shape of the degradation spectrum, particularly at low energies, is influenced by the ionization state of the gas.

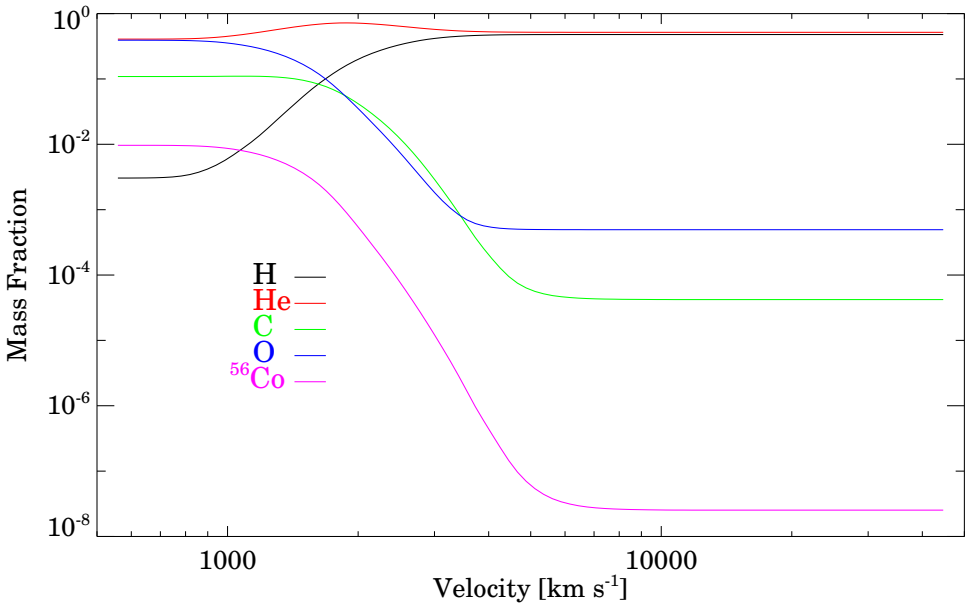

Figure 3.11: Illustration of the elemental mass fractions on a logarithmic scale as a function of velocity at day 127. We plot hydrogen (black), helium (red), carbon (green), oxygen (blue) and ^{56}Co (magenta) – five important elements in the model.

Uncertainties in the degradation spectrum are introduced by the choices in the number of energy bins, accuracies of the excitation and ionization cross sections, and by the choice of the high energy cut, E_{max}. The latter two will be discussed in Sec. 3.9. For the number of energy bins, we typically adopt N = 1000 extending from 1 eV to 1 keV. In Fig. 3.12, we also show another two degradation spectra computed with energy bins N = 100 (black) and N = 10 000 (blue). The flux in the N = 100 degradation spectrum is systematically lower than the other two, except at the high energy edge. The N = 10 000 spectrum is very close to the one with N = 1000, and hence the uncertainty arising from using 1000 energy bins is negligible. We also made spectral comparisons among the above three models. The models with 1000 and 10 000 energy bins showed no distinguishable differences, while the model with 100 energy bins was only slightly different from the other two. Interestingly, we later discovered that a smaller number of bins can be used, provided we scale the degradation

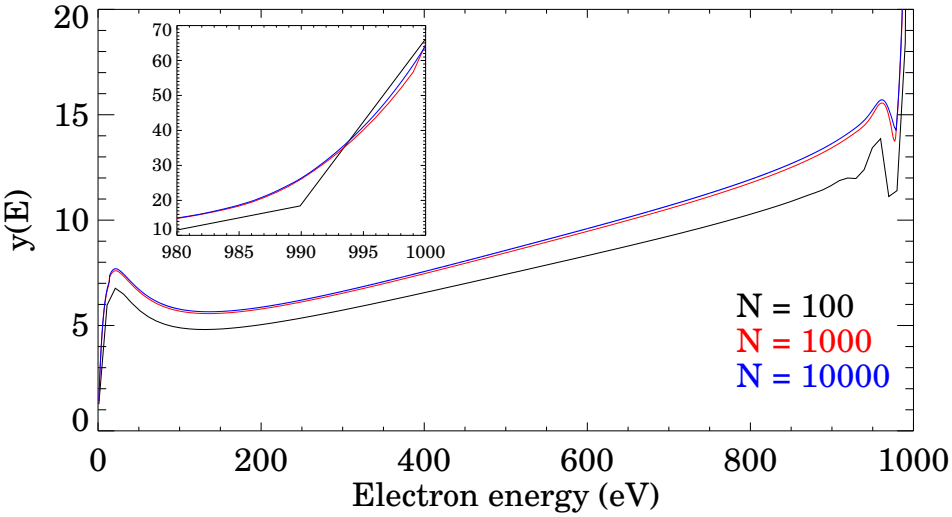

Figure 3.12: The degradation spectra at a model velocity of ~ 1000 km s^{-1} computed using different numbers of energy bins: 100 (black), 1000 (red), 10 000 (blue).

spectrum so that the fractional energies entering the three channels sum to unity.

3.4.2 Number density of non-thermal electrons

Knowing the degradation spectrum $y(E)$, the electron spectral density in space can be estimated from $y(E)/v$, where $v = \sqrt{2E/m_e}$. The number density of the non-thermal electron is then given by

$$N_e = \int_0^{E_{\max}} \frac{y(E)}{v} dE = \int_0^{E_{\max}} y(E) \sqrt{\frac{m_e}{2E}} dE \tag{3.13}$$

Fig. 3.13 shows the comparison of number density of the non-thermal and thermal electrons at day 127. The number density of the non-thermal electrons is many orders of magnitude smaller than that of the thermal electrons at all depths. The increase of the non-thermal electrons number density at inner regions is consistent with the increase of the ^{56}Co abundance shown in Fig. 3.11.

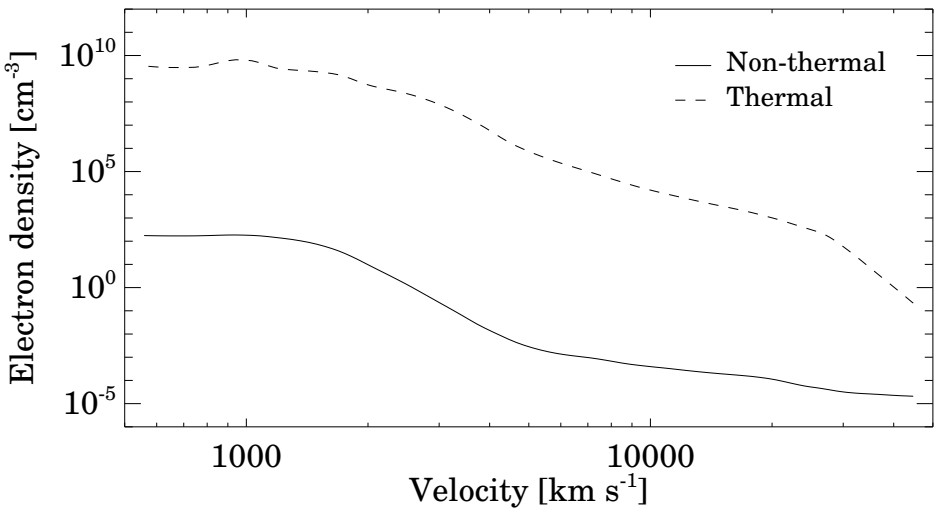

Figure 3.13: Comparison of the number density of the non-thermal electron (solid) and the thermal electron (dashed).

3.4.3 Energy fraction of the three channels

With the inclusion of non-thermal excitation and ionization, γ-rays deposit energy into all three channels. In Fig. 3.14, we plot the fraction of energy entering the three channels as a function of velocity. We also plot the ejecta ionization fraction X_e, which shows that the heating fraction is sensitive to X_e. In the outermost region, the heating fraction reaches unity as X_e becomes 1 – the highest ionization stage ions are unable to be ionized and excited, quenching the excitation and ionization processes. The high ionization fraction at this region is set by ionization freeze-out due to the time-dependent effects [88]. Between 3000 km s^{-1} and 10 000 km s^{-1}, non-thermal excitation and ionization become prominent where X_e becomes very small. As X_e increases inward from 3000 km s^{-1}, fractional non-thermal excitation and ionization decline and fractional heating rises and becomes dominant.

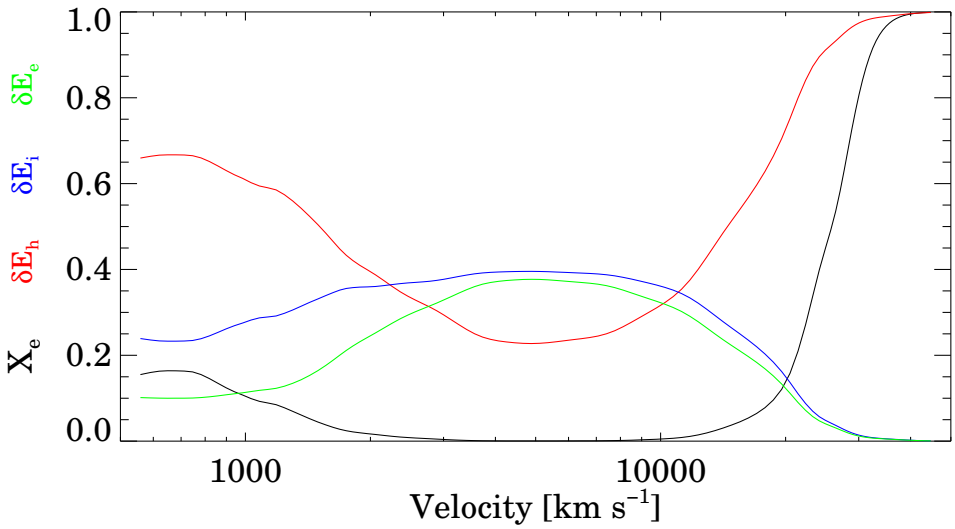

Figure 3.14: The fractional energy that goes into heating δE_h(red), ionization δE_i (blue) and excitation δE_e (green) in model D127_NT, as a function of velocity. The ejecta ionization fraction X_e, which is defined as the ratio of number of ions to number of atoms, is also shown (black).

3.4.4 Excitation and ionization

When non-thermal excitation and ionization occur, energy from non-thermal electrons is used to excite or ionize an atom. The Spencer-Fano equation (Eq. 3.1) implies that the abundances and the cross sections are the key to determine what energy a species "consumes". In this subsection, we study the fractional energies consumed by a species and compare them to the corresponding species.

In Fig. 3.15, we illustrate the fractional energies taken away from the non-thermal electrons by a species in both the excitation and ionization channels. The largest 5 consumers, summing over all depths, are plotted (solid lines). We overplot the fractional abundances of these 5 species (dashed lines). However, the calculations of fractional abundances excludes the highest ionization stages of all elements. These highest ionization stages are the ones in the model, not necessarily the same as the ion of an element with no electron left. For

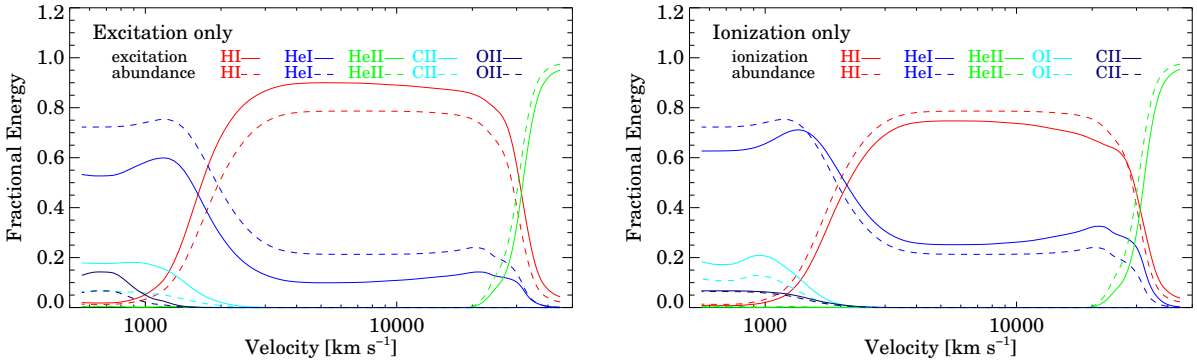

Figure 3.15: The largest 5 (summation over all depths) fractional energies taken away from the non-thermal electrons by species in the excitation (top) and ionization (bottom) channel (solid lines). The fractions of species abundances are overplotted for comparison. Importantly, the highest ionization stage of each element is excluded in the calculations of fractional abundances. (see the text for details).

instance, in our models, we utilize detailed model atoms for Fe II, Fe III, Fe IV, Fe V, Fe VI and Fe VII, then Fe VIII is the highest ionization stage for iron. The reason for excluding the highest ionization stages is that we treat these ionization stages as a single level, and so they don't have any excitation or ionization routes. In both channels, it is obvious that H I, He I and He II are the dominant consumers of non-thermal electron energy. He II is the main consumer above 30 000 km s^{-1}. In the middle region, both H I and He I are prominent. Due to low abundance of H, He I dominates the inner zone, although other species, like C I, C II, O I and O II also play a role. Fig. 3.15 shows that the species abundances, especially H I, He I and He II, have similar patterns to their fractional energies, in both channels. Such similarity indicates that allocation of the non-thermal energy is generally controlled, as expected, by the species abundances.

3.5 NON-THERMAL VS THERMAL MODELS

In this section, we present a comparison of the temperature and ionization structure between the non-thermal and thermal models. The spectral evolution of the two sequences will also be compared.

3.5.1 Comparison of the temperature structure

In Fig. 3.16, we compare the temperature structure between model D127_NT and the thermal model at day 127 (hereafter model D127). As mentioned previously, the non-thermal model generally has a lower temperature in the region between 1000 $\mathrm{km\,s^{-1}}$ and 5000 $\mathrm{km\,s^{-1}}$ where the non-thermal effects are crucial. The temperature for the two models above 5000 $\mathrm{km\,s^{-1}}$ is pretty flat (i.e., almost constant). This is an artifact – a floor temperature of 1500 K is imposed for the models to prevent numerical overflow. The flux mean opacity at 5000 $\mathrm{km\,s^{-1}}$ is of order 10^{-2}, thus the region above 5000 $\mathrm{km\,s^{-1}}$ has very little influence on spectral formation[2].

The decrease in the temperature can be understood as follows. The thermal model puts all decay energy into heating, while the non-thermal model only puts a portion of decay energy into heating. Moreover, the coupling between the gas and the radiation at this time is relatively weak, and hence, we expect that only the heating channel will substantially affect the temperature. Energy that has not gone into heat/temperature is stored up in ionization/excitation, driving the material even further away from LTE level populations.

Notice that the temperature of the two models is similar below 1000 $\mathrm{km\,s^{-1}}$, despite the existence of a substantial amount of ^{56}Ni. Even though the region is not in LTE, collisional processes are important, and there is a strong coupling between the radiation field and the gas, and thus energy initially deposited via the ionization and excitation channels can be thermalized. The fractions of energy entering the three channels are shown in Fig. 3.14. The heating fraction becomes dominant in the inner region, which is consistent with the temperature comparison in Fig. 3.16.

[2]This is confirmed by computing two models with different floor temperatures. The synthetic spectra show no distinguishable difference between models with floor temperatures of 1500 K and 4000 K.

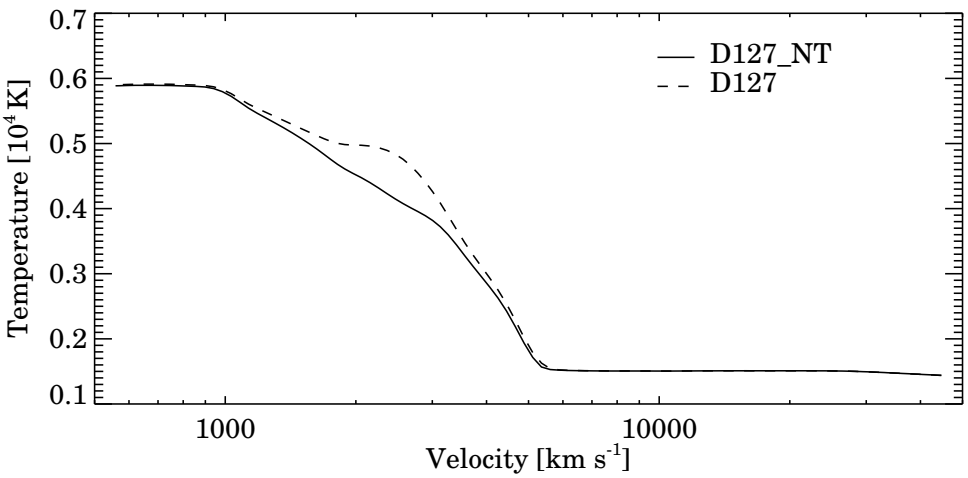

Figure 3.16: Comparison of temperature structure between model D127_NT (solid) and model D127 (dashed).

3.5.2 Controlling processes for H I and He I lines

In this section, we compare the hydrogen and helium ionization structure in the D127 and D127_NT models and study the processes controlling the H I and He I lines in the non-thermal model. The H and He ionization fractions for both the D127 and D127_NT models are illustrated in Fig. 3.17. In the cobalt region, the ionized H fraction has increased by up to an order of magnitude, while in the region above $v > 5000$ km s^{-1}, the ionization is unchanged, since ^{56}Co is deficient there.

While He remains neutral for $v < 10\,000$ km s^{-1}, the singly ionized He fraction is now significant. We can also see significant change in the He ionization fraction above the region where cobalt is abundant, which is due to a small amount of cobalt in the model. At large velocities, the ionization of both H and He is frozen, since the expansion time-scale is smaller than the recombination time-scale [89].

Fig. 3.18 shows the model spectra and the spectra with only bound-bound transitions of He I and H I at the optical band. Optical, as well as IR, H I and He I lines mainly originate below 2000 km s^{-1} in the non-thermal model, with a small fraction of the line flux coming

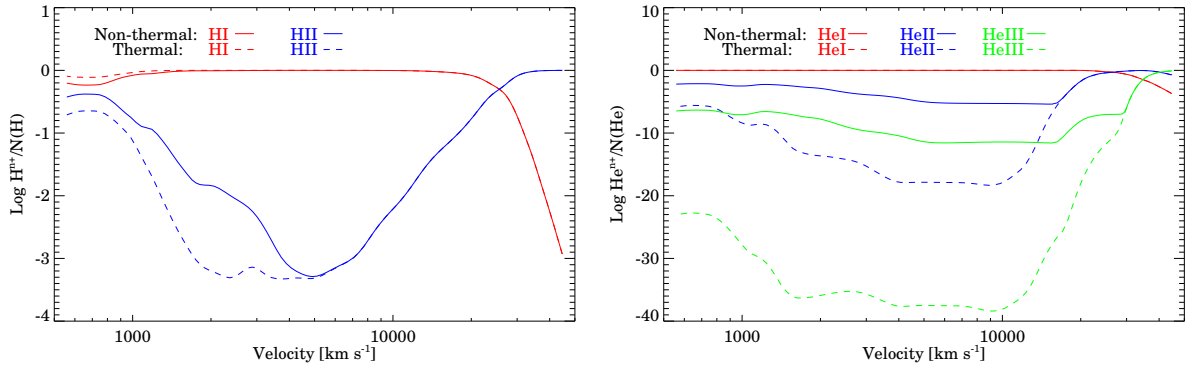

Figure 3.17: Logarithmic species fractions of different ionization stages for hydrogen (top) and helium (bottom). Comparison is made between model D127_NT (solid lines) and D127 (dashed lines).

from 2000 - 3000 km s^{-1} for some lines, e.g., He I 1.083 μm. H I lines in the thermal model (upper panel) are generally weak and He I lines are absent. In the non-thermal model (lower panel), all H I lines are strengthened, with Hα particularly boosted by non-thermal processes. He I lines also contribute significantly to the spectrum. While most optical He I lines are contaminated by other lines, He I 7065 Å might be a good diagnostic to infer the influence of non-thermal processes on helium. Notice that He I 4471 Å is excited in the non-thermal model but is absent from the spectra due to line-blanketing.

The prominence of He I 1.083 μm and He I 2.058 μm due to non-thermal processes at late times (t $\geq$ 200 d) was noted by Li and McCray [239], and observations showed He I 2.058 μm is more isolated [265]. In Fig. 3.19, we show the model spectra and the spectra with only bound-bound transitions of He I for models D127_NT and D127, focusing on the He I 2.058 μm line. Similar to the optical band, no He I line is present in model D127 in the wavelength range from 1.9 μm to 2.2 μm. However, He I 2.058 μm produces a prominent absorption feature in the D127_NT model. This feature has been seen in observations of SN 1987A [265], providing strong evidence for the influence of non-thermal processes on He I. Li and McCray [239] showed that He I 2.058 μm is mainly due to non-thermal excitation and He I 1.083 μm

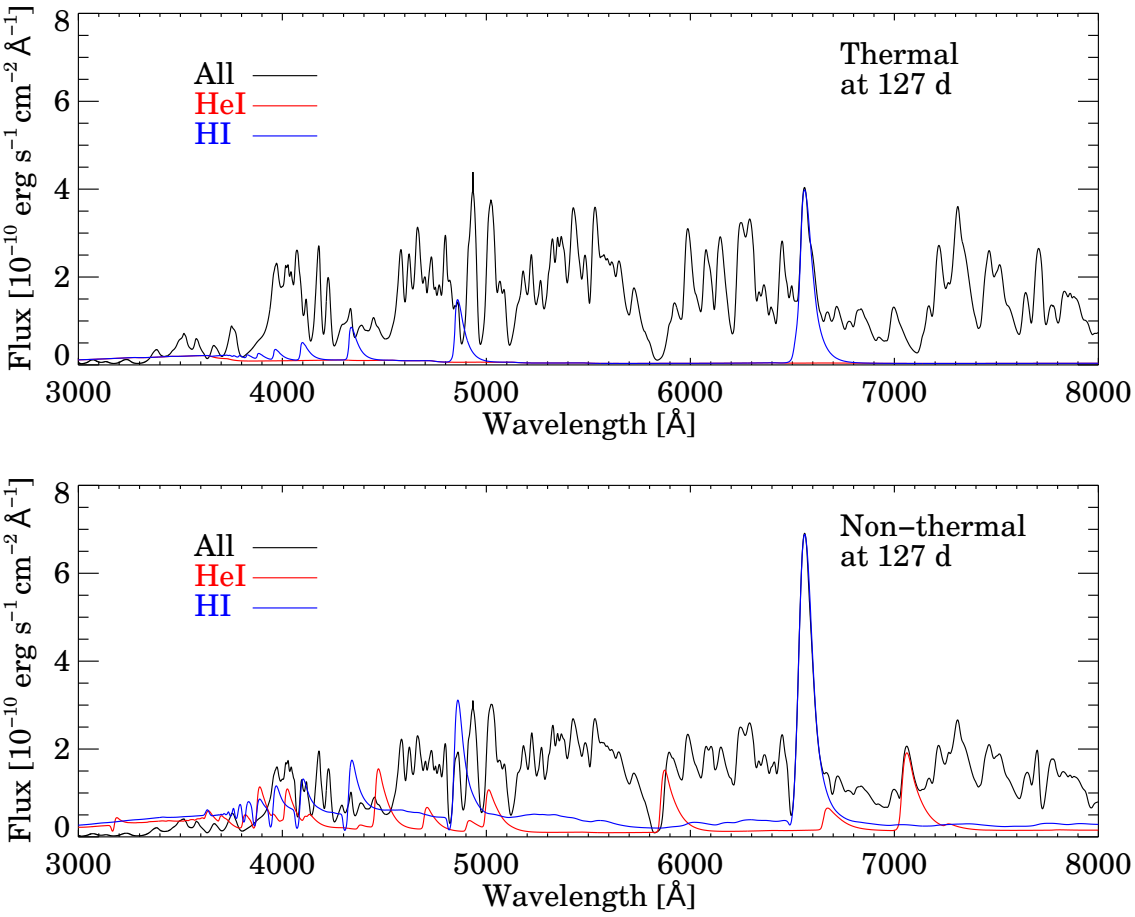

Figure 3.18: Upper panel: The D127 model spectrum (black) and the model spectra computed by including only bound-bound transitions of He I (red) and H I (blue) at optical band. Lower panel: Same as the upper panel, but for the D127_NT model.

is mainly excited by thermal electrons during $200\,\mathrm{d} \leq \mathrm{t} \leq 450\,\mathrm{d}$.

In Fig. 3.20, we illustrate the major fractional rates ($\geq 5\%$ at any depth) that populate and depopulate the states $1\mathrm{s}\,2\mathrm{p}\,^1\mathrm{P}^o$ and $1\mathrm{s}\,2\mathrm{p}\,^3\mathrm{P}^o$ of He I for model D127_NT. Positive normalized rates illustrate the routes that populate the state, while negative ones show the routes that depopulate the state. States $1\mathrm{s}\,2\mathrm{p}\,^1\mathrm{P}^o$ and $1\mathrm{s}\,2\mathrm{p}\,^3\mathrm{P}^o$ are the upper levels for the He I lines $2.058\,\mu$m and $1.083\,\mu$m, respectively. For the state $1\mathrm{s}\,2\mathrm{p}\,^1\mathrm{P}^o$, we confirm that non-

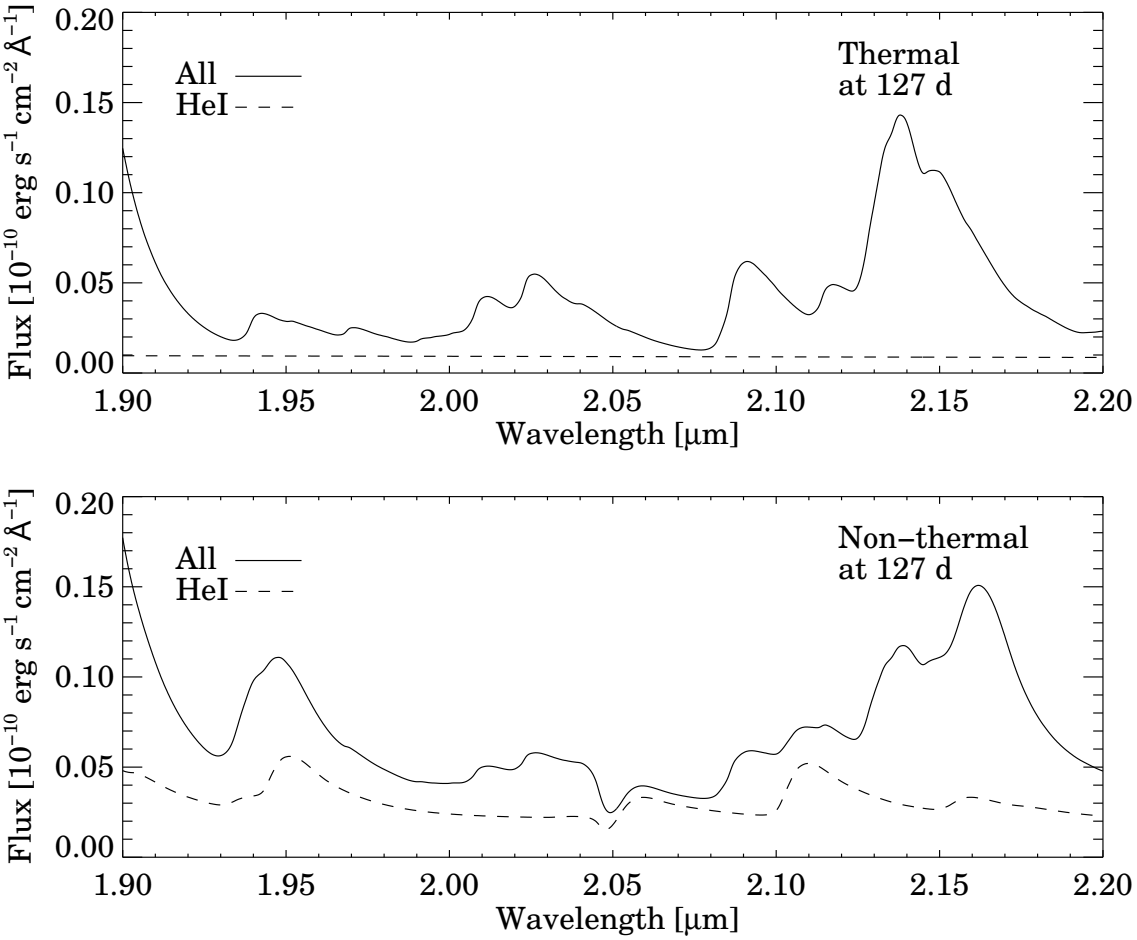

Figure 3.19: Illustration of model spectrum (solid) and model spectrum computed by including only bound-bound transitions of He I (dashed) for model D127 (top panel) and D127_NT (bottom panel) between 1.9 and 2.2 μm.

thermal excitation is the main excitation mechanism. Cascades from higher levels, especially the 1s 3d ^{1}D state, also play an important role at this stage.

For the state 1s 2p $^3P^o$, cascades from higher levels (mainly 1s 3s ^{3}S and 1s 3d ^{3}D) are the key processes to populate it below 3000 km s^{-1}. Recombination is also non-negligible. These are indirectly related to the non-thermal ionization processes. Thus, in contrast to the He I 2.058 μm line, non-thermal excitation is largely irrelevant for He I 1.083 μm. This is

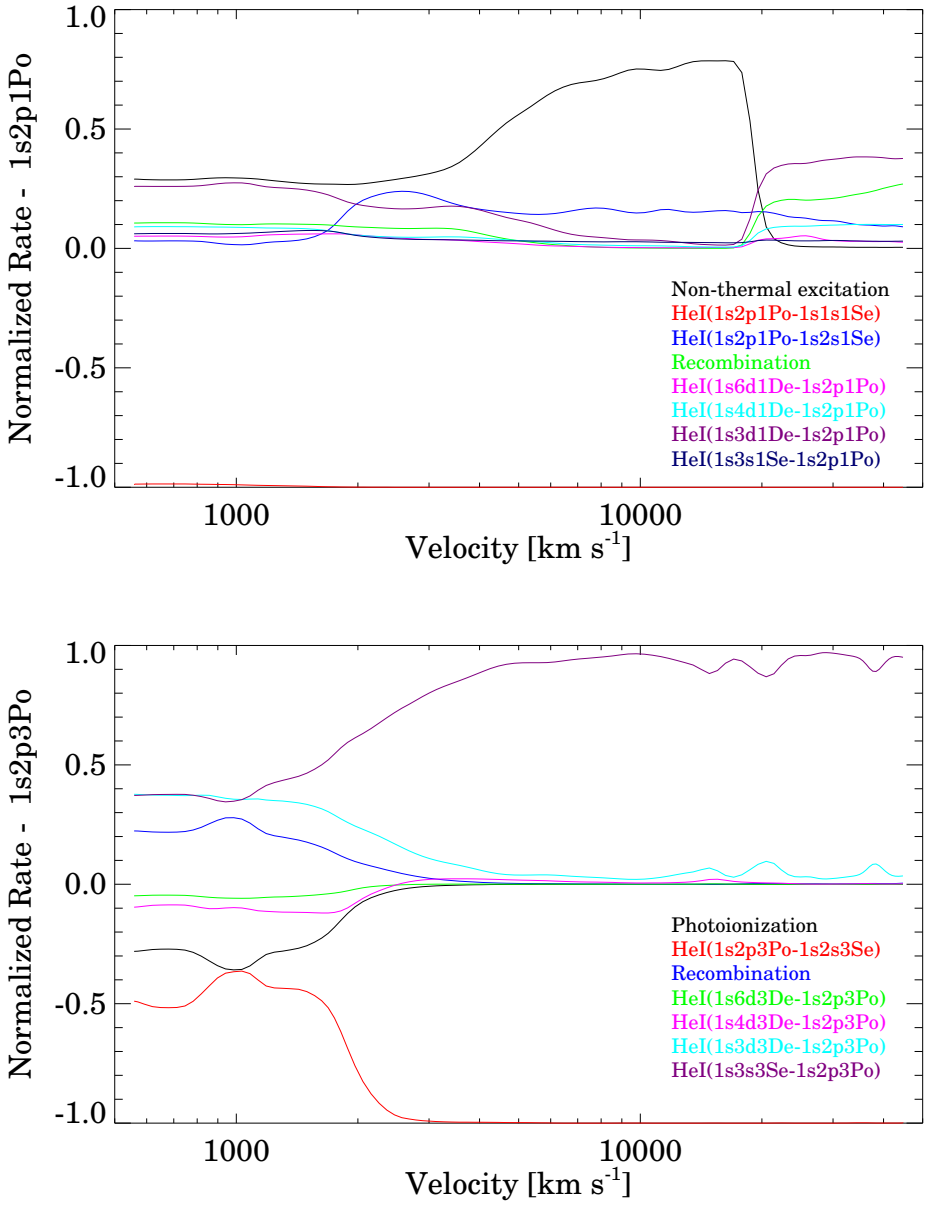

Figure 3.20: Top: Normalized rates for different processes that populate and depopulate the $1s\,2p\,{}^1P^o$ state of He I. Only processes with a fractional rate $\geq 5\%$ at more than one depth are shown. Bottom: Same as the top panel, but for the case of $1s\,2p\,{}^3P^o$ state of He I.

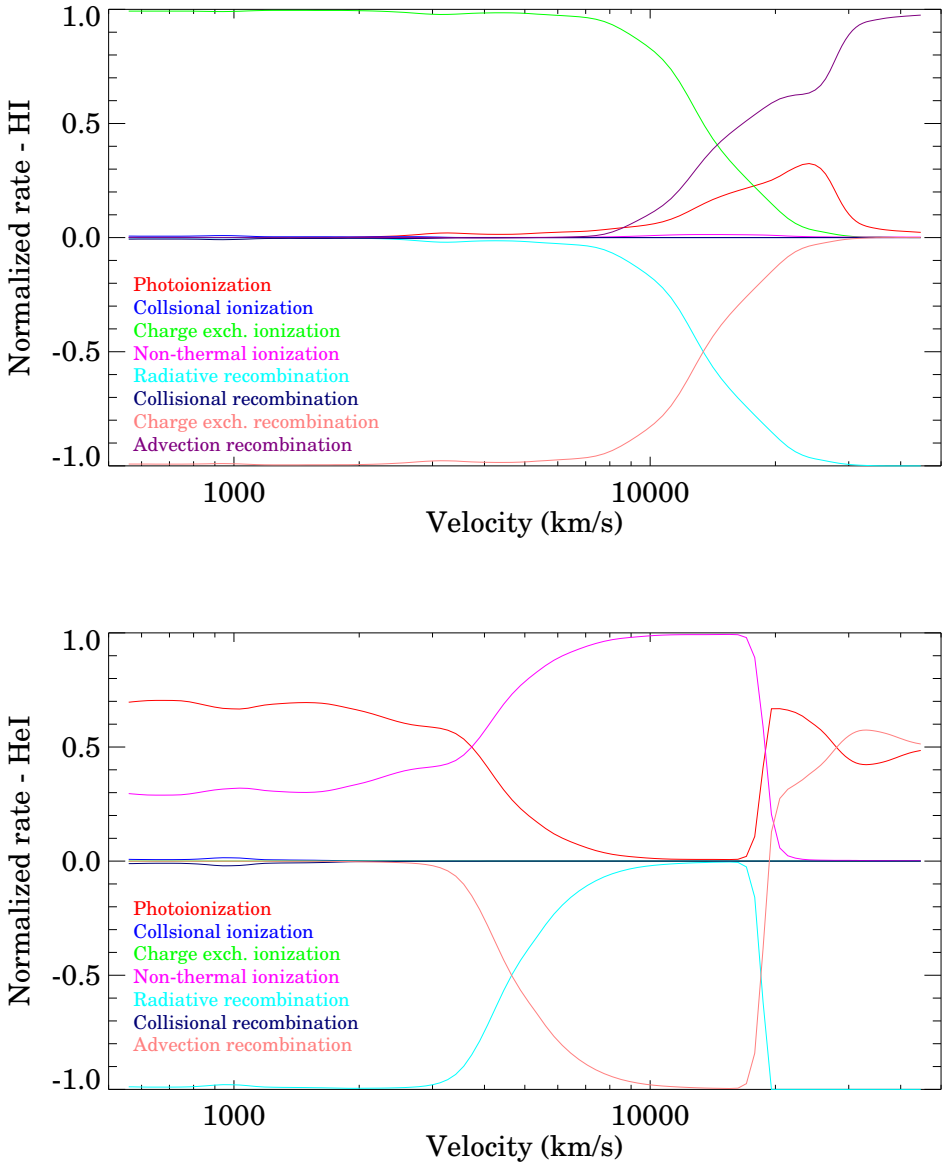

Figure 3.21: Normalized rates for H I (top) and He I (bottom), including all processes allowed in the modeling.

due to the difference in the collision strength behavior of the two transitions. Non-thermal excitation from the ground state ($1s\,1s\,^1S$) is generally the dominant excitation route, since the ground state is the most populated state. At low energies, the collision strength for the singlet transition (permitted transition), $\Omega(1s\,1s\,^1S - 1s\,2p\,^1P^o)$, is similar to that of the triplet transition (forbidden transition), $\Omega(1s\,1s\,^1S - 1s\,2p\,^3P^o)$. However, $\Omega(1s\,1s\,^1S - 1s\,2p\,^1P^o)$ grows significantly as the impact energy increases, while $\Omega(1s\,1s\,^1S - 1s\,2p\,^3P^o)$ is approximately constant at high energies. As a result, non-thermal excitation processes contribute much less to the triplet states than to the singlet states. Due to radiative excitation from $1s\,2s\,^3S$ to $1s\,3p\,^3P^o$ and subsequent decay to $1s\,3s\,^3S$, electron cascade from $1s\,3s\,^3S$, rather than $1s\,3d\,^3D$, is the dominant process populating the $1s\,2p\,^3P^o$ state above $3000\,\mathrm{km\,s^{-1}}$.

Despite the importance of non-thermal processes, we find that photoionization and recombination play a crucial, if not dominant, role in populating many other levels. However, in a "thermal" model, the photoionization and recombination rates are too small to produce a prominent effect. The trigger for the large photoionization and recombination rates is non-thermal processes. In Fig. 3.21 we show the normalized rates affecting the H I and He I ionization balance for model D127_NT. For H I, the fraction of non-thermal energy deposited via the ionization channel is small and photoionization and recombination are the dominant processes and they balance each other below $8000\,\mathrm{km\,s^{-1}}$. We check an individual level, $n = 1$, of H I in both models (D127_NT and D127), and find that the photoionization and recombination rates are increased by a factor of ~ 2 when non-thermal processes are included. For the He I $1s\,2p\,^1P^o$ state, non-thermal ionization and excitation rates in model D127_NT are 5 orders of magnitude greater than any rate in model D127. Below $3000\,\mathrm{km\,s^{-1}}$, non-thermal ionization becomes significant, and the radiative recombination rate is now balanced by the photoionization and the non-thermal ionization rates. Although the net non-thermal rate is not overwhelmingly dominant, it is crucial for controlling the ionization balance.

3.5.3 Comparison of optical and IR spectra

Fig. 3.22 shows the comparison of the optical and IR spectra between models D127_NT and D127. In the optical range (Fig. 3.22, top panel), D127_NT generally produces slightly lower

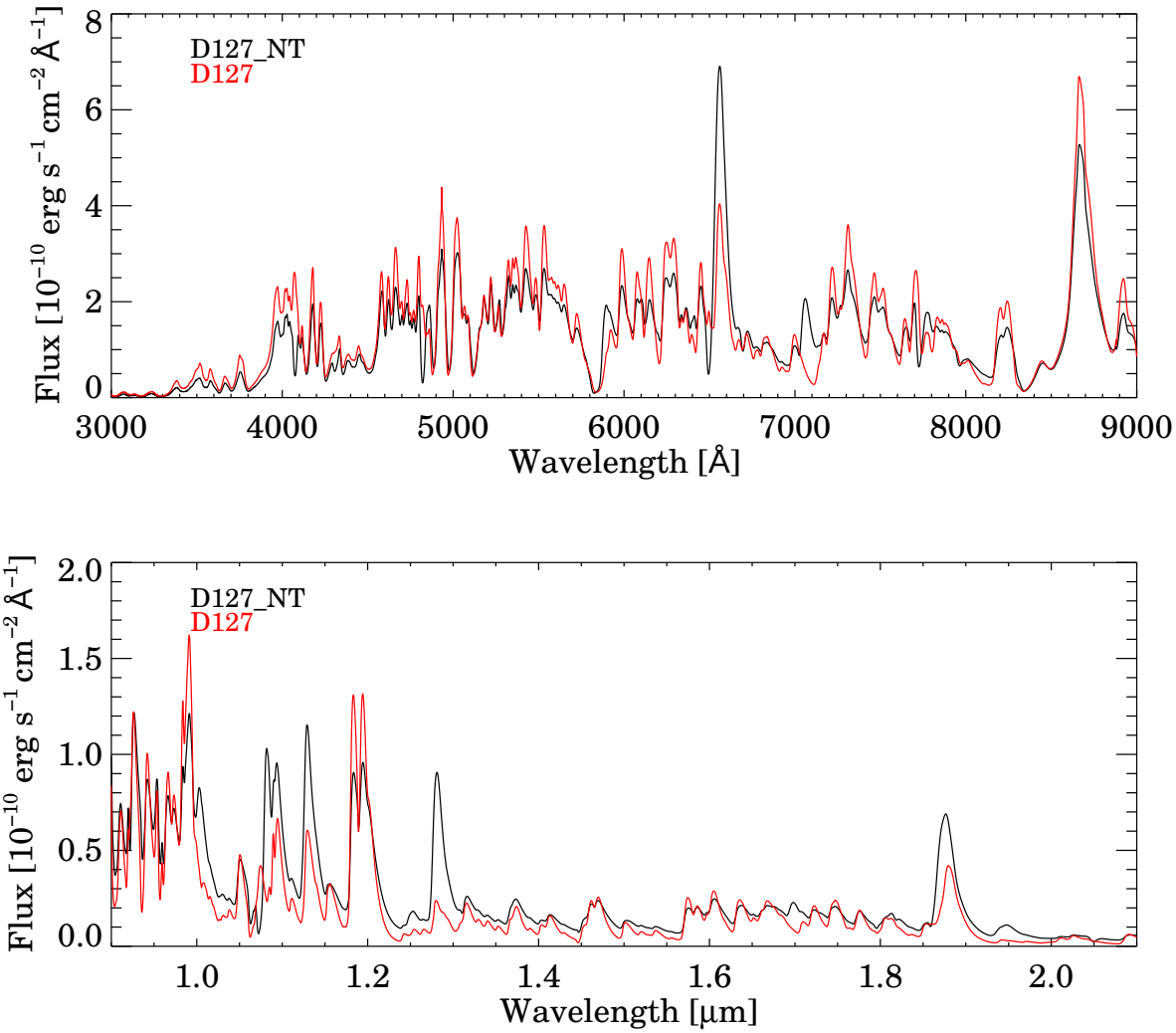

Figure 3.22: Comparison of optical and IR spectra between model D127_NT and D127.

fluxes but with two enhanced prominent features — Hα and He I 7065Å. The Ca II IR triplet is slightly weakened. In the bottom panel of Fig. 3.22, most of the lines are strengthened, such as He I 1.083 μm, Pa γ 1.094 μm, O I 1.129 μm, Pa β 1.281 μm and Pa α 1.875 μm. However, Ca II 1.184 μm and 1.195 μm are weakened.

Dessart and Hillier [90] found that in their SNe II-P models the Balmer lines suddenly disappeared at end of the photospheric phase – a result of the vanishing of Balmer-continuum photons. However, observations of Type II SNe show a strong Hα profile during the nebular

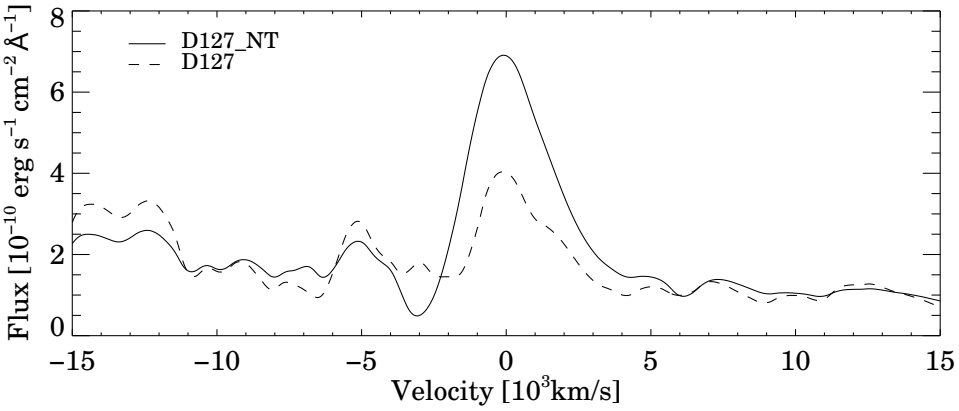

Figure 3.23: Comparison of the Hα profile between models D127_NT (solid) and D127 (dashed).

phase. They attributed this discrepancy to the exclusion of non-thermal excitation and ionization in the models. We present here the comparison of Hα at day 127 in Fig. 3.23. While Hα is almost absent in model D127, it shows a strong P Cygni Hα profile in model D127_NT. The emission component is stronger and wider and a P Cygni absorption trough is now present. The width of Hα is related to the outward mixing of ^{56}Ni. This may be helpful to determine the ^{56}Ni mixing in Type II SNe, as hydrogen is abundant in these SNe and Hα is one of the strongest features at nebular epochs.

3.5.4 Comparison of the spectral evolution

As mentioned in the previous section, Dessart and Hillier [90] were unable to reproduce the strong Hα at the nebular phase for red supergiant (RSG) models, which was speculated to be due to the neglect of non-thermal processes. Moreover, the mixing in their models may have been too weak. The best explanation for the persistence of Hα at late times is non-thermal excitation and ionization processes combined with mixing of H and ^{56}Ni. This has been one of the motivations for this study. In Fig. 3.24, we present the spectral evolution

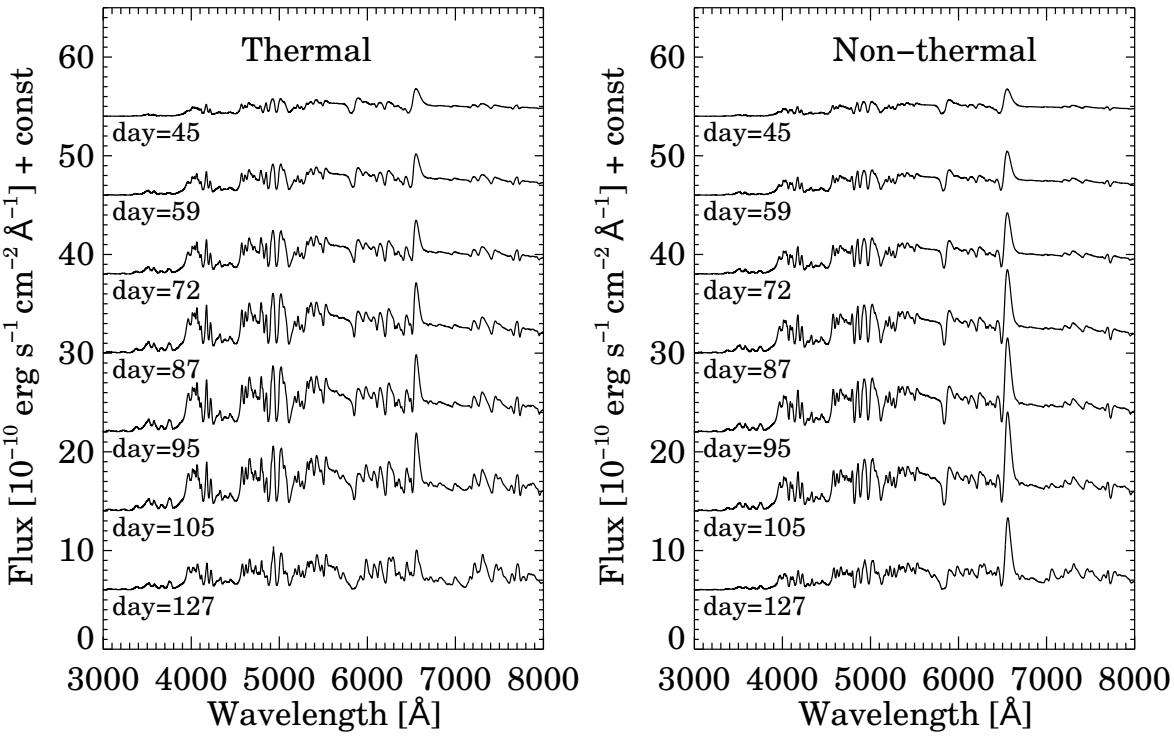

Figure 3.24: Left panel: montage of synthetic optical spectra for the thermal sequence. The days since breakout are labeled below each spectra. Right panel: montage of synthetic spectra at the same epochs shown in the left panel for the non-thermal sequence. The synthetic spectra are reddened with E(B-V) = 0.15 and scaled for a distance of 50 kpc. The most prominent difference between the spectra of the two sequences is the evolution of Hα – its strength persist at all times in the non-thermal sequence but it almost disappears at late times in the thermal sequence.

of the non-thermal and the thermal sequences. The disappearance of Hα is also observed in the thermal model for SNe resulting from a blue supergiant (BSG) progenitor. The strength of Hα increases till day 96, and then fades quickly. On day 140, no prominent feature is seen. The spectral evolution of the non-thermal sequence shows similarity, except for Hα, which has a stronger maximum strength at about day 96, decreases gradually after that, and

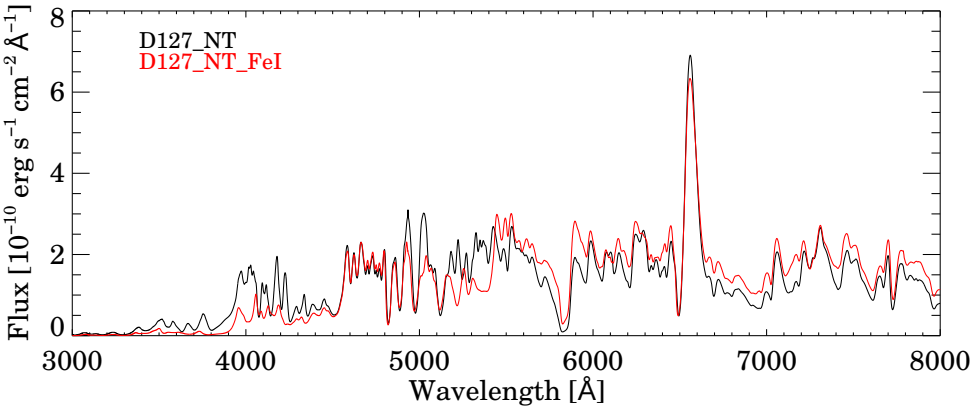

Figure 3.25: Comparison of optical spectral between model D127_NT and the model with Fe I (hereafter model D127_NT_FeI).

maintains a stronger signature on day 140. This confirms that the persistence of strong Hα emission during the nebular phase is closely related to non-thermal excitation and ionization. The non-thermal effects on spectra at day 54 are relatively small, confirming that the neglect of the non-thermal processes in earlier models is unlikely to have a significant influence on model spectra.

3.6 THE INFLUENCE OF Fe I

The source of opacity in SNe is complicated, since lots of IMEs and IGEs are synthesized during the explosion. Although a huge number of levels are included in the model, we are still missing some model atoms and the amount of levels of current model atoms may also be insufficient. Many of the missing model ions are the lowest ionization stages. These do not influence the spectra at early times when the ejecta is hot, but may significantly influence the opacity at late times when the ejecta becomes cold. Here, we explore the

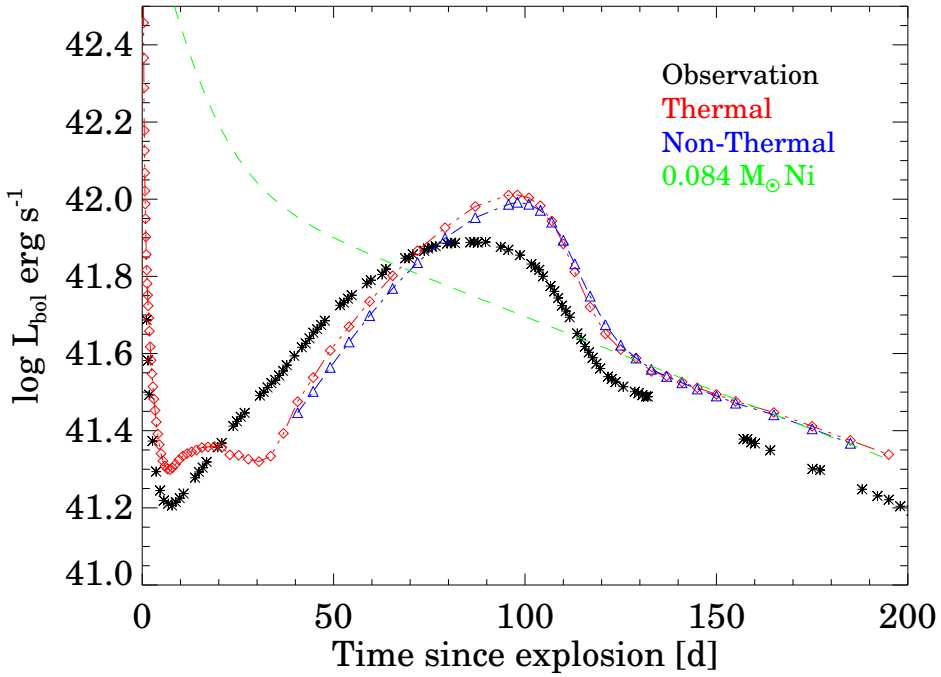

Figure 3.26: Comparison of the observed (black stars, Suntzeff and Bouchet 1990) bolometric light curve of SN 1987A to the theoretical bolometric light curves of the thermal (red) and non-thermal (blue) sequences, with symbols referring to the computed epochs of models. The observational bolometric light curve is constructed by using ultraviolet, optical and infrared photometry. A light curve resulting from the conversion of energy from the radioactive decay of 0.084 $M_\odot$ (green) is also shown for reference.

influence of Fe I. Oscillator strengths are from Kurucz [221][3], photoionization cross sections are from Bautista [22] (accesed through Nahar-OSU-Radiative-Atomic-Data web site), while collision rates among the lowest 10 levels are from Pelan and Berrington [303] (accessed from TIPBASE at cdsweb.u-strasbg.fr/tipbase/home.html).

We included Fe I at day 5 and ran a sequence of models with this new atom and with non-thermal excitation and ionization. Fig. 3.25 illustrates the comparison of the optical spectra

[3]Data from R. L. Kurucz is available online at http://kurucz.harvard.edu

at day 127. With the inclusion of Fe I, the emergent flux decreases appreciably between 3000 Å and 5500 Å, with the energy redistributed to longer wavelengths above 6000 Å. Many other atoms, such as Co I, Ti I and Sc II, may cause effects similar to Fe I. We will include more complete model atoms, as they become available, to better address line blanketing.

3.7 COMPARISON WITH THE OBSERVATIONS

SN 1987A is still one of the best observed and studied SNe, and it is about 50 kpc away from the earth. Although its progenitor was a BSG, there is still debate about the evolutionary channel that led to a SN explosion as a BSG [164, 226, 308]. In this section, we present photometric and spectroscopic comparison with the observations of SN 1987A. Our observational data is taken from CTIO [305]. For the synthetic spectra, we adopt the extinction curve of Cardelli et al. [44] and use a reddening of E(B-V)= 0.15. Panagia [299] derived the distance to SN 1987A to be 51.4 kpc with an uncertainty of 1.2 kpc. We adopt $d = 50$ kpc for consistency with Dessart and Hillier [89].

3.7.1 The synthetic and observed light curves

The comparison of the bolometric light curves is illustrated in Fig. 3.26, while Fig. 3.27 illustrates the comparison of the V-, R-, and I-band light curves. The theoretical bolometric light curve rebrightens at a later time than observation, which is probably due to insufficient outward mixing of ^{56}Ni [376, 94]. The delay of the predicted peak luminosity supports this idea. Both the thermal and non-thermal bolometric light curves predict a higher luminosity than the observed one, partly due to higher ^{56}Ni mass in our models. Suntzeff and Bouchet [358] derived a ^{56}Ni mass of $0.07\,M_\odot$, while we have $0.084\,M_\odot$ in the model, which is the amount that comes out of the explosion model. As the purpose of this work is to explore the influence of non-thermal processes, and not to fit the spectra of SN 1987A, we did not adjust the progenitor model, nor did we explore the influence of mixing, explosion energy, and mass cut in the progenitor model. The difference in the amount of ^{56}Ni only affects our results

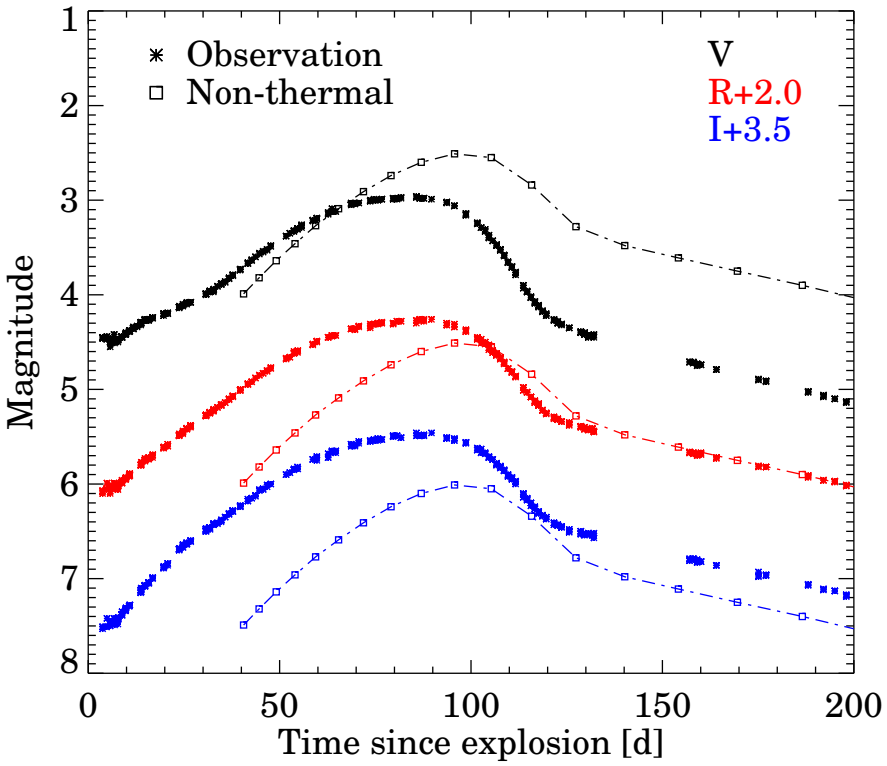

Figure 3.27: Comparison of the V-, R-, and I-band light curves of SN 1987A to the corresponding synthetic light curves. The observed V, R, and I magnitudes are shown in stars, and the synthetic V, R, and I magnitudes from the non-thermal sequence are plotted in squares connected by dashed-dotted lines. A scaling is applied to the R and I band magnitudes, both observed and synthetic, to optimize visualization. The synthetic photometry is computed by convolving the synthetic spectra with the Landolt filter bandpasses [225]. We applied a reddening of E(B-V)=0.15 and adopted a distance of 50 kpc.

quantitatively, not qualitatively. The hydrodynamical model, such as the size of the helium core and the enforcement of homology at the beginning of the modeling, also introduces uncertainties. Considering that we have no free parameter, the synthetic bolometric light curves agrees reasonably well with the observed bolometric light curves. We also plot a light

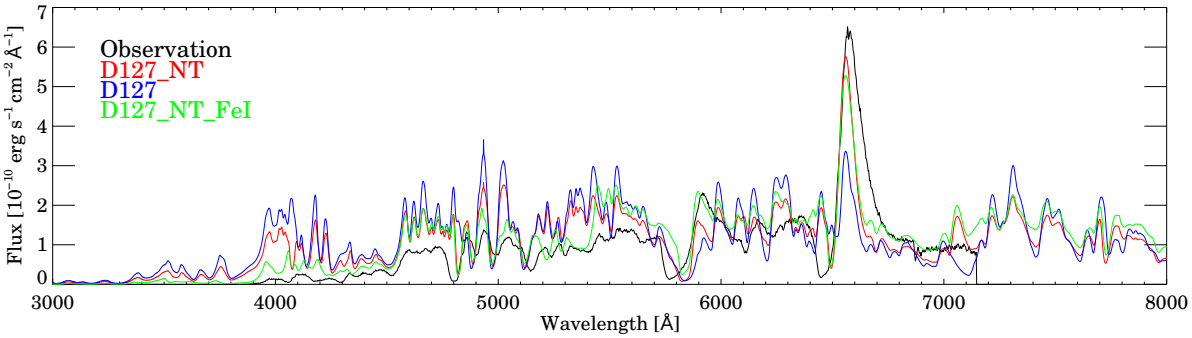

Figure 3.28: Comparison between observed spectrum of SN 1987A and the model spectra at day 127. A scaling is applied to the observed spectrum to correct for the difference between the spectroscopic (4.30) and the photometric (4.37) V-magnitude. The three model spectra are scaled by 0.07/0.084 according to the ^{56}Ni mass in SN 1987A and in the model.

curve resulting from the radioactive decay of 0.084 $M_\odot$ of ^{56}Ni. The agreement between this light curve and the synthetic bolometric light curve during the nebular epoch demonstrates that the energy source of the ejecta is totally dominated by radioactive decay.

Although the synthetic bolometric light curve is reasonably well reproduced, the synthetic multi-band light curves show varying degrees of systematic offsets. We are mainly interested in the nebular epochs when the impact of mixing is less important. The R-band magnitudes are close to the observations $\sim$ 130 days after explosion. However, the V- and I-band magnitudes show significant discrepancies (Fig. 3.27) on the tail of the light curve, with the V-band overestimated by $\sim$ 1 magnitude and the I-band underestimated by $\sim$ 0.4 magnitude. The difference in the ^{56}Ni mass between the models and SN 1987A translates into $\sim$ 0.2 magnitude in all bands. This does not remove the discrepancy in the V and I bands. However, the overestimation in the V-band and the underestimation in I-band indicate that strong line-blanketing effects are missing in the models. These would redistribute the V-band fluxes to the I-band, possibly alleviating the discrepancy. Future studies with more complete model atoms may quantify such redistribution. In fact, the non-thermal sequence with Fe I reduces

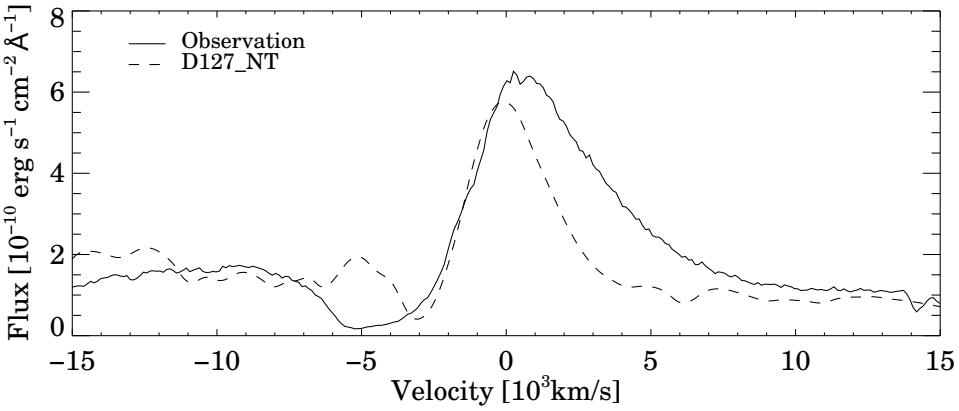

Figure 3.29: Same as Fig. 3.28, but it now shows the comparison of the Hα profile in the velocity space between observation (solid) and model D127_NT (dashed).

the V magnitudes by ~ 0.2 magnitude.

3.7.2 Spectral comparison

Fig. 3.28 shows a comparison of the observed optical spectra against the model spectra of D127_NT (red), D127 (blue) and D127_NT_FeI (green). The Hα profile is too weak in model D127, while both non-thermal models, D127_NT and D127_NT_FeI, show considerably stronger Hα. Models D127_NT and D127 show much stronger fluxes between 3000 Å and 6000 Å, which is reflected by the 1-magnitude offset in the V-band magnitudes in the previous section. The inclusion of Fe I improves the fit, mainly in the wavelength range from 3000 Å to 4500 Å.

In Fig. 3.29, we show the theoretical and observed Hα profiles in velocity space. While the peak of Hα in the non-thermal model is comparable to that of the observation the profile is narrower. The left emission wing of the profile fits the observation, but the Hα profile in the observation extends at least 3000 km s^{-1} further to the red than does the theoretical profile. Further, the P Cygni absorption component does not match — the minimum of the

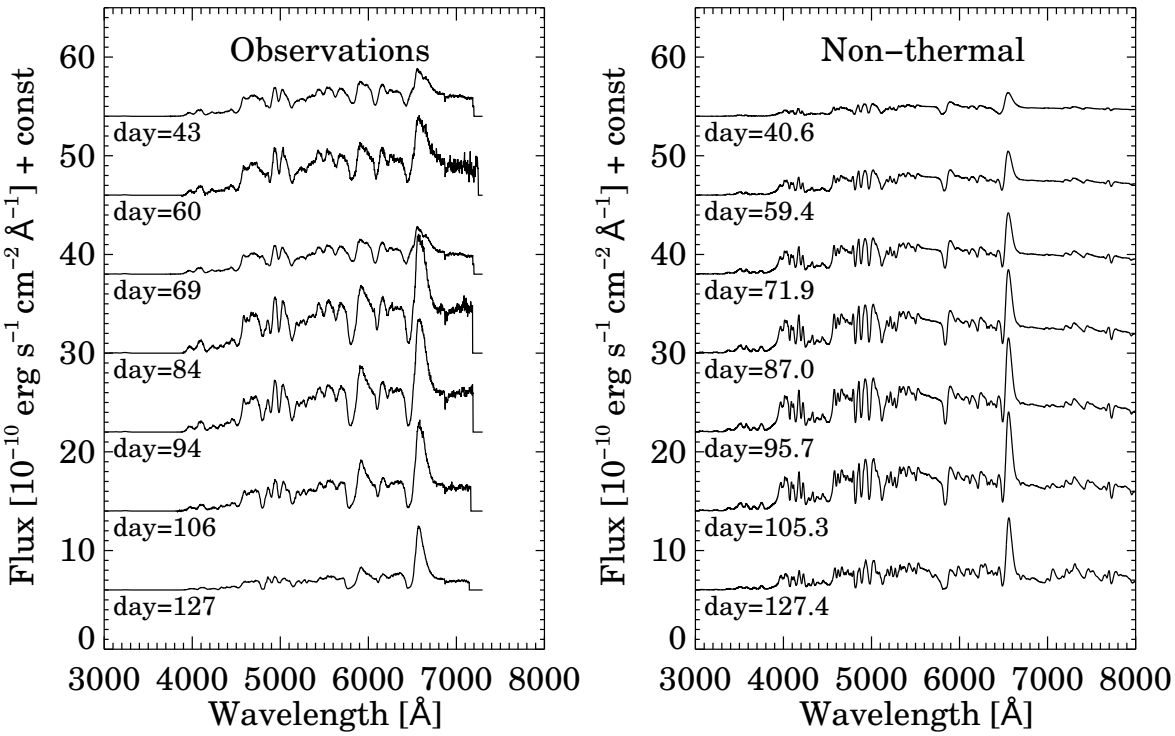

Figure 3.30: Left panel: montage of observed optical spectra of SN 1987A. The days since breakout are shown below each spectra. Right panel: montage of synthetic spectra of the non-thermal sequence. Each observed spectrum on the left is compared to a synthetic spectrum at roughly the same time since explosion. The synthetic spectra are reddened with E(B-V) = 0.15 and scaled for a distance of 50 kpc.

model absorption sits at 3000 $\mathrm{km\,s^{-1}}$, while observational minimum is at 5000 $\mathrm{km\,s^{-1}}$.

The full width at half maximum (FWHM) of Hα in the synthetic spectra is about 4000 $\mathrm{km\,s^{-1}}$, indicating that the main region that contributes to Hα is the core zone below 2000 $\mathrm{km\,s^{-1}}$. This is coincident with the region in which ^{56}Ni is abundant. The spatial distribution of ^{56}Ni depends on the degree of mixing. Mixing effects in SNe explosion are widely seen in 2D and 3D models, however in pure 1D hydrodynamic models mixing must be induced artificially. According to the observed broad Hα profile, our 1D hydrodynamical model

has insufficient mixing of ^{56}Ni. To constrain the mixing is not the goal of this thesis, but the influence of mixing will be discussed in Sec. 3.9. Another possible explanation is γ-ray transport. We made the assumption that all γ-rays deposit energy locally, but γ-ray transport makes it possible to deposit more energy at larger velocities. A discussion of the possible influence of γ-ray transport will be carried out in Sec. 3.9.

3.7.3 Comparison of the spectral evolution

In Fig. 3.30, the observations are shown on the left panel and the synthetic spectra are shown on the right panel. Recall that Balmer lines disappear suddenly at the end of the photospheric phase in the thermal sequence, thus the biggest improvement of the non-thermal sequence is the persistence of the strong Hα profile at late times. In the non-thermal sequence, the strength of the Hα profile first increases, and then decreases slowly, which is consistent with the observations. The Na I D lines are contaminated by He I 5875 Å. However, Na I D lines show behavior similar to Hα, being narrower and weaker than the observations. This is also related to the non-thermal effects, since higher H ionization produces more electrons, which leads to an increase in neutral Na [88]. The synthetic spectra are rich with weak lines around 4000 Å, while the observations show few weak lines there. Fe II is the main contributor to these lines. With the inclusion of Fe I, this discrepancy becomes much smaller. Moreover, the model does not contain scandium and barium, which may explain a few missing P Cygni profiles in the synthetic spectra. The absence of Ba II 6142 Å is suggestive. The absence of Sc II in our model likely leads to an underestimate of line blanketing around 4000 Å [90].

3.8 UNCERTAINTIES

3.8.1 Impact excitation and ionization cross sections

The uncertainty of the non-thermal solver mainly comes from the uncertainties of the electron impact excitation and ionization cross sections. As mentioned previously, the impact excitation cross sections are computed with the Bethe approximation, and the impact ioniza-

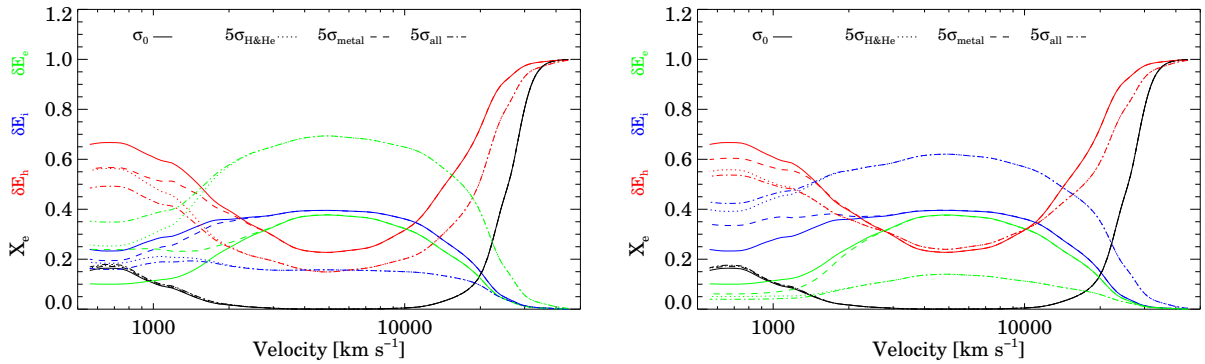

(a) Scale excitation cross sections

(b) Scale ionization cross sections

Figure 3.31: Comparison of the energy fractions of the three γ-ray decay channels in models in which we have artificially scaled the excitation or ionization cross sections. The model used for testing is the one at day 127 without including Fe I. Left: The 3 test cases of scaling the impact excitation cross sections. The scaling conditions are denoted in the figure. Different colors are fractions of different channels. The solid lines shows the fractions of the original model. The dotted lines, the dashed lines and the dashed-dotted lines represent the EH5 model, the EM5 model and the EA5 model, respectively. Right: The same as the left, but it shows the 3 cases of scaling the impact ionization cross sections. The dotted lines, the dashed lines and the dashed-dotted lines show the channel fractions of the IH5, IM5 and IA5 model, respectively.

Table 3.2: Combinations of species to scale the cross sections

Model	excitation	ionization
EH5	H and He by 5	Same
EM5	Metal species by 5	Same
EA5	All species by 5	Same
IH5	Same	H and He by 5
IM5	Same	Metal species by 5
IA5	Same	All species by 5

tion cross sections utilize the analytical formula of Arnaud and Rothenflug [9] with updated coefficients. The Bethe approximation is a high-energy approximation derived from the Born approximation that neglects the short range interaction between the perturbing electron and the atomic electron. van Regemorter [385] corrected the Gaunt factor according to existing experimental data and accurate calculations to allow the formula to be used at low energies. The Bethe approximation generally works better at high energies. For some less understood species, the Bethe approximation may break down even at high energies. The Arnaud and Rothenflug formula may have troubles for elements heavier than helium. Both experimental and theoretical cross sections are required to evaluate their uncertainties, but both of them are very difficult to estimate [37, 318, 317].

To investigate the influence of the uncertainties, we ran six test models by artificially scaling the impact excitation or ionization cross sections for different combinations of species. These test models were all based on the same input model computed using standard cross-sections, and were run until the populations and the radiation field were fully converged. Table 3.2 lists the combinations and scalings applied to the cross sections. In Fig. 3.31, we compare the fractional energies of the three channels in these six tests. In the case of varying the excitation cross sections (Fig. 3.31, left panel), increasing the excitation cross sections of H and He results in an increase of fractional energy in the excitation channel and

a decrease of fractional energy in the ionization channel. The change in the heating fraction is relatively small. An increase in the excitation cross sections of metal species has no effect above 2000 km s^{-1}, which is obviously due to their abundance deficiency. Below 2000 km s^{-1}, this also tends to increase the fraction of energy in the excitation channel and to decrease the fraction of energy in the ionization channel. The ejecta ionization fraction X_e in all cases is roughly the same, implying that the ionization structure of the ejecta is hardly affected. Varying the ionization cross sections (Fig. 3.31, right panel) has the reverse effect of varying the excitation cross sections – the increase of ionization cross sections results in an increase in the fractional energy of the ionization channel and a decrease in the fractional energy of the excitation energy. This is what we expect from the Spencer-Fano equation, given that the source term S(E) is fixed.

The fractional heating remains almost unchanged between 2500 km s^{-1} and 10 000 km s^{-1} when the ionization cross sections increase. This surprising behavior is related to a low ejecta ionization fraction, X_e, seen in Fig. 31(b). At these low-ionization fractions, the degradation spectra show that almost all electrons have degraded into very low energies and can no longer cause ionizations. Since an enhancement in the ionization cross-section does not dramatically change the number of secondary electrons produced, the ionization channel gains energy at the expense of the excitation channel. Conversely, a change in the excitation cross-sections does change the amount of energy entering the thermal channel. Crudely, excitation causes higher energy losses before the creation of a secondary electron via ionization. The competition between various processes is extremely sensitive to X_e. As X_e becomes appreciable (e.g., above 10 000 km s^{-1}.), many degraded electrons possess high energy. Increasing either the ionization or the excitation cross sections strengthens non-thermal processes at the expense of thermal energy deposition.

There are two types of uncertainties introduced by the approximations in computing the excitation and ionization cross sections. One is the uncertainty in the electron degradation spectrum. The second is the uncertainty in the rate for an individual process. For hydrogen these are explicitly coupled, but this is not necessarily so for other species since such species have a negligible influence on the degradation spectrum. In the six test cases, it turns out that the model spectra show no sizable difference. The Hα profile shows a slightly stronger

dependence on the impact cross sections of hydrogen. However, the two approximations adopted to compute the excitation and ionization cross sections produce fairly good calculations for hydrogen, which reduces our concern about such uncertainties. Generally, a factor of five in the uncertainties of the cross sections will not dramatically influence our results.

3.8.2 E_{max} for high energy electrons

Radioactive decay from ^{56}Ni and ^{56}Co generally produces fast electrons with energy $\sim 1\,\mathrm{MeV}$. However, in the non-thermal solver, we assume a source function that injects all electrons with an energy $E_{max} = 1\,\mathrm{keV}$, which is very small compared to reality. While this high energy cut also introduces another source of uncertainty, the Bethe approximation, the Arnaud & Rothenflug formula, and the electron thermal term, have similar asymptotic behaviors at high energy, so the uncertainty should be small as long as E_{max} is large enough. We have run two additional models with $E_{max} = 2\,\mathrm{keV}$ and $E_{max} = 0.5\,\mathrm{keV}$. The difference in the fractional energies entering the three channels between one of the test models and the model with $E_{max} = 1\,\mathrm{keV}$ is less than 5%, and the difference between the two test models is slightly larger. Importantly, the choice of E_{max} makes no difference to the spectra, despite the effects on the deposition fractions. Previous work by Xu and McCray [415] showed that the deposition fractions only have a weak sensitivity to E_{max}.

3.8.3 The time-dependence effects on non-thermal processes

Another uncertainty comes from the late inclusion of non-thermal excitation and ionization. At very early times the region where ^{56}Ni decays is in LTE, and the assumption that all the energy goes into heating is excellent. However, we included non-thermal excitation and ionization on day 40.6, when the time-dependent effect is already functioning at large velocities, in regions of low ionization and underabundant in ^{56}Ni/^{56}Co. We study this uncertainty in two ways. The first method is to compare the thermal and the non-thermal model at day 40.6. At this epoch, non-thermal excitation and ionization are still unimportant. The model spectrum is hardly affected by the inclusion of non-thermal processes. This is also the main reason why we start the non-thermal sequence at this epoch. The second method is to

compare two non-thermal models at a later time – one is evolved from day 40.6 and the other with immediate inclusion of non-thermal processes. At day 127, we found very subtle differences between the spectra of the two models. The Hα profile is only slightly weaker in the model with immediate inclusion of non-thermal processes. The above two tests indicate that the late inclusion of non-thermal excitation and ionization only introduces very small effects on the nebular spectra. Future studies will start with non-thermal processes, thereby removing such uncertainty.

3.9 DISCUSSION

The amount of mixing in SN 1987A has been widely debated (See Arnett et al. 1989 for a review). The two fundamental questions are what velocity hydrogen is mixed down to, and what velocity ^{56}Ni is mixed outward to. The latest 3D simulations of CCSNe [153] showed that significant amounts of hydrogen are transported into deep layers of the ejecta ($\leq$ 1000 km s^{-1}), and that a large amount of heavy elements are strongly mixed above 2000 km s^{-1}. These results are thought to be very similar to the case of SN 1987A. However, it is difficult to draw a conclusion, since the simulations have a different progenitor from SN 1987A. Kozma and Fransson [216] modeled the late time spectra of SN 1987A and found hydrogen was mixed down to $\leq$ 700 km s^{-1}(they needed the mixing to fit the observations).

Fassia and Meikle [112] modeled the He I 1.083 μm line and found some amount of ^{56}Ni is required to be mixed above 3000 km s^{-1} to obtain a best fit. Mitchell et al. [274] synthesized the spectrum of SN 1987A and argued that the strong Balmer lines at early times is due to non-thermal effects, which required a substantial amount of ^{56}Ni mixing out to 10 000 km s^{-1} in the hydrogen envelope – velocities much larger than predicted in hydrodynamic simulations. However, Utrobin and Chugai [379] and Dessart and Hillier [88] showed time-dependent ionization is the main reason for the strong Balmer lines. The inward mixing of hydrogen and outward mixing of heavy elements in SN 1987A are still open questions.

The scale of mixing also plays an important role. Microscopic mixing results in homogeneous compositions in the ejecta, while macroscopic mixing can lead to large-scale

compositional inhomogeneities. With microscopic mixing the mixed species can interact directly (e.g., charge exchange of H with Fe). With macroscopic mixing, this will not occur even if H and Fe are at the same radius (but different θ, ϕ). Microscopic mixing can be treated in 1D, while an accurate treatment of macroscopic mixing may require 3D models. In SN 1987A, the high velocity feature of iron-group emission lines (e.g., [Fe II] 17.94 μm and 25.99 μm [150]; [Ni II] 6.6 μm [62]), at late times strongly indicate macroscopic mixing. Fransson and Chevalier [119] showed that microscopic mixing can significantly change the observed spectra at late times, and Li et al. [240] emphasized the importance of a clumpy structure on the Fe/Co/Ni lines. Jerkstrand et al. [192] were able to reproduce reasonably the SN 1987A spectra 8 years after explosion with a purely macroscopic mixing model. Furthermore, hydrodynamical models were unable to produce efficient microscopic mixing [331, 280, 162].

Modeling the late time spectra of SN 1987A provides insight into the amount of mixing. The disappearance of Balmer continuum photons at the nebular phase makes non-thermal excitation and ionization the only way to reproduce the Balmer lines. However, the problem is complicated by the γ-ray transport. γ-rays interact with the medium through three processes: photoelectric ionization, Compton scattering and pair production. The decay of ^{56}Ni and ^{56}Co mainly produces γ-ray with energy of $\sim$ 1 MeV. At this energy range, Compton scattering is the dominant process. To give a rough estimate of the mean free path of a high energy electron before it is Compton scattered by atoms, we adopt an effective, purely absorptive, gray opacity $\kappa_\gamma = 0.06 Y_e$ cm^2 g^{-1} [362], where Y_e is the total number of electrons per baryon. The optical depth is calculated by,

$$d\tau = -\kappa_\gamma \rho ds \tag{3.14}$$

Assuming $Y_e = 0.5$ and integrating τ from velocity 1500 km s^{-1}, the place where ^{56}Co is still abundant, we obtain the mean free path of γ-ray is $\sim 1.0 \times 10^{14}$ cm, which means the photon can travel from velocity 1500 to 1700 km s^{-1} in model D127_NT. No doubt, very few γ-rays travel a long way before they interact with the medium and deposit their energies. A Monte Carlo code has been developed for computing the γ-ray transport [168], which will give a more detailed understanding of the mixing problem. We ran a test with allowance for

γ-ray transport at day 127 and, as expected, there is only a slight enhancement in the line strength and width of Hα.

The first discovery of hard X-rays in SN 1987A was made by Sunyaev et al. [359], approximately 5 months after the explosion, and the first detection of γ-rays was made by Matz et al. [259], shortly after the discovery of the hard X-rays. This suggests that γ-ray transport was beginning to become important at day 127. However, our model at day 154 gives an estimate that γ-rays can only travel from 1500 to 1800 $\mathrm{km\,s^{-1}}$ using the effective gray opacity κ_γ, which indicates an insufficient outward mixing of ^{56}Ni in the input. In fact, theoretical modeling of the bolometric, X-ray and γ-ray light curves require substantial outward mixing of ^{56}Ni into the hydrogen envelope [218, 10].

3.10 CONCLUSION

We developed a non-thermal solver, which takes into account ionization and excitation due to non-thermal electrons created by γ-rays that arise from the decay of ^{56}Ni and its daughter products, and incorporated it into our fully non-LTE time-dependent code to model SNe. We use the model 'lm18a7Ad' of Woosley on 0.27 days, which is enforced to be homologous as an initial input, and benchmark the non-thermal solver by comparing model results with the observations of SN 1987A.

Non-thermal models have lower temperature and more excited/ionized material in the region where the non-thermal processes are crucial. Fractional energy of non-thermal excitation/ionization is prominent at places with very small ejecta ionization fraction X_e. The spectral comparison with the thermal models shows that Hα is strongly increased at nebular epochs. At late times, He I lines, which are totally absent in the thermal models, are present in non-thermal models. While most He I lines are significantly contaminated by other lines, He I 2.058 μm provides an excellent opportunity to infer the influence of non-thermal processes on helium. He I 7065Å is a possible optical line that can be used to infer the influence of non-thermal effects in the nebular epoch. There are many O I lines locating near 1.129 μm, and they are also strengthened by non-thermal processes. Most of other lines are only weakly

affected at the epochs considered here.

Optical and IR He I lines mainly originate below 2000 km s^{-1}. We confirm that non-thermal excitation is the most important process for He I 2.058 μm. However, He I 1.083 μm is due to cascades from higher levels, which indirectly relate to non-thermal ionization. Although photoionization and recombination are prominent processes for populating many levels, non-thermal excitation and ionization are the processes controlling the ionization balance.

We also compare the non-thermal models with the observations. The re-brightening of the bolometric light curve peaks about 10 days later in our models. An underestimate in the amount of outward mixing of ^{56}Ni is the main reason for the delay. Although the synthetic bolometric light curve agrees reasonably with the observations, multi-band light curves show discrepancies in various degrees and reveal potential differences between the hydrodynamical model and SN 1987A or possible problems in our modeling. The opacity issue, related to limited levels in the atomic data or some missing species, is one possibility, considering that the V-band is overestimated and the I-band is underestimated. Hα maintains a strong profile at the nebular epochs in the non-thermal models, resembling observations of SN 1987A. However, the model Hα profile is much narrower than what we observed in SN 1987A, probably due to insufficient outward mixing of ^{56}Ni. Although hydrogen is abundant above 2000 km s^{-1} in the model, the lack of ^{56}Ni in this region and the assumption of local deposition of γ-rays make the non-thermal effects negligible there. We also compared the optical spectral evolution to the observations and found a satisfactory agreement.

The uncertainties introduced by various approximations and assumptions in the non-thermal solver have been investigated. The primary uncertainties are due to the not-well-known electron impact excitation and ionization cross sections of metal species. However, our results for a BSG model are largely dependent on accuracies of the cross sections for hydrogen and helium, since they are the most abundant two elements. The Bethe approximation and the Arnaud and Rothenflug formula produce very good estimates of the excitation and ionization cross sections for these two elements. Therefore, our conclusions are not affected by these uncertainties. Another source of uncertainty comes from the computation of the degradation spectrum, which arises from the choice of the number of energy bins and the

energy cutoff E_{max} at the high end of the degradation spectrum. We demonstrate that our choice for the number of energy bins, N = 1000, is sufficient to give a reliable degradation spectrum and using $E_{max} = 1000\,\mathrm{eV}$ in our model produces almost the same spectra as using $E_{max} = 2000\,\mathrm{eV}$. We also explore the time dependence of non-thermal processes and find there is only a very subtle effect on predicted spectra.

With the non-thermal solver, we are able to simulate SNe from photospheric to nebular phases continuously. The influence of non-thermal ionization and excitation on Type Ib and Type Ic models is being investigated [94]. As more and more nebular spectra are available, the comparison of observations with models will allow us to place constraints on the hydrodynamic models and nucleosynthesis. The non-thermal solver also provides opportunities to constrain mixing effects in SNe.

4.0 PART II. FULLY RELATIVISTIC RADIATIVE TRANSFER

4.1 DEVIATION FROM HUBBLE EXPANSION

Hubble expansion is an assumption broadly adopted when modeling SNe spectra. This is generally a good approximation and, as we shall see in Sec. 4.2, dramatically simplifies the transfer equations to be solved. However, in some regimes the assumption is invalid.

The progenitors of Type Ia SNe are thought to be WDs, which have radii of order of 10^{-2} $R_\odot$. The fast expansion of the ejecta makes it approximately homologous within a few minutes. WR stars, the potential progenitors of Type Ib and Ic SNe, have sizes $\sim$ 1-10 $R_\odot$, and it takes about 1 day for the Hubble expansion assumption to be reasonable. For SNe with BSG progenitors such as SN 1987A, homology becomes a good approximation a few days after they explode. For types of SNe mentioned above, the Hubble expansion assumption is generally valid before we discover them and carry out photometric and spectroscopic observations. However, the Hubble expansion assumption may breakdown for Type II-P SNe. RSGs have very extended radii up to 1000 $R_\odot$. Homologous expansion therefore, is not ensured for several weeks. As a result, erroneous conclusions can be drawn from a comparison of model spectra, computed under the assumption of homology, to early observations. Further, modeling SN ejecta is an initial value problem. Accurate modeling of the inner regions is necessary to correctly interpret late-time observations.

Despite the complexity in the radiative transfer equations, we develop a fully relativistic radiative transfer solver, including all terms in the radiative transfer equations, to model Type II-P SNe at early time.

4.2 TRANSFER EQUATIONS IN THE FULLY RELATIVISTIC FORM

The fully relativistic radiative transfer equation in the comoving frame, according to Mihalas and Mihalas [268], is

$$
\begin{aligned}
&\frac{\gamma}{c}(1+\beta\mu)\frac{\partial I(\mu,\nu)}{\partial t}+\gamma(\mu+\beta)\frac{\partial I(\mu,\nu)}{\partial r}\\
&\quad+\frac{\partial}{\partial\mu}\left\{\gamma(1-\mu^2)\left[\frac{(1+\beta\mu)}{r}-\gamma^2(\mu+\beta)\frac{\partial\beta}{\partial r}-\frac{\gamma^2}{c}(1+\beta\mu)\frac{\partial\beta}{\partial t}\right]I(\mu,\nu)\right\}\\
&\quad-\frac{\partial}{\partial\nu}\left\{\gamma\nu\left[\frac{\beta(1-\mu^2)}{r}+\gamma^2\mu(\mu+\beta)\frac{\partial\beta}{\partial r}+\frac{\gamma^2}{c}\mu(1+\beta\mu)\frac{\partial\beta}{\partial t}\right]I(\mu,\nu)\right\}\\
&\quad+\gamma\left\{\frac{2\mu+\beta(3-\mu^2)}{r}+\gamma^2(1+\mu^2+2\beta\mu)\frac{\partial\beta}{\partial r}+\frac{\gamma^2}{c}\left[2\mu+\beta(1+\mu^2)\right]\frac{\partial\beta}{\partial t}\right\}I(\mu,\nu)\\
&\quad=\eta(\nu)-\chi(\nu)I(\mu,\nu)
\end{aligned}
\tag{4.1}
$$

where $\beta = v/c$ and $\gamma = (1-\beta^2)^{(-1/2)}$, $\mu = \cos\theta$, and θ is defined as the angle between the normal of the area element a light ray passing through and the transfer direction of the light ray. ν is frequency and $I(\mu,\nu)$ is the specific intensity as defined in Sec. 2.1.1. $\eta(\nu)$ and $\chi(\nu)$ are the emissivity and opacity, respectively. All μ, ν, $I(\mu,\nu)$, $\eta(\nu)$ and $\chi(\nu)$ are quantities in the comoving frame. Similar to the Hubble flow solver which assumes the velocity law $v \propto r$, the fully relativistic solver uses the moment technique to solve the fully relativistic radiative transfer equation. The zeroth and first moment equations of radiative transfer are given by:

$$
\begin{aligned}
&\gamma\left(\frac{1}{c}\frac{\partial J_\nu}{\partial t}+\frac{\beta}{c}\frac{\partial H_\nu}{\partial t}\right)+\gamma\left(\frac{\partial H_\nu}{\partial r}+\beta\frac{\partial J_\nu}{\partial r}\right)\\
&+\frac{\gamma}{r}\left(2H_\nu+3\beta J_\nu-\beta K_\nu\right)+\gamma^3\frac{\partial\beta}{\partial r}\left(J_\nu+K_\nu+2\beta H_\nu\right)+\frac{\gamma^3}{c}\frac{\partial\beta}{\partial t}\left(2H_\nu+\beta J_\nu+\beta K_\nu\right)\\
&-\frac{\gamma\beta}{r}\left(J_\nu-K_\nu\right)-\gamma^3\frac{\partial\beta}{\partial r}\left(K_\nu+\beta H_\nu\right)-\frac{\gamma^3}{c}\frac{\partial\beta}{\partial t}\left(H_\nu+\beta K_\nu\right)\\
&-\frac{\gamma\beta\nu}{r}\left(\frac{\partial J_\nu}{\partial\nu}-\frac{\partial K_\nu}{\partial\nu}\right)-\gamma^3\nu\frac{\partial\beta}{\partial r}\left(\frac{\partial K_\nu}{\partial\nu}+\beta\frac{\partial H_\nu}{\partial\nu}\right)-\frac{\gamma^3\nu}{c}\frac{\partial\beta}{\partial t}\left(\frac{\partial H_\nu}{\partial\nu}+\beta\frac{\partial K_\nu}{\partial\nu}\right)\\
&=\eta_\nu-\chi_\nu J_\nu
\end{aligned}
\tag{4.2}
$$

and

$$
\begin{aligned}
&\gamma\left(\frac{1}{c}\frac{\partial H_\nu}{\partial t}+\frac{\beta}{c}\frac{\partial K_\nu}{\partial t}\right)+\gamma\left(\frac{\partial K_\nu}{\partial r}+\beta\frac{\partial H_\nu}{\partial r}\right)\\
&+\frac{\gamma}{r}\left(3K_\nu-J_\nu+2\beta H_\nu\right)+\gamma^3\frac{\partial\beta}{\partial r}\left(2H_\nu+\beta J_\nu+\beta K_\nu\right)+\frac{\gamma^3}{c}\frac{\partial\beta}{\partial t}\left(J_\nu+K_\nu+2\beta H_\nu\right)\\
&-\frac{\gamma\beta}{r}\left(H_\nu-N_\nu\right)-\gamma^3\frac{\partial\beta}{\partial r}\left(N_\nu+\beta K_\nu\right)-\frac{\gamma^3}{c}\frac{\partial\beta}{\partial t}\left(K_\nu+\beta N_\nu\right)\\
&-\frac{\gamma\beta\nu}{r}\left(\frac{\partial H_\nu}{\partial\nu}-\frac{\partial N_\nu}{\partial\nu}\right)-\gamma^3\nu\frac{\partial\beta}{\partial r}\left(\frac{\partial N_\nu}{\partial\nu}+\beta\frac{\partial K_\nu}{\partial\nu}\right)-\frac{\gamma^3\nu}{c}\frac{\partial\beta}{\partial t}\left(\frac{\partial K_\nu}{\partial\nu}+\beta\frac{\partial N_\nu}{\partial\nu}\right)\\
&=-\chi_\nu H_\nu
\end{aligned}
\tag{4.3}
$$

Since we are solving for the moments in the comoving frame, Eq. 4.2 and 4.3 are rearranged to lagrangian derivative form, i.e.,

$$
\begin{aligned}
&\frac{\gamma}{rc}\frac{D(r^3J_\nu)}{Dt}+\frac{\gamma\beta}{c}\frac{D(r^2H_\nu)}{Dt}+\gamma\frac{\partial(r^2H_\nu)}{\partial r}\left(1-\beta^2\right)+\frac{\gamma^3}{c}\frac{D\beta}{Dt}(r^2H_\nu)+\frac{1}{c}\frac{D\gamma}{Dt}(r^2J_\nu)\\
&-\frac{\gamma\beta\nu}{r}\frac{\partial(r^2J_\nu)}{\partial\nu}-\frac{\gamma^3\nu}{c}\frac{D\beta}{Dt}\frac{\partial(r^2H_\nu)}{\partial\nu}+\gamma\left(\frac{\partial\beta}{\partial r}-\frac{\beta}{r}\right)(r^2J_\nu)\\
&-\left(\frac{\nu}{c}\frac{D\gamma}{Dt}+\gamma\nu\frac{\partial\beta}{\partial r}-\frac{\gamma\beta\nu}{r}\right)\frac{\partial(r^2K_\nu)}{\partial\nu}\\
&=r^2\eta_\nu-\chi_\nu(r^2J_\nu)
\end{aligned}
\tag{4.4}
$$

and

$$
\begin{aligned}
&r^2H_\nu+\frac{\gamma}{\chi_\nu c}\frac{D(r^2H_\nu)}{Dt}-\frac{\gamma\beta\nu}{\chi_\nu r}\frac{\partial(r^2H_\nu)}{\partial\nu}+\left(\frac{2}{\chi_\nu c}\frac{D\gamma}{Dt}+\frac{2\gamma}{\chi_\nu}\frac{\partial\beta}{\partial r}-\frac{\gamma\beta}{\chi_\nu r}\right)(r^2H_\nu)\\
&=-\frac{\gamma}{\chi_\nu q_\nu}\frac{\partial(q_\nu r^2K_\nu)}{\partial r}-\frac{\gamma}{\chi_\nu c}\frac{D\beta}{Dt}(r^2J_\nu)+\frac{\gamma\beta^2}{\chi_\nu}\frac{\partial(r^2K_\nu)}{\partial r}-\frac{\gamma\beta}{\chi_\nu c}\frac{D(r^2K_\nu)}{Dt}\\
&+\left(\frac{1}{\chi_\nu c}\frac{D\gamma}{Dt}+\frac{\gamma}{\chi_\nu}\frac{\partial\beta}{\partial r}-\frac{\gamma\beta}{\chi_\nu r}\right)(r^2N_\nu)\\
&+\frac{\gamma^3\nu}{\chi_\nu c}\frac{D\beta}{Dt}\frac{\partial(r^2K_\nu)}{\partial\nu}+\left(\frac{\nu}{\chi_\nu c}\frac{D\gamma}{Dt}+\frac{\gamma\nu}{\chi_\nu}\frac{\partial\beta}{\partial r}-\frac{\gamma\beta\nu}{\chi_\nu r}\right)\frac{\partial(r^2N_\nu)}{\partial\nu}
\end{aligned}
\tag{4.5}
$$

where

$$
\frac{\partial\ln(r^2q_\nu)}{\partial r}=\frac{3f_\nu-1}{f_\nu r}
\tag{4.6}
$$

and the Lagrangian derivative is given by Eq. 2.12. The difficulty in solving the moment equations not only comes from the complexity of the equations, but also arises from the handling of the third moment of the specific intensity, i.e. N_ν. For the Hubble flow we have two moment equations with three unknowns (J_ν, H_ν, K_ν). To close the system, the Eddington factor, $f_\nu = K_\nu/J_\nu$, which is a well defined quantity, is introduced. However an additional factor $n_\nu = N_\nu/J_\nu$, which is a less well-defined Eddington factor, is required in the fully relativistic solver[1]. Similar to the Hubble solver, both the inner and outer boundary conditions are specified by the first moment equation (Eq. 4.5).

The numerical solution of the moments of the radiation field are obtained by differencing Eq. 4.4 and 4.5. The derivative of frequency is given by

$$\frac{\partial[J_\nu, H_\nu, K_\nu, N_\nu]}{\partial\nu} = \frac{1}{\Delta\nu}\left([J_{\nu_{k-1}}, H_{\nu_{k-1}}, K_{\nu_{k-1}}, N_{\nu_{k-1}}] - [J_{\nu_k}, H_{\nu_k}, K_{\nu_k}, N_{\nu_k}]\right) \tag{4.7}$$

where $\Delta\nu = \nu_{k-1} - \nu_k$ [169]. Moments of the radiation field are solved from high frequencies to low frequencies, because in the comoving frame the radiation field at each spatial location is coupled to that of bluer frequencies from other regions. Thus, values of the moments of the radiation field for the previous frequency (i.e., $J_{\nu_{k-1}}$, $H_{\nu_{k-1}}$, $K_{\nu_{k-1}}$, and $N_{\nu_{k-1}}$) are known when computing the values for current frequency (i.e., J_{ν_k}, H_{ν_k}, K_{ν_k}, and N_{ν_k}). The spatial derivatives are given by[2]

$$\frac{\partial[J_\nu, K_\nu]}{\partial r} = \frac{[J_{\nu,i+1}, K_{\nu,i+1}] - [J_{\nu,i}, K_{\nu,i}]}{r_{i+1} - r_i} \tag{4.8}$$

and

$$\frac{\partial[H_\nu, N_\nu]}{\partial r} = \frac{[H_{\nu,i+1}, N_{\nu,i+1}] - [H_{\nu,i}, N_{\nu,i}]}{r_{i+1/2} - r_{i-1/2}} \tag{4.9}$$

where $H_{\nu,i}$, and $N_{\nu,i}$ is defined on the middle grid point $r_{i+1/2} = (r_{i+1} + r_i)/2$. For the time derivative in the comoving frame, an implicit approach is adopted [168], which is given by

$$\left(\frac{DX}{Dt}\right)_n = \frac{X_n - X_{n-1}}{t_n - t_{n-1}} \tag{4.10}$$

[1]Ideally we could define $n_\nu = N_\nu/H_\nu$ but this can be ill defined since H can be zero.
[2]In fact, the code works in the optical depth τ-space, i.e. $d\tau = -\chi dr$, where χ is the opacity.

where X_n is any quantity with time derivatives in the radiative transfer equations, rate equations, and the radiative energy balance equation. An explicit approach for the rate equations, which says $n_i(t_n) = n_i(t_{n-1}) + \Gamma\Delta t$ (where Γ is the total rate for population n_i), suffers strong restrictions in the time step.

By virtue of the grouping in Eq 4.5 and the assistance of Eddington factors f_ν and n_ν, H_ν can be expressed in terms of J_ν, which is then substituted into Eq. 4.4. Details of the strategy to solve the moment equations are given in the APPENDIX B.

As mentioned in Sec. 2.4, CMFGEN uses a partial linearization technique to simultaneously obtain a solution to the radiative transfer equation and the statistical equilibrium (or kinetic) equations [169]. While the current solutions are solved by moment equations, corrections to the solutions are determined by virtue of linearization of the moment equations. As the moment equations are complex for fully relativistic radiative transfer, the linearization of these equations is also complicated.

CMFGEN starts with a gray solution when the ejecta is still optically thick. Thus, a new gray solution solver corresponding to the fully relativistic transfer equations is also needed to be implemented. Under the gray assumption, the opacity is independent of frequency. The Rosseland mean opacity is widely adopted as such frequency-independent opacity. It is defined by

$$\frac{1}{\chi_{\rm R}} \equiv \frac{\int_0^\infty \frac{1}{\chi_\nu}\frac{dB_\nu}{dT}d\nu}{\int_0^\infty \frac{dB_\nu}{dT}d\nu} \tag{4.11}$$

where B_ν is the black body radiation. The gray solution is generally a good initial estimate at depth. The gray equations are obtained by integrating Eqs. 4.4 and 4.5 over frequency, and are given by

$$\begin{aligned}
&\frac{\gamma}{rc}\frac{D(r^3J)}{Dt} + \frac{\gamma\beta}{c}\frac{D(r^2H)}{Dt} + \gamma\frac{\partial(r^2H)}{\partial r}\left(1-\beta^2\right) + \frac{2\gamma^3}{c}\frac{D\beta}{Dt}(r^2H) \\
&+\frac{1}{c}\frac{D\gamma}{Dt}(r^2J) + \frac{\gamma\beta}{r}(r^2J) + \left(\gamma\frac{\partial\beta}{\partial r} - \frac{\gamma\beta}{r}\right)(r^2J) \\
&+\left(\frac{1}{c}\frac{D\gamma}{Dt} + \gamma\frac{\partial\beta}{\partial r} - \frac{\gamma\beta}{r}\right)(r^2K) \\
&=r^2\eta - \chi(r^2J)
\end{aligned} \tag{4.12}$$

and

$$
\begin{aligned}
&r^2H + \frac{\gamma}{\chi c}\frac{D(r^2H)}{Dt} + \frac{\gamma\beta}{\chi r}(r^2H) + \left(\frac{2}{\chi c}\frac{D\gamma}{Dt} + \frac{2\gamma}{\chi}\frac{\partial\beta}{\partial r} - \frac{\gamma\beta}{\chi r}\right)(r^2H) \\
&= -\frac{\gamma}{\chi q}\frac{\partial(qr^2K)}{\partial r} - \frac{\gamma}{\chi c}\frac{D\beta}{Dt}(r^2J) + \frac{\gamma\beta^2}{\chi}\frac{\partial(r^2K)}{\partial r} - \frac{\gamma\beta}{\chi c}\frac{D(r^2K)}{Dt} - \frac{\gamma^3}{\chi c}\frac{D\beta}{Dt}(r^2K)
\end{aligned}
\tag{4.13}
$$

The statistical equilibrium equations and the energy equations are similar to the case of Hubble flow, except that the volume expansion factor, defined as the ratio of the current volume element to the volume element at a previous time step, is different.

4.3 INITIAL SETUP

Hydrodynamical models computed by V1D [247] are adopted to test the fully relativistic solver. The hydrodynamic code V1D ignores nucleosynthesis during the explosion. However, necleosynthesis in the core is largely irrelevant unless strong mixing occurs. We primarily focus on the early evolution in this testing and thus only material in the envelope is observed. The hydrodynamical models are evolved from three different progenitors with main sequence masses of $11\,M_\odot$, $15\,M_\odot$, and $20\,M_\odot$, respectively. For convenience, these sequences are termed s11_v1d, s15_v1d, and s20_v1d.

Even if the solver takes into account the non-Hubble structure in the ejecta, we still need to customize the hydrodynamical models for CMFGEN. The main reasons are that hydrodynamic and radiative transfer codes have very different resolutions in the outer region, and the non-monotonicity seen in some hydrodynamic models is not allowed in the fully relativistic solver. Hydrodynamic codes have very coarse grids at the exterior, while radiative transfer codes requires high resolution around $\tau = 1$ (i.e., the region from which the radiation escapes). We extend the hydrodynamic structure to the optically thin region with the velocity law $v = (v_f/r_f)r$, where v_f and r_f is the velocity and radius of the connecting point, above which the hydrodynamical model is truncated and attached by the velocity law. The connect point is chosen such that large velocity gradients at the outer boundary are avoided in CMFGEN, which could cause convergence issues. Such adjustments can significantly modify

the ejecta mass, but this does no harm at the testing stage. For the density structure, we assume a density exponent $N_\rho = -d\log\rho/d\log v = 20$.

Fig. 4.32 illustrates the comparisons of ejecta structures between hydrodynamical models and the adjusted initial input for CMFGEN. In the left column, the plots show the radius as a function of velocity and the radius displays an almost plateau part at the outer region, which means a large velocity gradient in hydrodynamic models. At the outer region, the ejecta is so underdense that the radiation field can accelerate the material to very high velocity. This feature is widely seen in hydrodynamic simulations for SNe.

4.4 TESTING

While CMFGEN performs numerous tests to check different components of the code, we are only concerned about checks for the fully relativistic solver. Various aspects of the solutions must be confirmed, which include the recovery of Hubble solver solutions in the case of a Hubble flow, the recovery of the LTE conditions at depth, satisfying the global energy constraint, etc. In this section, several methods we have used to test the fully relativistic solver will be presented.

4.4.1 Solution to homologous models

One easy way to test the solver is to compare the solutions with the Hubble solver by employing a homologously expanding ejecta. The two solvers are applied to run with the same ejecta in Dessart and Hillier [89]. The corrections to the solution after each corresponding iteration are almost identical because the $\sigma = d\ln(v)/d\ln(r) - 1$ and $D\beta/Dt$ terms are zeros, and there are only subtle differences in the radiative transfer equations between the two solvers. The σ terms result from the deviation of homologous expansion, while the $D\beta/Dt$ terms are caused by accelerations of the ejecta, which are currently assumed to be negligible.

The solutions of the temperature structure and the spectra from the two solvers are displayed in Fig. 4.33. The two solutions are almost identical, and thus both the results for

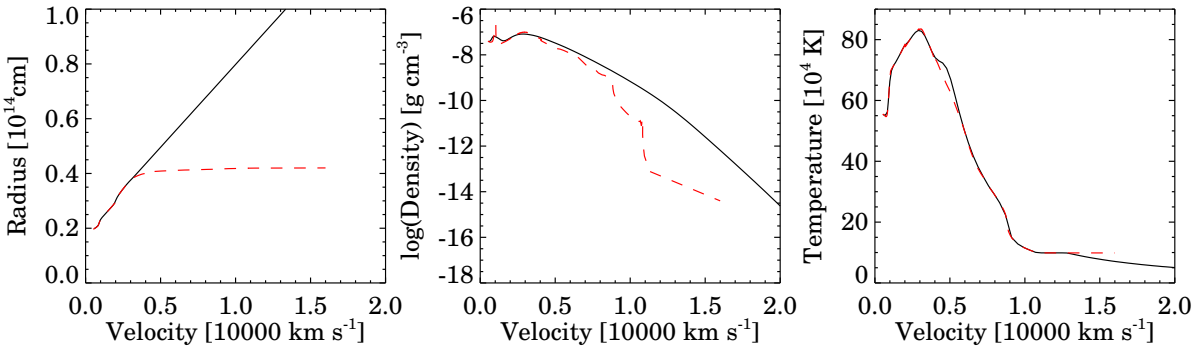

(a) s11_v1d

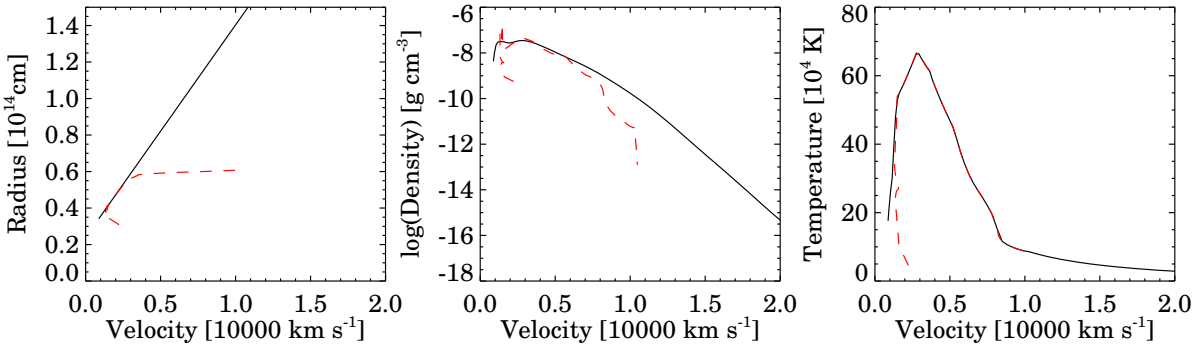

(b) s15_v1d

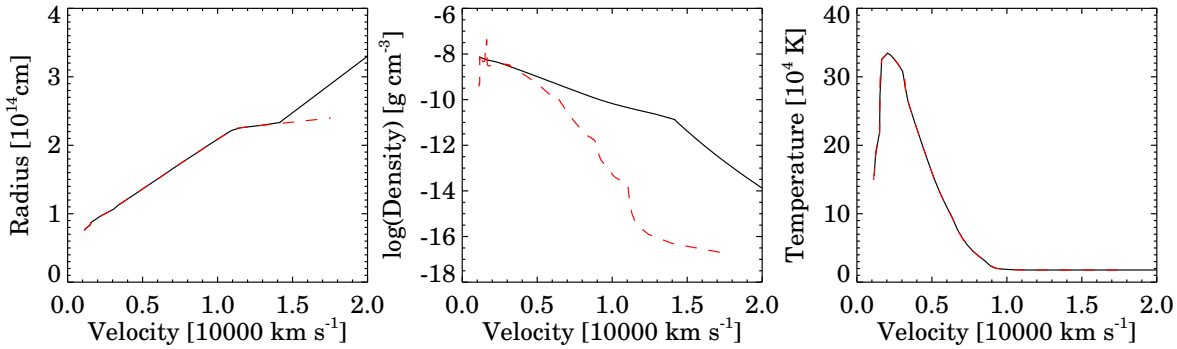

(c) s20_v1d

Figure 4.32: The ejecta properties of the adjusted models (black solid), which are used as initial models for CMFGEN, and of the original hydrodynamical models (red dashed) from V1D. The hydrodynamical model has a progenitor mass of $11\,M_\odot$, $15\,M_\odot$, and $20\,M_\odot$ from the top to bottom.

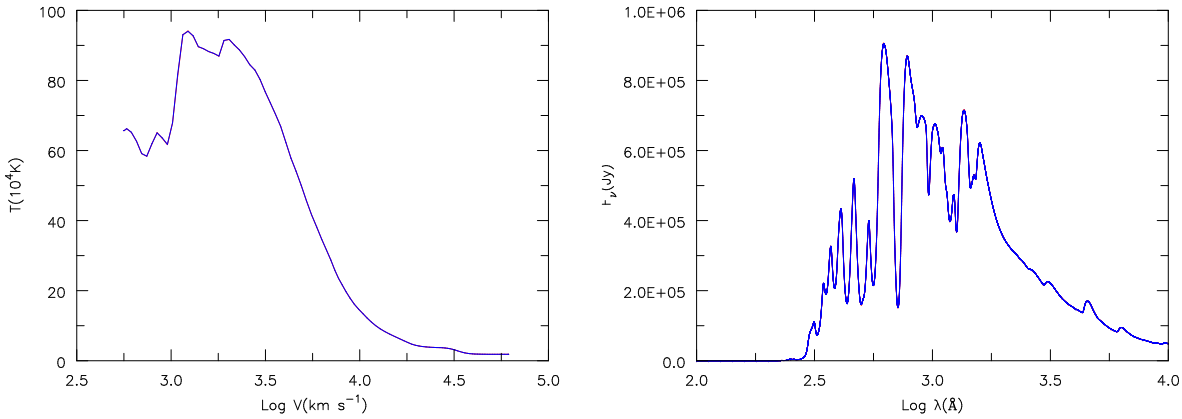

Figure 4.33: Comparison of the temperature structure (left) and the spectra (right) between two identical and homologous models computed by the Hubble solver (red) and the fully-relativistic solver (blue). The red curves are overlapped by the blue curves in both plots, indicating identical solutions for the two solvers.

the temperature structure and the spectra overlap without any distinguishable difference.

4.4.2 Departure coefficients

At large optical depth ($\tau_{\rm Rosseland} \gtrsim 10$), the LTE condition is recovered, and hence level populations are essentially in LTE. The departure coefficients, defined as the ratio of real population to the LTE population as noted previously in Sec. 2.4.3, are equal to 1. The departure coefficients for H I, O I, and Fe II at two epochs as a function of the Rosseland-mean optical depth are illustrated in Fig. 4.34.

In the optically thin region, deviations from LTE are highly significant – the departure coefficients can be several orders of magnitude smaller or greater than 1. The substantial deviation from LTE at small optical depth is expected. In the outer layers of the supernova ejecta, the opacity is generally dominated by electron scattering and line scattering, which drive the decoupling between the radiation field and the electron temperature. Also, the density is low at small optical depth, and thus there are insufficient collisions to establish

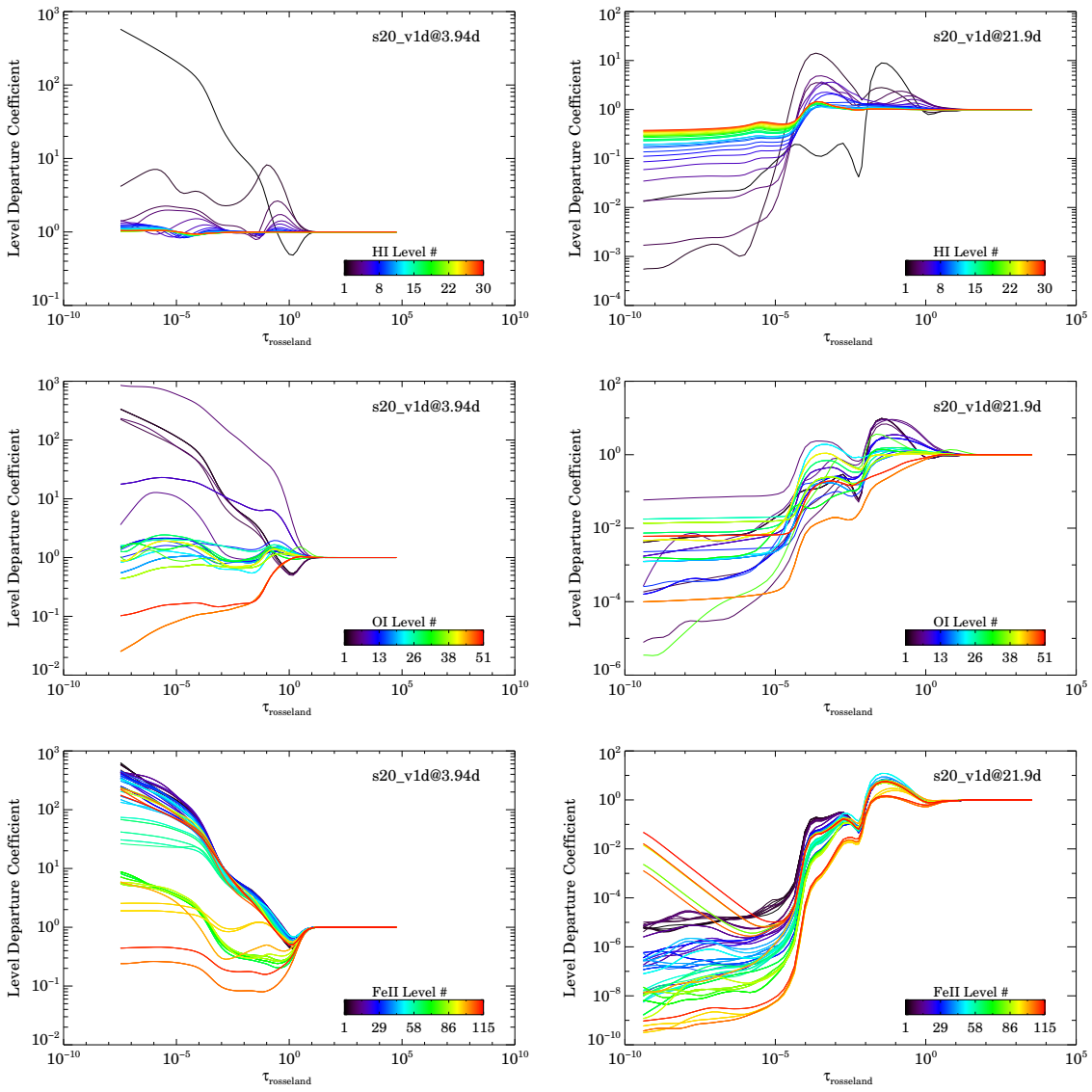

Figure 4.34: Left column: variation of the departure coefficients of H I (top), O I (middle), and Fe II levels versus Rosseland optical depth for model s20_v1d at 3.94 d after shock breakout. Right column: same as left, but for the model s20_v1d at 21.9 d after shock breakout. Non-LTE level populations computed by the fully-relativistic solver match closely their LTE counterpart in regions where the Rosseland mean optical depth $\tau_{\rm Rosseland} \gtrsim 10$. Departure from LTE is prevalently seen above $\tau_{\rm Rosseland} \eqsim 10$.

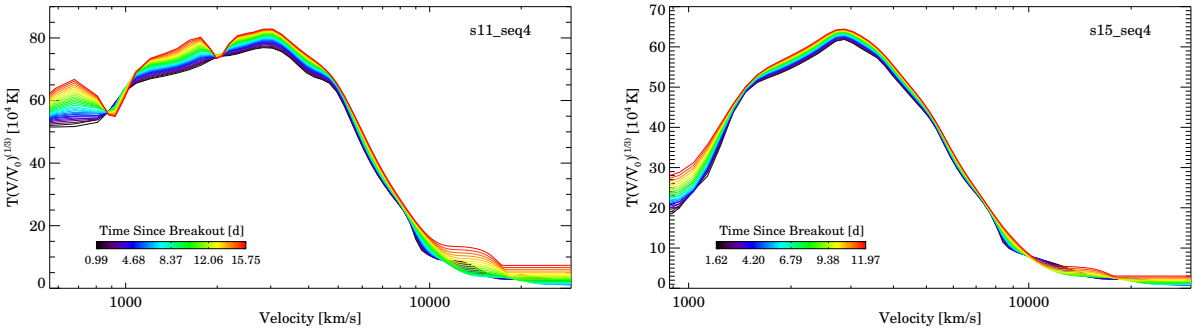

Figure 4.35: The quantity $T_n(\frac{V_n}{V_0})^{1/3}$ as a function of ejecta velocity for sequence s11_v1d (left) and s15_v1d (right). The time since breakout is differentiated by a color coding. For pure adiabatic expansion, $T_n(\frac{V_n}{V_0})^{1/3}$ represents the initial temperature of the ejecta, and thus these curves would lie on top of each other.

equilibrium. This confirms the necessity to allow for fully Non-LTE in modeling SNe.

4.4.3 Ejecta temperature

At large optical depth, the ejecta approaches adiabatic expansion, provided the energy deposition from radioactive decay is absent. Since radiation field is the dominant energy at depth, the equation of state of the photon gas is given by

$$T_n V_n^{1/3} = \text{const} \tag{4.14}$$

where T_n is the temperature at time step n and V_n is the volume element at a particular depth. In a Hubble flow, this relation can be simplified to $T \times r = \text{const}$. In general, the above relation can be rewritten as,

$$T_0 = T_n \left(\frac{V_n}{V_0}\right)^{1/3} = T_n \left(1 + \frac{v\Delta t}{r_0}(\sigma + 1)\right)^{1/3} \left(1 + \frac{v\Delta t}{r_0} + \frac{1}{2}\frac{a\Delta t^2}{r_0}\right)^{2/3} \tag{4.15}$$

where r_0 is the initial radius, v is the velocity of the ejecta, $\sigma = d\ln(v)/d\ln(r) - 1$, Δt is the time difference between time step n and 0, and a is the acceleration of the ejecta.

According to Eq. 4.15, the quantity $T_n \left(\frac{V_n}{V_0}\right)^{1/3}$ is necessarily identical to T_0, provided the ejecta undergoes adiabatic expansion and radioactive decay heating is ignored. In Fig. 4.35 the quantity $T_n \left(\frac{V_n}{V_0}\right)^{1/3}$ for s11_v1d and s15_v1d is illustrated. For the models displayed T changes by over a factor of 7, whereas the conserved quantity varies by up to 19%. We identify two causes for the observed variation – numerical error and diffusion.

The numerical error arises from the difference of the zeroth moment equation. While Eq. 4.15 gives an exact relation for the temperature in case of adiabatic expansion, the moment equation we solve (see Eq. 4.12) in the optically thick regime is approximately given by

$$\frac{1}{r^3}\frac{D(r^3 J)}{cDt} + \frac{\beta}{r}J + \frac{\beta\sigma}{r}(J+K) = 0 \tag{4.16}$$

By assuming $K = (1/3)J$ at depth, we obtain ($J \propto T^4$)

$$T_{\rm new} = \left(\frac{r_{\rm old}}{r_{\rm new}}\right)^{3/4} \left(\frac{1}{1 + v\Delta t/r_{\rm new}(4\sigma/3+1)}\right)^{1/4} T_{\rm old} \tag{4.17}$$

This relation tends to give a slightly higher temperature structure than that given by the adiabatic expansion. The size of the error depends on σ, the velocity of the ejecta, and the size of the time step Δt. Since $\sigma = 0$ for a pure Hubble flow, the error will also occur for a pure Hubble flow. For a rough estimate, the error for one time step is $\approx 0.3\%$ (assume $v\Delta t = 0.1 r_{\rm old}$ and $\sigma = 0.5$), which leads to a total cumulative error of $\approx 8\%$ from 0.99d to 15.75d. This error is obviously non-negligible, but it can be reduced by regrouping Eq. 4.16 into

$$\frac{1}{r^4}\frac{D(r^4 J)}{cDt} + \frac{\beta\sigma}{r}(J+K) = 0 \tag{4.18}$$

Ideally, this can exactly recover the adiabaticity in a Hubble flow. In a non-Hubble flow, this reduces the error from 0.3% to 0.01% in the case of $v\Delta t = 0.1 r_{\rm old}$ and $\sigma = 0.5$. This valuable test makes us aware that we should do the grouping as $D(r^4 J)/Dt$ rather than $D(r^3 J)/Dt$ in the difference equation. This may also partially help explain that synthetic flux in SN 1987A is higher than the observations at 127d [238]. Future studies should based

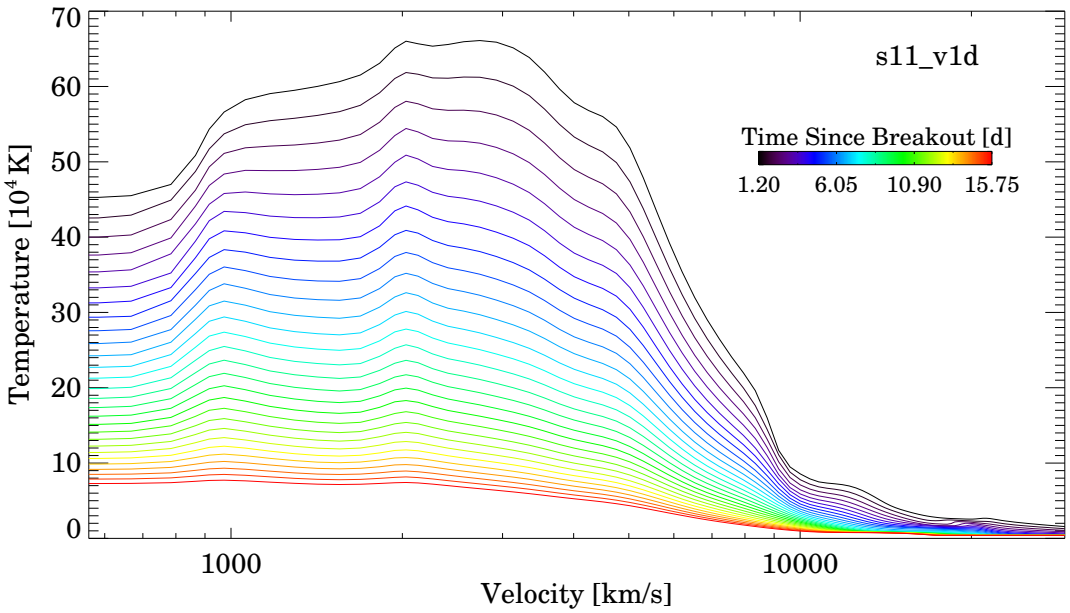

Figure 4.36: Model temperature evolution for the s11 sequence from 1.2 to 15.75d since explosion, which is encoded in color.

on this $D(r^4J)/Dt$ grouping, since temperature is one of the most important parameters in simulating the SN ejecta.

Another relevant issue is diffusion. The diffusion time scale is generally much longer than the age of the SN at early stage. Thus, diffusion is irrelevant for spectral formation. Small though it may be, diffusion can drive deviation from adiabaticity in the ejecta temperature. We estimated the diffusion time for two adjacent depths in the optically thick regions to be $t_{\rm diff} = \tau\Delta R/c = 10^4 \cdot (5 \cdot 10^{12})/(3 \cdot 10^{10}) \approx 19$d ($\tau$ is the optical depth across two adjacent points). This estimate is more relevant than diffusion time scale, since we are only concerned about the diffusion inside the optically thick region. Fig. 4.36 illustrates the model temperature evolution for the s11_v1d sequence. The temperature profile in early models shows two peaks at about 1000 km s^{-1} and 2000 km s^{-1}, enhancing radiation diffusion which depends on temperature gradient. This is reflected by the two troughs in Fig. 4.35 (left panel). When plotted as $T_n \left(\frac{V_n}{V_0}\right)^{1/3}$, the temperature at 1000 km s^{-1} and 2000 km s^{-1} is

cooler than what it should be in the adiabatic case. Moreover, the temperature distribution has become smoother with time (see Fig. 4.36), which is consistent with diffusion.

4.4.4 Global energy constraint

In a static stellar atmosphere, the radiative equilibrium equation and the zeroth moment equation imply that r^2H is conserved. While this condition does not hold in a SN envelope we can used the radiative equilibrium condition, and the zeroth moment equation to derive a global energy constraint.

The energy constraint equation for a Hubble flow has been derived in Hillier and Dessart [168], which is given by

$$r_{\rm max}^2 H(r_{\rm max}) = r^2 H(r) + \int_r^{r_{\rm max}} \left[\frac{r^2}{4\pi} \left(\frac{De_{\rm decay}}{Dt} - \rho \frac{De}{Dt} + \frac{P}{\rho} \frac{D\rho}{Dt} \right) - \frac{1}{cr^2} \frac{D(r^4 J)}{Dt} \right] dr \quad (4.19)$$

where J and H are the integrations of the zeroth and first moments of the radiation field over frequency, and other notations are the same as those in Sec. 2.3.3. For non-homologous ejecta, the energy constraint equation is given by

$$\begin{aligned} r_{\rm max}^2 H(r_{\rm max}) = r^2 H(r) &+ \gamma \int_r^{r_{\rm max}} \frac{r^2}{4\pi} \left(\frac{De_{\rm decay}}{Dt} - \rho \frac{De}{Dt} + \frac{P}{\rho} \frac{D\rho}{Dt} \right) dr \\ &- \gamma \int_r^{r_{\rm max}} \left[\frac{1}{cr^2} \frac{D(r^4 J)}{Dt} + \beta \sigma r (J + K) \right] dr \\ &- \gamma \int_r^{r_{\rm max}} \left[\frac{\gamma \beta}{c} \frac{D(r^2 H)}{Dt} + \frac{2\gamma^3}{c} \frac{D\beta}{Dt} H + \frac{1}{c} \frac{D\gamma}{Dt} (J + K) \right] dr \end{aligned} \quad (4.20)$$

where K is the integration of the second moment of the radiation field over frequency, and second orders terms of β are ignored in our calculation. In static atmospheres, Eq. 4.20 ends up with $r_{\rm max}^2 H(r_{\rm max}) = r^2 H(r)$, which means that the luminosity is conserved. In SNe, Eq. 4.20 generally has no real physical meaning, but provides a mathematical check for consistency of the solutions. When the equation is integrated across multiple shells it looses significance in that different regions of the atmosphere have not necessarily had time to communicate. Thus errors in the inner region may have no effect on the flux received by an observer. However if the equation is integrated across a "thin" shell, Eq. 4.20 has a clear

meaning in that the difference in flux can be related to radioactive decay, adiabatic cooling etc. i.e., it is an energy constraint. Fig. 4.37 shows the global energy constraint for a model in simulations based on s11_v1d and s20_v1d. The errors for the "conserved luminosity" in both models are small. In the outer region, the conservation of the right hand side of Eq. 4.20 is superb, while small deviations are seen in the inner region. Such deviations are largely due to acute changes in the ejecta properties [168], such as abundances, the hydrogen ionization front in Type II SNe, or the velocity structure in non-homologous cases. Since the departures arise from grid resolution issues, they can be improved by increasing the number of grids at the place where acute changes occur.

4.5 MODEL EVOLUTION

Table 4.3 lists the start and end time of the three sequences. The simulations started at a time when V1D roughly gives a monotonic velocity structure. After the explosion, radiation force is the dominant force for accelerating or decelerating the ejecta. However, monotonicity can be destroyed when taking into account the acceleration. As a result, we neglect accelerations in the modeling. For sequences s11_v1d and s15_v1d, they have only been evolved to 19.06d and 14.48d, respectively. The main reason is that these models are found to be unrealistic due to the modification of the velocity profile, and consequent changes in the ejecta masses. As the main goal of this study is to test the fully relativistic solver and not to compare with any observation, the validity of the initial models are not of concern. Future work will start with realistic hydrodynamical models and explore the difference between homologous and non-homologous sequences. However, sequence s20_v1d starts at a later time when the large velocity gradient part is relatively small, and only a high resolution outer region is attached at the end of the hydrodynamical structure. Thus, the ejecta properties of this sequence is reasonable, and its photospheric evolution, light curves, and spectral evolution will be presented below to illustrate the results of the solver.

Early time evolution of SNe is characterized by the properties of the photosphere, which is defined as the sphere where the electron scattering optical depth is 2/3. This is roughly

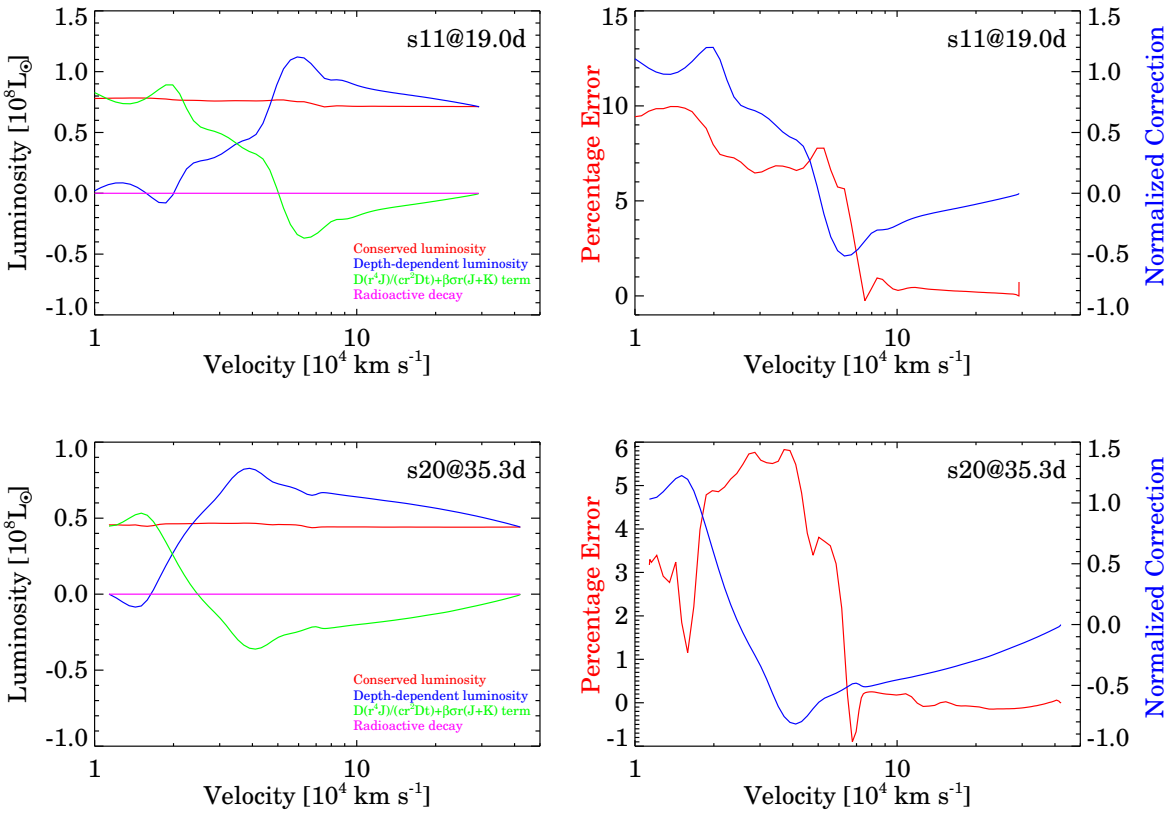

Figure 4.37: Top: Global energy constraint for a model in simulations based on s11_v1d. The left panel show the "conserved luminosity" (red; $r_{\rm max}^2 H(r_{\rm max})$), the depth-dependent luminosity (blue; $r^2 H(r)$), the $D(r^4 J)/(cr^2 Dt) + \beta\sigma r(J + K)$ term (green; $-\int_r^{r_{\rm max}} \left[\frac{1}{cr^2}\frac{D(r^4 J)}{Dt} + \beta\sigma r(J + K)\right] dr$), and the radioactive decay term (magenta; $\frac{De_{\rm decay}}{Dt}$) in Eq. 4.20 as a function of ejecta velocity. Bottom: same as top, but for a model in simulations based on s20_v1d.

the spectrum forming region. Fig. 4.38 illustrates the photospheric properties for the s20_v1d sequence. During the first week, the photospheric velocity and temperature evolve rapidly. The photospheric temperature falls dramatically due to the fast volume expansion rate and thus a significant cooling at such early time. As a result, the photospheric velocity decreases as the photosphere recedes into deeper layer of the ejecta. However, the photospheric radius keeps increasing since expansion of the ejecta outraces the receding of the photosphere.

Table 4.3: Start and end times for the simulations

Sequence	t_{init} (d)	t_{final} (d)
s11_v1d	0.90	19.06
s15_v1d	1.47	14.48
s20_v1d	3.59	134.28

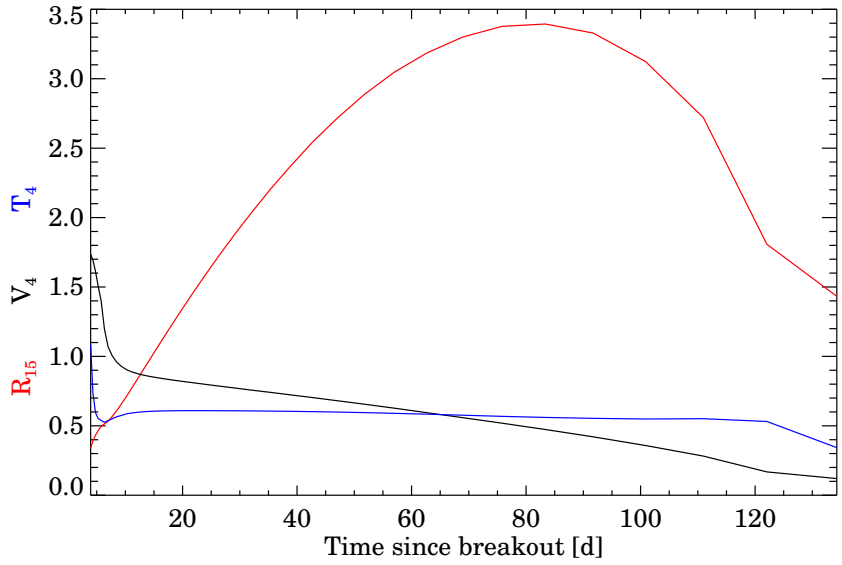

Figure 4.38: Evolution of photospheric velocity V_4 (black; $V_4 = V_{\rm phot}/10^4\,{\rm km\,s^{-1}}$), photospheric radius R_{15} (red; $R_{15} = R_{\rm phot}/10^{15}\,{\rm cm}$), and photospheric temperature T_4 (blue; $T_4 = T_{\rm phot}/10^4\,{\rm K}$) for the simulations based on model s20_v1d.

After the rapid evolution phase, the photospheric temperature becomes fairly constant, which is first set by the release of the shock deposition energy and then by the recombination wave of hydrogen. The recombination wave of hydrogen has a characteristic temperature of $\sim 6000\,{\rm K}$, which is seen in Fig. 4.38. The receding of the photosphere now becomes very slow, and hence the decreasing of the photospheric velocity slows down. The photospheric radius

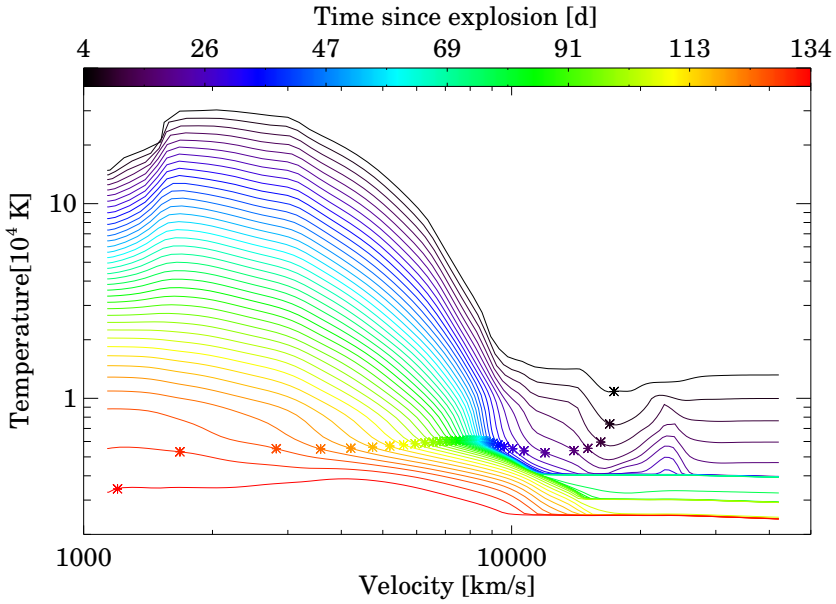

Figure 4.39: Evolution of the ejecta gas temperature from 4 to 134 d since shock breakout in the simulations based on model s20_v1d. Stars give the position of the photosphere. A color coding is used to differentiate the epochs.

keeps increasing until it reaches a peak value and falls quickly at the end of the photosphere phase, since the photosphere is disappearing as the ejecta becomes transparent.

Fig. 4.39 displays the evolution of the temperature structure for s20_v1d sequence, with the photospheric location marked by a star symbol. The temperature in the inner region is quite cold at late time, mainly due to the neglect of explosive nucleosynthesis in the hydrodynamical model. We emphasize that this is not our concern, since we are mainly focus on testing the fully relativistic solver and exploring early time evolution of a non-Hubble expanding ejecta.

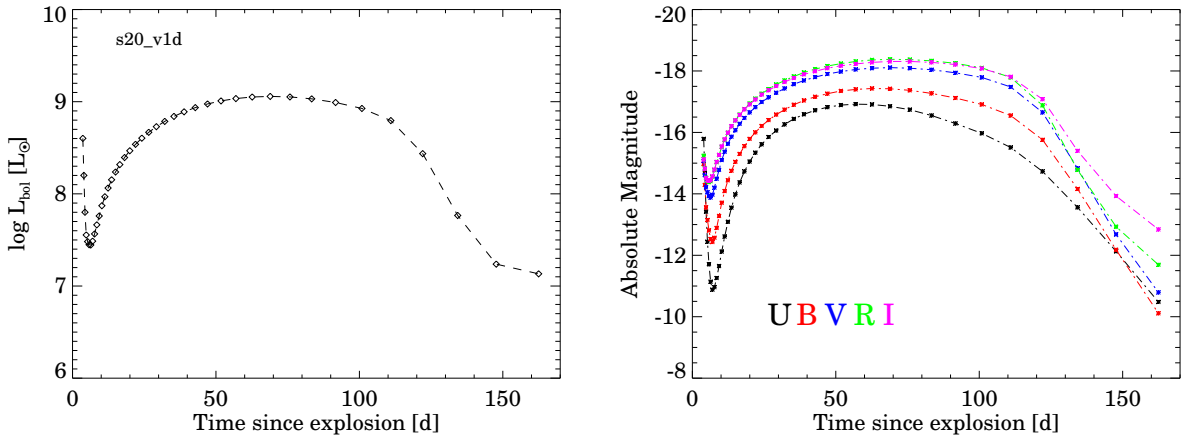

Figure 4.40: Top: bolometric light curve for the simulations based on model s20_v1d. Bottom: UBVRI light curves for simulations based model s20_v1d.

4.6 LIGHT CURVES AND SPECTRAL EVOLUTION

4.6.1 Bolometric and multi-band light curves

The bolometric light curve for the s20_v1d sequence is illustrated in Fig. 4.40 (left panel). The bolometric luminosity falls rapidly during the first week, and then rises gradually to the plateau phase. The rise in the light curve is due to release of stored thermal energy by the shock. Photometric observations of the normal Type II-P SN 1999em showed no rise phase in the bolometric light curve at early time [105]. Such behavior in the bolometric light curve is believed to be due to a dense central core in the pre-SN structure and faster expansion of the outer layers [52, 377].

The UBVRI light curves are shown in Fig. 4.40 (right panel). The VRI light curves resemble those in the theoretical work of Dessart and Hillier [90], whose hydrodynamical inputs were based on KEPLER [398] and evolved from progenitor masses of 15 $M_\odot$ and 25 $M_\odot$. However, the U- and B-band light curves are much brighter. This is not surprising at late times since V1D hydrodynamic models do not allow for explosive nucleosynthesis. The line-blanketing effect at U- and B-band is significantly underestimated due to lack of iron

group and intermediate mass elements. However, at early times the hydrodynamic structure should play a more important role since the pre-SN model utilizes the solar metallicity and synthesized material is not seen yet.

4.6.2 Spectral evolution

The optical and near-IR spectral evolution for the s20_v1d is presented in Fig. 4.41. The spectrum at 3d is characterized by Balmer lines since the photosphere resides in the outermost hydrogen envelope. After 4d, the spectra are obviously insufficient of line blanketing shorter than 5000 Å. As pointed out by Eastman et al. [103], the spectral evolution of a type II-P SN is controlled by changes in the ionization up to the middle of the plateau phase. The spectral properties are essentially governed by the ionization changes as long as the photosphere does not recede into the helium core and the photospheric compositions remain roughly the same.

4.7 DISCUSSION

4.7.1 Bias of distance measurements

Several methods have been suggested to measure the distance using Type II-P SNe, e.g., the expanding photosphere method [EPM; 204], the spectral-fitting expanding atmosphere method [SEAM; 21] and the standardized candle method [SCM; 154]. While SCM relies on the relation between the expansion velocity and the luminosity, both EPM and SEAM involve spectral modeling for the SNe (see Sec. 1.3 for detail description of EPM and SEAM). It has been widely assumed in the SNe spectral modeling that the ejecta are expanding homologously. However, this assumption may be poor at very early times. It introduces two uncertainties for distance measurements. First, the uncertainty arises from the spectral modeling. Many radiative transfer codes for modeling SNe spectra adopt the homology assumption. Even if the observations can be fitted by a model, the physical parameters of the model, e.g., the photospheric radius and the diluted factor ξ, are not necessarily correct for the observations. Second, both EPM and SEAM utilize the relation $R_{\rm phot} = v_{\rm phot} t$ (t

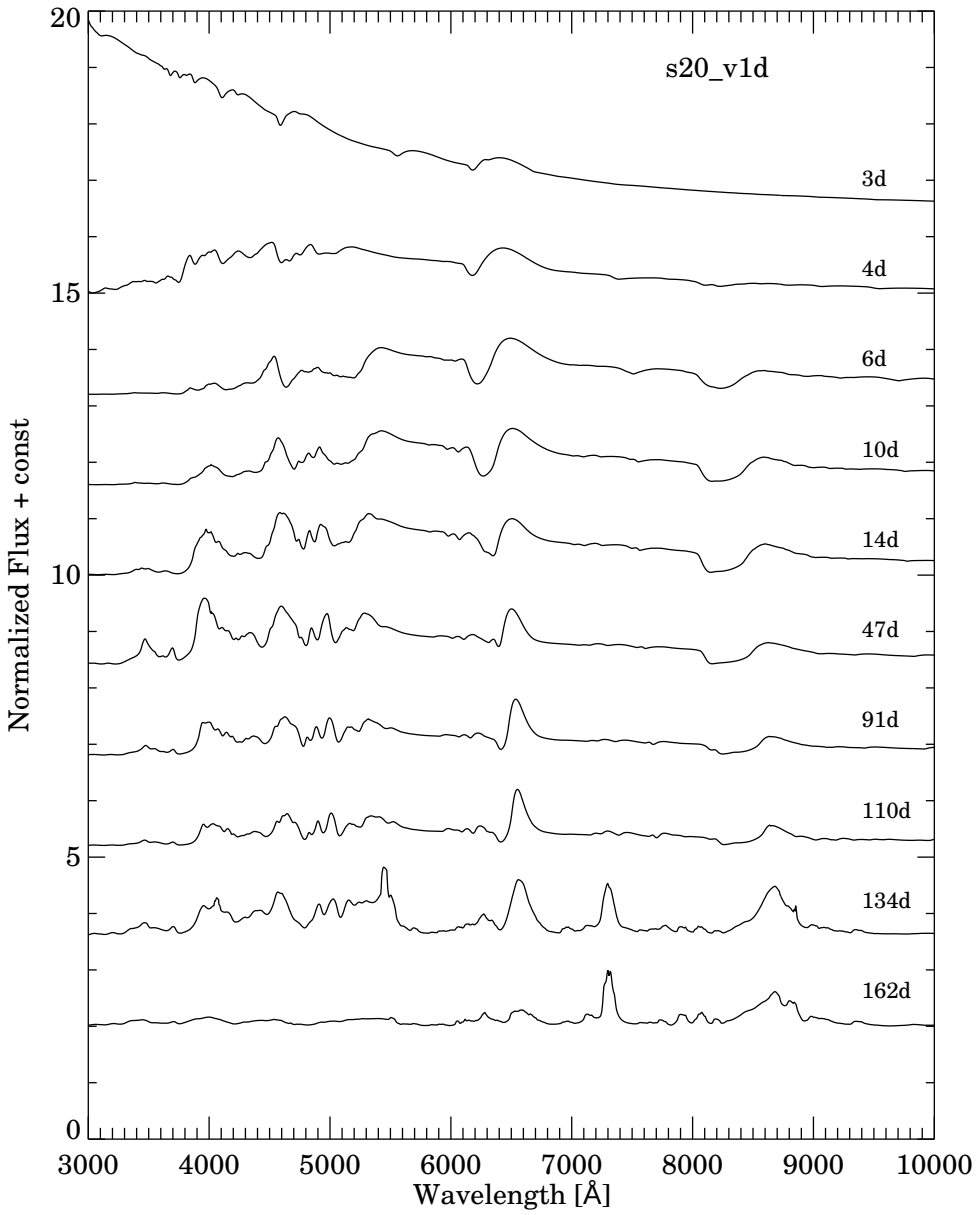

Figure 4.41: Spectral evolution for simulations based on model s20_v1d. Early spectra are blue and emission lines are rather weak. Hα (6563 Å) and Ca II triplet (around 8600 Å) are quite broad at early times, but Ca II triplet does not develop until 6d. The line-blanketing effect (mainly below 5000 Å) becomes prominent after 14d. The continuum fades gradually from 110d and the ejecta enters its nebular phase.

is the time since explosion), which is invalid at early epochs. Using early time Type II-P observations in EPM/SEAM therefore, introduces uncertainties in measuring the distances. Physically we know that homology is not true at early times and thus we need the relaxation of homology to allow early time data to be utilized.

4.8 CONCLUSIONS

We have implemented the fully relativistic solver, which takes into account all terms in the radiative transfer equations, into CMFGEN. A linearization routine was also implemented to compute the change in the radiation field for an unknown change in the opacities and emissivities. A corresponding solver for the gray solution was also developed to facilitate the convergence of the large optical depth region.

Hydrodynamical models from V1D with different RSG progenitor masses of $11\,M_\odot$, $15\,M_\odot$, and $20\,M_\odot$, are employed and evolved to different epochs. The $11\,M_\odot$ and $15\,M_\odot$ sequences are only evolved to ~ 15 days due to unphysical properties arising from modifications to the velocity profile. To avoid non-monotonicity in the velocity structure, the acceleration terms have been ignored in the simulations. We are able to simulate Type II-P SNe from very early time when the ejecta is highly non-homologous.

Various checks have been made to verify the solutions. The solver gives the same results as the Hubble solver for homologously expanding ejecta. LTE is recovered at depth as expected, which can be seen from the departure coefficients of H I, O I, and Fe II. We found a numerical issue which could drive temperature deviation from adiabacity. Diffusion was also important, even though radiation did not necessarily diffuse all the way to the surface. The global energy constraint gives consistent checks for models at different epochs.

The significant deviation from a Hubble flow evaluated in Type II-P SNe is expected to have appreciable effect on their spectra. The fully relativistic solver presented here will allow better modeling of early time spectra in the future. As mentioned earlier, modeling SNe is an initial value problem, and thus even late time spectra can be affected. Further, the fully relativistic solver will also allow a more realistic comparison of the hydrodynamic

models and the observations.

5.0 PART III. ETA CARINAE

5.1 INTRODUCTION

η Carinae is one of the most massive luminous stars in the galaxy, and belongs to the class of Luminous Blue Variables (LBVs) that have exhibited a giant eruption [77]. Both nebular [79] and stellar studies [e.g., 172] found evidence for CNO processed material (i.e, N and He enhancements, and C and O depletion), indicating that it is an evolved star. It is a binary system with a period of 5.5 yrs [74, 73, 185, 65, 307, 406, 1, 285, 76, 75].

The Homunculus is is a bipolar structure consisting of material ejected by the great eruption of η Carinae in the 1840s [278, 341, 69]. Polarimetric and spectroscopic observations shows that it is primarily a reflection nebula at X-ray, UV, visual, and near-IR wavelengths [366, 367, 388, 262, 329, 167, 203, 66]. By studying both intrinsic Homunculus emission, and reflected stellar emission lines, the geometry of the Homunculus can be reconstructed [82, 329, 5, 167]. In a coarse sense the Homunculus resembles two alembics joined at their necks and centered on the star, with most of the ejected mass in the alembic bottoms [70]. The two "alembics" are called the SE (southeast), approaching lobe and the NW (northwest), receding lobe, relative to the observer.

The reflected emission lines also provide a means for probing the wind geometry, since the reflected emission lines allow us to view the star from different directions. An early study of reflected Hα profiles, obtained by Hubble Space Telescope Space Telescope Imaging Spectrograph (HST/STIS), suggested that the wind was latitude-dependent during the high state [344] when the star shows high excitation emission lines (e.g., [Fe III] and [Ne III], and He I emission lines – e.g., Damineli et al. 75). P Cygni absorption components are associated with Hα, Hβ Fe II and some He I emission lines at higher latitudes, while these absorption

components are absent at lower latitudes. This was interpreted as evidence for a bipolar wind, with the wind having lower ionization and higher density at higher latitudes. This contradicts earlier ideas that in a rapidly rotating star, the polar wind should have a lower density than the equatorial wind [310, 397, 396]. Instead it supports the idea that line-driven winds of massive stars are influenced by gravity darkening [67, 297, 129, 298]. In a rapidly rotating star the higher flux over the pole is (generally) more important than the lower gravity at the equator, and consequently the mass-loss rate is expected to be higher at the pole. Infrared interferometric studies appear to confirm that the wind is denser at the pole [50, 401]. However, it might also be possible to interpret the infrared observations using a binary model [140].

However, the overwhelming evidence that η Carinae is a binary system means that the simple picture of an axisymmetric bipolar wind needs to be re-examined. First, the binary companion will create a cavity in the wind of the primary. Second, its radiation field could potentially alter the ionization of the primary wind. Both effects will lead to an apparent wind asymmetry. Indeed, Hillier et al (2001) interpreted the absence of Hα and Fe II P Cygni absorption components at most binary phases as evidence for influence by the companion star. Recent modeling of the influence of the companion on observed line profiles have shown that it can explain the lack of P Cygni absorption towards the primary star [142].

The Weigelt blobs, discovered by Weigelt and Ebersberger [400], were shown by Davidson et al. [81] to be the source of the narrow nebular emission seen in ground spectra. The blobs lie close to the star ($0.1 - 0.4''$), move at low speeds of ~ 50 km s^{-1} [81], and emit high excitation nebular lines (e.g., [Fe III], [Ar III], and [S III] emission lines) which disappear for a brief period every 5.5 years [e.g., 76, 75]. Around the same time there is a dramatic change in the X-ray light curve [185].

Gull et al. [146] showed that the broad, blue-shifted [Fe III] emission across the extended high state places the hot secondary on the near side of the primary as the binary companion spends most of its time near apastron in the highly elliptical orbit. This, and other evidence, suggests that the events occur around periastron, and that apastron is located on our side of the primary [251]. As apastron is on our side, the secondary can influence the primary wind for a substantial fraction of the 5.5-year period. There have also been controversial

suggestions that apastron lies on the far side of the primary [197, 109].

During periastron passage, the P Cygni absorption components on Hδ, and the Fe II lines strengthen dramatically [285]. This is consistent with the idea that the companion is briefly enveloped by the primary wind on the far side and is no longer capable of ionizing the stellar wind along our sight line. At periastron the wind spectrum is more consistent with other P Cygni stars, such as HDE 316285. An alternative explanation, proposed by Smith et al. [344], suggests a shell ejection which occurs primarily at low latitudes leading to a more spherically symmetric wind structure. In this picture, the wind would show axial symmetry which is not expected in the binary scenario except at conjunction when the secondary is behind the LBV primary.

When interpreting the P Cygni absorption components, two other factors should also be considered. First, the higher Balmer lines show P Cygni absorption at all phases [285]. Observationally, this is easily explained in a scenario where the companion star primarily influences the ionization of the wind in the outer, Hα-forming region. It is not so easily explained in the "shell-ejection" model. Second, the strength of the H I P Cygni absorption component depends on both the wind density and ionizing flux. Either a reduction in the mass-loss rate, or an increase in the ionizing flux, can make the absorption components disappear.

The most detailed study using the reflected profiles to study the wind geometry was by Smith et al. [344], who used a single slit position, and primarily studied the Hα absorption component. As noted earlier, Smith et al. [344] concluded that η Carinae's primary had an axisymmetric wind. Additional, but more limited studies, have been done from the ground by Stahl et al. [353], with the primary aim of trying to understand the 5.5-year-period event by utilizing observations that look at the star from different directions. More recently, Mehner et al. [263] used observations in the SE lobe to try to interpret changes in the primary spectrum seen near the recent 2009 event. The observed changes in the primary spectra around the 2009 event, and the views from the pole, are not easily reconciled with any model.

In this study we use mapping data from March 2000, which covers the whole Homunculus, to study the wind asymmetry. We concentrate on the Hα emission component, and to a lesser

extent on the absorption component. For a simple axisymmetric wind, and in the absence of other complicating factors, the emission EW should show a simple axisymmetric distribution.

We organize this chapter as follows: The optical mapping across the Homunculus is described in §5.2, while an overview of the Hα line profiles is presented in §5.3. We will describe the EW map in §5.4 and discuss the global variation in §5.4.2 and pixel-to-pixel variation in §5.4.7. A brief discussion of the core region is given in §5.4.5, while in §5.4.8 we discuss the implications of the map. In §5.5 we examine the Hα absorption component in the SE lobe, generating a map of the velocity of the absorption minimum. The optical depth of the Homunculus is discussed in §5.6.

5.2 OPTICAL MAPPING OF THE HOMUNCULUS

The HST/STIS observations were part of the STIS GTO program (Gull, 2000, HST 8483) whose purpose was to map the Homunculus and substructure including the Little Homunculus. The primary data set is from the March 2000 STIS CCD observations at phase ∼0.45, near apastron. These observations utilized the $52'' \times 0.1''$ slit and the G750M grating, with a spectral resolving power R∼5000, and covered the spectral range from 6488 Å to 7052 Å. The exposure time for mapping the Homunculus was 80 s with a subset of five positions centered on η Carinae of 8 s and a single observation of 0.8 s centered on the central source. The slit position angle, limited by HST solar panel orientation requirements, was -35°. This is almost parallel to the projected polar axis of the Homunculus, which has a position angle of 132° [262]. Exposures, spanning the entire Homunculus, were obtained at 49 different positions separated by $0.25''$. As the aperture width is $0.1''$ the data does not satisfy the Nyquist sampling theorem.

Another data set obtained under GO program 9420 (PI: K. Davidson), sampling Hα across the foreground SE Lobe, was recorded on December 2002, during the late high state preceding the 2003.5 minimum. Four different exposures with exposure time of 220 or 232 s were taken with the $52'' \times 0.2''$ aperture at various offsets from η Carinae at a position angle (PA) of -115° (See Fig. 5.42).

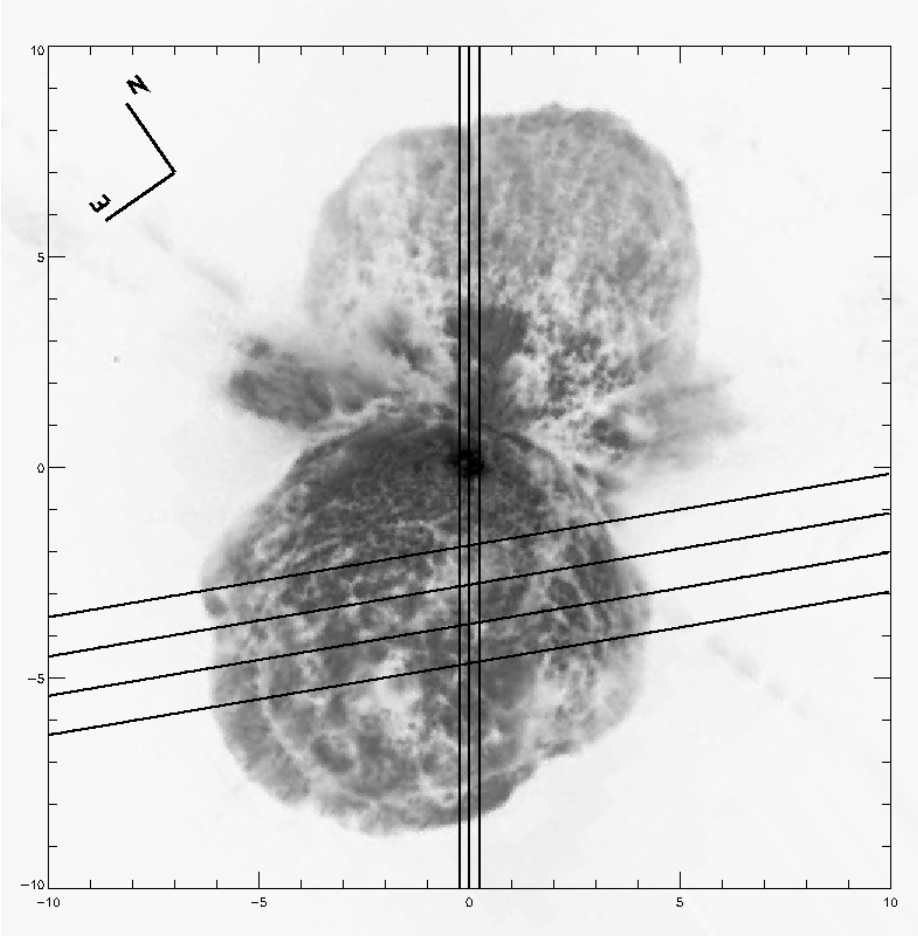

Figure 5.42: This figure is the HST/WFPC2 image obtained in 1995. The lines show the positions of the slits in different observations. The three vertical slits are the central three slits of the mapping observation in 2000. There are 49 observations with different offsets from the central source, covering the whole Homunculus. The other 4 lines (almost horizontal) show the slit positions and slit orientation in the December 2002 observations, which provide good information to explore the variation in SE lobe near periastron passage, just before the start of the low ionization state.

The Homunculus has a fairly definite 3D shape, and each projected position on the nebula can be mapped to a stellar surface position with corresponding latitudinal and longitudinal coordinates, which are defined in terms of the equatorial debris as the equatorial plane.

To study the positional variation in the Hα EW across the Homunculus, we created a 3D data cube with dimensions of slit offset from the central source, position along the slit, and wavelength using the 2000 mapping data. The pixel position is defined in a coordinate system with the X-axis aligned perpendicular to the slits and Y-axis aligned along the slits and with the origin at the central source. The 2002 data set is used only as an auxiliary to analyze the SE lobe.

Due to the brightness of central source, the 80 s exposure on the central source is saturated near the star. An improved spectral image, with emphasis on the central source spectrum, was constructed using shorter exposure spectra to replace the saturated data, and longer exposure spectra elsewhere. However, analysis of the composite data, and comparison with data from adjacent slit positions (offsets are $\pm 0.25''$), show that the data are severely corrupted. We attribute the corrupted data to the CCD bleeding and charge transfer inefficiency effects, and discard these regions in our analysis.

5.3 THE POSITIONAL APPEARANCES OF HYDROGEN PROFILES

The scattering of light by dust is angle-dependent – back-scattering is much less efficient than the forward-scattering. As the NW lobe of the Homunculus is located beyond the central source, or tilted away from us (back scattering), its continuum intensity is much smaller than that from the SE lobe, which is tilted towards us (forward scattering). Therefore, profiles in the SE lobe have much better signal-to-noise ratios.

In the NW lobe, the Hα profiles show a wide diversity in their appearance (Fig. 5.43). Most of the profiles show evidence of multiple components, indicating reflection from multiple structures. Two of the components can be associated with scattering from the front and rear sides; the origin of other components is less obvious. There is also a strong (narrow) absorption component which gradually weakens and finally disappears with increasing latitude. Similar results can be seen in Smith et al. [344].

Conversely, the Hα profiles in the SE lobe show less variation, and generally show only the front component; evidently the reflected component from the back wall of the SE lobe is

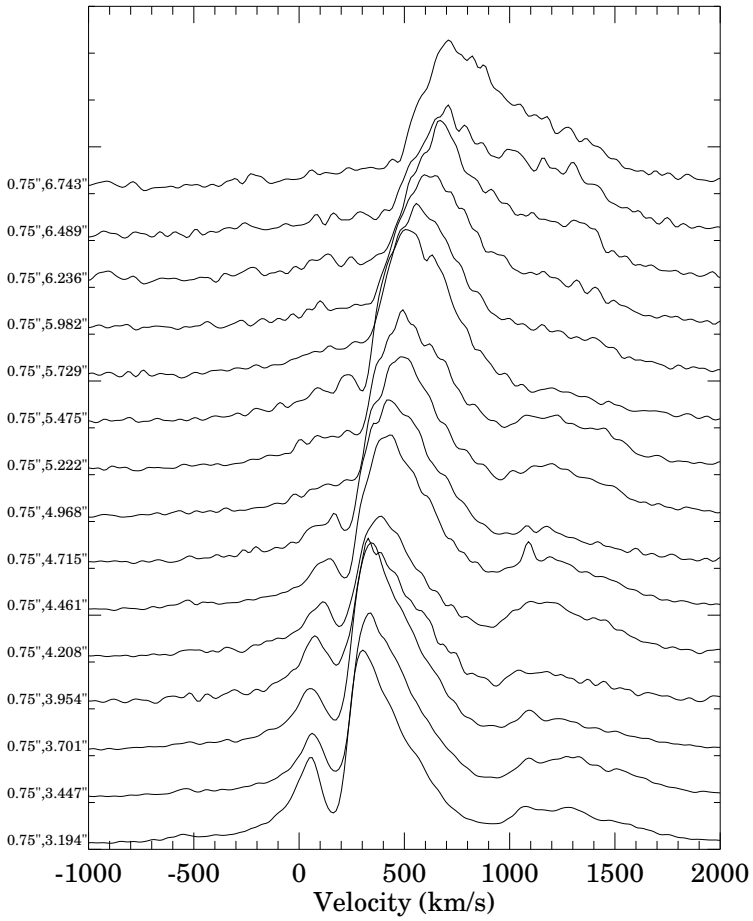

Figure 5.43: An illustration of the typical variation in Hα profiles along the slit offset by $0.75''$ from the central slit with their positions shown on the left of the profiles. As we move up along the slit, the absorption component gets smaller and perhaps disappear around $5''$. A reflection component from the rear of the NW lobe gives rise to a second broad component at $v \sim 1200\,\mathrm{km\,s^{-1}}$.

too weak to be easily discerned. Evidence for the existence of the back reflected component is seen in the infrared [337] and from polarization observations [329]. The Hα P Cygni absorption shows substantial variations both across a lobe, and between the lobes.

Emission profiles within a few arcseconds of the central source are complicated, with intrinsic Hα and [N II] doublet emission blending with the scattered lines. Such contamination

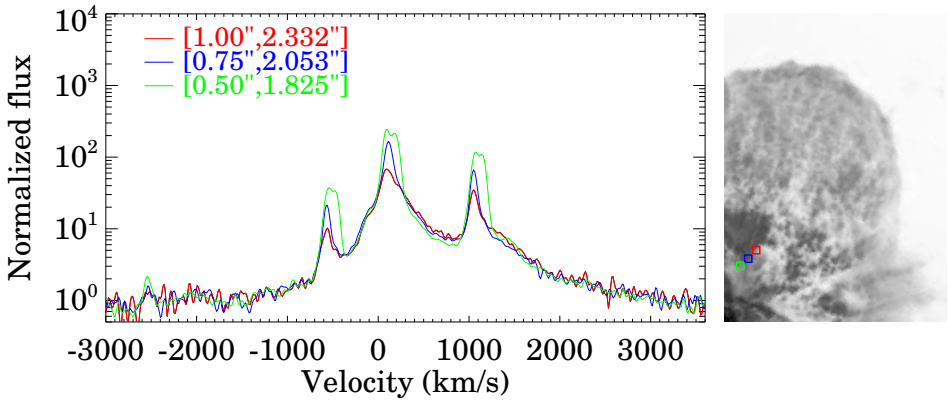

Figure 5.44: Illustration of the Hα and [N II] blend in the core of the Homunculus (left panel). The profiles are complex blend of scattered and intrinsic emission. The right panel shows the location of the regions sampled in the left panel. Note that η Carinae is at the position in the bottom left corner.

will be discussed in section §5.4. While the Weigelt blobs are very important for the narrow emission at their locations, they cannot account for the narrow spatially-extended emission throughout the central core. Fig. 5.44 shows three Hα profiles near the central source, with [N II] 6548 Å and 6583 Å lines sitting at the blue and red wings of Hα. The Hα profiles consist of both a broad and narrow component. While the broad Hα component is due to reflection from the central source, the narrow Hα component, as well as the nitrogen doublet, is most likely due to intrinsic emission, since they occur close to their respective laboratory wavelengths. The narrow Hα component becomes stronger as we look closer to the central source. This supports the conclusions of King et al. [203] that unpolarized intrinsic emission decreases the percentage polarization in regions close to the central source.

5.4 THE EQUIVALENT WIDTH MAP OF Hα

In this section, we present the method used to compute a Hα EW map utilizing the mapping data. The uncertainties in the EW map are also calculated through error propagation. We describe the global and local variations and finally discuss possible causes for these variations.

5.4.1 Calculation of EW and uncertainty

An accurate EW map requires an accurate determination of the continuum and the extent of Hα line. As the continuum in the neighborhood of the Hα profile is linear we fit the continuum, using a least square approach, with

$$f(\lambda) = a + b(\lambda - \lambda_0), \tag{5.1}$$

where λ_0 is the rest wavelength of Hα line. On the red side we use a spectral range from 6720 Å to 6750 Å to determine the continuum, while on the blue side a spectral range from 6490 Å to 6520 Å is used. Unfortunately, the Hα profile almost extends to the blue edge of the spectral range for the G750M grating setting centered at 6768 Å (6490 to 7040 Å), and this limits the accuracy to which the continuum can be determined. Different spectral ranges have been chosen on the red side to check the normalization and the uncertainties.

To accurately measure the Hα EW, a wide spectral range from 6520 Å to 6650 Å (~ -2000 km s^{-1} to 4000 km s^{-1}) is used. Such a wide range is necessary to include the extensive electron scattering wings, and to allow for the systematic redshift in the reflected Hα profile induced by dust scattering, which can be up to twice the expansion velocity of the Homunculus. We do not make any allowance for the P Cygni absorption component; thus variations in its strength will cause variations in the EW of Hα. In the SE lobe, the extreme case for P Cygni absorption is is less than 5% of the emission. The absorption contribution in the NW lobe is different from that in the SE lobe and detailed discussion is presented in §5.5.

One caveat is that the [N II] $\lambda\lambda$6548, 6583 Å lines are not excluded. The close vicinity of these two lines to Hα, the large width of Hα, and the non-Gaussian profiles, complicate

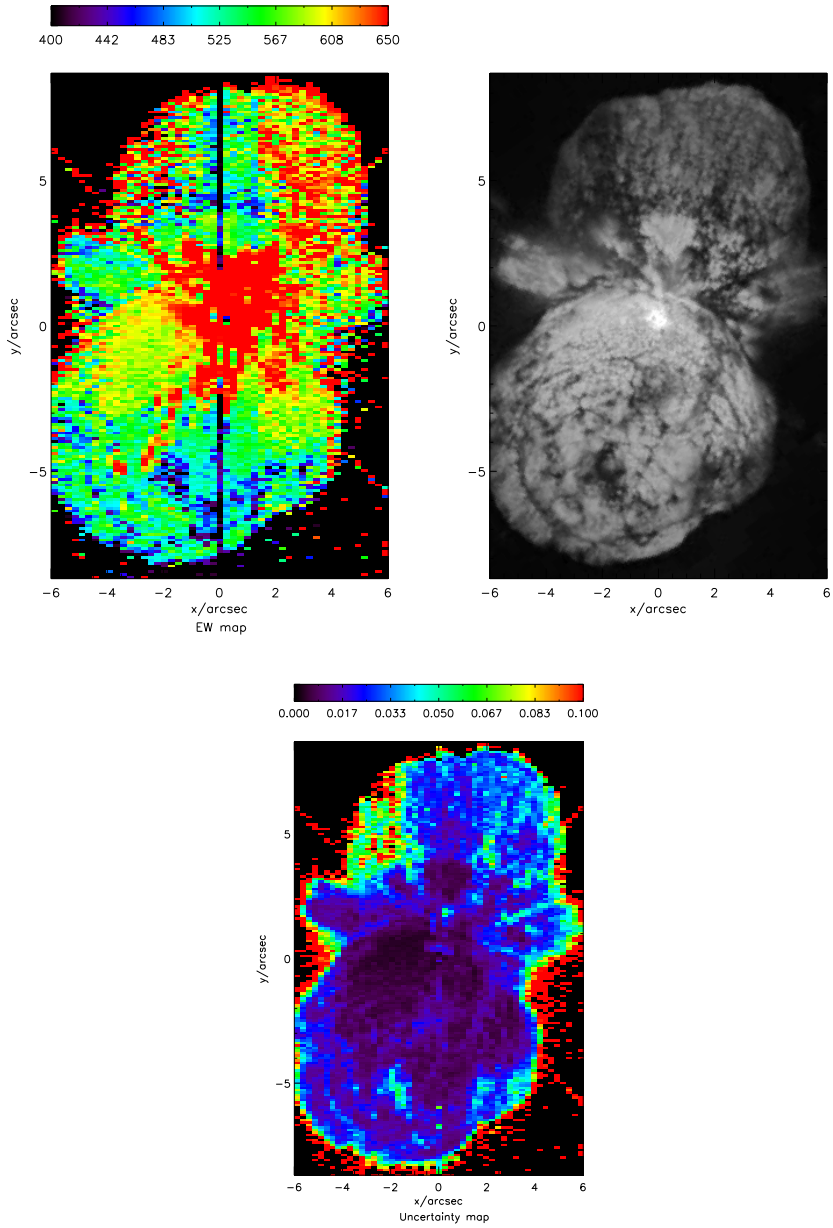

Figure 5.45: The EW map and the uncertainty map. The color bars show the range for each map. The coordinates are in unit of arcseconds, with the origin on the central source. The dark vertical stripe in the left image contains corrupted data, while the red-cross is due to the diffraction spikes originating from the HST secondary mirror support structure.

separation of these three lines, especially using an automated procedure. Fortunately, while [N II] lines can be very strong, they appear only within a small region, which is very close to the central source. In the most extreme case, the EW of the two [N II] lines can be 60% as large as that of Hα. We pay special attention to these regions and ensure that any conclusion drawn here is not influenced by the [N II] contamination.

The uncertainty is quantified by error propagation. In the least square fit process, we are able to calculate the uncertainties σ_a and σ_b of parameters a and b, and the covariance COV(a, b) between them. Therefore, the uncertainty of f, i.e. σ_f, is obtained by

$$\sigma_f^2 = \sigma_a^2 + \sigma_b^2(\lambda - \lambda_0)^2 + 2ab \cdot \mathrm{COV}(a,\, b) \tag{5.2}$$

In the left panel of Fig. 5.45, we show the plot of the Hα EW (EW map), with the EW outside the Homunculus set to zero. For display purposes, we select a maximum value of 650 Å and a minimum value of 400 Å. Pixels with EW greater than 650 Å appear primarily in regions close to the central source, and at the edge of the Homunculus. In the latter case the continuum determination is difficult because of low flux. The central slit can be ignored, because of the bleeding effect discussed in §5.2.

Contribution from HST diffraction spikes of η Carinae is evident in the map. This is not a reduction artifact; rather it arises because the EW of Hα is larger on the star than in the Homunculus [167, 171, 344]. Flux originating from the bright central core is scattered by the secondary support of the telescope, thus contaminating the profile scattered by the Homunculus.

A map showing the fractional errors in the EW map is shown in the right panel of Fig. 5.45. For the uncertainty map we select 10% as the ceiling value. As apparent from the figure, most of the pixels have uncertainties smaller than 5%. The uncertainties in the upper left region are considerably larger due to the lower signal-to-noise ratio of the spectra. Besides this region, large uncertainties are primarily located at the edge of the Homunculus – this also results from low signal-to-noise ratios and the difficulty in determining the continuum.

5.4.2 Positional variation of the EW map

As readily evident from the EW map (see Fig. 5.45), the EW of Hα varies systematically across the Homunculus. The variations are complicated, and are not easily interpreted. If the wind had a simple bipolar structure, we would expect the EW in the SE lobe to show a circular symmetric variation (about the polar axis). However, such a variation is not seen.

In the NW lobe, the EW map appears to separate into 3 principal "stripes", with a central stripe (2 arcseconds broad) showing systematically lower EWs than the adjacent regions. The stripe on the right is very patchy, showing significant variation in EW on relatively small spatial scales. The significance, and the cause of the variations will be discussed in §5.4.3. In the NW, we can also recognize the "paddle" in the disk, appearing to be a red feature around the position from 2.43″ to 3.70″ away from the central source (but cut by the bad central column).

In the SE lobe, the map is much smoother and the structure is more definitive. One reason may be that reflection appears to be dominated by a single component. A better signal-to-noise ratio also helps to reduce the uncertainties. Several striking structures can be identified. At low latitudes, we see two elliptical structures, on either side of the central slit, which have systematically larger EWs than the rest of the SE lobe. We also see a spike-like feature (unrelated to the diffraction spikes), running SE, and which shows larger EWs than its neighborhood. Hereafter, we call this structure the EW "sword". The "hole", detected in the mid- and near-IR images [343, 364], has generally smaller EWs than the rest of the SE lobe.

5.4.3 The Equatorial disk and NW lobe

As noted previously, the NW lobe shows 3 distinct stripes, with the EWs substantially lower in the stripe running NW, and centered on the star. On either side of this stripe, the EWs are larger, although there are also indications of substantial variations on small scales. Interestingly, the stripe with smaller EWs appears to an extension of the paddle. We restrict our comparisons to the central and right stripes, since EW measurements in the left stripe has substantially larger uncertainties.

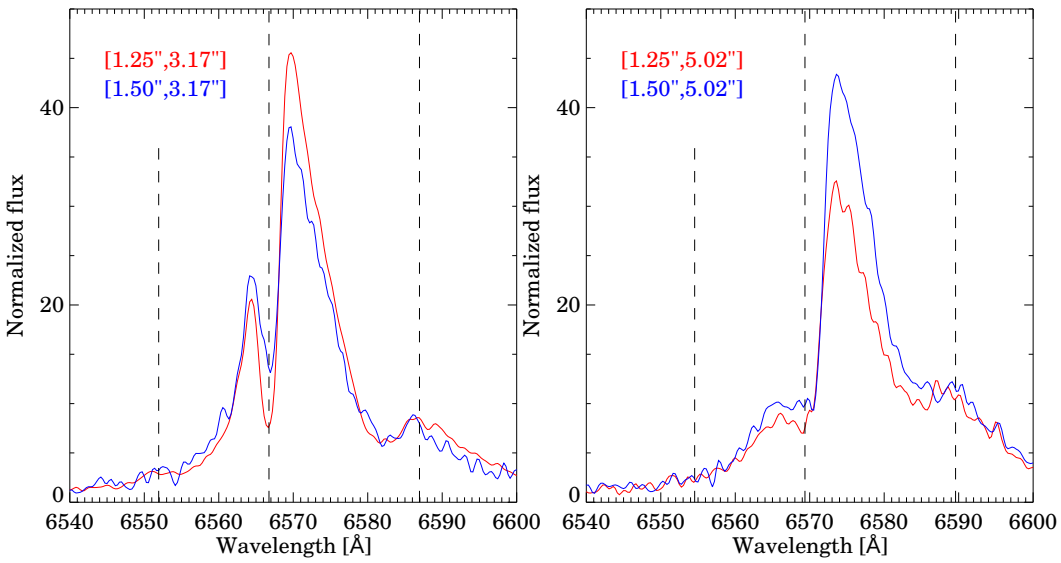

Figure 5.46: Illustration of Hα profiles from the central (red) and the right (blue) stripes at low (left panel) and high (right panel) latitudes in the NW lobe, with the coordinates shown in the square brackets. The dashed lines indicate the locations of [N II] 6548 Å, Hα 6562.8 Å and [N II] 6584 Å lines with a systematic velocity shift of 180 km s^{-1} (left panel) and 300 km s^{-1} (right panel) with respect to the rest wavelength of Hα.

Fig. 5.46 illustrates two comparisons of Hα profiles between the two stripes at low and high latitudes. The profiles have very different shapes so any uncertainty in continuum definition cannot account for the difference. To assist line identification, we also apply a systematic velocity shift to the [N II] 6548 Å, Hα 6562.8 Å, and [N II] 6584 Å lines and infer their positions with dashed lines. While [N II] 6548 Å is not clearly recognized, both Hα 6562.8 Å and [N II] 6584 Å have their correspondences, which are a deep trough component on red side of Hα and a little bump on top of the reflected component from the rear wall. This suggests that the trough feature is due to Hα absorption. As we shall discuss in §5.5, this is not the classic P Cygni absorption associated with the wind of the primary.

One disconcerting aspect regarding the variations in the NW lobe is that they are roughly aligned with the slit, and confined to the central 11 columns. This suggests a possible

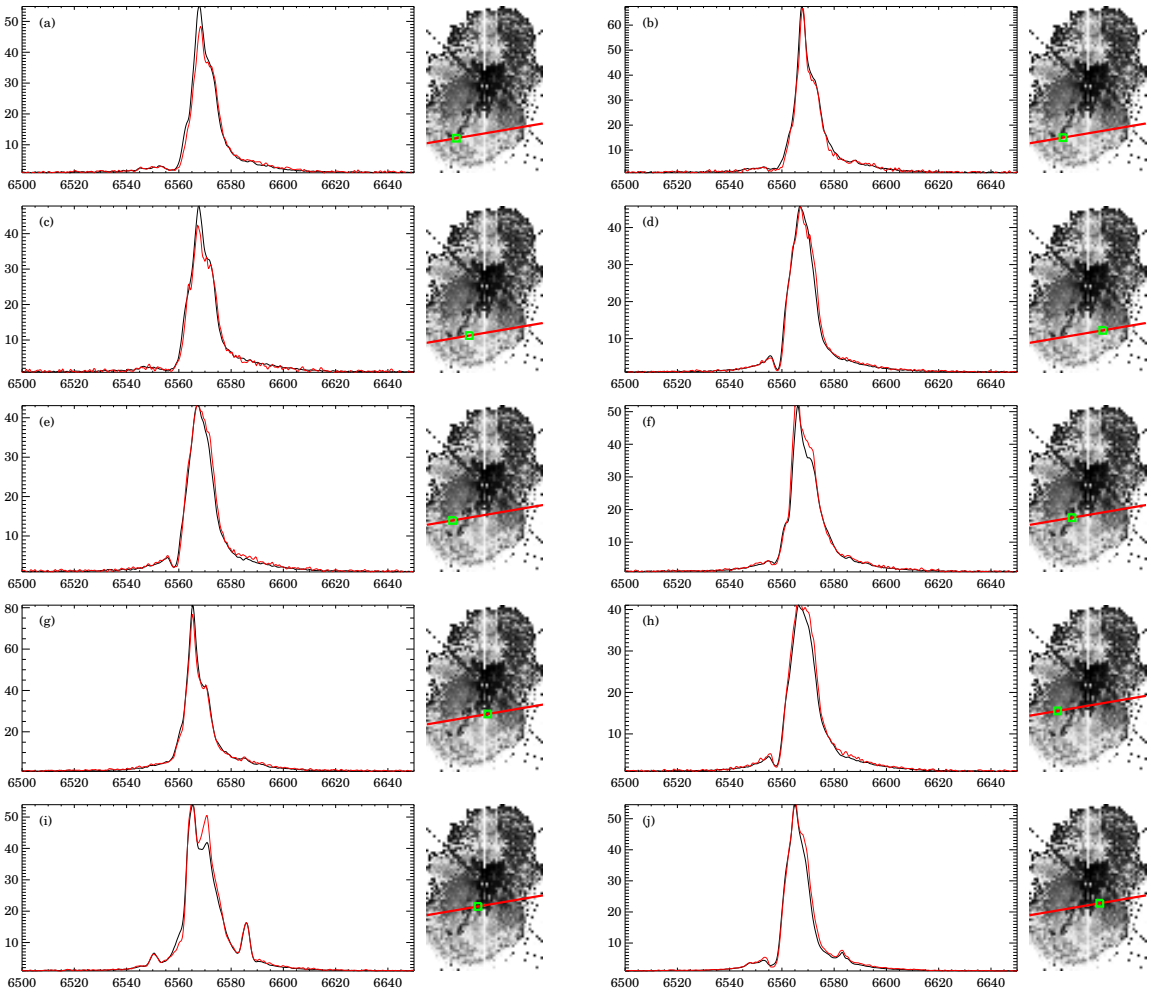

Figure 5.47: Profile comparison of SE lobe between two data sets described in § 5.2. The map on the right in each plot is an EW map, using histogram equalization as an image processing method to increases the local contrast. The black profiles belongs to the 2000 data set recorded at PA = -35°, and the red profiles come from the 2002 data set recorded at PA= -115°. The red line in the right map of each panel shows the slit in the 2002 observation and the green square marks the position that we are looking at. As one can see, this second observation covers part of the "EW sword" and the "hole".

instrumental effect. Unfortunately no independent observations are available to provide a check. Although there are a few long slit observations of the NW lobe undertaken, they do not provide more information – they have very similar orientations and have poor signal-to-noise ratios in the Homunculus because they primarily focused on the central source. However, the effect appears not to be present in the SE lobe data; we argue that the effect is real, not instrumental.

5.4.4 SE lobe

The EW map of the SE lobe is generally much smoother that that of the NW lobe. Additionally, the EWs in the SE lobe appear to be latitude-dependent, with larger values seen at lower latitudes.

Near the polar region, we can see a large zone with particularly small EWs. It partially coincides with the "hole" discussed by Smith et al. [343]. This "hole" is also seen in the optical image [277] and in both near- and mid-IR images [364], which coincides with the pole of the SE lobe. Another large area with very small EWs is located at the lower right.

This variation has been further confirmed by another STIS/CCD data set obtained in December 2002. In this data set, the slit is oriented at a very different position angle and has several different offsets from the central source. Even though the positions can not be matched exactly, we find an excellent consistency between these two data sets. Fig. 5.47 shows some comparisons. The normalized profiles from the two data sets are almost identical. Spectra of the "hole" have also been examined, and no conflict is found.

5.4.5 Core region

The EWs show a significant enhancement in the central region, which extends as far as two arcseconds from the star. This enhancement is not a reflection of the wind geometry – it is due to contamination by narrow hydrogen and nitrogen emissions (see Fig. 5.44), and perhaps the greater EW seen on the central star also plays an important role [167].

This central enhancement spatially coincides with the radio emission image in the study of Duncan and White [97]. In Fig. 5.48, we show their radio image at the same epoch.

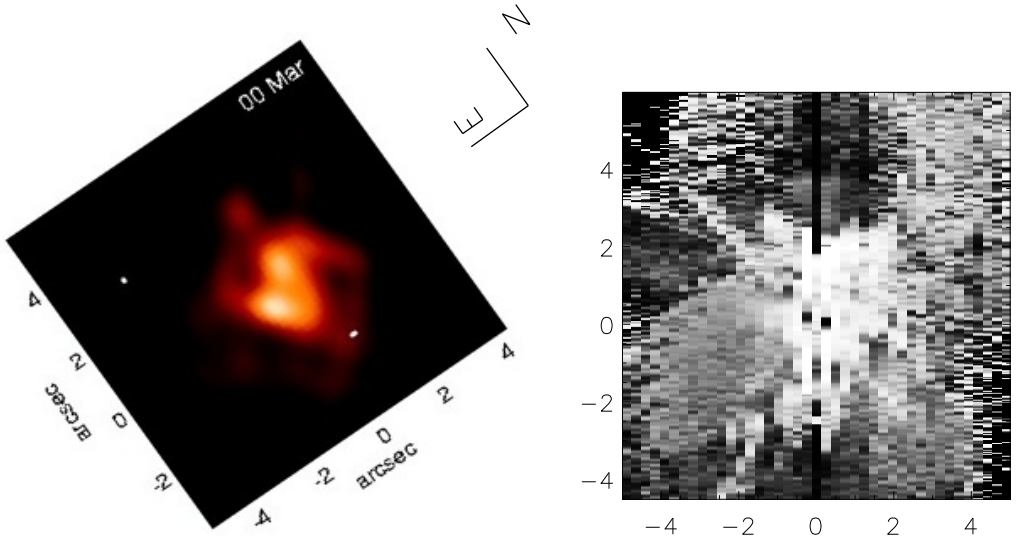

Figure 5.48: Left panel: radio emission extracted from Duncan and White [97]. The image is taken in March 2000, which is the same period as the optical spectroscopic observation. Since the slit has a non-zero orientation in our data sets, we have rotated the image 35° clockwise to facilitate comparison with our EW map. Right panel: central part of the EW map in greyscale.

Although the morphologies of the EW map and the radio image are not perfectly matched, they show considerable similarity. As a result, the radio observation provides very useful information to help understand the EW enhancement in this area. While the radio emission is confined within the core region, large EWs are also seen below the core region. Duncan and White [97] pointed out that the radio enhancement is most probably due to UV photons from the hot companion ionizing the surrounding material [405]. Most likely, the narrow optical lines arise from the same ionized gas.

5.4.6 The EW "sword"

In the SE lobe, there is a spike-like feature with greater EWs than its surroundings. This is the EW "sword" mentioned in § 5.4.2. In Fig. 5.49, we show lobe spectra at the EW "sword"

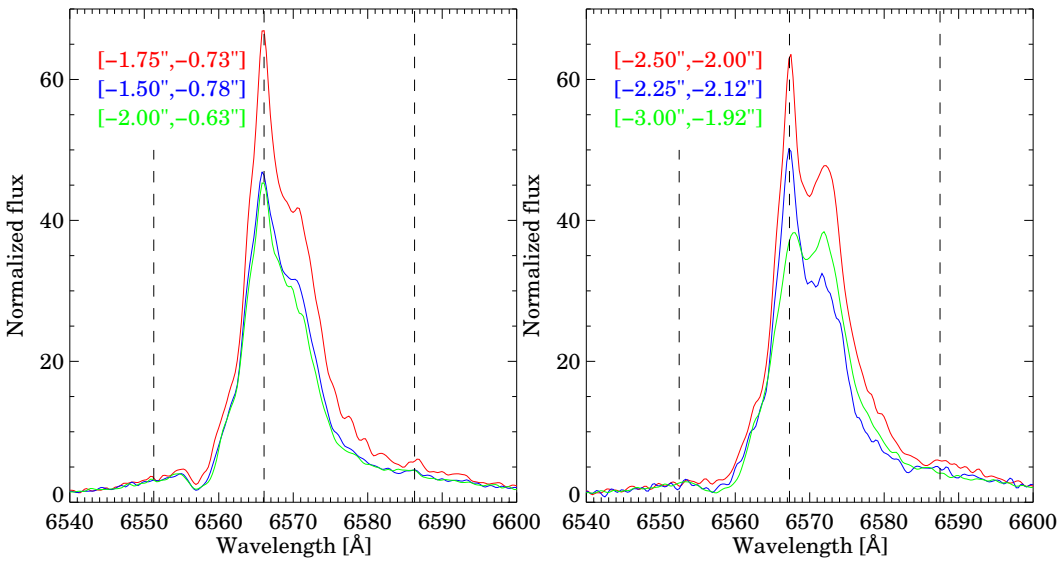

Figure 5.49: Illustration of Hα profiles at the "EW sword" (red) and nearby regions (blue and green). The dashed lines indicate the locations of [N II] 6548 Å, Hα 6562.8 Å and [N II] 6584 Å lines with a systematic velocity shift of 150 km s^{-1} (left panel) and 205 km s^{-1} (right panel) to the rest wavelength of Hα.

region and nearby regions. The normalized "sword" Hα profiles have a much greater EW than those nearby, and exhibit a strong narrow component, which is probably not coming from the primary of η Carinae. In Fig. 5.49, we also show the positions of [N II] 6548 Å, Hα 6562.8 Å, and [N II] 6584 Å with a systematic velocity shift of 150 km s^{-1} (left panel) and 205 km s^{-1}(right panel). The systematic velocities are chosen so that the Hα 6562.8 Å line is aligned with the peak of the narrow component. While there is no indication of the nitrogen doublet for lobe spectra close to the "sword" region, [N II] 6584 Å can be clearly inferred in the "sword" spectra. [N II] 6548 Å is too weak to be seen. This feature is further confirmed by the 2002 data set (Fig. 5.47(f)).

Interestingly, the EW "sword" is correlated with the continuum intensity. In Fig. 5.50, we illustrate the images of Hα emission at various wavelengths. A careful examination of these images reveals that the fluxes of the "sword" region at wavelengths of 6525 Å, 6553 Å, 6609 Å,

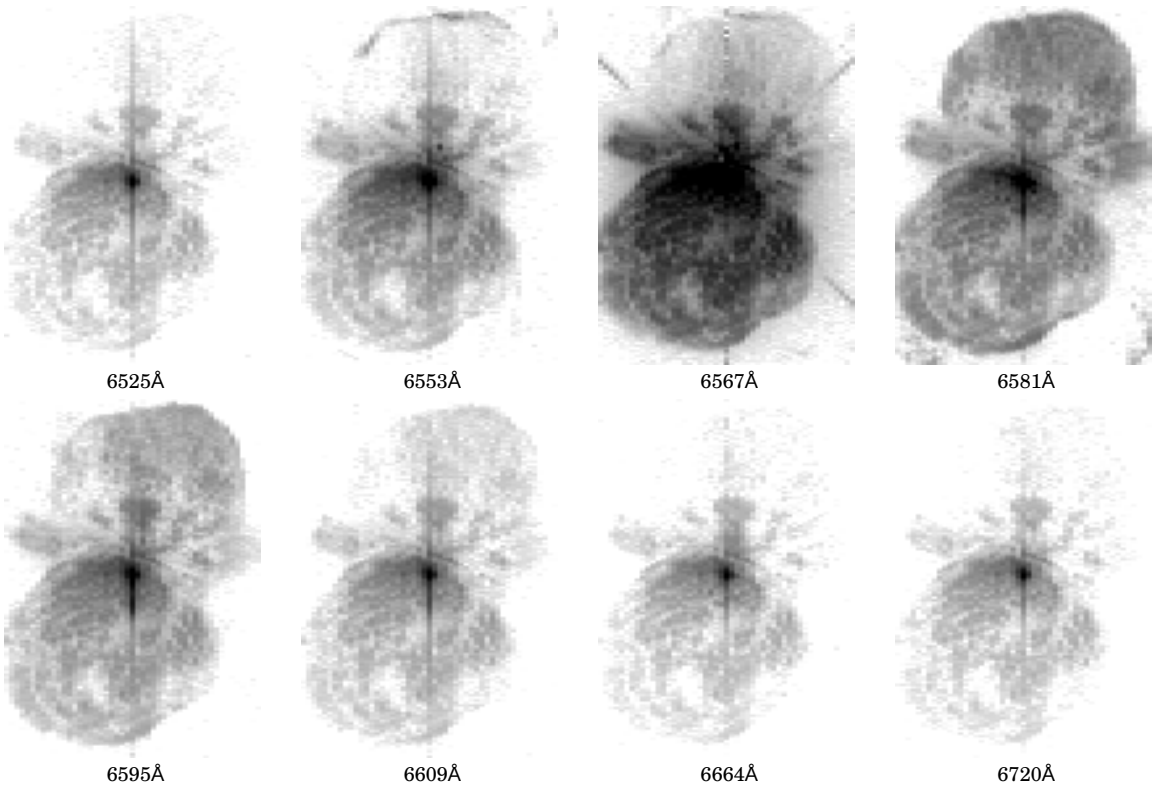

Figure 5.50: Illustration of Hα emission images at various wavelengths. The central stripe is due to CCD bleeding effect mentioned previously. Diffraction spikes can also be seen in some of images. The "hole" and the "paddle" are discernible in the images. Note that the fluxes in the EW "sword" region are slightly smaller than its surroundings in the images with wavelengths of 6525 Å, 6553 Å, 6609 Å, 6664 Å, and 6720 Å.

6664 Å, and 6720 Å are slightly smaller than nearby regions. Further discussion is made in § 5.4.8. We have also examined the Hβ data that cover about 1/3 of the Homunculus, including part of the EW "sword" region. Although some pixels have low signal-to-noise ratios, the Hβ EW map generally shows greater EWs in the "sword" region.

5.4.7 The pixel-to-pixel variation

Suppose Hα originates in the stellar wind, then the emission would come from a region $< 0.1''$, which is substantially smaller than the location of the dust scattering region ($\sim 4''$ to $8''$). At this distance the star is almost a point source, and hence we would not expect a sharp changes in the EW on the small scale. However, we find significant changes at scales of $0.25''$ in the EW map. At small separations in the vertical or horizontal direction, the EW can change by as much as 40%, well beyond the computed uncertainties. Figure 5.51 illustrates two good examples. In each plot the four normalized profiles are from close positions, but their EWs show substantial differences. In addition to changes in EW, there are changes in profile shape – the green profile in the bottom plot of Figure 5.51 is significantly broader than the other profiles. The lower panel in each plot shows that the normalization is accurate.

In the EW map (Fig. 5.45, left panel), pixel-to-pixel variation is apparently common in the NW lobe. In the SE lobe, variations are less frequent, but still exist. Some variation certainly is due to low signal-to-noise ratio and thus large uncertainty in the determination of the continuum, e.g., the edge of the Homunculus and the left stripe of the NW lobe. Other pixel-to-pixel variations between pixels with good signal-to-noise ratio, especially those in the SE lobe, are not so easily explained, and are discussed in §5.4.8.2.

5.4.8 Interpretation of the EW map

5.4.8.1 The NW lobe One of our concerns is the three stripes in the NW lobe of the EW map. As noted earlier, variations in the SE lobe are confirmed by observations taken at different epochs, and with different slit position angles. This lends support to the reality of the observations in the NW lobe, but does not provide proof. As the fluxes are substantially lower in the NW lobe than in the SE lobe, any uncertainty in background correction, or any contribution by instrumental scattered light, will have a larger effect on the EWs in the NW lobe. However, the dissimilarity between profiles from the central and the right stripes (see Fig. 5.46) suggests that explanations, other than a data reduction issue, are needed.

We propose four possibilities to explain the variation in the NW lobe.

1. The narrow "nebular" absorption component is spatially variable, leading to variations

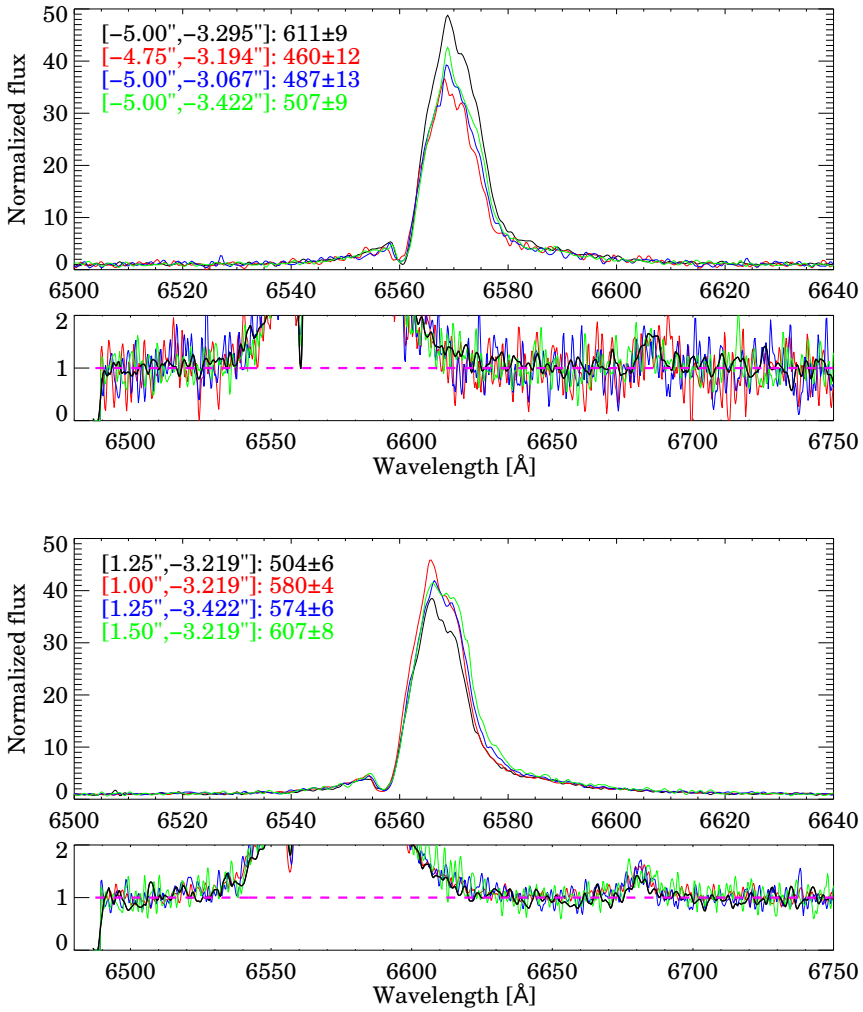

Figure 5.51: Top two panels: illustration of pixel-to-pixel variation – four nearby continuum-normalized profiles are plotted with the spatial coordinates indicated in the square bracket and the EW and uncertainty indicated after the colon. The subpanel focuses on the normalization of the four profiles. Bottom pair of panels: same as upper panel but shows another example of small scale variations. A careful study of the plots at higher resolutions show that the profiles also differ in shape. For example, in the lower panel the green profile is significantly broader on the long wavelength side than the black profile. Such a variation cannot be due to an error in the normalization of the continuum.

in the EWs. Some of the variation in EW also occurs because the "nebular" absorption occurs at different wavelengths in the scattered Hα profile. P Cygni absorption is generally not seen in the NW lobe spectra. Note that the skirt material in the "paddle" region is ionized, but the rest of the skirt is at least partly neutral. Likely part of the NW lobe is also ionized in a similar geometry leading to extensive narrow absorption that the radiation must pass through.

2. The primary wind is asymmetric. We see a combination of light emanating from two directions and being scattered by two (or more) dust regions into our line of sight. The variations in EW would then arise from variations in the relative contributions of these components.
3. In the central stripe we see more continuum light, perhaps emanating from the companion star. This could occur if the dust is clumpy and variable on relatively small spatial scale. Depending on the sight line, the relative extinctions towards the primary and secondary stars could be different. Observationally, we know that the dust extinction varies on a scale of $0.1''$ [e.g., 50] – the central source suffers much more extinction than does the Weigelt blobs [167, 80].
4. Similar to (iii), but the dust does not occult the primary star and its wind uniformly. Such an effect could explain, for example, why the EW of Hα on the central star is much larger than elsewhere in the Homunculus.

The double-peak feature (see Fig. 5.43 at +50 and +300 km s^{-1}) in the NW lobe is caused by an absorption component rather than two emission components. There are two reasons for reaching this conclusion. First, the total width of the "two components" is similar to the width of Hα in other regions. Second, the possibility that the red component is [N II] 6548 Å can be ruled out by the absence of [N II] 6583 Å, since the ratio of the strengths of the two lines is roughly $R = I_{6583}/I_{6548} = 3$. Such a strong absorption component seen in and around the "paddle" can potentially change the EW. Interestingly, we also find an association of the absorption with the wind inappropriate. As apparent from Fig. 5.52, where we compare the Hα profiles in the NW to that of the star, the absorption (seen in both profiles at $\sim$-50 km s^{-1}) is not associated with the wind (the "nebular" absorption at $\sim$-320 km s^{-1} in the solid profile). Associating the absorption with the Little Homunculus also seems impossible

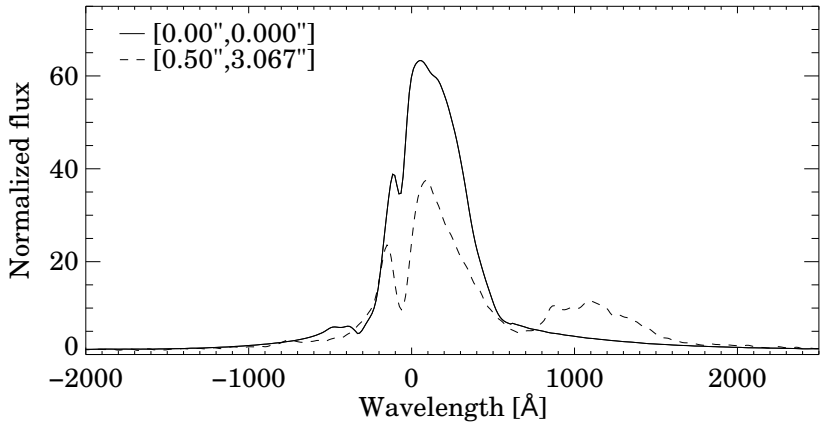

Figure 5.52: Comparison of a Hα profile in the NW lobe (dashed profile; coordinates indicated in the square brackets) with that of the central source (solid profile). The continua have been rectified to unity, and the two profiles have been shifted so that they are aligned. The Hα profile of the central source is much stronger that that of the lobe. The later shows strong "nebular" absorption.

– such absorption is absent in the SE lobe, where the Little Homunculus is also evident (see Fig. 3 in Smith 337).

Johansson et al. [194] attributed this absorption to metastable hydrogen, $2s^2S$, located in extended low-density ejecta. Since the ejection is not isotropic, it is not surprising that we only see this absorption in a particular region.

At low latitudes where the absorption component is strong, possibility (i) is the most likely reason for the observed EW variations. However, at high latitudes where we saw two distinct stripes, the absorption component is weak or absent. Other factors must also play a role.

5.4.8.2 The SE lobe To see more clearly the latitude dependence of EW in the SE lobe, we plot an axisymmetric model over the EW map in this lobe (see Fig. 5.53) using the 2D geometry in Smith [337]. The 3D model is rotated and tilted to the right angle according to Davidson et al. [82]. The ejecta are obviously not rigorously axisymmetric, but

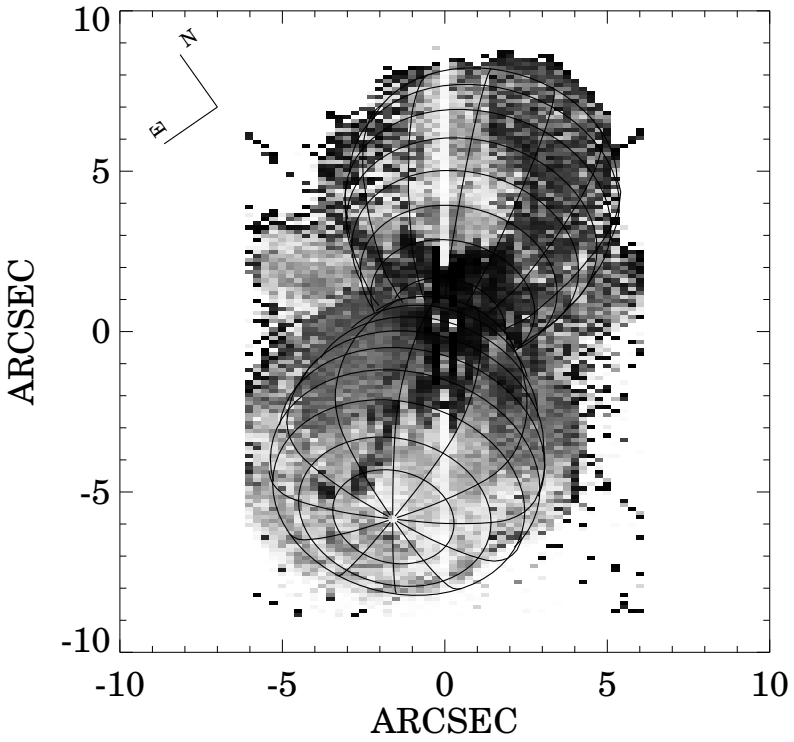

Figure 5.53: The EW map overlapped by a 3D axisymmetric model using the geometry of the Homunculus obtained by [337]. The model is tilted 41° according to the results in Davidson et al. [82]. It is also rotated 13° clockwise to align with the polar axis of the Homunculus. Obviously, the SE lobe is not perfectly axisymmetric.

the comparison provides useful information about what degree of axial symmetry.

At low latitudes, there are two elliptical structures with enhanced EWs on both sides of the central source. These structures look like an extension of the "butterfly" nebula resolved in the near-IR using the Very Large Telescope (VLT) adaptive optics system [50]. This is a complex dusty structure with spatial extensions of about 2″. Smith [337] suggested that the "butterfly" structure is part of the equatorial torus that has been disrupted by the stellar wind, while Artigau et al. [12] argued that the "butterfly" structure is some clumps and filaments ejected at different epochs rather than a coherent physical structure or equatorial torus. The spatial similarity between the "butterfly" nebula and the enhanced EWs regions

may indicate a relationship between the EW and the dust. Dust extinction at small scales can block the continuum but not the Hα emission that originates at larger scales, leading to EW variations associated with the small scale dust.

The consistent results between the Hα and Hβ data indicate that the EW "sword" is a real effect rather than a background subtraction problem. The inference of a strong narrow Hα component from the the corresponding [N II] 6584 Å line in the "sword" spectra (see Fig. 5.49) and its relative constant shift to the Hα profile indicate it is likely a reflected component from the Weigelt blobs. In fact, a similar narrow component is also seen in other profiles (see the green and blue profiles in Fig. 5.49), but not as strong as the one in the "sword" profile. The correlation between the "sword" region and slightly lower fluxes probably indicate more dust extinction in these directions, leading to a larger fractional contribution of the narrow component and hence a greater EW.

5.4.8.3 Pixel-to-pixel variations Pixel-to-pixel variations were carefully confirmed. This is done in several ways. Uncertainties in the EW are within 5%, while the variations can be up to 40%. A smoothing process was accomplished by averaging the EWs of ten pixels, but it did not eliminate the variations or reduce them to acceptable levels. We also used several other regions to normalize the profiles, but pixel-to-pixel variations are still found. Several possibilities can be suggested:

1. The wind is asymmetric and emits Hα with different EWs in different directions. Theoretically, all the EWs should be at least a combination of two velocity-shifted components – one reflected by the front side of the Homunculus, and the other by the rear side. The combined EWs will be a value between the two components depending on the fractional contribution. For two nearby pixels, if the front component and the back component have substantially different EWs and they also have very different contributions to the two profiles, then the EWs of these two pixels will display a considerable difference. This can happen if the dust density changes on small scales, which is seen in the WFPC2 image (Fig. 5.42).
2. Variations of the light contributed by the companion can also be crucial, if the dust is distributed irregularly. In directions not blocked by dust, more light may be contributed

by the secondary star.

3. Small scale structures between the photosphere and the Hα forming region would block the continuum but not the Hα emission. Although Hα originates far from the stellar photosphere, Hα EW strongly depends on the continuum coming from the star. Wind clumping has been widely accepted, and this would provide very different opacities for the continua in different directions. Dust could also induce differences in the continuum in different directions.

As mentioned previously, possibility (i) may account for the situation in the NW lobe, because the strength of the absorption, and its location relative to the Hα-emitting region vary across the lobe. However, pixel-to-pixel variations are seen in the SE lobe, where the rear component cannot be easily discerned. Further, an argument against this is that variations in the contributions of the front and rear scattering surfaces should cause changes in polarization. Surprisingly, the polarization structure in the SE lobe is remarkably smooth [329, 203]. Dust at small scales has been exhaustively studied and found to have complex structure [e.g., 167, 50]. Differences both in the continuum and in the profile shape may be caused by a high concentration of inhomogeneous dust.

5.5 ABSORPTION CONSTRAINTS ON THE WIND STRUCTURE

5.5.1 P Cygni absorption in the SE lobe

The issue whether the wind of η Carinae is latitude-dependent is still under debate [344, 321, 140]. We explore this problem by looking at the P Cygni absorption in the SE lobe. The P Cygni absorption is directly caused by material in line of sight, thus quantifying the P Cygni absorption is (potentially) a more direct way to constrain the wind geometry. However, measurement of the P Cygni absorption across the Homunculus requires a precise procedure to fit the profile, which is not trivial. There are several reasons for this – Hα absorption subtracting from the Hα emission profile is not small, the absorption is located adjacent to the rapidly rising emission profile, and the absorption is seen against the blue

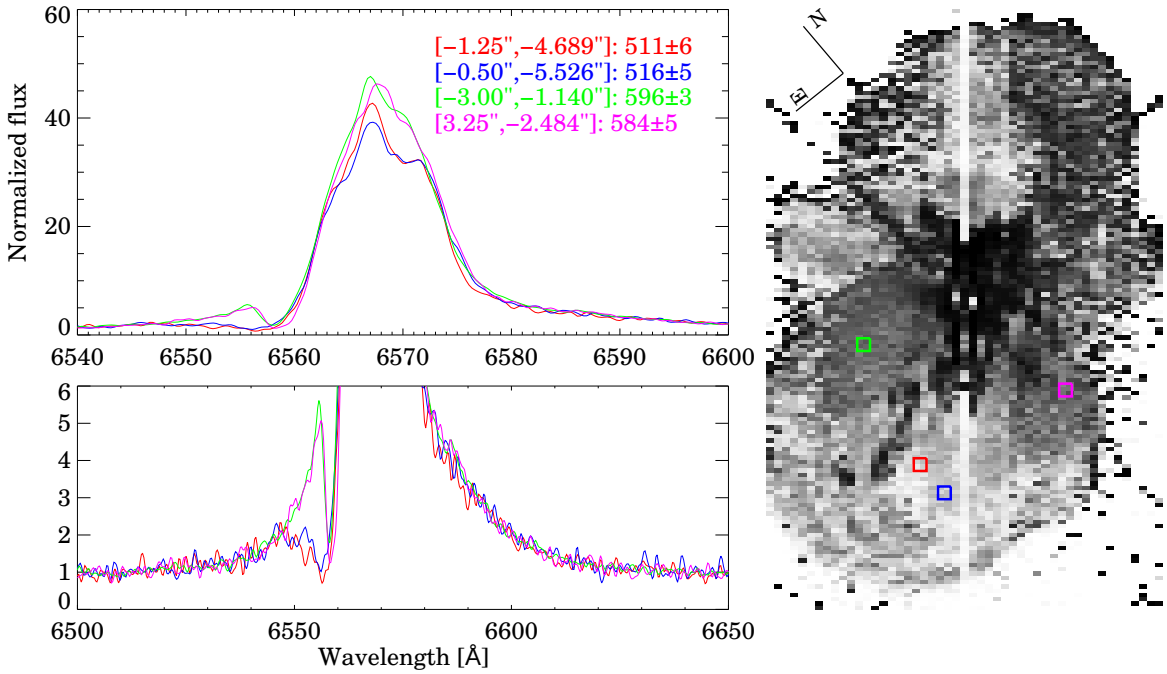

Figure 5.54: Comparison of Hα line profiles from four spatially distinct locations in the SE lobe. The four profiles have been normalized to unity continuum and shifted in wavelength to allow convenient comparison. The bottom left panel shows the same profiles as the upper left panel, but focuses on the absorption component. The right panel indicates the positions of the four profiles with corresponding colors. Note the striking similarity in the absorption component for the 45° pair (red and blue), and for the polar pair (green and magenta).

electron scattering wing.

We first explore the issue of a latitude-dependent wind by looking at the P Cygni absorption in the SE lobe, and find that the absorption is circularly symmetric with latitudinal dependence. In Fig. 5.54, we show four selected profiles, two at low latitudes and the other two at high latitudes. Differences in the absorption component between low and high latitudes are evident, while considerable similarity is seen between profiles at roughly the same latitude.

Smith et al. [344] used profiles along a single slit position to argue that the terminal

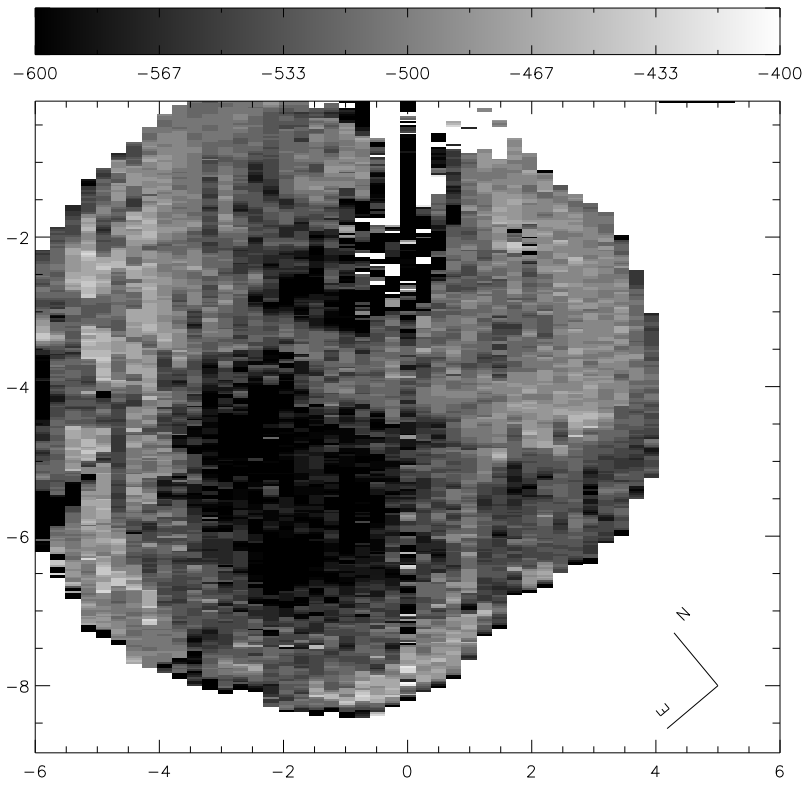

Figure 5.55: A map of velocity at the minimum of the absorption component with respect to the centroid of the Hα profile in the SE lobe.

velocity of wind is latitude-dependent. Here, we use the velocity at the minimum of the absorption (V_{min}) rather than the terminal velocity[1] to constrain the wind geometry. The reason why we use this velocity is that the terminal velocity is hard to determine at high latitude, which can be seen in Fig. 5.54. The zero velocity is defined at the centroid of the Hα profile, not at the rest wavelength of Hα. This definition is useful in the way that it is less affected by Doppler shift due to scattering, the determination of which requires the knowledge of the geometry and the expansion velocity of the Homunculus. The result of the measured V_{min} is shown in Fig. 5.55. The circular symmetry in V_{min} is striking. At least to the first order, the absorption in the SE lobe is axially symmetric and latitude-dependent.

[1]Terminal velocity is defined here as the maximum blueward extent of the P Cygni absorption. In the observations of Smith et al. [344] absorption extending out to -1000 km s^{-1} is detected in Hα.

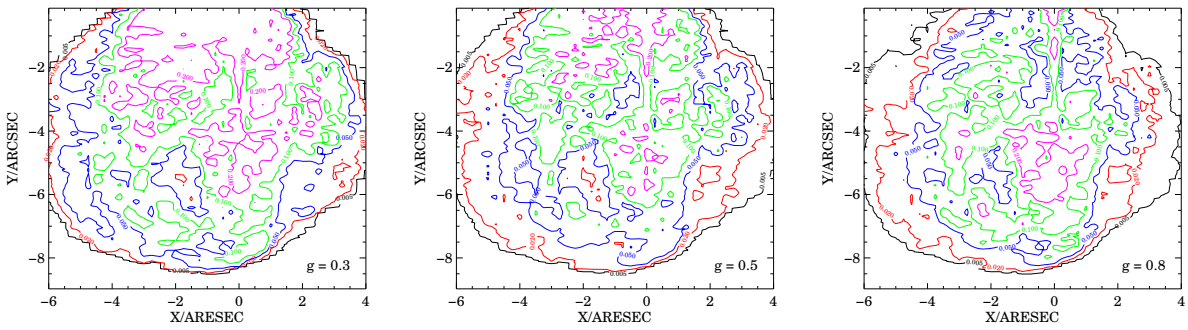

Figure 5.56: Illustration of optical depth maps of SE lobe with g of 0.3 (left), 0.5 (middle) and 0.8 (right) in the phase function. The color contours correspond to levels of 0.005 (black), 0.02 (red), 0.05 (blue), 0.1 (green), and 0.2 (magenta).

5.5.2 Abnormality of the P Cygni absorption

The unusual nature of the P Cygni Balmer absorption in spectra of the primary star was stressed by Hillier et al. [172]. They pointed out that the P Cygni absorptions of Balmer lines are much weaker than the extreme P Cygni star HDE 316285, although the emission spectrum of the primary closely resembles that of HDE 316285. Synthetic spectra of LBVs show that the absorption components of Hα and Hβ generally have a minimum intensity much less than that of the adjacent continuum (Fig. 5.57).

As discovered in our previous investigations of η Carinae, P Cygni, and HDE 316285 two distinct wind solutions exist [170, 172, 283]. In one case the neutral hydrogen fraction is of order 10^{-6} throughout the wind, and strong P Cygni absorption components are not seen. In the second case, the neutral hydrogen fraction increases with distance from the star (because ionizations from the $n = 2$ state are becoming less efficient). Only in this case do we observe the strong P Cygni profiles associated with the Balmer lines. Moreover, only in this case (if the wind is dense enough) do we get strong permitted Fe II emission. The transitions between the two solutions is often sudden, occurring (for example) with relatively small changes in the stellar luminosity (few percent).

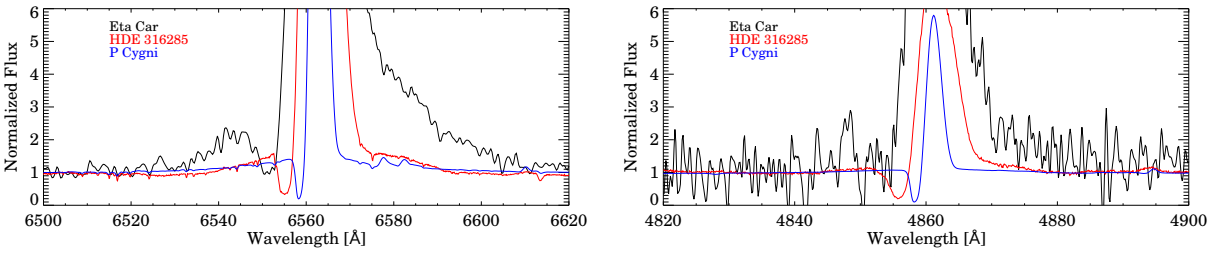

Figure 5.57: Top: Comparison of a Hα profile in SW lobe (black) with those of the P Cyngi stars HDE 316285 (red) and P Cygni (blue). Notice how shallow the absorption component of Eta Car is compared with that of the other 2 stars. Bottom: same as top panel, but shows the comparison of Hβ profiles.

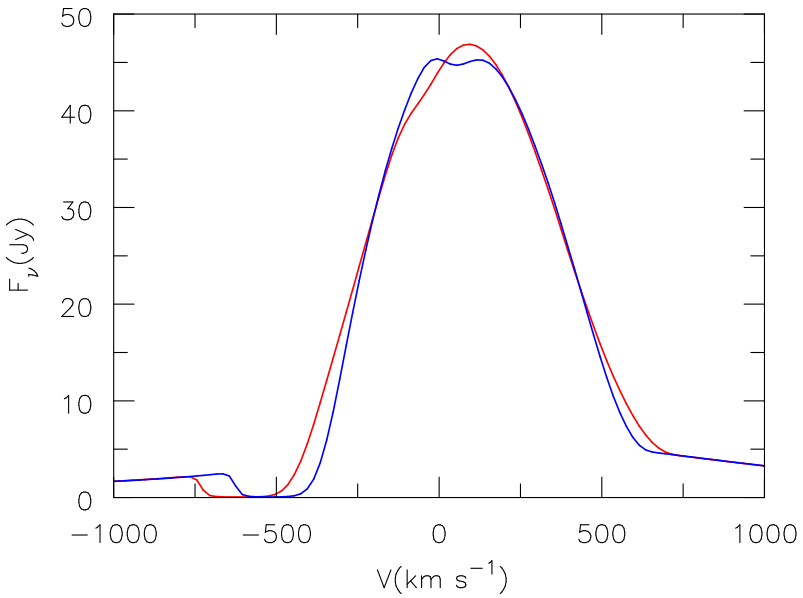

Figure 5.58: 2D radiative transfer simulation of Hα profile from pole-on (red) and 45 degree (blue) views based on scaled 1D models. The velocity is assumed to scale like $1 + 0.3\cos^4\theta$. At 90 degree, $V_\infty = 650$, while at 45 degree, $V_\infty = \sim 540\,\mathrm{km\,s^{-1}}$.

Smith et al. [344] showed that the absorption components vary significantly in strength across the SE lobe. More specifically, the strength and extent of the absorption component varies with latitude, which is seen in Fig. 5.54. Further, the circular symmetry in the V_{min} map also indicates a latitude-dependent absorption component. Surprisingly, despite dramatic variations in the strength and width of the absorption component, the line widths (e.g., at FWHM) of the Hα emissions are almost identical. This is surprising since a latitude-dependent wind would also predict the line-width of Hα to vary with latitude. In Figure 5.58, we show a comparison of 2D radiative transfer simulation of Hα profiles from pole-on and 45 degree views. The 2D model is based on scaled 1D models with the velocity being assumed to scale as $1 + 0.3\cos^4\theta$. At 90 degree, $V_\infty = 650$, while at 45 degree, $V_\infty =\sim 540\,\mathrm{km\,s^{-1}}$. One obvious difference between these two profiles is the width of the emission component. If we see high velocity absorption coming from the wind, we should, in the simplest scenario, also expect to see broader emission. While a variation in V_∞ of 100 to 200 $\mathrm{km\,s^{-1}}$ cannot be ruled out by the observations, its is difficult to reconcile polar wind velocities of $1000\,\mathrm{km\,s^{-1}}$ (as suggested by Smith et al. [344]) with the observed emission line widths. Another difficulty, is that P Cygni absorption associated with Hα is not readily identified in the NW lobe [§5.4.8.1; 167].

The "large" intensity at V_{min} and the constant width of Hα emission indicate a serious problem in our understanding of the absorption component. We propose two possibilities to explain these.

1. The absorption component is influenced by the companion. The companion star changes the ionization structure of the primary wind and hence alters the P Cygni absorption component.

2. The absorption is not due to the wind but to high velocity neutral hydrogen gas between the central source and the dust of the Homunculus. This scenario still requires that the companion influences the primary wind. However, it provides a very simple explanation of why the velocity of the absorption (and the V_∞ measured by Hillier et al. [172]) is correlated with the Homunculus velocity field. Smith et al. [344] argued against non-wind absorption on the basis that it is variable. The density and velocity structure of gas interior to the Homunculus would depend on the mass-loss history of η Carinae since the great eruption.

With the first scenario it is difficult to explain the apparent axial symmetry exhibited by V_{min}. Moreover, the absorption component should be sensitive to the orbital position of the companion. The comparison between the 2000 and 2002 data sets (Fig. 5.47), shows no significant change in the emission components, and only minor changes in the absorption components for some of the profiles. These are probably real, but the significance is difficult to judge because the positions are not perfectly matched. The temporal comparisons Smith et al. [344] do show some variation in the high velocity wings, although again the emission components show no large scale change.

Previous studies evaluated a semimajor axis of ~ 15 AU [65, 294] for the orbit, but more than half of the Hα flux originate beyond 15 AU in the Hillier et al. [172] model. However, the consistency in the Hα profile in the two data sets taken at orbital phases 0.45 and 0.9 is not surprising, since the orbit is highly elliptical (e>0.9).

Recently, Groh et al. [142] carried out a 2-D radiative transfer studied on the UV and optical spectra, with consideration of the wind-wind collision (WWC) cavity. They were able to reproduce the weak absorption component of Hα during apastron, because of lower column density and optical depth in line of sight induced by the cavity. Their results showed that the absorption component not only varies with latitude, but also varies with azimuthal angles due to the presence of the cavity. However, Smith et al. [344] showed that the latitudinal dependence only applies to phases near apastron and is not applicable to a broad range of phases across periastron, which they interpreted as evidence for a shell ejection near periastron. It would be interesting to compare the latitudinal dependence of the absorption component between 2-D radiative transfer models and the observations near the periastron. Groh et al. [142] also found that the absorption component of η Carinae shows azimuthal variations. However, the longitudinal dependence is not seen in the reflection profile at higher latitudes, for example, the green and magenta profiles in Fig. 5.54. This could be possible if the wind-wind collision cavity is so small that the line of sight at higher latitudes does not pass through it. This could also explain why the Hα absorption components between phases 0.45 and 0.9 are almost identical in Fig. 5.47.

The second suggestion also has difficulties in providing a viable explanation. Absorption due to the Little Homunculus has been suggested [e.g., 321] but its velocity ($\sim$150 km s^{-1}) is

too low to explain the "P Cygni" absorption associated with Hα. Smith and Ferland [340] modeled the Homunculus as a double shell structure, aiming to reproduce the survival and the thickness of molecular hydrogen shell observed in Smith [337]. They found an inner atomic shell exists inside the H_2 shell. This could potentially account for the observed absorption, and would naturally explain the observed axial-symmetry. However, such a model predicts that the absorption associated with Hα should be much stronger than the absorption associated with Hβ (assuming an ISM like scenario, and since the oscillator strength of Hβ is 1/6 of that of Hα). A comparison of Hβ and Hα absorption is shown in Fig. 5 of Smith et al. [344] from which it is apparent that the absorption at Hα is not much stronger than that at Hβ – indeed, at some velocities the absorption on Hβ appears to be stronger. Additional support for the idea that the absorption originates from the neutral, or atomic, shell comes from the observation by Mehner et al. [263], who suggested stronger absorption relative to emission in Hδ than in Hα inferred at phases 0.83 and 0.96. The higher velocity absorption (extending to 1000 $\mathrm{km\,s^{-1}}$) might be related to high velocity absorption seen on UV lines just before periastron [141], and which is thought to arise in the wind interaction regions.

However, much evidence favors a companion-associated absorption. Richardson et al. [321] discussed the Hα variations during the 2009.0 spectroscopic event, arguing that the strength of Hα and the development of the P Cygni absorption around the periastron agreed qualitatively with the wind-wind collision in a binary model. They also suggested that the broad Hα absorption during the 2009.0 spectroscopic event, also seen from the polar view in Smith et al. [344], is due to less obscuration of the primary's wind by the companion. Nielsen et al. [285] presented the variation of H I λ4103 (Hδ) during the 2003.5 minimum. Their results showed that the absorption component disappeared for a short period before the minimum – consistent with the idea that the absorption component is related to the companion.

Last but not least, Mehner et al. [263] showed that the behaviors of He II λ4687 EW and radial velocity between direct and polar views in the 2009 event were quite similar. These results contradict the association of helium line velocities with the orbital motion. Rather, the observations indicate that ionization changes, and changes in the bow shock structure

may also be playing an important role.

5.6 OPTICAL DEPTH OF THE HOMUNCULUS

As is well known, the Homunculus is primarily a reflection nebula [e.g. 366, 367, 388]. However, the optical depth of the Homunculus has been a subject of debate [e.g. 78, 277, 329, 340] – is it optically thin or optically thick? This is relevant in the present discussion since the optical depth affects the visibility of different structures in the Homunculus which potentially influence observed line profiles.

Undoubtedly, the Homunculus shows wide variation in optical depth. Some sight lines clearly have larger optical depth than others [277]. However, using simplified and approximate optical depth models to understand the Homunculus have been of great interest [78, 167, 277, 329, 340]. Here we start with the optically thin assumption and investigate the results with the aid of various observations.

Assuming an optically thin pure scattering Homunculus nebula, the relation between the observed flux and the optical depth (due to pure scattering) is given by

$$F_{\rm obs} = \tau \frac{F_\star R_\star^2}{4\pi r^2} \frac{dA}{d^2 \cos\theta} p(\theta) 10^{(-\frac{A_\alpha}{2.5})} \tag{5.3}$$

where $F_{\rm obs}$, $F_\star$ are the observed and surface flux of η_A, $R_\star$ is the stellar radius, r is the distance from the central source to the dust of the Homunculus, dA is an area element of the Homunculus covered by a pixel, τ is the optical depth for the elemental area, θ is the angle between the line from the central star to the elemental area and line of sight, $p(\theta)$ is the phase function for scattering and A_α is the extinction (near H_α) towards the Homunculus as seen from the earth. For simplicity, zero extinction from the central source to the dust of the Homunculus is adopted.

The interstellar color excess derived from the depth of the 2200 Å band is E(B-V) = $\sim$ 0.4 [387]. We adopt an average value of 4 from estimates of selective extinction R_V [350, 363, 368]. The extinction at R-band is then roughly $\Delta m = 1.2$. We adopt $F_\star$ from the Hillier et al.

[172] model and the Homunculus shape in Smith [337] for computing r and θ. For simplicity, we also adopt the Henyey-Greenstein phase function, which is

$$p(\theta) = \frac{1 - g^2}{[1 + g^2 - 2g\cos(\theta)]^{3/2}} \tag{5.4}$$

where g is a parameter that ranges from -1 to 1. When $g = 0$ the scattering is isotropic, when $g > 0$ forward scattering is dominant, while for $g < 0$ backscattering is dominant. The elemental area dA is computed by

$$dA = (d\,d\alpha)(d\,d\beta) \tag{5.5}$$

where $d\alpha$ and $d\beta$ are the width and length of a pixel in arcsec, which gives rise to a conversion factor $d\alpha d\beta = 0.0253506 \times 0.1 = 0.00253506$.

Fig. 5.56 illustrates our results of optical depth calculation for three different g values. As to be expected, the estimated optical depths across the Homunculus are smaller than unity, and typically less than 0.2. For the nearly isotropic case ($g = 0.3$), the scattering angle is largely irrelevant, which means that stronger flux near the star is caused by more scatterers. In the more realistic case ($g = 0.8$), the optical depth becomes more circularly symmetric about the hole. In this case the brightening seen in the NW of the SE lobe arises purely from the forward scattering properties of the dust, rather than a density effect. The same phenomena also explains why the NW lobe is fainter than the south. A simple optically thick scattering layer does not produce the observed intensity across the SE lobe.

With this simple scenario, the SE hole represents a region where there is a paucity of dust. Smith et al. [343] argued that the coincidence between the near- and mid-IR dark feature and the optical "hole" indicated a paucity of dust at the "hole". Note that this is not the only explanation – a different illuminating intensity would also cause the hole to appear darker at both infrared and optical wavelengths.

The optical depth of the Homunculus has been discussed previously. Davidson and Ruiz [78] estimated the optical depth of the dusty shell to be $\tau \approx 3$ - 4, but they used a simple isotropic-scattering model, and the analysis was based on primitive (by today's standards) observations. A characteristic of the high quality HST images of the Homunculus is the

"blister" like appearance which is very prevalent in optical and UV images, and becomes less evident at longer wavelengths [277]. In the 1042M filter ($\lambda_c \sim 10183\,\text{Å}$) the contrast ranges from 20% to 80%, whereas the dark lanes in the F336W filter attenuate between 30% to 100% of the light. Using the contrast seen in images taken in the F336 filter, Morse et al. [277] estimated the optical depth covered the range from 0.2 to 10. In the V band, the images suggest that the visual extinction in some regions is as high as 3 magnitudes.

The above calculations assume no attenuation along the line of sight to the Homunculus, and imply that the dust density along different sight lines varies by at least a factor of 20. An alternative explanation is to assume that much of the observed intensity variation arises in variations in dust extinction along the line of sight to the Homunculus. This would also provide a simple explanation for the decreasing contrast at longer wavelengths. Since the extinction drops towards longer wavelengths the illuminating flux would become more uniform.

There are several other lines of evidence that argue that the optical depth through the Homunculus is not large. These include polarization observations, the low extinction to the Weigelt blobs and the Little Homunculus, and the visibility of broad forbidden [Fe II] in ground spectra of the central regions ($\sim 1''$) of the Homunculus.

Polarization studies show that the Homunculus is highly polarized reaching values in excess of 30% in the NW lobe and over 20% in the SE lobe [395, 261, 329, 203]. Most polarization models for the Homunculus assume an optically thin shell and ignore multiple scattering [45, 261, 329]. The polarization study of Schulte-Ladbeck et al. [329] showed "single shell" optically thick models are unable to reproduce the observed polarization – their results favored an optically thin model. Further, the observed Hα polarization profiles indicated the presence of back reflected component (e.g. in the SE), although the presence of two scattering structures is not easily recognized in the Hα profile [329]. This presence of both reflection components is difficult to explain in an opaque Homunculus.

Double shell models, in which the outer shell is primarily absorbing, might be able to tolerate higher optical depths. The inner shell would produce the polarization, and the outer shell would simply act to reduce the intensity. The absorption cannot be too large, since we observe roughly 10% of the stellar intensity in the V band originating from the Homunculus.

King et al. [203] found there was no correlation between the surface brightness and the polarization. They attribute the low intensity of the "hole" to an inhomogeneous absorbing material located between us and the scatterers. This model might be consistent with that of Smith and Ferland [340] in which an outer molecular shell of H_2 surrounds a smaller ionized shell (see below). In order to get a match between the similar optical and IR polarizations, the size distribution of scatterers must be finely tuned [203].

Davidson et al. [80] estimated the visual extinction to the central source as 6.1±0.6 while Hillier et al. [172] obtained a value of 7 mag. The extinction law (due to both the ISM and CSM) deduced by Hillier et al. [172] was quite unusual – over the optical band the extinction law could be characterized by a Cardelli et al. [44] law with $R_V = 5$, E(B-V)= 1.0, and 2 magnitudes of grey extinction.

As noted by Hillier and Allen [167], the extinction suffered by the central source is much larger than that suffered by the narrow line emitting region now known the be the Weigelt blobs [80]. Verner et al. [386] estimated the visual extinction, A_V, to the Weigelt blobs as $\sim$0.5 (assuming $R_V = 3.1$). Their estimate ignored gray extinction and is in rough agreement with a more recent measurement by Mehner et al. [263]. Surprisingly, this extinction is even less than that usually quoted for the ISM extinction towards η Carinae [E(B-V)=0.4, $A_V = 1.2$; 387].

Hillier and Allen [167] showed that ground-based observations display much stronger [Fe II] lines in the core than in the lobes. Moreover, such strong [Fe II] emission is not expected from a classic stellar wind, as evidenced, for example, by spectra of HDE 316285. The presence of strong [Fe II] lines (particularly obvious on the SE side of the primary star) can be explained by occultation – absorption of the continuum emitting region is (much) larger than that of the more extended [Fe II] emitting region [171]. Spectra of these lines taken 0.2 to 0.5 arcseconds SE off the star are broadly consistent with that expected from the wind. Recent observations are consistent with this observation – the broad lines have weakened as the central source has become brighter [75]. It is very difficult to see how these broad [Fe II] lines could be strong in ground based spectra if they suffered the same extinction as the central star – the extinction must be substantially less.

Emission lines arising from the Little Homunculus also seem to require that the Ho-

munculus has a relatively low visual extinction. The observed [Fe II] lines emanating from the Little Homunculus are consistent with an E(B-V) of 0.5 mag [186], very similar to that of the Weigelt blobs. Much larger values would necessitate an unusually high gas temperature [186].

A counter argument to the Homunculus having a relative low optical depth is provided by Smith [337]. Infrared observations show that the outer skin of the Homunculus contains the majority of the mass and is predominantly in the form of H_2. Smith and Ferland [340] calculated the necessary density for molecular hydrogen to survive, and their results indicated a visual extinction of 4.5 to 9 mag. Although smaller grains may help to produce a high degree of polarization [367, 388, 261, 262, 390], the derived temperature requires the grains to be greater than 0.2 μm in radius [340]. In their analysis Smith and Ferland [340] assumed that all Lyman continuum photons have been absorbed by the primary wind, the Homunculus is illuminated by a 20,000 K black body, they ignore the companion, and assume all extinction occurs in the atomic shell ($A_V \sim 1$ mag) and molecular shell ($A_V \sim 3.5$ to 8 mag).

5.7 CONCLUSION

We have used long-slit STIS mapping data to explore the geometry of the primary wind. We compute an EW map of Hα covering the whole Homunculus. Both global and pixel-to-pixel variations are found in the map. Pixel-to-pixel variations are possibly due to different contributions by the rear and front walls of the Homunculus. Global variations show patterns that are much more complicated than that expected from an axisymmetric wind. The interpretations of the global variations in the EW map are summarized below.

1. A three-stripe feature that appears to be aligned with the slit is seen in the EW map. While the variation in the left stripe is due to uncertainty in the normalization, we exclude background subtraction and normalization problems for the central and the right stripes. We propose and discuss various possibilities and find the most probable one is associated with a strong external absorption component, which is anisotropic and probably induced by

metastable hydrogen. Multiple scattering components with different fractional contributions may also be crucial.

2. The EWs in the SE lobe appear to be strongly latitude-dependent, with greater EWs generally seen at lower latitudes and smaller EWs seen at higher latitudes. This may be a consequence of an axisymmetric wind, or may be a consequence of asymmetric dust absorption close to the star. The large EW of Hα measured towards the central star, much larger than that measured elsewhere in the Homunculus, is very difficult to explain with a purely axisymmetric wind. A variation in dust extinction, on very small scales ($< 0.1''$) offers a possible solution.

3. We find a similarity between the structure of the radio emission and the large-EW core region. The large EWs are found to be possibly caused by strong intrinsic emissions ([N II] 6548 Å 6583 Å and Hα). Both the radio emission and the intrinsic emissions can be explained by the penetration of UV photons from the hot companion.

4. A mysterious structure, the EW "sword", with greater EWs has been found in the SE lobe. Both Hα and Hβ data sets indicate a narrow component comes into play. Such narrow emission may simply arise from more dust extinction of the central star and thus a larger fractional contribution of the narrow component, likely due to the Weigelt blobs.

We also computed the velocity at minimum of the absorption component across the SE lobe. The V_{min} map shows a striking circular symmetry, which strongly indicates an axisymmetric absorbing structure in the SE lobe. Previously it was assumed that this absorbing structure represents the primary wind, however there are problems with this interpretation. First, the Hα absorption has a much larger residual intensity than expected based on the absorption seen towards the primary star during the event, and as seen in the classic P Cygni stars P Cygni and HDE 316285. Second, the width of Hα profile does not appear to vary significantly with latitude, despite the inferred variation in the wind's terminal velocity. One way to explain the lack of absorption is that the companion is influencing the ionization structure of the wind, even in the polar region. However, it is difficult to understand why the absorption should be symmetric about the pole if it is caused by the primary wind, whose ionization structure, and perhaps density structure, is modified by the asymmetrically located binary companion. One possibility is that the absorption is not produced by the pri-

mary wind – rather it arises from gas associated with the Homunculus. This explanation would explain why the velocity of the absorption is strongly correlated with the Homunculus velocity field.

A simplified model is used to compute the optical depth of the SE lobe. The results show a general agreement with an optically thin dust shell in the Homunculus. The optical depth map also indicates a circular symmetry across SE lobe and less dust at the "hole". We argue from various evidence, e.g., the observed polarization, the low extinction towards the Weigelt blobs and the Little Homunculus, and the visibility of the ground-based [Fe II] lines, that the optical light received from the Homunculus predominately arises from regions that are optically thin.

During the 2009 event the primary star was seen to undergo large changes [263]. These changes, and those seen from the SE lobe are not easily interpreted. We think that dust extinction, arising close to the star in the primary wind, must be influencing what we observe even with HST. A crucial but unanswered question is what is the location of the dust that occults the central source? If it is located in the Homunculus it is difficult to understand why it is so effective at occulting only the central star and not the Weigelt blobs nor the primary wind on scales of 0.2 to 0.5 arcseconds. Further, if the dust is at large distances, it is difficult to understand the variability timescales [257]. On the other hand, if the dust is relatively close to the primary (perhaps generated in the wind-wind collision, e.g., Falceta-Gonçalves et al. 110, Smith 339), it is potentially easier to explain the small-scale spatial variability of the dust extinction, and the variability time scale. One way to test the influence of dust is to examine the wavelength dependence of changes in the spectrum of the primary star.

The mapping data of the Homunculus have revealed rich information about the central sources and the Homunculus nebula, although many questions remain unanswered. Mapping observations at different orbital phases, as well as directions covering a broader wavelength region with additional diagnostics, will help to constrain the influence of the companion on the primary's wind. New mapping data will also provide independent checks on the variations in the NW lobe and the existence of EW "sword". Polarization measurements with high spatial resolution will answer the question of whether pixel-to-pixel variations in the SE lobe are caused by different contributions from the rear and front sides of the Homunculus.

The Homunculus is ripe for detailed modeling to explain both the optical and near IR intensities, optical and near IR polarization data, and the longer wavelength dust emission. Additional spectropolarimetry observations, similar to those of Meaburn et al. [262] would also be very useful.

6.0 PART IV. FUNDAMENTAL PARAMETERS AND THE EUV FLUX OF ϵ CANIS MAJORIS

6.1 INTRODUCTION

ϵ Canis Majoris (ϵ CMa) is a B2 II star located in an extended region of the Local Bubble, which is an asymmetric cavity due to multiple supernova explosions that happened within the last 10 Myr [254]. This extended region also appears to have an extremely low gas density as in the Local Bubble [402], which provides a rarefied "interstellar tunnel" to ϵ CMa.

The most interesting aspect of ϵ CMa is its EUV ($\lambda \lesssim 700$ Å) flux – ϵ CMa outshines all other sources in this band [380], thanks to the sparse gas along the line of sight. The EUV flux of ϵ CMa is responsible for the ionization state of the Local Cloud, which is a region of warm and diffuse interstellar gas immersed in the Local Bubble with a temperature of $\sim$ 6000 - 7000 K and a density of $n_H = 0.1 - 0.3\,\mathrm{cm}^{-3}$ [222]. The physical parameters of the Local Cloud are key elements needed to understand the local environment we are living in. As ϵ CMa is the brightest stellar EUV source in the sky, measuring and understanding the EUV flux from this object can give support to the direct measurement of the ionization fraction of the Local Cloud, which is otherwise hard to measure using lines of sight due to low density. EUV flux measurement of ϵ Canis Majoris also offers an opportunity to gauge the accuracy of the atmospheric spectral modeling in this band. Model atmosphere codes have been intensively tested and compared with observations at wavelength longward than 912 Å. On the other hand, the EUV flux, which is easily absorbed by dust and interstellar gas due to its large opacity, is hard to detect for distant objects. The discovery that ϵ CMa showed a strong EUV excess [49] has attracted many theorists to explain it by atmosphere models.

It was shown by Cassinelli et al. [49] that the non-LTE plane parallel models of both Kurucz [220] and Hubeny and Lanz [178] fail to reproduce the EUV excess. Najarro et al. [282] studied the EUV excess of ϵ CMa in terms of a sequence of spherical non-LTE models, constructed with an early version of the CMFGEN code developed by Hillier [165, 166]. Their models were relative simple, especially in that they neglected the line-blanketing effects induced by hundreds of thousands of overlapping metal lines, which was later shown to be important in hot stars [169, 258]. Najarro et al. [282] included stellar winds and found that mass loss is crucial for the formation of the hydrogen and helium continua, but their models still underestimated the observed EUV flux. Schaerer and de Koter [324] used their own atmosphere code and also underestimated the EUV flux for ϵ CMa. They found line-broadening induced by turbulence can significantly increase the line-blanketing effect and reduce the EUV flux. Aufdenberg et al. [14] carried out another study using a spherical non-LTE fully line-blanketed model atmosphere, and found that their spherical models produce much stronger EUV fluxes than plane parallel models with the same parameters. Although they were able to reproduce the EUV flux from ϵ CMa, they attributed a discrepancy in the UV band to the uncertainties introduced by the calibration of the absolute flux. However, this discrepancy is larger than that normally associated with the IUE calibration.

Table 6.4 lists some of the previous determinations of $T_{\rm eff}$ and $\log g$ for ϵ CMa. Some of the determinations were made as part of a systematic survey of a large number of stars, while others specifically focused on ϵ CMa.

Table 6.4: Previous parameter determinations for ϵ CMa

$T_{\rm eff}$ (K)	$\log g$ (cgs)	Reference	Method
20,990±760	N/A	Code et al. [60]	1[a]
24,750	3.65	Gies and Lambert [132]	1
21,000±1,500	3.19±0.15	Hoare et al. [175]	1
22,000	3.2	Cassinelli et al. [49]	2[b]
21,750	3.5	Aufdenberg et al. [14]	2
23,000±1,000	3.30±0.15	Morel et al. [275]	1
23,240	N/A	Zorec et al. [420]	1
22,000	3.2	Lefever et al. [228]	1

[a] Part of a systematic survey.

[b] Detailed individual study.

There have been new observations since the last atmosphere modeling focusing on ϵ CMa, e.g., the JHK$_s$ band measurements in 2MASS and UV and optical spectra by HST/STIS. HST/STIS spectra with accurate flux calibrations will provide an independent check to the IUE UV spectra. With the availability of new observations, atomic data, and improved model atmospheres, we regain the interest to reinvestigate the EUV problem in ϵ CMa. We model the spectra of ϵ CMa using the fully non-LTE line-blanketing atmosphere code CMFGEN [169]. In an effort to reproduce its spectral energy distribution (SED), we try to determine the best estimates for the effective temperature ($T_{\rm eff}$), the surface gravity ($\log g$), the mass loss rate ($\dot{M}$), and the reddening (E(B-V)) of ϵ CMa.

6.2 OBSERVATIONAL DATA

Table 6.5 lists the measured properties of ϵ CMa. The angular diameter of ϵ CMa was measured by Hanbury Brown et al. [156] using the Narrabri optical intensity interferometer. The parallax was determined with a new reduction of astrometric data in the HIPPARCOS

mission by van Leeuwen [384]. With this new parallax value, the distance of ϵ CMa is 124 ± 2 pc, about 30% smaller than the value 188 pc given by Bohlin [29]. With the angular diameter and revised distance the radius can be derived to be $10.7 \pm 0.7\, R_{\odot}$. Hubrig et al. [179] estimated a longitudinal (along the line of sight) magnetic field of 200 ± 48 G, while Bagnulo et al. [17] derived a value of 127 ± 60 G. Such a magnetic field may have moderate influences on the line-driven wind outflows[1] [373].

Table 6.5: Stellar parameters for ϵ CMa

Parameter	Value
m_V [a]	1.513
Parallax [b]	8.05 ± 0.14 mas
D [c]	124 ± 2 pc
θ_D [d]	0.80 ± 0.05 mas
N_H [e]	$0.7 - 1.2 \times 10^{18}$ cm^{-2}
$R_{\star}$ [f]	$10.7 \pm 0.7\, R_{\odot}$
Vsin i [g]	25 km s^{-1}

[a] Reed [319].

[b] van Leeuwen [384].

[c] This work.

[d] Hanbury Brown et al. [156].

[e] Code et al. [60].

[f] This work.

[g] Abt et al. [2].

The optical spectra used for the analysis were obtained by the ESO Multi-mode Instrument (EMMI) on the New Technology Telescope (NTT) and were taken by Dietrich Baade in 1996. The data were downloaded from the ESO archive. These are echelle spectra which uti-

[1] The significance of the magnetic field can be characterized by the "wind magnetic confinement parameter" $\eta^{\star} = 0.4 B_{100}^2 R_{12}^2 / \dot{M}_{-6} v_8$, i.e., the ratio between magnetic field energy density and kinetic energy density of the wind, where $B_{100} = B/(100G)$, $R_{12} = R_{\star}/(10^{12}\mathrm{cm})$, $\dot{M}_{-6} = \dot{M}/(10^{-6}\mathrm{M}_{\odot}\,\mathrm{yr}^{-1})$, and $v_8 = v_{\infty}/(10^8 \mathrm{cm}\, s^{-1})$.

lize high orders of diffracted light to obtain high dispersion spectra. The ESO-NTT/EMMI data presented here have a resolving power of $R \sim 28000$ and a coverage of wavelength from 4100-8550 Å. The reduction is performed by fitting a blaze function to the continuum using the MPFIT IDL routine. For orders whose continua are difficult to determine, for instance, the spectral range covering Hα profile, we interpolate the coefficients of the blaze function from the two adjacent orders.

The EUV spectrum, obtained by the Extreme Ultraviolet Explorer (EUVE) by Cassinelli et al. [49] as part of EUVE Guest Investigator Program, covers the spectral range from 70-740 Å with an average spectral resolution of $\lambda/\Delta\lambda \sim 250$. The data have been calibrated to absolute flux and corrected for a neutral hydrogen column density of 1×10^{18} cm^{-2}. The archival UV spectra were taken by the International Ultraviolet Explorer (IUE) and were downloaded from the Mikulski Archive for Space Telescopes (MAST). These UV data were processed by the NEWSIPS software [83], and were also calibrated to absolute flux. The UV photometric data are from the Belgian/UK Ultraviolet Sky Survey Telescope (S2/68) on TD-1 [188]. The U-, B-, and V-band magnitudes are adopted from Reed [319]. Color-corrected IR photometry at 12 μm and 25 μm taken by Infrared Astronomical Satellite (IRAS) is from Cassinelli et al. [49].

The 2MASS All Sky Catalog of Point Sources [71] also covers ϵ CMa, which provided the J,H, and K_s photometry. These data are shown in Table 6.6 with the zero flux of the filters determined by Cohen et al. [61].

Table 6.6: JHK$_s$ photometry of 2MASS All Sky Catalog of Point Sources for ϵ CMa

Filter	Effective wavelength (μm)	Magnitude[a]	Flux (m=0) (erg s^{-1} cm^{-2} Å^{-1})[b]
J	1.235	1.98±0.30	3.129×10^{-10}
H	1.662	2.16±0.29	1.133×10^{-10}
K_s	2.159	2.22±0.31	4.283×10^{-11}

[a] Cutri et al. [71].

[b] Cohen et al. [61].

The New Generation Stellar Library (NGSL) also includes spectroscopic observations for ϵ CMa. NGSL spectra were observed by HST/STIS with three different gratings (G230LB, G430L, and G750L), covering a wavelength range from ∼2000 Å to ∼ 10 000 Å. The accuracy of the flux calibration is 3% [158].

6.3 MODELS

CMFGEN is a fully non-LTE line-blanketing radiative transfer code for modeling hot stars [169]. Since first introduced in calculations of Wolf-Rayet (W-R) stars [165], the code has been significantly updated and includes the following processes: bound-free; bound-bound (including two-photon emission); free-free; dielectronic recombination; electron scattering; Rayleigh scattering by hydrogen; inner-shell ionization by X-rays; collisional ionization/recombination; collisional excitation/de-excitation and charge exchange reactions with H and He. It treats all elements in non-LTE and uses an iterative strategy to solve the radiative transfer equations, statistical and radiative equilibrium equations simultaneously. CMFGEN has been tested extensively in W-R stars, O stars , B stars, A stars, luminous blue variables (LBV) and supernovae (SNe) [30, 173, 256, 85].

The element abundances adopted in our model calculations are listed in Table 6.7. The model atoms utilized are the following: H I, He I, He II, C II, C III, C IV, C V, N II, N III, N IV, N V, O II, O III, O IV, O V, O VI, Ne II, Ne III, Ne IV, Mg II, Si II, Si III, Si IV, Si V, S II, S III, S IV, S V, S VI, Fe II, Fe III, Fe IV, Fe V, and Fe VI. A large amount of levels are included, especially ions of iron. For example, we have 1038 levels for Fe III, 1000 levels for Fe IV, and 1000 levels for Fe V. To reduce the complexity in handling so many levels, the technique of super levels, pioneered by Anderson [6], is adopted in the calculations [169].

In our studies, a large number of models with different combinations of $T_{\rm eff}$, $\log g$, and $\dot{M}$ are computed. We label our models in the following way: a model with $T_{\rm eff} = 21500\,{\rm K}$, $\log g = 3.2$ and $\dot{M} = 2 \times 10^{-9}\,{\rm M_\odot\,yr^{-1}}$ is termed T215g32M2em9. Our grid of model atmospheres covers the temperature range from 20500 to 24000 K, with an increment of 500 K. In the $\log g$ space, the models cover a range from 3.0 to 3.6, with an increment of 0.1. While

Table 6.7: Element abundances used in model calculations

Element	Mass Fraction	$Z/Z_{\rm sun}$	$Z_{\rm sun}$
H	7.027×10^{-1}	1.00	7.01×10^{-1}
He	2.811×10^{-1}	1.00	2.80×10^{-1}
C	2.050×10^{-3}	0.67	3.05×10^{-3}
N	2.100×10^{-3}	1.91	1.10×10^{-3}
O	7.540×10^{-3}	0.79	9.54×10^{-3}
Ne	1.740×10^{-3}	1.00	1.74×10^{-3}
Mg	3.220×10^{-4}	0.50	6.47×10^{-4}
Si	6.990×10^{-4}	1.00	6.99×10^{-4}
S	3.650×10^{-4}	1.00	3.65×10^{-4}
Fe	1.360×10^{-3}	1.00	1.36×10^{-3}

most of the models have a mass loss rate of $1 \times 10^{-9}\,{\rm M}_\odot\,{\rm yr}^{-1}$ and $1 \times 10^{-8}\,{\rm M}_\odot\,{\rm yr}^{-1}$, we also computed several models with other values of the mass loss rate. All models are run with a turbulent velocity of $10\,{\rm km\,s}^{-1}$. Different models do not match the observed optical fluxes exactly. However, since the discrepancies are small, and the models are effectively almost plane-parallel, we can scale the fluxes to match the observations. Revised parameters, such as M, L, $\dot{M}$, can be obtained by simple scaling relations, while $T_{\rm eff}$ and $\log g$ are model invariants.

6.4 RESULTS

6.4.1 Balmer line wings fitting

Balmer line wings are one of the strongest constraints of atmosphere structure. In most of stars, hydrogen is the most abundant element, and hence hydrogen lines are do not suffer

uncertainty issue arising from uncertainties in abundance. In hot stars, the Stark broadening of hydrogen lines is largely determined by the electron density (produced by the ionization of hydrogen), which depends on $\log g$. In this section, we present our fits of model Hα and Hβ wings to the echelle spectra. Despite high resolutions, echelle spectra are not excellent data for Balmer profile fitting, because of the difficulty in determining their continua. However, the concerns are minimized as we performed the reduction procedure carefully and multiple lines are used to check the results. Moreover, our model grids have surface gravity step of 0.1, for which the echelle spectra can still provide useful constraints.

Figure 6.59 and Figure 6.60 show our fittings of Hα and Hβ wings. The observed spectrum is an averaged echelle spectrum from 4 observations. A convolution procedure has been applied to all models to obtain the same instrumental resolution as the observations. In each panel, we show models with different $\log g$ for a fixed temperature. For a higher $T_{\rm eff}$, a larger $\log g$ is required to fit the wings. The best fits for both Hα and Hβ wings are listed in Table 6.8. The slight inconsistency between Hα and Hβ results arises from both the continuum determination of the observations and the influence of mass loss. While Hα wings fitting suffers a greater uncertainty from continuum normalization and is more sensitive to the mass loss rate, Hβ wings fitting generally provides more accurate results. Other Balmer lines are inappropriate for this study due to poor normalization of their continua.

6.4.2 Balmer jump

The Balmer jump at 3646 Åis another interesting diagnostic of conditions in the stellar atmosphere [279, 64]. The magnitude of the Balmer jump depends on the opacities on both sides of the jump, which depends largely on the effective temperature and electron density. High accuracy of the calibrated NGSL spectra provides an ideal opportunity for estimating the effective temperature and the surface gravity.

In Figure 6.61, we illustrate the Balmer jump comparison of the NGSL spectrum and a series of models. The synthetic spectra are all scaled to fit the discontinuity at 3646 Å. It is obvious that models with $T_{\rm eff} = 22000\,{\rm K}$ (top panel) produce too strong Balmer jumps. As the effective temperature increases, the magnitude of the Balmer jump decreases. The

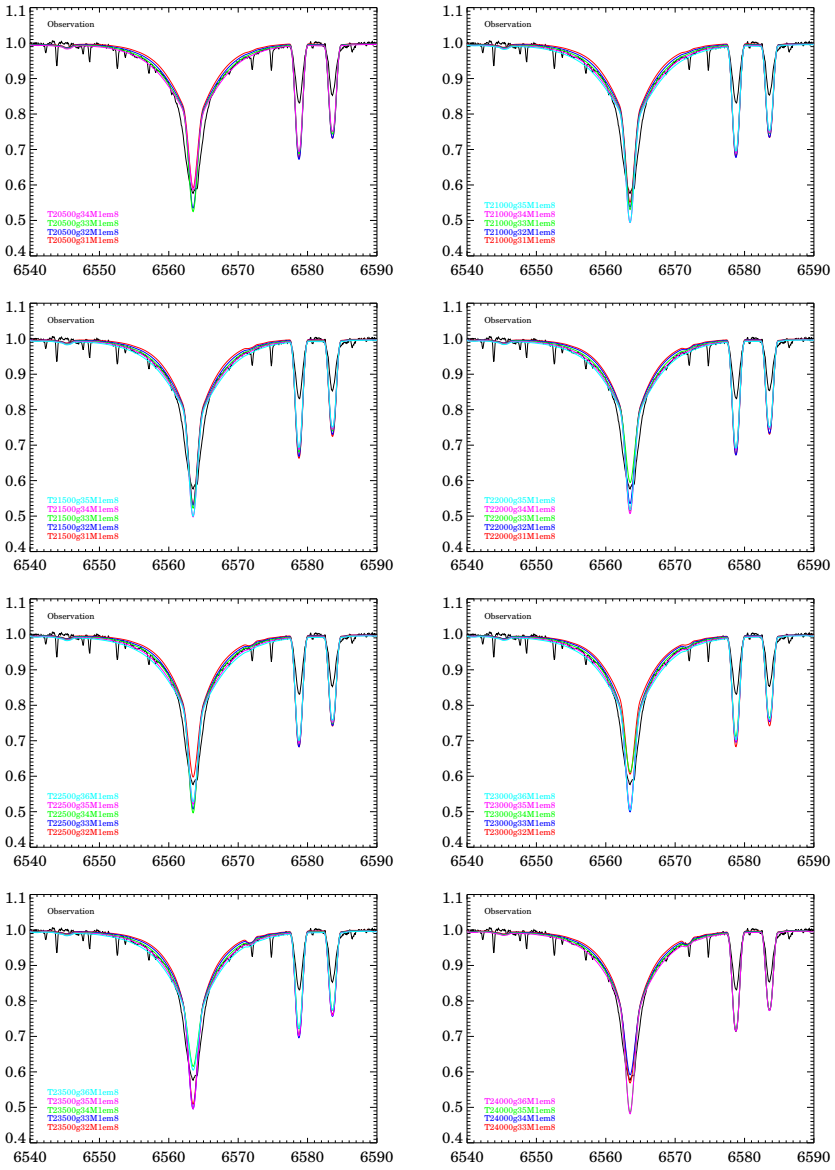

Figure 6.59: Fitting the wings of Hα. The x-axis for all plots is wavelength in unit of Å. The models have a microturbulence of 10 $\mathrm{km\,s^{-1}}$. The synthetic spectra have a resolution of 0.2 Å, similar to the observations. Also, a rotational velocity $v \sin i = 25\ \mathrm{km\,s^{-1}}$ has been applied to the model spectra. Models in the same panel have the same temperature, and the temperatures in the plot from top to bottom and from left to right are 20500, 21000, 21500, 22000, 22500, 23000, 23500, and 24000 K, respectively.

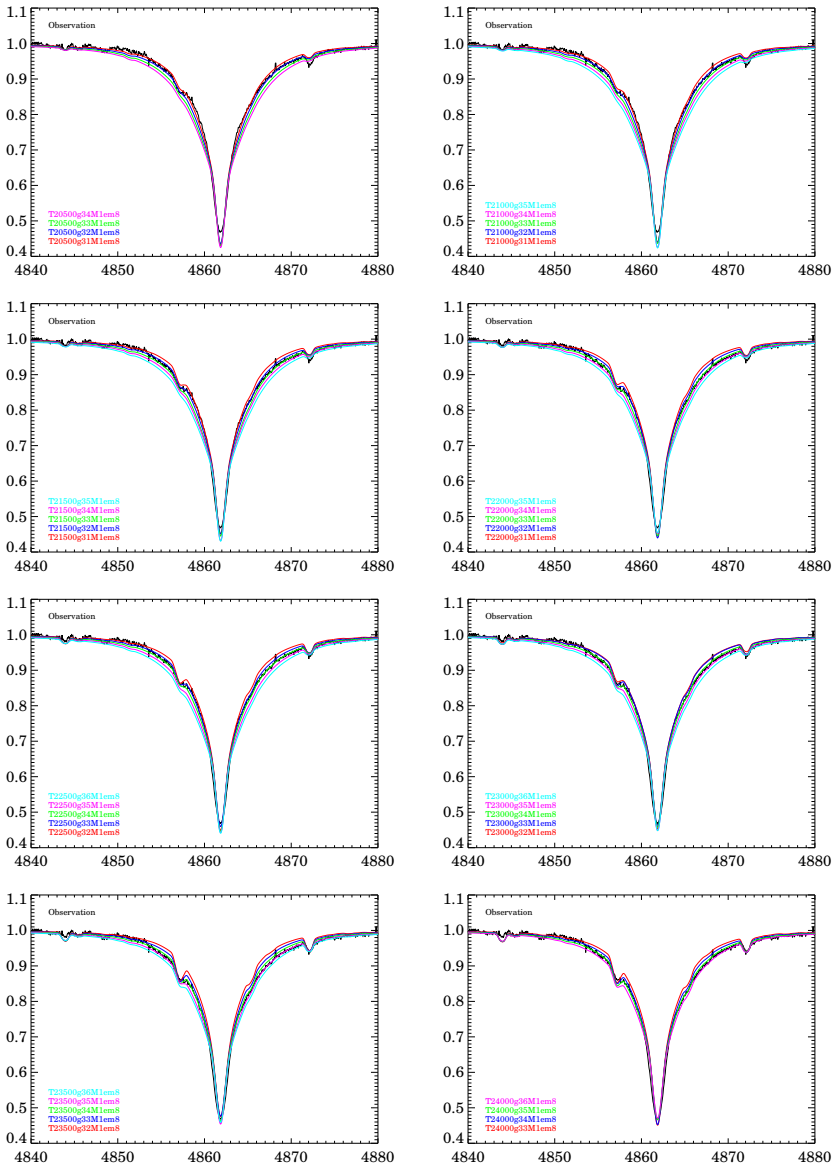

Figure 6.60: Same as Figure 6.59, but illustrate the fit to Hβ.

Table 6.8: $T_{\rm eff}$ and $\log g$ combinations that give the best fits to the wings of the Hα profile.

	Hα	Hβ
$T_{\rm eff}$ (K)	$\log g$	$\log g$
20500	3.3	3.2
21000	3.3	3.2
21500	3.3	3.2
22000	3.4	3.3
22500	3.4	3.4
23000	3.4	3.4
23500	3.5	3.5
24000	3.5	3.5

best fit to the Balmer jump is the model with $T_{\rm eff} = 23000\,{\rm K}$ and $\log g = 3.4$. Models with $T_{\rm eff} = 23500\,{\rm K}$ (bottom panel) are also able to reproduce the size of the Balmer jump, but the continua of the synthetic spectra show apparent deviation from the observation.

6.4.3 Equivalent widths of silicon lines

Some metal lines are sensitive to the effective temperature $T_{\rm eff}$, and hence are excellent diagnostics of $T_{\rm eff}$. Because silicon lines are prominent and absorption lines from several ionization stages are generally present, Si II, III, and IV lines have been frequently chosen as good indicators of $T_{\rm eff}$ in B-type stars [23, 24]. In this study, several strong silicon lines are selected for diagnostics – Si III $\lambda\lambda$ 4553, 4568, 4575 Å, Si IV λ 4631 Å, and Si II 5741 Å. Other potential diagnostic lines, arising from He II, O II, and Al III are also available for ϵ CMa. However, He II and Al III lines are generally weak, and the strengths of carbon, nitrogen, and oxygen lines depend on their abundances, which are still quite uncertain for B stars [e.g. 132, 72, 315, 316, 250]. Therefore, we tend to avoid using these lines.

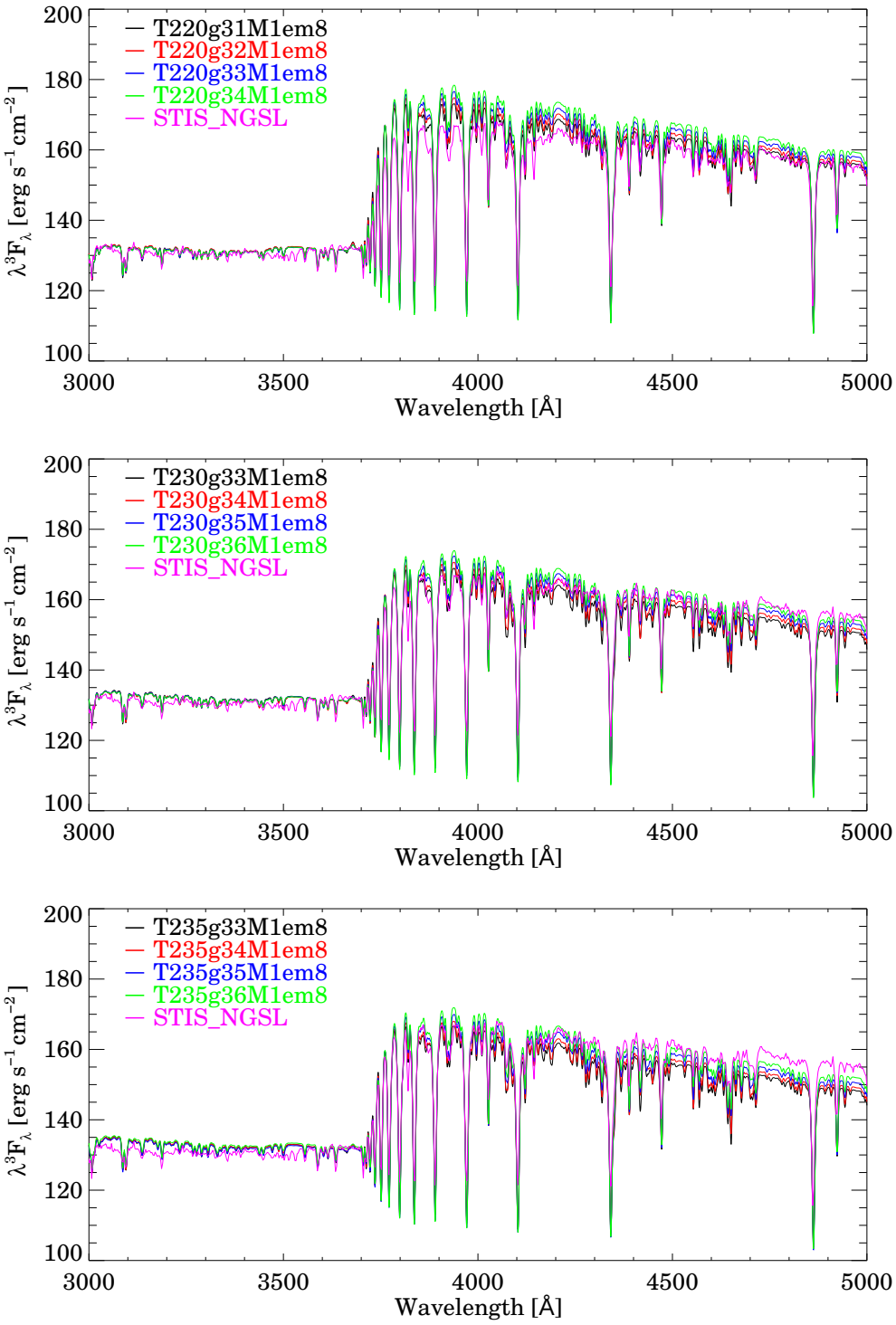

Figure 6.61: The Balmer jump comparison of the NGSL spectrum and synthetic spectra with $T_{\rm eff}$ = 22000 (top), 23000 (middle), and 23500 K (bottom). All synthetic spectra have been scaled to fit the discontinuity at 3646 Å.

By comparing the EWs between model and observation strong constraints, in principle, can be placed on the effective temperature. However, one trouble with this method is that the EW of a line is also dependent on the microturbulence ξ. Gies and Lambert [132] determined that ξ is around 10 $\mathrm{km\,s^{-1}}$ for B stars, and their non-LTE analysis showed $\xi = 11.5$ $\mathrm{km\,s^{-1}}$ for ϵ CMa. To allow exploration of the microturbulence, model spectra are computed by adopting 4 values of microturbulence, i.e., 5 $\mathrm{km\,s^{-1}}$, 7.5 $\mathrm{km\,s^{-1}}$, 10 $\mathrm{km\,s^{-1}}$, and 15 $\mathrm{km\,s^{-1}}$. However, spectra computed with $\xi = 5$ and 7.5 $\mathrm{km\,s^{-1}}$ generally give too small EWs for all lines, and consequently are not considered as good estimates of the microturbulence for ϵ CMa. In Figure 6.62, models that have the closest EWs to the observation in $T_{\rm eff}$-log g plane are illustrated. If at a given temperature, all models with different surface gravities have greater or smaller EWs than the observation, then we assume no good fit exists at this temperature. The least square fits to the best-fits models is also performed for each line, which is also shown in Figure 6.62. Ideally, all the fitting lines are expected to intersect at one point. However, various uncertainties, e.g., errors in the observed EWs arising from the continuum determination, errors in the atomic data, and errors in the model atmosphere, may prevent this. For $\xi = 10$ $\mathrm{km\,s^{-1}}$, a high temperature ($\sim$ 24000 K) is preferred to reproduce the EWs of silicon lines; while for $\xi = 15$ $\mathrm{km\,s^{-1}}$, the results favor a low temperature ($\sim$ 21000 K). If adopting $\xi = 10$ $\mathrm{km\,s^{-1}}$, which resembles the value in the study of Gies and Lambert [132], then the silicon line diagnostic prefers a higher effective temperature than the canonical value of $\sim$ 22000 K.

6.4.4 Spectral energy distribution

Spectral energy distribution is widely used to constrain the fundamental stellar parameters. We present in this section the SED comparison of ϵ CMa between models and observations.

The SEDs of model T235g36M1em8 and T220g32M1em8 from EUV to IR are displayed in Figure 6.63. The synthetic spectra are scaled by a distance of 124 pc, which is derived from the 8.05±0.14 parallax from van Leeuwen [384]. Adopted spectroscopic and photometric measurements are also displayed in the figure. The sources of the observations have been described in Section 6.2.

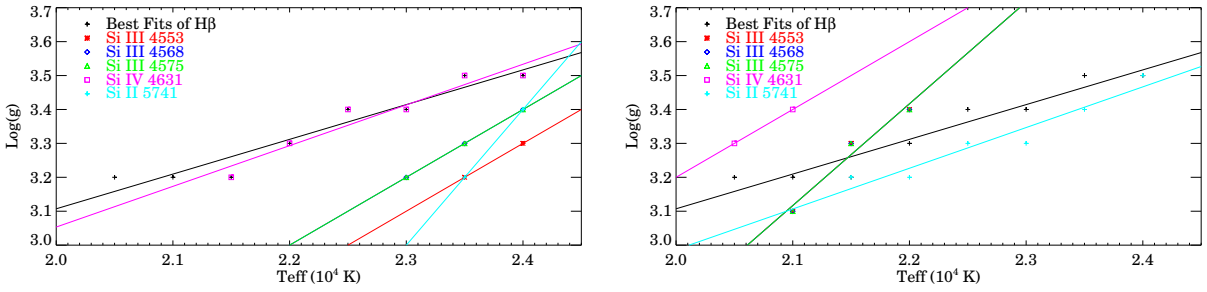

Figure 6.62: The best EW fitting models (symbols) for $\xi = 10\ \mathrm{km\,s^{-1}}$ (left panel) and $\xi = 15\ \mathrm{km\,s^{-1}}$ (right panel). The lines are the least square fits to the dots with corresponding colors. Note that the fitting lines for Si III 4568 (blue) and 4575 Å (green) are overlapped in the top panel, and the fitting lines for Si III 4553 (red), 4568 (blue) and 4575 Å (green) are overlapped in the bottom panel. The models with the best Hβ wing profile fitting (black) are also shown for assistance.

Figure 6.63 illustrates that the observed He I and H I continua in the EUV can be well fitted by model T235g33M1em8. Besides $T_{\rm eff}$, both $\log g$ and $\dot{M}$ influence the magnitude of the jump at 504 Å. Cassinelli et al. [49] found that the Kurucz model without mass loss had a large jump at the He I edge. Despite the influence of $T_{\rm eff}$, this jump can be well reproduced with a mass loss rate of $\sim \dot{M} = 1.0 \times 10^{-8}\,\mathrm{M_\odot\,yr^{-1}}$ in our models. The mechanism for producing the He I continuum has been discussed in Najarro et al. [282]. They showed that even a very weak wind can dramatically increase the escape probability of Lyman and He I continuum photons, since the velocity field induces photon escape in the hydrogen and He I resonance lines.

It is evident that the synthetic spectra show a moderate discrepancy with both IUE and NGSL spectra in the top panel of Figure 6.63. For convenient comparison, Figure 6.64 (upper panel) focuses on the spectra at UV band. Model T235g33M1em8 overestimates the UV flux by $\sim$25%. The same problem was mentioned by Aufdenberg et al. [14], which they attributed to calibration issues. However, the NGSL spectra, which have a higher calibration accuracy (2-3%), show similar flux levels to the IUE spectra, which rules out the possibility

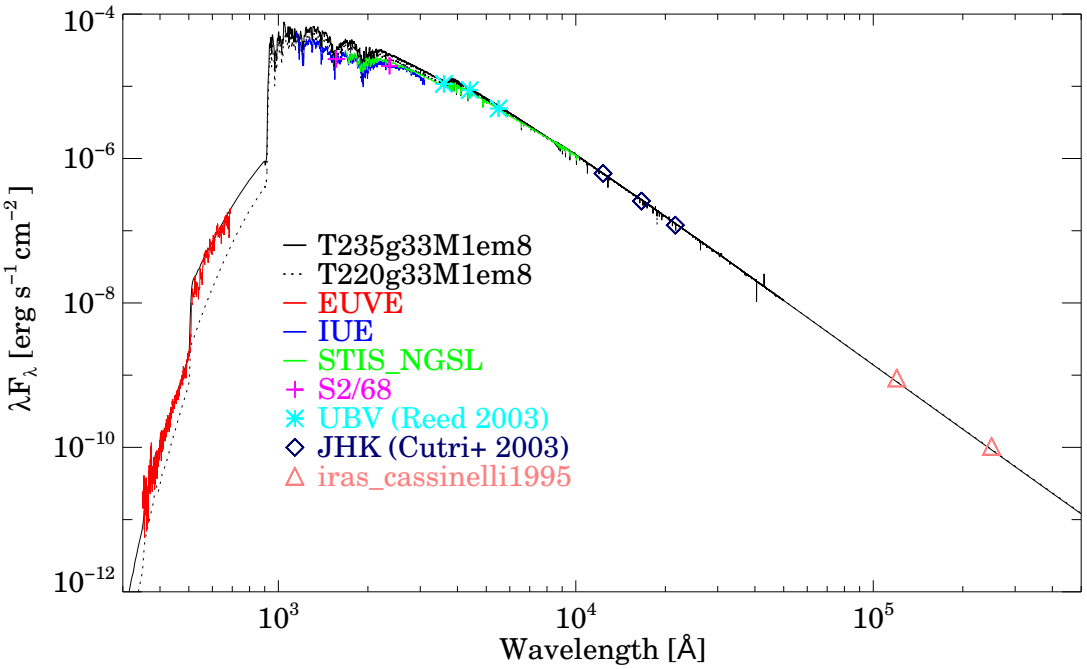

Figure 6.63: Comparison of spectral energy distribution for models T235g33M1em8 (black solid) and T220g32M1em8 (black dashed) with observations. The synthetic spectra have been scaled by a distance of 124 pc. The EUV spectrum (red) has been corrected for interstellar neutral hydrogen with column density of 1×10^{18} cm^{-2}. The IUE (blue) and NGSL (green) spectra have been smoothed to a resolution of 5 Å. Other photometric measurements are also indicated in the figure. While there is broad agreement between the model and observations, a significant discrepancy can be seen in the UV range(around 2000 Å).

that the discrepancy is due to an error in flux calibration. Although model T220g32M1em8 can slightly improve the SED fitting in the UV band, it significantly underestimates the EUV flux.

Observed IR excess has been discussed in previous studies [49, 14]. Cassinelli et al. [49] argued that IR excess and the weak Lyman continuum might be solved simultaneously if the temperature of the IR formation region increased 1000 - 2000 K, since the Lyman continuum should roughly form in the same layers as the IR. Observed IR excess is still seen at 12 μm

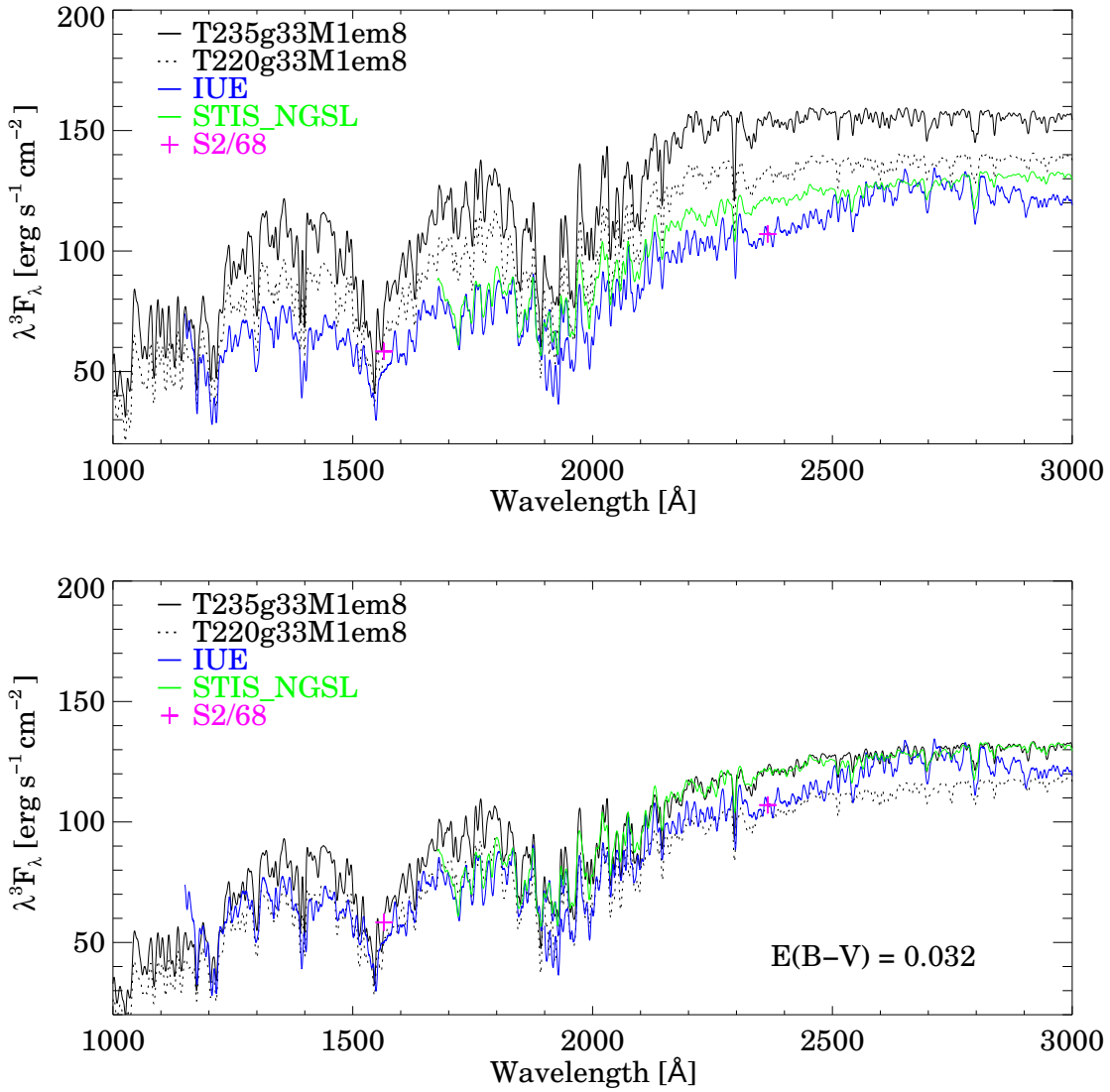

Figure 6.64: Top: comparison of synthetic and observed spectra in the UV band. The plot shows the quantity $\lambda^3 F_\lambda$ to facilitate comparison. Synthetic spectra for model T235g33M1em8 (black solid) and T220g33M1em8 (black dotted), and observed IUE (blue) and STIS NGSL (green) spectra are illustrated. The UV photometry from S2/68 (magenta) observation is also shown. Bottom: same as the top, but a reddening of $E(B-V) = 0.032$ is applied to the synthetic spectra. All spectra have a resolution of 5 Å.

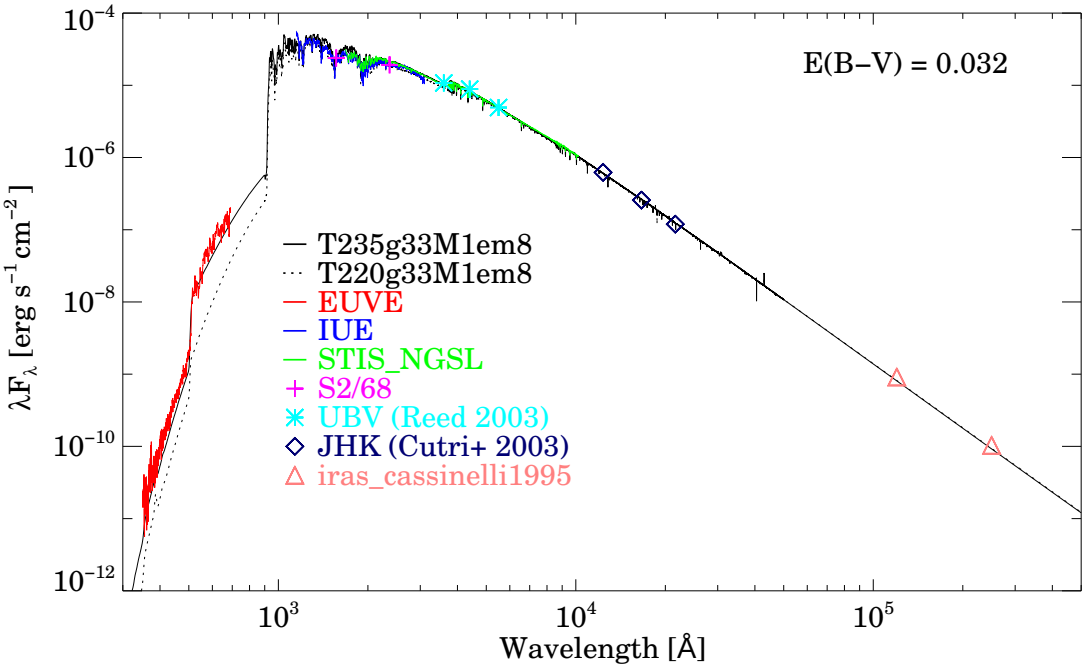

Figure 6.65: Same as the Figure 6.65, but a reddening of E(B-V)=0.032 has been applied to the synthetic spectra. With a non-zero reddening there is a much better agreement between model and observations in the UV range.

and 25 μm, which is 15% and 14% for model T235g33M1em8. However, both models agree with the recent measurements of J, H, and K_s-band magnitudes [71] within $\sim$5%.

Although reddening is widely thought to be zero toward ϵ CMa, careful exploration on the NGSL spectra reveals indications of reddening. Synthetic spectra show a sharp change at around 2200 Å, while the NGSL spectrum is smooth near 2200 Å (see Figure 6.63, top panel), which may be due to the 2200 Å bump in the reddening curve. In the bottom panel of Figure 6.64 and Figure 6.65, we show the SED fitting and UV spectral comparison with a reddening of $E(B-V) = 0.032$. Such value of reddening is derived in terms of χ^2-fit to the NGSL spectrum by varying the distance and the amount of reddening, and the distance derived from this χ^2-fit is 124 kpc. It can be seen that the discrepancy in the UV band has disappeared. The reddened synthetic spectra of model T235g33M1em8 agrees remarkably

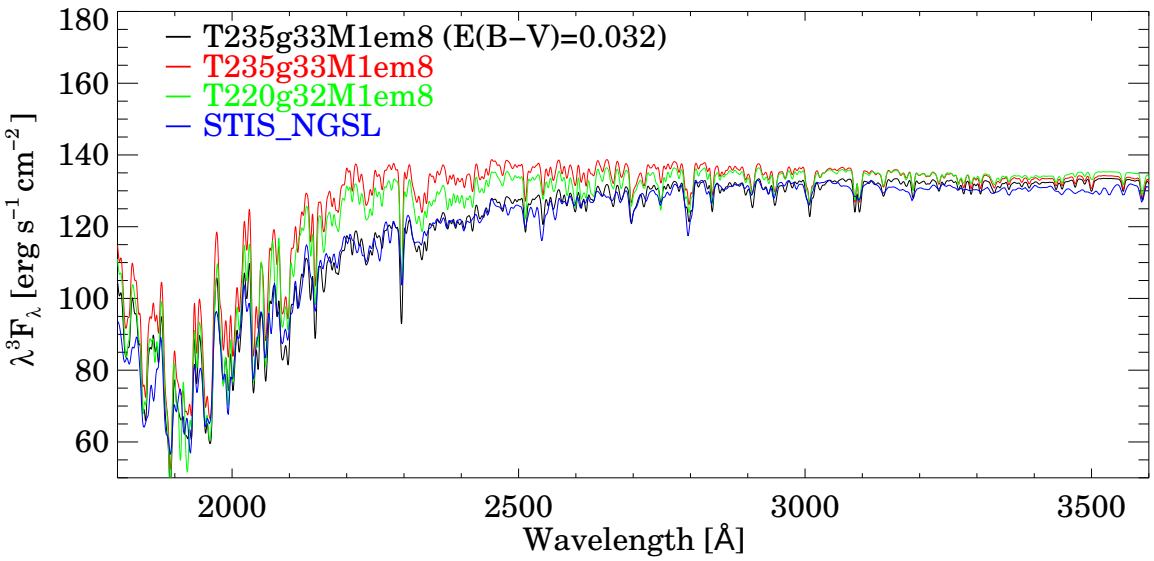

Figure 6.66: Spectral comparison at UV band around 2200 Å. Synthetic spectra of models T235g33M1em8 with reddening of E(B-V) = 0.032 (black) and without reddening (red), and of model T220g32M1em8 without reddening (green) are compared with STIS/NGSL observations. All synthetic spectra have been scaled to fit the observations around 3500 Å. Notice how the reddened model matches the observations much better over the relatively line-free region extending from 2100 Å to 3000 Å.

well with the NGSL spectra, for both the continuum and the line features. This is especially true for wavelengths around 2200 Å. Figure 6.66 illustrates the comparison of synthetic and NGSL spectra. Since none of the distance, radius, or angular diameter measurements are precise enough, we allow the synthetic spectra to scale up or down to fix the NGSL spectrum around 3500 Å. It is evident that neither model T235g33M1em8 and T220g32M1em8 can fit the NGSL spectrum shape around 2200 Å. The reddened T235g33M1em8 model not only fits this shape, it also reproduces the right slope seen in the NGSL optical spectrum. Moreover, the agreements in the line features excludes the possibility of additional line-blanketing effects. Although the EUV flux of model T235g33M1em8 is now slightly smaller than the observation, it is within the uncertainties due to the EUV flux calibration and

neutral hydrogen column density. Gry et al. [144] estimated an upper limit of the interstellar neutral hydrogen column density of $5 \times 10^{17}\,\mathrm{cm}^{-2}$, which is a factor of 2 smaller than our adopted value. IR fluxes are almost unaffected by a reddening of 0.032. The synthetic J, H, and K_s flux are still within $\sim 5\%$ error of the observations.

6.5 DISCUSSION

The effective temperature $T_{\rm eff}$ and the surface gravity $\log g$ are two fundamental parameters for stars. The estimate of these two parameters for ϵ CMa has been a great challenge to atmosphere model, due to the unsolved EUV problem. Several techniques have been used to determine $T_{\rm eff}$ and $\log g$ in this study. However, none of these techniques is perfect. We discuss in this section the potential problems that can affect our results and possible explanations.

6.5.1 Continuum determination of echelle spectra

One of the advantages of echelle spectra is that they utilize high order dispersion to obtain high resolution spectra. However, because of order curvature, continuum rectification is difficult. Results that rely on echelle spectra are influenced by how well the continua are determined. The problem is more severe for Hα than for Hβ, since Hα covers a large portion of the order of spectra. However, the blaze function for this order should be similar to the adjacent orders. Therefore, the coefficients of Hα blaze function are obtained by interpolating the coefficients of adjacent orders. Hβ covers a smaller wavelength range, and its continuum can still be determined independently.

A simple method is carried out to understand the quality of our continuum determination – to check the symmetry of the wings of the profile. If the continuum is good, the extensive wings on both sides, due to electron scattering, should be symmetric. Expectedly, the symmetry in wings is seen in both normalized Hα and Hβ profiles. Despite a reasonable determination of the continuum, a better approach is to wait for a high-resolution single order

spectrum for ϵ CMa. Considering the important role ϵ CMa plays in many astrophysical field, it deserves more attention and studies.

6.5.2 Microturbulence

When utilizing the EWs of silicon lines to constrain the effective temperature, microturbulence comes into the analysis as a "free" parameter. While microturbulence broadens the line profile and conserves the EWs for unsaturated lines, it widens the wavelength range covered by absorption and increases the EWs for saturated lines. A canonical way to measure microturbulence is to utilize the curve of growth [18]. Microturbulence is induced to explain the EW of a saturated line when the observed EW is greater than the theoretical one computed by using only natural and thermal broadening.

The theoretical EWs based on a model atmosphere are also influenced by non-LTE effect. Gies and Lambert [132] derived a microturbulent velcoty ξ of 18.8 $\mathrm{km\,s^{-1}}$ on basis of LTE models, but their non-LTE analysis only required $\xi = 11.5$ $\mathrm{km\,s^{-1}}$. In this study, we adopt 2 microturbulent velocities $\xi = 10$ and 15 $\mathrm{km\,s^{-1}}$, which are close to the value given by the non-LTE result. The results inferred from the 2 values are substantially different. The EW analysis favors a high effective temperature (~ 24000 K) if adopting $\xi = 10$ $\mathrm{km\,s^{-1}}$, while the results from $\xi = 15$ $\mathrm{km\,s^{-1}}$ prefer a low effective temperature (~ 21000 K). In fact, Gies and Lambert [132] also derived a high effective temperature of $T_{\rm eff} = 24500$ K, and their large surface gravity $\log g = 3.65$ is also indicated by the wings fitting of Balmer lines, provided $T_{\rm eff} = 24500$ K.

6.5.3 Mass loss

Mass loss is thought to be an important factor to reproduce the EUV spectra of ϵ CMa. The velocity field introduced by even a weak wind is enough to dramatically increase the escape probability of hydrogen and He I resonance line photons, leading to an increase in the hydrogen and He I continua in ϵ CMa [282]. A similar mechanism for the He II continuum operates in O stars [124].

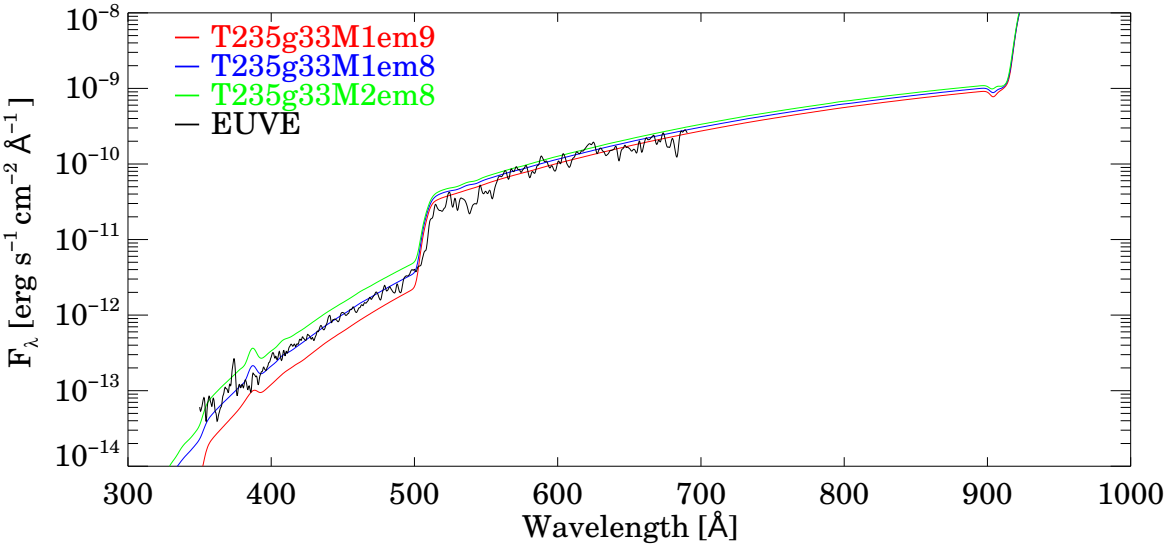

Figure 6.67: Comparison of EUV spectra with different mass loss rates. The EUVE observation is provided for reference (black). All models have been normalized in the optical. While models with this temperature and gravity match optical diagnostics they provide a poor fit to EUV observations, even after allowing for significant mass-loss by a stellar wind.

Cassinelli et al. [49] showed that both LTE and non-LTE models with no wind were unable to reproduce the EUV excess, and they estimated that a stellar wind as weak as $\dot{M} = 1 \times 10^{-8}\,\mathrm{M}_\odot\,\mathrm{yr}^{-1}$ could only have limited contribution. Najarro et al. [282] studied the stellar wind effect in detail and their results showed a great improvement with the aid of wind, but the EUV excess were still unable to be fully explained. Our models also indicate that mass loss alone is not sufficient to explain the EUV excess. Figure 6.67 illustrates the synthetic EUV spectra with the same $T_{\mathrm{eff}} = 23500\,\mathrm{K}$ and $\log g = 3.3$, but with different mass loss rates. A model with a higher $\dot{M}$ tends to have more EUV flux than that with a lower $\dot{M}$. While He I continuum is sensitive to $\dot{M}$ and can be increased significantly by a higher $\dot{M}$, Lyman continuum above the He I edge depends only weakly on $\dot{M}$. Moreover, in the model with $\dot{M} = 2 \times 10^{-8}\,\mathrm{M}_\odot\,\mathrm{yr}^{-1}$, undesirable line profiles begin to show up (see Figure 6.68). For example, wings of Hα become much shallower and some part of wings are above the continuum. Drew et al. [96] inferred a mass loss rate of $\dot{M} = (8 \pm 2) \times 10^{-9}\,\mathrm{M}_\odot\,\mathrm{yr}^{-1}$

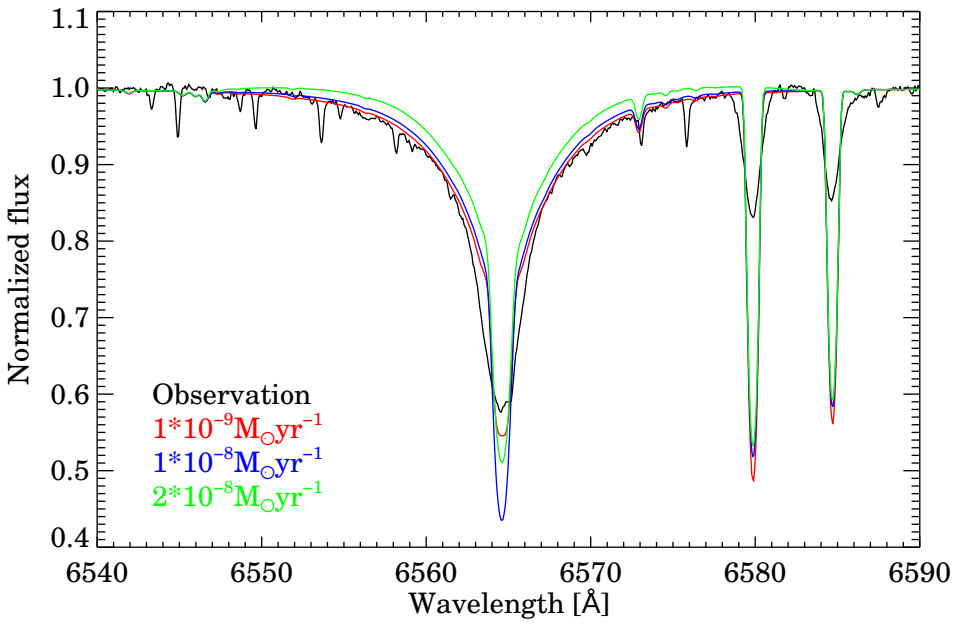

Figure 6.68: Illustration of Hα profiles for models with the same $T_{\rm eff} = 23500\,{\rm K}$ and $\log g = 3.3$, but with different ass loss rates. The mass lost rates are indicated in the plot. Notice that, some parts of the Hα wings in the $\dot{M} = 2 \times 10^{-8}\,{\rm M}_{\odot}\,{\rm yr}^{-1}$ model (blue) are above the continuum.

from observed X-ray spectra. Thus, employing a much higher mass loss rate above $\dot{M} = 1 \times 10^{-8}\,{\rm M}_{\odot}\,{\rm yr}^{-1}$ is not a solution to the EUV excess and could also be unphysical. The successful reproduction of the hydrogen and He I EUV continua largely relies on a higher effective temperature $T_{\rm eff}$.

6.5.4 Reddening

The long-standing EUV discrepancy can be solved by a CMFGEN model with an effective temperature of 23500 K, a surface gravity of 3.3, and a reddening of $E(B-V) = 0.032$. The non zero-reddening is very surprising – due to the low gas column density in the Local Bubble the reddening towards ϵ CMa is generally thought to be negligible. Measurements along line of sight were carried out by Gry et al. [144], Gry and Jenkins [143]. The relationship between

the neutral hydrogen column density N_H and total extinction at the V band A_V in a galaxy is given by, e.g. Güver and Özel [149],

$$N_H(\mathrm{cm}^{-2}) = (2.21 \pm 0.09) \times 10^{21} A_V \tag{6.1}$$

With the neutral hydrogen column density of $\sim 1 \times 10^{18}\,\mathrm{cm}^{-2}$ and a typical value of ratio of total to selective extinction $R_V = A_V/E(B-V) = 3.1$, the reddening $E(B-V)$ is smaller than 0.01. However, this relationship may not be applicable if circumstellar reddening is present. To our knowledge, the reddening to ϵ CMa has not been directly measured. Moreover, the IR excess at $12\,\mu$m and $25\,\mu$m is another indication for existence of non-negligible amount of dust. However, the origin of such dust is unclear. One possibility is that it may come from previous mass loss of the star.

6.5.5 Other possibilities

Other possibilities for explaining the EUV flux of ϵ CMa also exist. One possibility is that unknown problems may exist in the EUV data reduction. This possibility has been claimed by Gregorio et al. [139], who also pointed out the possibility that the spectra might be different when observed at different epochs due to stellar variability. The absolute flux calibration uncertainty of EUVE is about $\pm 20\%$ [334]. However, the model with $T_{\mathrm{eff}} = 22000\,\mathrm{K}$ and $\log g = 3.2$ predicts the EUV flux about an order of magnitude smaller. Although Aufdenberg et al. [14] gave a reasonable fit to the EUV with $T_{\mathrm{eff}} = 22000\,\mathrm{K}$, they also found that a more physically realistic model with more ions treated in non-LTE predicted less He I continuum flux. More importantly, their derivation of a cooler temperature also depends on the adoption of a lower neutral column hydrogen density.

Another possibility is that B stars are not so well understood as we think. There may be some important physical processes that is missing in the currently used atmosphere codes, particularly physics associated with the stellar wind. Stellar winds of B stars are more difficult to understand than those of O stars, because B stars do not show strong UV resonance lines and they are usually not detected in radio wavelengths, both of which are important diagnostics for wind properties. Our understanding of the stellar winds in B stars is possibly

incomplete.

The measured rotational velocity for ϵ CMa is about 25-35 $\mathrm{km\,s^{-1}}$[374, 2]. However, rapidly rotating stars observed pole-on could deceive us, e.g., Vega [136, 147, 148, 304]. The possibility of observing ϵ CMa pole-on can only make the UV discrepancy worse, since pole-on observations produce UV deficit compared to edge-on observations [138]. However, rapid rotation induces an absorption line with a weak central emission that has been observed in Vega [137, 148, Charles Warren, private communication]. This is not seen in ϵ CMa, which rules out such possibility.

6.6 CONCLUSIONS

We have reanalyzed the important giant star ϵ CMa which lies in the Local Bubble, and determined the effective temperature $T_{\rm eff}$ and surface gravity $\log g$ based on model atmospheres computed by the fully non-LTE line-blanketed code CMFGEN.

We have utilized four methods to constrain $T_{\rm eff}$ and $\log g$ of ϵ CMa – fitting of the Hα and Hβ wings, fitting to the Balmer jump, comparison of the model and observational EWs of selected silicon lines, and SED fitting. With an adopted microturbulence $\xi = 10\,\mathrm{km\,s^{-1}}$, H$\alpha$ and Hβ wings and silicon lines diagnosis yield a relatively high $T_{\rm eff}$ of $\sim 24000\,\mathrm{K}$ and a $\log g$ of ~ 3.5, while Balmer jump diagnosis prefers a model with $T_{\rm eff} = 23000\,\mathrm{K}$ and $\log g = 3.4$.

When fitting the SED, the observed EUV flux, which is corrected for an interstellar neutral hydrogen column density of $1 \times 10^{-18}\,\mathrm{cm^{-2}}$, can be reproduced by using a model with $T_{\rm eff} = 23500\,\mathrm{K}$, $\log g = 3.3$, and $\dot{M} = 1 \times 10^{-8}\,\mathrm{M_\odot\,yr^{-1}}$. Moderate discrepancies are seen in the UV band. The similarity between the NGSL spectra from HST/STIS and the IUE spectra excludes the possibility due to errors in UV flux calibration. The remarkable agreements in the line features between the model and the NGSL spectra also rules out a substantial underestimate of the line-blanketing effects. The model matches the observations at J, H, and K_s bands, but observed IR excess at $12\,\mu$m and $25\,\mu$m remains.

Inspection of NGSL spectra indicates that the star suffers non-negligible reddening. This

is surprising since the neutral hydrogen density is generally accepted to be exceptionally low [402, 144, 143]. With a reddening of $E(B-V) = 0.032$, a model with $T_{\rm eff} = 23500\,{\rm K}$ can perfectly match the NGSL spectra, as well as obtain excellent agreements at other bands, except at $12\,\mu$m and $25\,\mu$m. IR excess seen at $12\,\mu$m and $25\,\mu$m is another indication for existence of an appreciable amount of dust.

Underlying uncertainties in the techniques used in this study are also discussed. The concern with the continuum determination for Hα and Hβ in the echelle spectra is lessened by checking the symmetry of the normalized profiles and comparing results for Hα and Hβ. Although microturbulence can significantly change our estimate of effective temperature, our adopted value of microturbulence infers an effective temperature consistent with the EUV observations. Mass loss can also paly a role in the analysis, but its influence is relatively small within reasonable estimates of mass loss rate.

Other possible explanations are also suggested to interpret the SED of ϵ CMa, e.g. unknown problems in EUV data reduction, stellar variability, and unknown physics that is not included in current codes.

7.0 CONCLUSIONS OF THE THESIS

In this chapter, all the work done in this thesis will be briefly summarized. We highlight our results and conclusions and propose future directions in related field.

7.1 NON-THERMAL PROCESSES IN SUPERNOVAE

We implemented non-thermal processes that arise from radioactive decay into the radiative transfer code CMFGEN for SNe simulation. The non-thermal process solver has been applied to model a SN with BSG progenitor. Comparison between simulations with and without non-thermal processes is made and various effects due to non-thermal excitation and ionization have been identified. Non-thermal models show lower temperature and more excited/ionized material in the region where the non-thermal processes are crucial. The prominence of the non-thermal processes is associated with small ejecta ionization fraction X_e. The Hα profile is significantly enhanced at nebular epochs. Being absent in thermal models at late times, He I lines are present but mostly contaminated by other lines in non-thermal models. However, He I 2.058 μm and He I 7065Å provide an excellent opportunity to infer the influence of non-thermal processes on helium.

Non-thermal excitation has been confirmed to be the most important process for He I 2.058 μm. However, He I 1.083 μm is due to cascades from higher levels, which indirectly relate to non-thermal ionization. In non-thermal models, non-thermal excitation and ionization are the processes controlling the ionization balance, even if photoionization and recombination are prominent processes for populating many levels.

We compared the light curves and spectra of the non-thermal simulations with SN 1987A

observations. Reasonable agreements have been found between models and observations. Moderate differences seen in the multi-band light curves indicate an possible underestimate in line-blanketing.

The uncertainties introduced by various approximations and assumptions in the non-thermal solver have been investigated thoroughly. The primary uncertainties are due to the not-well-known electron impact excitation and ionization cross sections of metal species. In general, the total uncertainties are small in our treatments in the approximations and assumptions.

The non-thermal solver make it possible to model SNe from photospheric to nebular phases continuously and accurately. Dessart et al. [94] showed that non-thermal ionization and excitation are crucial to differentiate Type Ib/Ic SNe. Non-thermal effects in Type Ia SNe, which is necessarily important since Type Ia SNe synthesize huge amount of ^{56}Ni, are under investigation. With new generation of sky surveys, more and more nebular spectra will be available, allowing us to place constraints on the hydrodynamic models and nucleosynthesis. The non-thermal solver also provides opportunities to constrain the degree of mixing.

7.2 FULLY RELATIVISTIC RADIATIVE TRANSFER OF SNE

We developed a fully relativistic radiative transfer solver, which takes into account all relativistic terms except radiative acceleration terms, in aim to model Type II-P SNe. We performed various checks to verify the solutions. In case of homologous expansion, the fully relativistic solver gives the same results as the Hubble solver. LTE is recovered at depth as expected, which can be seen from the departure coefficients of H I, O I, and Fe II. Material at large optical depth undergoes adiabatic expansion (in the absence of radioactive decay heating), which is seen in all simulations. The global energy constraint gives consistent checks for models at different epochs.

Type II-P SNe are the most common type of SN in the universe and have been found to be good distance indicators using EPM and SEAM. Current simulations based on the

homology assumption can potentially introduce uncertainties when modeling Type II-P SNe due to the non-negligible initial radius at explosion and acceleration of the ejecta by the radiation field. Future simulations with the fully relativistic solver will explore the effects due to deviation from homology in Type II-P SNe. Uncertainties due to these effects when measuring the cosmological distance will also be investigated.

7.3 THE WIND GEOMETRY OF η CARINAE

The long-slit STIS mapping data have been used to study the wind geometry of η Carinae. In the computed Hα EW map, both global and pixel-to-pixel variations have been identified. Global variations indicate possible deviations from an axisymmetric wind. Pixel-to-pixel variations may arise from different contributions of components from the rear and front walls of the Homunculus.

The computed velocities at minimum of the absorption component in the SE lobe are highly circularly symmetric with respect to the projected polar axis. By comparing the residual intensity of the absorption component and examining the width of Hα profile, we propose that the absorption seen in SE may arise from gas associated with the Homunculus rather than the primary wind.

We computed the optical depth of the SE lobe in terms of a simplified model. The optical depth maps show a general agreement with an optically thin dust shell in the Homunculus. We also argued from various evidence, e.g., the observed polarization, the low extinction towards the Weigelt blobs and the Little Homunculus, and the visibility of the ground-based [Fe II] lines, that the Homunculus is most probably optically thin.

It is very difficult to fully understand η Carinae, since it is such a complicated object. Many fundamental questions remain to be answered. Observations mapping the Homunculus are useful in understanding η Carinae and the structures around it. Upcoming data observed at similar and different orbital phases can provide both consistency checks of our results and information on the influence of the companion. Future 3D simulations will help to uncover the the nature of η Carinae and to resolve many questions that we don't understand. The

Homunculus is also ripe for detailed modeling to explain both the optical and near IR intensities, optical and near IR polarization data, and the longer wavelength dust emission. Additional spectropolarimetry observations, similar to those of Meaburn et al. [262] would also be very useful.

7.4 THE PHYSICAL PARAMETERS OF ϵ CANIS MAJORIS

We have performed several techniques to determine the physical parameters of ϵ CMa. Our results generally favor an effective temperature of ~ 24000 K and a surface gravity of ~ 3.4. CMFGEN models produce an excellent EUV fit to the observation with $T_{\rm eff} = 23500$ K, $\log g = 3.3$, and $\dot{M} = 1 \times 10^{-8}\,{\rm M}_{\odot}\,{\rm yr}^{-1}$. Inspection of NGSL spectra indicates that the star suffers non-negligible reddening. By applying a reddening of $E(B-V) = 0.032$, which is obtained by χ^2-fitting, the synthetic UV spectrum strongly agrees with the observations, reconciling the longstanding problem in ϵ CMa.

Moderate inconsistency is still seen in our results, which may arise from the uncertainty in the continuum determination. To give more stringent constraint on the surface gravity, we really need high resolution non-echelle spectra for ϵ CMa. The non-negligible reddening found here is surprising. Future observations should search for possible circumstellar dust around ϵ CMa.

APPENDIX A

ABBREVIATION SUMMARY

BH: Black Hole

BSG: Blue Supergiant

CCSN: Core-Collapse Supernova

CSM: Circumstellar Material

EPM: Expanding Photosphere Method

EW: Equivalent Width

FWHM: Full Width at Half Maximum

GRB: Gamma-Ray Burst

IGE: Iron-Group Elements

IME: Intermediate-Mass Elements

LBV: Luminous Blue Variable

LMC: Large Magellanic Cloud

LTE: Local Thermodynamic Equilibrium

MHD: Magneto-Hydrodynamics

MRI: Magneto-Rotational Instability

NS: Neutron Star

RGB: Red Giant Branch

RMI: Richtmyer-Meshkov Instability

RSG: Red Supergiant

RTE: Radiative Transfer Equation

RTI: Rayleigh-Taylor Instability

SASI: Standing Accretion Shock Instability

SCM: Standardized Candle Method

SEAM: Spectral-fitting Expanding Atmosphere Method

SED: Spectral Energy Distribution

SN: Supernova

SNR: Supernova Remnant

WC: Wolf-Rayet stars show dominant carbon and no nitrogen lines WD: White Dwarf

WN: Wolf-Rayet stars show dominant nitrogen and some carbon lines W-R: Wolf-Rayet star

WWC: Wind-Wind Collision

APPENDIX B

STRATEGY TO SOLVE THE MOMENT EQUATIONS

The moment equations to be solved in the fully relativistic solver are given by Eq. 4.4 and 4.5, i.e.,

$$\begin{aligned}
&\frac{\gamma}{rc}\frac{D(r^3J_\nu)}{Dt}+\frac{\gamma\beta}{c}\frac{D(r^2H_\nu)}{Dt}+\gamma\frac{\partial(r^2H_\nu)}{\partial r}\left(1-\beta^2\right)+\frac{\gamma^3}{c}\frac{D\beta}{Dt}(r^2H_\nu)+\frac{1}{c}\frac{D\gamma}{Dt}(r^2J_\nu)\\
&-\frac{\gamma\beta\nu}{r}\frac{\partial(r^2J_\nu)}{\partial\nu}-\frac{\gamma^3\nu}{c}\frac{D\beta}{Dt}\frac{\partial(r^2H_\nu)}{\partial\nu}-\left(\frac{\nu}{c}\frac{D\gamma}{Dt}+\gamma\nu\frac{\partial\beta}{\partial r}-\frac{\gamma\beta\nu}{r}\right)\frac{\partial(r^2K_\nu)}{\partial\nu}\\
&=r^2\eta_\nu-\chi_\nu(r^2J_\nu)
\end{aligned}\tag{B.1}$$

and

$$\begin{aligned}
&r^2H_\nu+\frac{\gamma}{\chi_\nu c}\frac{D(r^2H_\nu)}{Dt}-\frac{\gamma\beta\nu}{\chi_\nu r}\frac{\partial(r^2H_\nu)}{\partial\nu}+\left(\frac{2}{\chi_\nu c}\frac{D\gamma}{Dt}+\frac{2\gamma}{\chi_\nu}\frac{\partial\beta}{\partial r}-\frac{\gamma\beta}{\chi_\nu r}\right)(r^2H_\nu)\\
&=-\frac{\gamma}{\chi_\nu q_\nu}\frac{\partial(q_\nu r^2K_\nu)}{\partial r}-\frac{\gamma}{\chi_\nu c}\frac{D\beta}{Dt}(r^2J_\nu)+\frac{\gamma\beta^2}{\chi_\nu}\frac{\partial(r^2K_\nu)}{\partial r}-\frac{\gamma\beta}{\chi_\nu c}\frac{D(r^2K_\nu)}{Dt}\\
&+\left(\frac{1}{\chi_\nu c}\frac{D\gamma}{Dt}+\frac{\gamma}{\chi_\nu}\frac{\partial\beta}{\partial r}-\frac{\gamma\beta}{\chi_\nu r}\right)(r^2N_\nu)\\
&+\frac{\gamma^3\nu}{\chi_\nu c}\frac{D\beta}{Dt}\frac{\partial(r^2K_\nu)}{\partial\nu}+\left(\frac{\nu}{\chi_\nu c}\frac{D\gamma}{Dt}+\frac{\gamma\nu}{\chi_\nu}\frac{\partial\beta}{\partial r}-\frac{\gamma\beta\nu}{\chi_\nu r}\right)\frac{\partial(r^2N_\nu)}{\partial\nu}
\end{aligned}\tag{B.2}$$

[268]. The spatial differences of the moments of the radiation field are given by

$$\frac{\partial[J_\nu,K_\nu]}{\partial r}=\frac{[J_{\nu,i+1},K_{\nu,i+1}]-[J_{\nu,i},K_{\nu,i}]}{r_{i+1}-r_i}\tag{B.3}$$

and

$$\frac{\partial[H_\nu, N_\nu]}{\partial r} = \frac{[H_{\nu,i+1}, N_{\nu,i+1}] - [H_{\nu,i}, N_{\nu,i}]}{r_{i+1/2} - r_{i-1/2}} \tag{B.4}$$

[269] where $H_{\nu,i}$, and $N_{\nu,i}$ is defined on the middle grid point $r_{i+1/2} = (r_{i+1} + r_i)/2$ and as noted in Sec. 4.2 the code works in the optical depth τ-space, i.e. $d\tau = -\chi dr$, where χ is the opacity. The frequency differences are given by

$$\frac{\partial[J_\nu, H_\nu, K_\nu, N_\nu]}{\partial \nu} = \frac{1}{\Delta\nu}\left([J_{\nu_{k-1}}, H_{\nu_{k-1}}, K_{\nu_{k-1}}, N_{\nu_{k-1}}] - [J_{\nu_k}, H_{\nu_k}, K_{\nu_k}, N_{\nu_k}]\right) \tag{B.5}$$

where $\Delta\nu = \nu_{k-1} - \nu_k$ [169]. With the moments of the radiation field for previous time step and previous frequency, and the Eddington factor $f_\nu = K_\nu/J_\nu$ and $h_\nu = N_\nu/J_\nu$ [271, 169], $H_{\nu_n,i}$ (at depth i) can be expressed in terms of $J_{\nu_n,i}$ and $J_{\nu_n,i+1}$ using difference equation of Eq. B.2,

$$H_{\nu_n,i} = p_i J_{\nu_n,i} + q_i J_{\nu_n,i+1} + y_i \tag{B.6}$$

where p_i, q_i, and y_i are all known coefficients. Note that $H_{\nu_n,i}$, $J_{\nu_n,i}$, $J_{\nu_n,i+1}$ are for the current unknown frequency, and that all terms from the previous (bluer) frequency are contained in the y_i. This expression is substituted into the difference equation of Eq. B.1 to eliminate H_ν, which results in,

$$A_i J_{i-1} + B_i J_i + C_i J_{i+1} = X_i \tag{B.7}$$

[271] where A_i, B_i, C_i, and X_i are coefficients that can be computed [270]. The inner and outer boundary conditions are given by specifying the flux (H_ν) in Eq. B.2, which can be written as,

$$A_{\mathrm{ND}} J_{\mathrm{ND}-1} + B_{\mathrm{ND}} J_{\mathrm{ND}} = X_{\mathrm{ND}} \tag{B.8}$$

and

$$B_1 J_1 + C_1 J_2 = X_1 \tag{B.9}$$

where ND is the maximum number of depth. Eqs. B.7, B.8, and B.9 form a tridiagonal system, which can be handled with numerical linear algebra.

BIBLIOGRAPHY

[1] Z. Abraham, D. Falceta-Gonçalves, T. P. Dominici, L.-Å. Nyman, P. Durouchoux, F. McAuliffe, A. Caproni, and V. Jatenco-Pereira. Millimeter-wave emission during the 2003 low excitation phase of η Carinae. *A&A*, 437:977–981, July 2005. doi: 10.1051/0004-6361:20041604.

[2] H. A. Abt, H. Levato, and M. Grosso. Rotational Velocities of B Stars. *ApJ*, 573:359–365, July 2002. doi: 10.1086/340590.

[3] I. Agnoletto, S. Benetti, E. Cappellaro, L. Zampieri, M. Turatto, P. Mazzali, A. Pastorello, M. Della Valle, F. Bufano, A. Harutyunyan, H. Navasardyan, N. Elias-Rosa, S. Taubenberger, S. Spiro, and S. Valenti. SN 2006gy: Was it Really Extraordinary? *ApJ*, 691:1348–1359, Feb. 2009. doi: 10.1088/0004-637X/691/2/1348.

[4] S. Akiyama, J. C. Wheeler, D. L. Meier, and I. Lichtenstadt. The Magnetorotational Instability in Core-Collapse Supernova Explosions. *ApJ*, 584:954–970, Feb. 2003. doi: 10.1086/344135.

[5] D. A. Allen and D. J. Hillier. The Shape of the Homunchulus Nebula around Eta-Carinae. *Proceedings of the Astronomical Society of Australia*, 10:338–+, 1993.

[6] L. S. Anderson. Line blanketing without local thermodynamic equilibrium. II - A solar-type model in radiative equilibrium. *ApJ*, 339:558–578, Apr. 1989. doi: 10.1086/167317.

[7] G. C. Anupama, T. Sivarani, and G. Pandey. Early time optical spectroscopy of supernova SN 1998S. *A&A*, 367:506–512, Feb. 2001. doi: 10.1051/0004-6361:20000427.

[8] I. Aretxaga, S. Benetti, R. J. Terlevich, A. C. Fabian, E. Cappellaro, M. Turatto, and M. della Valle. SN 1988Z: spectro-photometric catalogue and energy estimates*. *MNRAS*, 309:343–354, Oct. 1999. doi: 10.1046/j.1365-8711.1999.02830.x.

[9] M. Arnaud and R. Rothenflug. An updated evaluation of recombination and ionization rates. *A&APS*, 60:425–457, June 1985.

[10] W. D. Arnett and A. Fu. The late behavior of supernova 1987A. I - The light curve. II - Gamma-ray transparency of the ejecta. *ApJ*, 340:396–425, May 1989. doi: 10.1086/167402.

[11] W. D. Arnett, J. N. Bahcall, R. P. Kirshner, and S. E. Woosley. Supernova 1987A. *ARA&A*, 27:629–700, 1989. doi: 10.1146/annurev.aa.27.090189.003213.

[12] É. Artigau, J. C. Martin, R. M. Humphreys, K. Davidson, O. Chesneau, and N. Smith. Penetrating the Homunculus—Near-Infrared Adaptive Optics Images of Eta Carinae. *AJ*, 141:202, June 2011. doi: 10.1088/0004-6256/141/6/202.

[13] L. H. Auer and D. Mihalas. Non-Lte Model Atmospheres. III. a Complete-Linearization Method. *ApJ*, 158:641–+, Nov. 1969. doi: 10.1086/150226.

[14] J. P. Aufdenberg, P. H. Hauschildt, S. N. Shore, and E. Baron. A Spherical Non-LTE Line-blanketed Stellar Atmosphere Model of the Early B Giant epsilon Canis Majoris. *ApJ*, 498:837, May 1998. doi: 10.1086/305565.

[15] W. Baade and F. Zwicky. Remarks on Super-Novae and Cosmic Rays. *Physical Review*, 46:76–77, July 1934. doi: 10.1103/PhysRev.46.76.2.

[16] C. Badenes and D. Maoz. The Merger Rate of Binary White Dwarfs in the Galactic Disk. *ApJL*, 749:L11, Apr. 2012. doi: 10.1088/2041-8205/749/1/L11.

[17] S. Bagnulo, J. D. Landstreet, L. Fossati, and O. Kochukhov. Magnetic field measurements and their uncertainties: the FORS1 legacy. *A&A*, 538:A129, Feb. 2012. doi: 10.1051/0004-6361/201118098.

[18] G. A. Bakos. Abundances of Heavy Elements in Late-Type Stars. *JRASC*, 65:222, Oct. 1971.

[19] Z. Barkat and J. C. Wheeler. SN 1987A - Was Sanduleak -69 deg 202 mixed up? *ApJ*, 342:940–944, July 1989. doi: 10.1086/167650.

[20] E. Baron, P. H. Hauschildt, D. Branch, S. Austin, P. Garnavich, H. B. Ann, R. M. Wagner, A. V. Filippenko, T. Matheson, and J. Liebert. Non-LTE spectral analysis and model constraints on SN 1993J. *ApJ*, 441:170–181, Mar. 1995. doi: 10.1086/175347.

[21] E. Baron, P. E. Nugent, D. Branch, and P. H. Hauschildt. Type IIP Supernovae as Cosmological Probes: A Spectral-fitting Expanding Atmosphere Model Distance to SN 1999em. *ApJL*, 616:L91–L94, Dec. 2004. doi: 10.1086/426506.

[22] M. A. Bautista. Atomic data from the IRON Project. XX. Photoionization cross sections and oscillator strengths for Fe I. *A&APS*, 122:167–176, Apr. 1997. doi: 10.1051/aas:1997327.

[23] S. R. Becker and K. Butler. SI II, III and IV in non-LTE for temperature determination in B-stars. *A&A*, 235:326–334, Aug. 1990.

[24] S. R. Becker and K. Butler. Non-LTE equivalent widths for SI II, III and IV. *A&APS*, 84:95–132, July 1990.

[25] H. A. Bethe and J. R. Wilson. Revival of a stalled supernova shock by neutrino heating. *ApJ*, 295:14–23, Aug. 1985. doi: 10.1086/163343.

[26] G. S. Bisnovatyi-Kogan and A. A. Ruzmaikin. The accretion of matter by a collapsing star in the presence of a magnetic field. II - Selfconsistent stationary picture. *Ap&SS*, 42:401–424, July 1976. doi: 10.1007/BF01225967.

[27] S. Blinnikov, P. Lundqvist, O. Bartunov, K. Nomoto, and K. Iwamoto. Radiation Hydrodynamics of SN 1987A. I. Global Analysis of the Light Curve for the First 4 Months. *ApJ*, 532:1132–1149, Apr. 2000. doi: 10.1086/308588.

[28] J. M. Blondin, A. Mezzacappa, and C. DeMarino. Stability of Standing Accretion Shocks, with an Eye toward Core-Collapse Supernovae. *ApJ*, 584:971–980, Feb. 2003. doi: 10.1086/345812.

[29] R. C. Bohlin. The ultraviolet calibration of the Hubble Space Telescope. I - Secondary standards of absolute ultraviolet flux and the recalibration of IUE. *ApJ*, 308:1001–1012, Sept. 1986. doi: 10.1086/164568.

[30] J.-C. Bouret, T. Lanz, and D. J. Hillier. Lower mass loss rates in O-type stars: Spectral signatures of dense clumps in the wind of two Galactic O4 stars. *A&A*, 438:301–316, July 2005. doi: 10.1051/0004-6361:20042531.

[31] D. V. Bowen, K. C. Roth, D. M. Meyer, and J. C. Blades. Interstellar and Circumstellar Optical and Ultraviolet Lines Toward SN 1998S. *ApJ*, 536:225–238, June 2000. doi: 10.1086/308913.

[32] R. Bowers and J. R. Wilson. Collapse of iron stellar cores. *ApJ*, 263:366–376, Dec. 1982. doi: 10.1086/160510.

[33] I. Bray and Y. Ralchenko. http://atom.murdoch.edu.au/CCC-WWW/index.html. *http://atom.murdoch.edu.au/CCC-WWW/index.html*, 2001.

[34] T. J. Bronder, I. M. Hook, P. Astier, D. Balam, C. Balland, S. Basa, R. G. Carlberg, A. Conley, D. Fouchez, J. Guy, D. A. Howell, J. D. Neill, R. Pain, K. Perrett, C. J. Pritchet, N. Regnault, M. Sullivan, S. Baumont, S. Fabbro, M. Filliol, S. Perlmutter, and P. Ripoche. SNLS spectroscopy: testing for evolution in type Ia supernovae. *A&A*, 477:717–734, Jan. 2008. doi: 10.1051/0004-6361:20077655.

[35] R. Buras, M. Rampp, H.-T. Janka, and K. Kifonidis. Improved Models of Stellar Core Collapse and Still No Explosions: What Is Missing? *Physical Review Letters*, 90(24): 241101, June 2003. doi: 10.1103/PhysRevLett.90.241101.

[36] R. Buras, H.-T. Janka, M. Rampp, and K. Kifonidis. Two-dimensional hydrodynamic core-collapse supernova simulations with spectral neutrino transport. II. Models for different progenitor stars. *A&A*, 457:281–308, Oct. 2006. doi: 10.1051/0004-6361: 20054654.

[37] P. G. Burke, V. M. Burke, and K. M. Dunseath. Electron-impact excitation of complex atoms and ions. *Journal of Physics B Atomic Molecular Physics*, 27:5341–5373, Nov. 1994. doi: 10.1088/0953-4075/27/21/024.

[38] A. Burrows, E. Livne, L. Dessart, C. D. Ott, and J. Murphy. A New Mechanism for Core-Collapse Supernova Explosions. *ApJ*, 640:878–890, Apr. 2006. doi: 10.1086/500174.

[39] A. Burrows, E. Livne, L. Dessart, C. D. Ott, and J. Murphy. An acoustic mechanism for core-collapse supernova explosions. *NewAR*, 50:487–491, Oct. 2006. doi: 10.1016/j.newar.2006.06.046.

[40] A. Burrows, L. Dessart, E. Livne, C. D. Ott, and J. Murphy. Simulations of Magnetically Driven Supernova and Hypernova Explosions in the Context of Rapid Rotation. *ApJ*, 664:416–434, July 2007. doi: 10.1086/519161.

[41] A. Burrows, E. Livne, L. Dessart, C. D. Ott, and J. Murphy. Features of the Acoustic Mechanism of Core-Collapse Supernova Explosions. *ApJ*, 655:416–433, Jan. 2007. doi: 10.1086/509773.

[42] E. Cappellaro, R. Evans, and M. Turatto. A new determination of supernova rates and a comparison with indicators for galactic star formation. *A&A*, 351:459–466, Nov. 1999.

[43] E. Cappellaro, M. Riello, G. Altavilla, M. T. Botticella, S. Benetti, A. Clocchiatti, J. I. Danziger, P. Mazzali, A. Pastorello, F. Patat, M. Salvo, M. Turatto, and S. Valenti. Death rate of massive stars at redshift ~ 0.3. *A&A*, 430:83–93, Jan. 2005. doi: 10.1051/0004-6361:20041256.

[44] J. A. Cardelli, G. C. Clayton, and J. S. Mathis. The relationship between infrared, optical, and ultraviolet extinction. *ApJ*, 345:245–256, Oct. 1989. doi: 10.1086/167900.

[45] T. F. Carty, H. G. Perkins, R. F. Warren-Smith, and S. M. Scarrott. A size distribution of silicate grains in Eta Carinae. *MNRAS*, 189:299–304, Oct. 1979.

[46] J. P. Cassinelli. Stellar winds. *ARA&A*, 17:275–308, 1979. doi: 10.1146/annurev.aa.17.090179.001423.

[47] J. P. Cassinelli and G. L. Olson. The effects of coronal regions on the X-ray flux and ionization conditions in the winds of OB supergiants and Of stars. *ApJ*, 229:304–317, Apr. 1979. doi: 10.1086/156956.

[48] J. P. Cassinelli, G. L. Olson, and R. Stalio. The structure of the winds and coronae of O stars derived from H-alpha line-profile analyses. *ApJ*, 220:573–581, Mar. 1978. doi: 10.1086/155938.

[49] J. P. Cassinelli, D. H. Cohen, J. J. Macfarlane, J. E. Drew, A. E. Lynas-Gray, M. G. Hoare, J. V. Vallerga, B. Y. Welsh, P. W. Vedder, I. Hubeny, and T. Lanz. EUVE

spectroscopy of epsilon Canis Majoris (B2 II) from 70 to 730 A. *ApJ*, 438:932–949, Jan. 1995. doi: 10.1086/175135.

[50] O. Chesneau, M. Min, T. Herbst, L. B. F. M. Waters, D. J. Hillier, C. Leinert, A. de Koter, I. Pascucci, W. Jaffe, R. Köhler, C. Alvarez, R. van Boekel, W. Brandner, U. Graser, A. M. Lagrange, R. Lenzen, S. Morel, and M. Schöller. The sub-arcsecond dusty environment of Eta Carinae. *A&A*, 435:1043–1061, June 2005. doi: 10.1051/0004-6361:20041395.

[51] R. A. Chevalier. The hydrodynamics of Type II supernovae. *ApJ*, 207:872–887, Aug. 1976. doi: 10.1086/154557.

[52] A. Chieffi, I. Domínguez, P. Höflich, M. Limongi, and O. Straniero. Theoretical light curves of Type II-P supernovae and applications to cosmology. *MNRAS*, 345:111–122, Oct. 2003. doi: 10.1046/j.1365-8711.2003.06958.x.

[53] N. N. Chugai. Broad emission lines from the opaque electron-scattering environment of SN 1998S. *MNRAS*, 326:1448–1454, Oct. 2001. doi: 10.1046/j.1365-8711.2001.04717.x.

[54] N. N. Chugai. Asymmetry of ^{56}Ni ejecta and polarization in the type-IIP supernova 2004dj. *Astronomy Letters*, 32:739–746, Nov. 2006. doi: 10.1134/S1063773706110041.

[55] N. N. Chugai and I. J. Danziger. Supernova 1988Z - Low-Mass Ejecta Colliding with the Clumpy Wind. *MNRAS*, 268:173, May 1994.

[56] N. N. Chugai, S. I. Blinnikov, A. Fassia, P. Lundqvist, W. P. S. Meikle, and E. I. Sorokina. The origin of the high-velocity circumstellar gas around SN 1998S. *MNRAS*, 330:473–480, Feb. 2002. doi: 10.1046/j.1365-8711.2002.05086.x.

[57] N. N. Chugai, S. I. Blinnikov, R. J. Cumming, P. Lundqvist, A. Bragaglia, A. V. Filippenko, D. C. Leonard, T. Matheson, and J. Sollerman. The Type IIn supernova 1994W: evidence for the explosive ejection of a circumstellar envelope. *MNRAS*, 352:1213–1231, Aug. 2004. doi: 10.1111/j.1365-2966.2004.08011.x.

[58] N. N. Chugai, S. N. Fabrika, O. N. Sholukhova, V. P. Goranskij, P. K. Abolmasov, and V. V. Vlasyuk. Optical Observations of Type-IIP Supernova 2004dj: Evidence for Asymmetry of the 56Ni Ejecta. *Astronomy Letters*, 31:792–805, Dec. 2005. doi: 10.1134/1.2138766.

[59] D. D. Clayton, M. D. Leising, L.-S. The, W. N. Johnson, and J. D. Kurfess. The Co-57 abundance in SN 1987A. *ApJL*, 399:L141–L144, Nov. 1992. doi: 10.1086/186627.

[60] A. D. Code, R. C. Bless, J. Davis, and R. H. Brown. Empirical effective temperatures and bolometric corrections for early-type stars. *ApJ*, 203:417–434, Jan. 1976. doi: 10.1086/154093.

[61] M. Cohen, W. A. Wheaton, and S. T. Megeath. Spectral Irradiance Calibration in the Infrared. XIV. The Absolute Calibration of 2MASS. *AJ*, 126:1090–1096, Aug. 2003. doi: 10.1086/376474.

[62] S. W. J. Colgan, M. R. Haas, E. F. Erickson, S. D. Lord, and D. J. Hollenbach. Day 640 infrared line and continuum measurements: Dust formation in SN 1987A. *ApJ*, 427:874–888, June 1994. doi: 10.1086/174193.

[63] S. A. Colgate and R. H. White. The Hydrodynamic Behavior of Supernovae Explosions. *ApJ*, 143:626–+, Mar. 1966. doi: 10.1086/148549.

[64] P. S. Conti. Spectroscopic studies of O-type stars. III. The effective-temperature scale. *ApJ*, 179:181–188, Jan. 1973. doi: 10.1086/151857.

[65] M. F. Corcoran, K. Ishibashi, J. H. Swank, and R. Petre. The X-Ray Light Curve of η Carinae: Refinement of the Orbit and Evidence for Phase-dependent Mass Loss. *ApJ*, 547:1034–1039, Feb. 2001. doi: 10.1086/318416.

[66] M. F. Corcoran, K. Hamaguchi, T. Gull, K. Davidson, R. Petre, D. J. Hillier, N. Smith, A. Damineli, J. A. Morse, N. R. Walborn, E. Verner, N. Collins, S. White, J. M. Pittard, K. Weis, D. Bomans, and Y. Butt. Waiting in the Wings: Reflected X-Ray Emission from the Homunculus Nebula. *ApJ*, 613:381–386, Sept. 2004. doi: 10.1086/423024.

[67] S. R. Cranmer and S. P. Owocki. The effect of oblateness and gravity darkening on the radiation driving in winds from rapidly rotating B stars. *ApJ*, 440:308–321, Feb. 1995. doi: 10.1086/175272.

[68] P. A. Crowther. Physical Properties of Wolf-Rayet Stars. *ARA&A*, 45:177–219, Sept. 2007. doi: 10.1146/annurev.astro.45.051806.110615.

[69] D. G. Currie, D. M. Dowling, E. J. Shaya, J. Hester, P. Scowen, E. J. Groth, R. Lynds, E. J. O'neil, Jr., and Wide Field/Planetary Camera Instrument Definition Team. Astrometric Analysis of the Homunculus of eta Carinae With the Hubble Space Telescope. *AJ*, 112:1115–+, Sept. 1996. doi: 10.1086/118083.

[70] D. G. Currie, D. M. Dowling, E. J. Shaya, J. J. Hester, HST WF/Pc Instrument Definition Team, and HST WFPC2 Instrument Definition Team. 3-D Structure of the Bipolar Dust Shell of η Carinae. In H. U. Käufl & R. Siebenmorgen, editor, *The Role of Dust in the Formation of Stars*, page 89, 1996.

[71] R. M. Cutri, M. F. Skrutskie, S. van Dyk, C. A. Beichman, J. M. Carpenter, T. Chester, L. Cambresy, T. Evans, J. Fowler, J. Gizis, E. Howard, J. Huchra, T. Jarrett, E. L. Kopan, J. D. Kirkpatrick, R. M. Light, K. A. Marsh, H. McCallon, S. Schneider, R. Stiening, M. Sykes, M. Weinberg, W. A. Wheaton, S. Wheelock, and N. Zacarias. 2MASS All-Sky Catalog of Point Sources (Cutri+ 2003). *VizieR Online Data Catalog*, 2246:0, Mar. 2003.

[72] S. Daflon, K. Cunha, and S. R. Becker. Chemical Abundances of OB Stars in the Cepheus OB2 Association. *ApJ*, 522:950–959, Sept. 1999. doi: 10.1086/307683.

[73] A. Damineli. The 5.52 Year Cycle of Eta Carinae. *ApJL*, 460:L49+, Mar. 1996. doi: 10.1086/309961.

[74] A. Damineli, P. S. Conti, and D. F. Lopes. Eta Carinae: a long period binary? *New Astronomy*, 2:107–117, July 1997. doi: 10.1016/S1384-1076(97)00008-0.

[75] A. Damineli, D. J. Hillier, M. F. Corcoran, O. Stahl, J. H. Groh, J. Arias, M. Teodoro, N. Morrell, R. Gamen, F. Gonzalez, N. V. Leister, H. Levato, R. S. Levenhagen, M. Grosso, J. F. A. Colombo, and G. Wallerstein. A multispectral view of the periodic events in η Carinae. *MNRAS*, 386:2330–2344, June 2008. doi: 10.1111/j.1365-2966.2008.13214.x.

[76] A. Damineli, D. J. Hillier, M. F. Corcoran, O. Stahl, R. S. Levenhagen, N. V. Leister, J. H. Groh, M. Teodoro, J. F. Albacete Colombo, F. Gonzalez, J. Arias, H. Levato, M. Grosso, N. Morrell, R. Gamen, G. Wallerstein, and V. Niemela. The periodicity of the η Carinae events. *MNRAS*, 384:1649–1656, Mar. 2008. doi: 10.1111/j.1365-2966.2007.12815.x.

[77] K. Davidson and R. M. Humphreys. Eta Carinae and Its Environment. *ARA&A*, 35:1–32, 1997. doi: 10.1146/annurev.astro.35.1.1.

[78] K. Davidson and M. T. Ruiz. Scattering by dust and the photographic appearance of eta Carinae. *ApJ*, 202:421–424, Dec. 1975. doi: 10.1086/153991.

[79] K. Davidson, R. J. Dufour, N. R. Walborn, and T. R. Gull. Ultraviolet and visual wavelength spectroscopy of gas around ETA Carinae. *ApJ*, 305:867–879, June 1986. doi: 10.1086/164301.

[80] K. Davidson, D. Ebbets, G. Weigelt, R. M. Humphreys, A. R. Hajian, N. R. Walborn, and M. Rosa. HST/FOS spectroscopy of ETA Carinae: the star itself, and ejecta within 0.3 arcsec. *AJ*, 109:1784–1796, Apr. 1995. doi: 10.1086/117408.

[81] K. Davidson, D. Ebbets, S. Johansson, J. A. Morse, F. W. Hamann, B. Balick, R. M. Humphreys, G. Weigelt, and A. Frank. HST/GHRS Observations of the Compact Slow Ejecta of ETA Carinae. *AJ*, 113:335–345, Jan. 1997. doi: 10.1086/118256.

[82] K. Davidson, N. Smith, T. R. Gull, K. Ishibashi, and D. J. Hillier. The Shape and Orientation of the Homunculus Nebula Based on Spectroscopic Velocities. *AJ*, 121:1569–1577, Mar. 2001. doi: 10.1086/319419.

[83] M. D. de La Pena, J. Nichols-Bohlin, K. L. Levay, and A. Michalitsianos. The IUE Final Archive – Scientific Evaluation and Results with NEWSIPS Data. *Astronomical Data Analysis Software and Systems*, 3:127, 1994.

[84] C. De Loore and D. Vanbeveren. A binary evolutionary model for the progenitor of SN 1987 A. *A&A*, 260:273–282, July 1992.

[85] L. Dessart and D. J. Hillier. Quantitative spectroscopy of photospheric-phase type II supernovae. *A&A*, 437:667–685, July 2005. doi: 10.1051/0004-6361:20042525.

[86] L. Dessart and D. J. Hillier. Distance determinations using type II supernovae and the expanding photosphere method. *A&A*, 439:671–685, Aug. 2005. doi: 10.1051/0004-6361:20053217.

[87] L. Dessart and D. J. Hillier. Quantitative spectroscopic analysis of and distance to SN1999em. *A&A*, 447:691–707, Feb. 2006. doi: 10.1051/0004-6361:20054044.

[88] L. Dessart and D. J. Hillier. Time-dependent effects in photospheric-phase Type II supernova spectra. *MNRAS*, 383:57–74, Jan. 2008. doi: 10.1111/j.1365-2966.2007.12538.x.

[89] L. Dessart and D. J. Hillier. Supernova radiative-transfer modelling: a new approach using non-local thermodynamic equilibrium and full time dependence. *MNRAS*, 405:2141–2160, July 2010. doi: 10.1111/j.1365-2966.2010.16611.x.

[90] L. Dessart and D. J. Hillier. Non-LTE time-dependent spectroscopic modelling of Type II-plateau supernovae from the photospheric to the nebular phase: case study for 15 and 25 Msun progenitor stars. *MNRAS*, 410:1739–1760, Jan. 2011. doi: 10.1111/j.1365-2966.2010.17557.x.

[91] L. Dessart and D. J. Hillier. Synthetic line and continuum linear-polarization signatures of axisymmetric Type II supernova ejecta. *MNRAS*, 415:3497–3519, Aug. 2011. doi: 10.1111/j.1365-2966.2011.18967.x.

[92] L. Dessart, D. J. Hillier, S. Gezari, S. Basa, and T. Matheson. SN 1994W: an interacting supernova or two interacting shells? *MNRAS*, 394:21–37, Mar. 2009. doi: 10.1111/j.1365-2966.2008.14042.x.

[93] L. Dessart, D. J. Hillier, E. Livne, S.-C. Yoon, S. Woosley, R. Waldman, and N. Langer. Core-collapse explosions of Wolf-Rayet stars and the connection to Type IIb/Ib/Ic supernovae. *MNRAS*, 414:2985–3005, July 2011. doi: 10.1111/j.1365-2966.2011.18598.x.

[94] L. Dessart, D. J. Hillier, C. Li, and S. Woosley. On the nature of supernovae Ib and Ic. *MNRAS*, 424:2139–2159, Aug. 2012. doi: 10.1111/j.1365-2966.2012.21374.x.

[95] T. Dotani, K. Hayashida, H. Inoue, M. Itoh, and K. Koyama. Discovery of an unusual hard X-ray source in the region of supernova 1987A. *Nature*, 330:230, Nov. 1987. doi: 10.1038/330230a0.

[96] J. E. Drew, M. G. Hoare, and M. Denby. Soft X-ray observations of the early B giants Beta and Epsilon CMa. *MNRAS*, 266:917, Feb. 1994.

[97] R. A. Duncan and S. M. White. Radio evidence of recent mass ejection from η Carinae. *MNRAS*, 338:425–427, Jan. 2003. doi: 10.1046/j.1365-8711.2003.06287.x.

[98] R. C. Duncan and C. Thompson. Formation of very strongly magnetized neutron stars - Implications for gamma-ray bursts. *ApJL*, 392:L9–L13, June 1992. doi: 10.1086/186413.

[99] L. Dunne, S. Eales, R. Ivison, H. Morgan, and M. Edmunds. Type II supernovae as a significant source of interstellar dust. *Nature*, 424:285–287, July 2003. doi: 10.1038/nature01792.

[100] V. V. Dwarkadas. On luminous blue variables as the progenitors of core-collapse supernovae, especially Type IIn supernovae. *MNRAS*, 412:1639–1649, Apr. 2011. doi: 10.1111/j.1365-2966.2010.18001.x.

[101] E. Dwek and I. Cherchneff. The Origin of Dust in the Early Universe: Probing the Star Formation History of Galaxies by Their Dust Content. *ApJ*, 727:63, Feb. 2011. doi: 10.1088/0004-637X/727/2/63.

[102] R. G. Eastman and R. P. Kirshner. Model atmospheres for SN 1987A and the distance to the Large Magellanic Cloud. *ApJ*, 347:771–793, Dec. 1989. doi: 10.1086/168168.

[103] R. G. Eastman, S. E. Woosley, T. A. Weaver, and P. A. Pinto. Theoretical light curve of a Type 2p supernova. *ApJ*, 430:300–310, July 1994. doi: 10.1086/174404.

[104] R. S. Ellis, M. Sullivan, P. E. Nugent, D. A. Howell, A. Gal-Yam, P. Astier, D. Balam, C. Balland, S. Basa, R. G. Carlberg, A. Conley, D. Fouchez, J. Guy, D. Hardin, I. Hook, R. Pain, K. Perrett, C. J. Pritchet, and N. Regnault. Verifying the Cosmological Utility of Type Ia Supernovae: Implications of a Dispersion in the Ultraviolet Spectra. *ApJ*, 674:51–69, Feb. 2008. doi: 10.1086/524981.

[105] A. Elmhamdi, I. J. Danziger, N. Chugai, A. Pastorello, M. Turatto, E. Cappellaro, G. Altavilla, S. Benetti, F. Patat, and M. Salvo. Photometry and spectroscopy of the Type IIP SN 1999em from outburst to dust formation. *MNRAS*, 338:939–956, Feb. 2003. doi: 10.1046/j.1365-8711.2003.06150.x.

[106] L. M. Ensman and S. E. Woosley. Explosions in Wolf-Rayet stars and Type Ib supernovae. I - Light curves. *ApJ*, 333:754–776, Oct. 1988. doi: 10.1086/166785.

[107] A. C. Fabian and M. J. Rees. On the variability of the X-ray emission from supernova 1987A. *Nature*, 335:50, Sept. 1988. doi: 10.1038/335050a0.

[108] A. C. Fabian and R. Terlevich. X-ray detection of Supernova 1988Z with the ROSAT High Resolution Imager. *MNRAS*, 280:L5–L8, May 1996.

[109] D. Falceta-Gonçalves and Z. Abraham. Constraining the orbital orientation of η Carinae from H Paschen lines. *MNRAS*, 399:1441–1446, Nov. 2009. doi: 10.1111/j.1365-2966.2009.15364.x.

[110] D. Falceta-Gonçalves, V. Jatenco-Pereira, and Z. Abraham. Dust Formation Events in Colliding Winds: An Application to Eta Car. 15:71–71, Jan. 2003.

[111] S. W. Falk and W. D. Arnett. Radiation Dynamics, Envelope Ejection, and Supernova Light Curves. *ApJS*, 33:515, Apr. 1977. doi: 10.1086/190440.

[112] A. Fassia and W. P. S. Meikle. ˆ56Ni dredge-up in Supernova 1987A. *MNRAS*, 302: 314–320, Jan. 1999. doi: 10.1046/j.1365-8711.1999.02127.x.

[113] A. Fassia, W. P. S. Meikle, W. D. Vacca, S. N. Kemp, N. A. Walton, D. L. Pollacco, S. Smartt, A. Oscoz, A. Aragón-Salamanca, S. Bennett, T. G. Hawarden, A. Alonso, D. Alcalde, A. Pedrosa, J. Telting, M. J. Arevalo, H. J. Deeg, F. Garzón, A. Gómez-Roldán, G. Gómez, C. Gutiérrez, S. López, M. Rozas, M. Serra-Ricart, and M. R. Zapatero-Osorio. Optical and infrared photometry of the Type IIn SN 1998S: days 11-146. *MNRAS*, 318:1093–1104, Nov. 2000. doi: 10.1046/j.1365-8711.2000.03797.x.

[114] A. Fassia, W. P. S. Meikle, N. Chugai, T. R. Geballe, P. Lundqvist, N. A. Walton, D. Pollacco, S. Veilleux, G. S. Wright, M. Pettini, T. Kerr, E. Puchnarewicz, P. Puxley, M. Irwin, C. Packham, S. J. Smartt, and D. Harmer. Optical and infrared spectroscopy of the type IIn SN 1998S: days 3-127. *MNRAS*, 325:907–930, Aug. 2001. doi: 10.1046/j.1365-8711.2001.04282.x.

[115] R. A. Fesen. An Optical Survey of Outlying Ejecta in Cassiopeia A: Evidence for a Turbulent, Asymmetric Explosion. *ApJS*, 133:161–186, Mar. 2001. doi: 10.1086/319181.

[116] A. V. Filippenko. Optical Spectra of Supernovae. *ARA&A*, 35:309–355, 1997. doi: 10.1146/annurev.astro.35.1.309.

[117] A. V. Filippenko and W. L. W. Sargent. Spectroscopic evidence for inhomogeneities in the ejecta of the Type Ib supernova 1985F. *ApJL*, 345:L43–L46, Oct. 1989. doi: 10.1086/185548.

[118] R. J. Foley, A. V. Filippenko, C. Aguilera, A. C. Becker, S. Blondin, P. Challis, A. Clocchiatti, R. Covarrubias, T. M. Davis, P. M. Garnavich, S. W. Jha, R. P. Kirshner, K. Krisciunas, B. Leibundgut, W. Li, T. Matheson, A. Miceli, G. Miknaitis, G. Pignata, A. Rest, A. G. Riess, B. P. Schmidt, R. C. Smith, J. Sollerman, J. Spyromilio, C. W. Stubbs, N. B. Suntzeff, J. L. Tonry, W. M. Wood-Vasey, and A. Zenteno. Constraining Cosmic Evolution of Type Ia Supernovae. *ApJ*, 684:68–87, Sept. 2008. doi: 10.1086/589612.

[119] C. Fransson and R. A. Chevalier. Late emission from supernovae - A window on stellar nucleosynthesis. *ApJ*, 343:323–342, Aug. 1989. doi: 10.1086/167707.

[120] C. Fransson and C. Kozma. The freeze-out phase of SN 1987A - Implications for the light curve. *ApJL*, 408:L25–L28, May 1993. doi: 10.1086/186822.

[121] C. Fransson, P. M. Challis, R. A. Chevalier, A. V. Filippenko, R. P. Kirshner, C. Kozma, D. C. Leonard, T. Matheson, E. Baron, P. Garnavich, S. Jha, B. Leibundgut, P. Lundqvist, C. S. J. Pun, L. Wang, and J. C. Wheeler. Hubble Space Telescope and Ground-based Observations of SN 1993J and SN 1998S: CNO Processing in the Progenitors. *ApJ*, 622:991–1007, Apr. 2005. doi: 10.1086/426495.

[122] D. B. Friend and D. C. Abbott. The theory of radiatively driven stellar winds. III - Wind models with finite disk correction and rotation. *ApJ*, 311:701–707, Dec. 1986. doi: 10.1086/164809.

[123] C. L. Fryer, P. A. Mazzali, J. Prochaska, E. Cappellaro, A. Panaitescu, E. Berger, M. van Putten, E. P. J. van den Heuvel, P. Young, A. Hungerford, G. Rockefeller, S.-C. Yoon, P. Podsiadlowski, K. Nomoto, R. Chevalier, B. Schmidt, and S. Kulkarni. Constraints on Type Ib/c Supernovae and Gamma-Ray Burst Progenitors. *PASP*, 119: 1211–1232, Nov. 2007. doi: 10.1086/523768.

[124] R. Gabler, A. Gabler, R. P. Kudritzki, J. Puls, and A. Pauldrach. Unified NLTE model atmospheres including spherical extension and stellar winds - Method and first results. *A&A*, 226:162–182, Dec. 1989.

[125] A. Gal-Yam and D. C. Leonard. A massive hypergiant star as the progenitor of the supernova SN 2005gl. *Nature*, 458:865–867, Apr. 2009. doi: 10.1038/nature07934.

[126] A. Gal-Yam, D. C. Leonard, D. B. Fox, S. B. Cenko, A. M. Soderberg, D.-S. Moon, D. J. Sand, W. Li, A. V. Filippenko, G. Aldering, and Y. Copin. On the Progenitor of SN 2005gl and the Nature of Type IIn Supernovae. *ApJ*, 656:372–381, Feb. 2007. doi: 10.1086/510523.

[127] A. Gal-Yam, P. Mazzali, E. O. Ofek, P. E. Nugent, S. R. Kulkarni, M. M. Kasliwal, R. M. Quimby, A. V. Filippenko, S. B. Cenko, R. Chornock, R. Waldman, D. Kasen, M. Sullivan, E. C. Beshore, A. J. Drake, R. C. Thomas, J. S. Bloom, D. Poznanski, A. A. Miller, R. J. Foley, J. M. Silverman, I. Arcavi, R. S. Ellis, and J. Deng. Supernova 2007bi as a pair-instability explosion. *Nature*, 462:624–627, Dec. 2009. doi: 10.1038/nature08579.

[128] T. J. Galama, P. M. Vreeswijk, J. van Paradijs, C. Kouveliotou, T. Augusteijn, H. Böhnhardt, J. P. Brewer, V. Doublier, J.-F. Gonzalez, B. Leibundgut, C. Lidman, O. R. Hainaut, F. Patat, J. Heise, J. in't Zand, K. Hurley, P. J. Groot, R. G. Strom, P. A. Mazzali, K. Iwamoto, K. Nomoto, H. Umeda, T. Nakamura, T. R. Young, T. Suzuki, T. Shigeyama, T. Koshut, M. Kippen, C. Robinson, P. de Wildt, R. A. M. J. Wijers, N. Tanvir, J. Greiner, E. Pian, E. Palazzi, F. Frontera, N. Masetti, L. Nicastro, M. Feroci, E. Costa, L. Piro, B. A. Peterson, C. Tinney, B. Boyle, R. Cannon, R. Stathakis, E. Sadler, M. C. Begam, and P. Ianna. An unusual supernova in the error box of the γ-ray burst of 25 April 1998. *Nature*, 395:670–672, Oct. 1998. doi: 10.1038/27150.

[129] K. G. Gayley, S. P. Owocki, and S. R. Cranmer. Sudden Radiative Braking in Colliding Hot-Star Winds. *ApJ*, 475:786–+, Feb. 1997. doi: 10.1086/303573.

[130] R. D. Gehrz and E. P. Ney. Confirmation of Dust Condensation in the Ejecta of Supernova 1987a. *Proceedings of the National Academy of Science*, 87:4354–4357, June 1990. doi: 10.1073/pnas.87.11.4354.

[131] C. L. Gerardy, R. A. Fesen, P. Höflich, and J. C. Wheeler. Detection of CO and Dust Emission in Near-Infrared Spectra of SN 1998S. *AJ*, 119:2968–2981, June 2000. doi: 10.1086/301390.

[132] D. R. Gies and D. L. Lambert. Carbon, nitrogen, and oxygen abundances in early B-type stars. *ApJ*, 387:673–700, Mar. 1992. doi: 10.1086/171116.

[133] R. Gilmozzi, A. Cassatella, J. Clavel, C. Fransson, R. Gonzalez, C. Gry, N. Panagia, A. Talavera, and W. Wamsteker. The progenitor of SN1987A. *Nature*, 328:318–320, July 1987. doi: 10.1038/328318a0.

[134] A. Grafe, C. J. Sweeney, and T. W. Shyn. Measurement of absolute differential cross sections for the excitation of atomic hydrogen to its n =2 level by electron impact. *Phys. Rev. A*, 63:052715, Apr 2001. doi: 10.1103/PhysRevA.63.052715. URL http://link.aps.org/doi/10.1103/PhysRevA.63.052715.

[135] E. K. Grassberg, V. S. Imshennik, and D. K. Nadyozhin. On the Theory of the Light Curves of Supernovate. *Ap&SS*, 10:28–51, Jan. 1971. doi: 10.1007/BF00654604.

[136] R. O. Gray. Is Vega a rapid rotator seen pole on? *JRASC*, 79:237, 1985.

[137] R. O. Gray. The spectroscopic and photometric effects of rotation in the A-type stars. *JRASC*, 82:336–348, Dec. 1988.

[138] R. O. Gray. The Problems with Vega. In C. Sterken, editor, *The Future of Photometric, Spectrophotometric and Polarimetric Standardization*, volume 364, page 305, Apr. 2007.

[139] A. Gregorio, R. Stalio, L. Broadfoot, F. Castelli, M. Hack, and J. Holberg. UVSTAR observations of Adara (epsilon CMa): 575-1250 Å. *A&A*, 383:881–891, Mar. 2002. doi: 10.1051/0004-6361:20020049.

[140] J. H. Groh, T. I. Madura, S. P. Owocki, D. J. Hillier, and G. Weigelt. Is Eta Carinae a Fast Rotator, and How Much Does the Companion Influence the Inner Wind Structure? *ApJL*, 716:L223–L228, June 2010. doi: 10.1088/2041-8205/716/2/L223.

[141] J. H. Groh, K. E. Nielsen, A. Damineli, T. R. Gull, T. I. Madura, D. J. Hillier, M. Teodoro, T. Driebe, G. Weigelt, H. Hartman, F. Kerber, A. T. Okazaki, S. P. Owocki, F. Millour, K. Murakawa, S. Kraus, K.-H. Hofmann, and D. Schertl. Detection of high-velocity material from the wind-wind collision zone of Eta Carinae across the 2009.0 periastron passage. *A&A*, 517:A9, July 2010. doi: 10.1051/0004-6361/200913937.

[142] J. H. Groh, D. J. Hillier, T. I. Madura, and G. Weigelt. On the influence of the companion star in Eta Carinae: 2D radiative transfer modelling of the ultraviolet and optical spectra. *MNRAS*, 423:1623–1640, June 2012. doi: 10.1111/j.1365-2966.2012.20984.x.

[143] C. Gry and E. B. Jenkins. Local clouds: Ionization, temperatures, electron densities and interfaces, from GHRS and IMAPS spectra of epsilon Canis Majoris. *A&A*, 367:617–628, Feb. 2001. doi: 10.1051/0004-6361:20000459.

[144] C. Gry, L. Lemonon, A. Vidal-Madjar, M. Lemoine, and R. Ferlet. The interstellar void in the direction to ϵ CMa: local clouds and hot gas. *A&A*, 302:497, Oct. 1995.

[145] M. Gryziński. Classical theory of atomic collisions. i. theory of inelastic collisions. *Phys. Rev.*, 138:A336–A358, Apr 1965. doi: 10.1103/PhysRev.138.A336. URL http://link.aps.org/doi/10.1103/PhysRev.138.A336.

[146] T. R. Gull, K. E. Nielsen, M. F. Corcoran, T. I. Madura, S. P. Owocki, C. M. P. Russell, D. J. Hillier, K. Hamaguchi, G. V. Kober, K. Weis, O. Stahl, and A. T. Okazaki. The extended interacting wind structure of Eta Carinae. *MNRAS*, 396:1308–1328, July 2009. doi: 10.1111/j.1365-2966.2009.14854.x.

[147] A. F. Gulliver, S. J. Adelman, C. R. Cowley, and J. M. Fletcher. Metallic line profiles of the AO V star VEGA. *ApJ*, 380:223–229, Oct. 1991. doi: 10.1086/170577.

[148] A. F. Gulliver, G. Hill, and S. J. Adelman. Vega: A rapidly rotating pole-on star. *ApJL*, 429:L81–L84, July 1994. doi: 10.1086/187418.

[149] T. Güver and F. Özel. The relation between optical extinction and hydrogen column density in the Galaxy. *MNRAS*, 400:2050–2053, Dec. 2009. doi: 10.1111/j.1365-2966.2009.15598.x.

[150] M. R. Haas, E. F. Erickson, S. D. Lord, D. J. Hollenbach, S. W. J. Colgan, and M. G. Burton. Velocity-resolved far-infrared spectra of forbidden Fe II - Evidence for mixing and clumping in SN 1987A. *ApJ*, 360:257–266, Sept. 1990. doi: 10.1086/169115.

[151] I. Hachisu, M. Kato, and K. Nomoto. A Wide Symbiotic Channel to Type IA Supernovae. *ApJ*, 522:487–503, Sept. 1999. doi: 10.1086/307608.

[152] I. Hachisu, M. Kato, K. Nomoto, and H. Umeda. A New Evolutionary Path to Type IA Supernovae: A Helium-rich Supersoft X-Ray Source Channel. *ApJ*, 519:314–323, July 1999. doi: 10.1086/307370.

[153] N. J. Hammer, H.-T. Janka, and E. Müller. Three-dimensional Simulations of Mixing Instabilities in Supernova Explosions. *ApJ*, 714:1371–1385, May 2010. doi: 10.1088/0004-637X/714/2/1371.

[154] M. Hamuy and P. A. Pinto. Type II Supernovae as Standardized Candles. *ApJL*, 566:L63–L65, Feb. 2002. doi: 10.1086/339676.

[155] M. Hamuy, P. A. Pinto, J. Maza, N. B. Suntzeff, M. M. Phillips, R. G. Eastman, R. C. Smith, C. J. Corbally, D. Burstein, Y. Li, V. Ivanov, A. Moro-Martin, L. G. Strolger, R. E. de Souza, S. dos Anjos, E. M. Green, T. E. Pickering, L. González, R. Antezana, M. Wischnjewsky, G. Galaz, M. Roth, S. E. Persson, and R. A. Schommer. The Distance to SN 1999em from the Expanding Photosphere Method. *ApJ*, 558:615–642, Sept. 2001. doi: 10.1086/322450.

[156] R. Hanbury Brown, J. Davis, and L. R. Allen. The angular diameters of 32 stars. *MNRAS*, 167:121–136, Apr. 1974.

[157] R. P. Harkness, J. C. Wheeler, B. Margon, R. A. Downes, R. P. Kirshner, A. Uomoto, E. S. Barker, A. L. Cochran, H. L. Dinerstein, D. R. Garnett, and R. M. Levreault. The early spectral phase of type Ib supernovae - Evidence for helium. *ApJ*, 317:355–367, June 1987. doi: 10.1086/165283.

[158] S. Heap and D. J. Lindler. Constraining Galaxy Evolution With Hubble's Next Generation Spectral Library. In M. Chávez Dagostino, E. Bertone, D. Rosa Gonzalez, and L. H. Rodriguez-Merino, editors, *New Quests in Stellar Astrophysics. II. Ultraviolet Properties of Evolved Stellar Populations*, pages 273–281, Mar. 2009.

[159] A. G. Hearn. The mass loss from the O 9.5 Ib supergiant, zeta Orionis, derived from the H-alpha profile. *A&A*, 40:277–283, May 1975.

[160] A. Heger, N. Langer, and S. E. Woosley. Presupernova Evolution of Rotating Massive Stars. I. Numerical Method and Evolution of the Internal Stellar Structure. *ApJ*, 528: 368–396, Jan. 2000. doi: 10.1086/308158.

[161] A. Heger, C. L. Fryer, S. E. Woosley, N. Langer, and D. H. Hartmann. How Massive Single Stars End Their Life. *ApJ*, 591:288–300, July 2003. doi: 10.1086/375341.

[162] M. Herant and S. E. Woosley. Postexplosion hydrodynamics of supernovae in red supergiants. *ApJ*, 425:814–828, Apr. 1994. doi: 10.1086/174026.

[163] A. Herrero, R. P. Kudritzki, J. M. Vilchez, D. Kunze, K. Butler, and S. Haser. Intrinsic parameters of galactic luminous OB stars. *A&A*, 261:209–234, July 1992.

[164] W. Hillebrandt, P. Hoeflich, A. Weiss, and J. W. Truran. Explosion of a blue supergiant - A model for supernova SN1987A. *Nature*, 327:597–600, June 1987. doi: 10.1038/327597a0.

[165] D. J. Hillier. Modeling the extended atmospheres of WN stars. *ApJS*, 63:947–964, Apr. 1987. doi: 10.1086/191187.

[166] D. J. Hillier. An iterative method for the solution of the statistical and radiative equilibrium equations in expanding atmospheres. *A&A*, 231:116–124, May 1990.

[167] D. J. Hillier and D. A. Allen. A spectroscopic investigation of Eta Carinae and the Homunculus Nebula. I - Overview of the spectra. *A&A*, 262:153–170, Aug. 1992.

[168] D. J. Hillier and L. Dessart. Time-dependent radiative transfer calculations for supernovae. *MNRAS*, 424:252–271, July 2012. doi: 10.1111/j.1365-2966.2012.21192.x.

[169] D. J. Hillier and D. L. Miller. The Treatment of Non-LTE Line Blanketing in Spherically Expanding Outflows. *ApJ*, 496:407–+, Mar. 1998. doi: 10.1086/305350.

[170] D. J. Hillier, P. A. Crowther, F. Najarro, and A. W. Fullerton. An optical and near-IR spectroscopic study of the extreme P Cygni-type supergiant HDE 316285. *A&A*, 340: 483–496, Dec. 1998.

[171] D. J. Hillier, K. Davidson, K. Ishibashi, and T. Gull. Eta Carinae: The Central Star. In T. R. Gull, S. Johannson, and K. Davidson, editors, *Eta Carinae and Other Mysterious Stars: The Hidden Opportunities of Emission Spectroscopy*, volume 242 of *Astronomical Society of the Pacific Conference Series*, page 15, 2001.

[172] D. J. Hillier, K. Davidson, K. Ishibashi, and T. Gull. On the Nature of the Central Source in η Carinae. *ApJ*, 553:837–860, June 2001. doi: 10.1086/320948.

[173] D. J. Hillier, T. Gull, K. Nielsen, G. Sonneborn, R. Iping, N. Smith, M. Corcoran, A. Damineli, F. W. Hamann, J. C. Martin, and K. Weis. The UV Scattering Halo of the Central Source Associated with η Carinae. *ApJ*, 642:1098–1116, May 2006. doi: 10.1086/501225.

[174] J. Hjorth, J. Sollerman, P. Møller, J. P. U. Fynbo, S. E. Woosley, C. Kouveliotou, N. R. Tanvir, J. Greiner, M. I. Andersen, A. J. Castro-Tirado, J. M. Castro Cerón, A. S. Fruchter, J. Gorosabel, P. Jakobsson, L. Kaper, S. Klose, N. Masetti, H. Pedersen, K. Pedersen, E. Pian, E. Palazzi, J. E. Rhoads, E. Rol, E. P. J. van den Heuvel, P. M. Vreeswijk, D. Watson, and R. A. M. J. Wijers. A very energetic supernova associated with the γ-ray burst of 29 March 2003. *Nature*, 423:847–850, June 2003. doi: 10.1038/nature01750.

[175] M. G. Hoare, J. E. Drew, and M. Denby. The first measurement of the Lyman continuum emission from normal stars. *MNRAS*, 262:L19–L22, May 1993.

[176] P. Hoeflich, J. C. Wheeler, and F. K. Thielemann. Type IA Supernovae: Influence of the Initial Composition on the Nucleosynthesis, Light Curves, and Spectra and Consequences for the Determination of Omega M and Lambda. *ApJ*, 495:617, Mar. 1998. doi: 10.1086/305327.

[177] J. C. Houck and C. Fransson. Analysis of the Late Optical Spectra of SN 1993J. *ApJ*, 456:811–+, Jan. 1996. doi: 10.1086/176699.

[178] I. Hubeny and T. Lanz. Non-LTE line-blanketed model atmospheres of hot stars. 1: Hybrid complete linearization/accelerated lambda iteration method. *ApJ*, 439:875–904, Feb. 1995. doi: 10.1086/175226.

[179] S. Hubrig, M. Briquet, P. De Cat, M. Schöller, T. Morel, and I. Ilyin. New magnetic field measurements of β Cephei stars and slowly pulsating B stars. *Astronomische Nachrichten*, 330:317, Apr. 2009. doi: 10.1002/asna.200811187.

[180] J. P. Hughes, C. E. Rakowski, D. N. Burrows, and P. O. Slane. Nucleosynthesis and Mixing in Cassiopeia A. *ApJL*, 528:L109–L113, Jan. 2000. doi: 10.1086/312438.

[181] R. M. Humphreys and K. Davidson. Studies of luminous stars in nearby galaxies. III - Comments on the evolution of the most massive stars in the Milky Way and the Large Magellanic Cloud. *ApJ*, 232:409–420, Sept. 1979. doi: 10.1086/157301.

[182] R. M. Humphreys and K. Davidson. The luminous blue variables: Astrophysical geysers. *PASP*, 106:1025–1051, Oct. 1994. doi: 10.1086/133478.

[183] U. Hwang, J. M. Laming, C. Badenes, F. Berendse, J. Blondin, D. Cioffi, T. DeLaney, D. Dewey, R. Fesen, K. A. Flanagan, C. L. Fryer, P. Ghavamian, J. P. Hughes, J. A. Morse, P. P. Plucinsky, R. Petre, M. Pohl, L. Rudnick, R. Sankrit, P. O. Slane, R. K. Smith, J. Vink, and J. S. Warren. A Million Second Chandra View of Cassiopeia A. *ApJL*, 615:L117–L120, Nov. 2004. doi: 10.1086/426186.

[184] I. Iben, Jr. and A. V. Tutukov. On the evolution of close binaries with components of initial mass between 3 solar masses and 12 solar masses. *ApJS*, 58:661–710, Aug. 1985. doi: 10.1086/191054.

[185] K. Ishibashi, M. F. Corcoran, K. Davidson, J. H. Swank, R. Petre, S. A. Drake, A. Damineli, and S. White. Recurrent X-Ray Emission Variations of η Carinae and the Binary Hypothesis. *ApJ*, 524:983–987, Oct. 1999. doi: 10.1086/307859.

[186] K. Ishibashi, T. R. Gull, K. Davidson, N. Smith, T. Lanz, D. Lindler, K. Feggans, E. Verner, B. E. Woodgate, R. A. Kimble, C. W. Bowers, S. Kraemer, S. R. Heap, A. C. Danks, S. P. Maran, C. L. Joseph, M. E. Kaiser, J. L. Linsky, F. Roesler, and D. Weistrop. Discovery of a Little Homunculus within the Homunculus Nebula of η Carinae. *AJ*, 125:3222–3236, June 2003. doi: 10.1086/375306.

[187] K. Iwamoto, T. R. Young, N. Nakasato, T. Shigeyama, K. Nomoto, I. Hachisu, and H. Saio. Instabilities and Mixing in SN 1993J. *ApJ*, 477:865–+, Mar. 1997. doi: 10.1086/303729.

[188] C. Jamar, D. Macau-Hercot, A. Monfils, G. I. Thompson, L. Houziaux, and R. Wilson. *Ultraviolet bright-star spectrophotometric catalogue. A compilation of absolute spectrophotometric data obtained with the Sky Survey Telescope (S2/68) on the European Astronomical Satellite TD-1.* Nov. 1976.

[189] H.-T. Janka, R. Buras, F. S. Kitaura Joyanes, A. Marek, M. Rampp, and L. Scheck. Neutrino-driven supernovae: An accretion instability in a nuclear physics controlled environment. *Nuclear Physics A*, 758:19–26, July 2005. doi: 10.1016/j.nuclphysa.2005.05.008.

[190] H.-T. Janka, K. Langanke, A. Marek, G. Martínez-Pinedo, and B. Müller. Theory of core-collapse supernovae. *Phys. Rep.*, 442:38–74, Apr. 2007. doi: 10.1016/j.physrep.2007.02.002.

[191] D. J. Jeffery. Analysis of SN 1987A polarimetry. *ApJ*, 375:264–287, July 1991. doi: 10.1086/170187.

[192] A. Jerkstrand, C. Fransson, and C. Kozma. The ^{44}Ti-powered spectrum of SN 1987A. *A&A*, 530:A45+, June 2011. doi: 10.1051/0004-6361/201015937.

[193] C. C. Joggerst, A. Almgren, and S. E. Woosley. Three-dimensional Simulations of Rayleigh-Taylor Mixing in Core-collapse Supernovae with Castro. *ApJ*, 723:353–363, Nov. 2010. doi: 10.1088/0004-637X/723/1/353.

[194] S. Johansson, T. R. Gull, H. Hartman, and V. S. Letokhov. Metastable hydrogen absorption in ejecta close to η Carinae. *A&A*, 435:183–189, May 2005. doi: 10.1051/0004-6361:20041193.

[195] L. C. Johnson. Approximations for Collisional and Radiative Transition Rates in Atomic Hydrogen. *ApJ*, 174:227, May 1972. doi: 10.1086/151486.

[196] P. C. Joss, P. Podsiadlowski, J. J. L. Hsu, and S. Rappaport. Is supernova 1987A a stripped asymptotic-branch giant in a binary system? *Nature*, 331:237–240, Jan. 1988. doi: 10.1038/331237a0.

[197] A. Kashi and N. Soker. The orientation of the η Carinae binary system. *MNRAS*, 390:1751–1761, Nov. 2008. doi: 10.1111/j.1365-2966.2008.13883.x.

[198] M. Kato and I. Hachisu. A New Estimation of Mass Accumulation Efficiency in Helium Shell Flashestoward Type IA Supernova Explosions. *ApJL*, 513:L41–L44, Mar. 1999. doi: 10.1086/311893.

[199] K. S. Kawabata, M. Tanaka, K. Maeda, T. Hattori, K. Nomoto, N. Tominaga, and M. Yamanaka. Extremely Luminous Supernova 2006gy at Late Phase: Detection of Optical Emission from Supernova. *ApJ*, 697:747–757, May 2009. doi: 10.1088/0004-637X/697/1/747.

[200] K. Kifonidis, T. Plewa, H.-T. Janka, and E. Müller. Non-spherical core collapse supernovae. I. Neutrino-driven convection, Rayleigh-Taylor instabilities, and the formation and propagation of metal clumps. *A&A*, 408:621–649, Sept. 2003. doi: 10.1051/0004-6361:20030863.

[201] K. Kifonidis, T. Plewa, L. Scheck, H.-T. Janka, and E. Müller. Non-spherical core collapse supernovae. II. The late-time evolution of globally anisotropic neutrino-driven explosions and their implications for SN 1987 A. *A&A*, 453:661–678, July 2006. doi: 10.1051/0004-6361:20054512.

[202] Y.-K. Kim and M. E. Rudd. Binary-encounter-dipole model for electron-impact ionization. *Phys. Rev. A*, 50:3954–3967, Nov 1994. doi: 10.1103/PhysRevA.50.3954. URL http://link.aps.org/doi/10.1103/PhysRevA.50.3954.

[203] N. L. King, A. Nota, J. R. Walsh, N. Panagia, T. R. Gull, A. Pasquali, M. Clampin, and L. E. Bergeron. A Hubble Space Telescope Polarization Study of Dust in the η Carinae Homunculus. *ApJ*, 581:285–306, Dec. 2002. doi: 10.1086/344168.

[204] R. P. Kirshner and J. Kwan. Distances to extragalactic supernovae. *ApJ*, 193:27–36, Oct. 1974. doi: 10.1086/153123.

[205] R. P. Kirshner and J. Kwan. The envelopes of type II supernovae. *ApJ*, 197:415–424, Apr. 1975. doi: 10.1086/153527.

[206] F. S. Kitaura, H.-T. Janka, and W. Hillebrandt. Explosions of O-Ne-Mg cores, the Crab supernova, and subluminous type II-P supernovae. *A&A*, 450:345–350, Apr. 2006. doi: 10.1051/0004-6361:20054703.

[207] R. I. Klein and R. A. Chevalier. X-ray bursts from Type II supernovae. *ApJL*, 223: L109–L112, Aug. 1978. doi: 10.1086/182740.

[208] I. K. W. Kleiser, D. Poznanski, D. Kasen, T. R. Young, R. Chornock, A. V. Filippenko, P. Challis, M. Ganeshalingam, R. P. Kirshner, W. Li, T. Matheson, P. E. Nugent, and J. M. Silverman. Peculiar Type II supernovae from blue supergiants. *MNRAS*, 415: 372–382, July 2011. doi: 10.1111/j.1365-2966.2011.18708.x.

[209] C. S. Kochanek. The Astrophysical Implications of Dust Formation during the Eruptions of Hot, Massive Stars. *ApJ*, 743:73, Dec. 2011. doi: 10.1088/0004-637X/743/1/73.

[210] C. S. Kochanek, J. F. Beacom, M. D. Kistler, J. L. Prieto, K. Z. Stanek, T. A. Thompson, and H. Yüksel. A Survey About Nothing: Monitoring a Million Supergiants for Failed Supernovae. *ApJ*, 684:1336–1342, Sept. 2008. doi: 10.1086/590053.

[211] R. Kotak. Core-Collapse Supernovae as Dust Producers. In F. Bresolin, P. A. Crowther, and J. Puls, editors, *IAU Symposium*, volume 250 of *IAU Symposium*, pages 437–442, June 2008. doi: 10.1017/S1743921308020802.

[212] R. Kotak and J. S. Vink. Luminous blue variables as the progenitors of supernovae with quasi-periodic radio modulations. *A&A*, 460:L5–L8, Dec. 2006. doi: 10.1051/0004-6361:20065800.

[213] K. Kotake, H. Sawai, S. Yamada, and K. Sato. Magnetorotational Effects on Anisotropic Neutrino Emission and Convection in Core-Collapse Supernovae. *ApJ*, 608:391–404, June 2004. doi: 10.1086/392530.

[214] C. Kozma and C. Fransson. Gamma-ray deposition and nonthermal excitation in supernovae. *ApJ*, 390:602–621, May 1992. doi: 10.1086/171311.

[215] C. Kozma and C. Fransson. Late Spectral Evolution of SN 1987A. I. Temperature and Ionization. *ApJ*, 496:946–+, Mar. 1998. doi: 10.1086/305409.

[216] C. Kozma and C. Fransson. Late Spectral Evolution of SN 1987A. II. Line Emission. *ApJ*, 497:431–+, Apr. 1998. doi: 10.1086/305452.

[217] O. Krause, S. M. Birkmann, T. Usuda, T. Hattori, M. Goto, G. H. Rieke, and K. A. Misselt. The Cassiopeia A Supernova Was of Type IIb. *Science*, 320:1195–, May 2008. doi: 10.1126/science.1155788.

[218] S. Kumagai, T. Shigeyama, K. Nomoto, M. Itoh, and J. Nishimura. Hard X-rays and gamma-rays from SN 1987 A and mixing of the supernova ejecta. *A&A*, 197:L7–L10, May 1988.

[219] W. Kundt. Are supernova explosions driven by magnetic springs. *Nature*, 261:673, June 1976. doi: 10.1038/261673a0.

[220] R. L. Kurucz. Model Atmospheres for Population Synthesis. In B. Barbuy & A. Renzini, editor, *The Stellar Populations of Galaxies*, volume 149 of *IAU Symposium*, page 225, 1992.

[221] R. L. Kurucz. Including All the Lines. In I. Hubeny, J. M. Stone, K. MacGregor, and K. Werner, editors, *American Institute of Physics Conference Series*, volume 1171 of *American Institute of Physics Conference Series*, pages 43–51, Sept. 2009. doi: 10.1063/1.3250087.

[222] R. Lallement, J. L. Linsky, J. Lequeux, and V. B. Baranov. Physical and Chemical Characteristics of the ISM Inside and Outside the Heliosphere. *SSR*, 78:299–304, Oct. 1996. doi: 10.1007/BF00170816.

[223] H. J. G. Lamers and A. W. A. Pauldrach. The formation of outflowing disks around early-type stars by bi-stable radiation-driven winds. *A&A*, 244:L5–L8, Apr. 1991.

[224] H. J. G. L. M. Lamers. Mass loss from luminous blue variables. In K. Davidson, A. F. J. Moffat, and H. J. G. L. M. Lamers, editors, *IAU Colloq. 113: Physics of Luminous Blue Variables*, volume 157 of *Astrophysics and Space Science Library*, pages 135–146, 1989.

[225] A. U. Landolt. UBVRI photometric standard stars in the magnitude range 11.5-16.0 around the celestial equator. *AJ*, 104:340–371, July 1992. doi: 10.1086/116242.

[226] N. Langer, M. F. El Eid, and I. Baraffe. Blue supergiant supernova progenitors. *A&A*, 224:L17–L20, Oct. 1989.

[227] N. Langer, A. Deutschmann, S. Wellstein, and P. Höflich. The evolution of main sequence star + white dwarf binary systems towards Type Ia supernovae. *A&A*, 362: 1046–1064, Oct. 2000.

[228] K. Lefever, J. Puls, T. Morel, C. Aerts, L. Decin, and M. Briquet. Spectroscopic determination of the fundamental parameters of 66 B-type stars in the field-of-view of the CoRoT satellite. *A&A*, 515:A74, June 2010. doi: 10.1051/0004-6361/200911956.

[229] B. Leibundgut and N. B. Suntzeff. Optical Light Curves of Supernovae. In K. Weiler, editor, *Supernovae and Gamma-Ray Bursters*, volume 598 of *Lecture Notes in Physics, Berlin Springer Verlag*, pages 77–90, 2003.

[230] E. J. Lentz, E. Baron, D. Branch, P. H. Hauschildt, and P. E. Nugent. Metallicity Effects in Non-LTE Model Atmospheres of Type IA Supernovae. *ApJ*, 530:966–976, Feb. 2000. doi: 10.1086/308400.

[231] E. J. Lentz, E. Baron, P. Lundqvist, D. Branch, P. H. Hauschildt, C. Fransson, P. Garnavich, N. Bastian, A. V. Filippenko, R. P. Kirshner, P. M. Challis, S. Jha, B. Leibundgut, R. McCray, E. Michael, N. Panagia, M. M. Phillips, C. S. J. Pun, B. Schmidt, G. Sonneborn, N. B. Suntzeff, L. Wang, and J. C. Wheeler. Analysis of Type IIn SN 1998S: Effects of Circumstellar Interaction on Observed Spectra. *ApJ*, 547:406–411, Jan. 2001. doi: 10.1086/318363.

[232] D. C. Leonard and A. V. Filippenko. Spectropolarimetry of Core-Collapse Supernovae. In M. Turatto, S. Benetti, L. Zampieri, and W. Shea, editors, *1604-2004: Supernovae as Cosmological Lighthouses*, volume 342 of *Astronomical Society of the Pacific Conference Series*, page 330, Dec. 2005.

[233] D. C. Leonard, A. V. Filippenko, A. J. Barth, and T. Matheson. Evidence for Asphericity in the Type IIN Supernova SN 1998S. *ApJ*, 536:239–254, June 2000. doi: 10.1086/308910.

[234] D. C. Leonard, A. V. Filippenko, D. R. Ardila, and M. S. Brotherton. Is It Round? Spectropolarimetry of the Type II-p Supernova 1999EM. *ApJ*, 553:861–885, June 2001. doi: 10.1086/320959.

[235] D. C. Leonard, A. V. Filippenko, E. L. Gates, W. Li, R. G. Eastman, A. J. Barth, S. J. Bus, R. Chornock, A. L. Coil, S. Frink, C. A. Grady, A. W. Harris, M. A. Malkan, T. Matheson, A. Quirrenbach, and R. R. Treffers. The Distance to SN 1999em in NGC 1637 from the Expanding Photosphere Method. *PASP*, 114:35–64, Jan. 2002. doi: 10.1086/324785.

[236] D. C. Leonard, S. M. Kanbur, C. C. Ngeow, and N. R. Tanvir. The Cepheid Distance to NGC 1637: A Direct Test of the Expanding Photosphere Method Distance to SN 1999em. *ApJ*, 594:247–278, Sept. 2003. doi: 10.1086/376831.

[237] D. C. Leonard, A. V. Filippenko, M. Ganeshalingam, F. J. D. Serduke, W. Li, B. J. Swift, A. Gal-Yam, R. J. Foley, D. B. Fox, S. Park, J. L. Hoffman, and D. S. Wong. A non-spherical core in the explosion of supernova SN 2004dj. *Nature*, 440:505–507, Mar. 2006. doi: 10.1038/nature04558.

[238] C. Li, D. J. Hillier, and L. Dessart. Non-thermal excitation and ionization in supernovae. *MNRAS*, 426:1671–1686, Oct. 2012. doi: 10.1111/j.1365-2966.2012.21198.x.

[239] H. Li and R. McCray. The He I emission lines of SN 1987A. *ApJ*, 441:821–829, Mar. 1995. doi: 10.1086/175405.

[240] H. Li, R. McCray, and R. A. Sunyaev. Iron, Cobalt, and Nickel in SN 1987A. *ApJ*, 419:824, Dec. 1993. doi: 10.1086/173534.

[241] W. Li, J. S. Bloom, P. Podsiadlowski, A. A. Miller, S. B. Cenko, S. W. Jha, M. Sullivan, D. A. Howell, P. E. Nugent, N. R. Butler, E. O. Ofek, M. M. Kasliwal, J. W. Richards, A. Stockton, H.-Y. Shih, L. Bildsten, M. M. Shara, J. Bibby, A. V. Filippenko, M. Ganeshalingam, J. M. Silverman, S. R. Kulkarni, N. M. Law, D. Poznanski, R. M. Quimby, C. McCully, B. Patel, K. Maguire, and K. J. Shen. Exclusion of a luminous red giant as a companion star to the progenitor of supernova SN 2011fe. *Nature*, 480:348–350, Dec. 2011. doi: 10.1038/nature10646.

[242] W. Li, J. Leaman, R. Chornock, A. V. Filippenko, D. Poznanski, M. Ganeshalingam, X. Wang, M. Modjaz, S. Jha, R. J. Foley, and N. Smith. Nearby supernova rates from the Lick Observatory Supernova Search - II. The observed luminosity functions and fractions of supernovae in a complete sample. *MNRAS*, 412:1441–1472, Apr. 2011. doi: 10.1111/j.1365-2966.2011.18160.x.

[243] X.-D. Li and E. P. J. van den Heuvel. Evolution of white dwarf binaries: supersoft X-ray sources and progenitors of type IA supernovae. *A&A*, 322:L9–L12, June 1997.

[244] M. Limongi and A. Tornambe. He stars and He-accreting CO white dwarfs. *ApJ*, 371: 317–331, Apr. 1991. doi: 10.1086/169894.

[245] Q.-Z. Liu, J.-Y. Hu, H.-R. Hang, Y.-L. Qiu, Z.-X. Zhu, and Q.-Y. Qiao. The supernova 1998S in NGC 3877: Another supernova with Wolf-Rayet star features in pre-maximum spectrum. *A&APS*, 144:219–225, June 2000. doi: 10.1051/aas:2000208.

[246] W.-M. Liu, W.-C. Chen, B. Wang, and Z. W. Han. Helium-star evolutionary channel to super-Chandrasekhar mass type Ia supernovae. *A&A*, 523:A3, Nov. 2010. doi: 10.1051/0004-6361/201014180.

[247] E. Livne. An implicit method for two-dimensional hydrodynamics. *ApJ*, 412:634–647, Aug. 1993. doi: 10.1086/172950.

[248] L. B. Lucy. Nonthermal excitation of helium in type Ib supernovae. *ApJ*, 383:308–313, Dec. 1991. doi: 10.1086/170787.

[249] A. G. Lyne and D. R. Lorimer. High birth velocities of radio pulsars. *Nature*, 369: 127–129, May 1994. doi: 10.1038/369127a0.

[250] L. S. Lyubimkov, S. I. Rostopchin, and D. L. Lambert. Surface abundances of light elements for a large sample of early B-type stars - III. An analysis of helium lines in

spectra of 102 stars. *MNRAS*, 351:745–767, June 2004. doi: 10.1111/j.1365-2966.2004.07825.x.

[251] T. I. Madura, T. R. Gull, S. P. Owocki, J. H. Groh, A. T. Okazaki, and C. M. P. Russell. Constraining the absolute orientation of η Carinae's binary orbit: a 3D dynamical model for the broad [Fe III] emission. *MNRAS*, 420:2064–2086, Mar. 2012. doi: 10.1111/j.1365-2966.2011.20165.x.

[252] A. Maeder and G. Meynet. Diffusive mixing by shears in rotating stars. *A&A*, 313:140–144, Sept. 1996.

[253] A. Maeder and G. Meynet. The Evolution of Rotating Stars. *ARA&A*, 38:143–190, 2000. doi: 10.1146/annurev.astro.38.1.143.

[254] J. Maíz-Apellániz. The Origin of the Local Bubble. *ApJL*, 560:L83–L86, Oct. 2001. doi: 10.1086/324016.

[255] F. Mannucci, M. Della Valle, N. Panagia, E. Cappellaro, G. Cresci, R. Maiolino, A. Petrosian, and M. Turatto. The supernova rate per unit mass. *A&A*, 433:807–814, Apr. 2005. doi: 10.1051/0004-6361:20041411.

[256] W. L. F. Marcolino, D. J. Hillier, F. X. de Araujo, and C. B. Pereira. Detailed Far-Ultraviolet to Optical Analysis of Four [WR] Stars. *ApJ*, 654:1068–1086, Jan. 2007. doi: 10.1086/509316.

[257] J. C. Martin, K. Davidson, and M. D. Koppelman. The Chrysalis Opens? Photometry from the η Carinae Hubble Space Telescope Treasury Project, 2002-2006. *AJ*, 132:2717–2728, Dec. 2006. doi: 10.1086/508933.

[258] F. Martins, D. Schaerer, and D. J. Hillier. On the effective temperature scale of O stars. *A&A*, 382:999–1004, Feb. 2002. doi: 10.1051/0004-6361:20011703.

[259] S. M. Matz, G. H. Share, M. D. Leising, E. L. Chupp, and W. T. Vestrand. Gamma-ray line emission from SN1987A. *Nature*, 331:416–418, Feb. 1988. doi: 10.1038/331416a0.

[260] R. McCray. Supernova 1987A revisited. *ARA&A*, 31:175–216, 1993. doi: 10.1146/annurev.aa.31.090193.001135.

[261] J. Meaburn, R. D. Wolstencroft, and J. R. Walsh. Echelle and spectropolarimetric observations of the Eta Carinae nebulosity. *A&A*, 181:333–342, July 1987.

[262] J. Meaburn, J. R. Walsh, and R. D. Wolstencroft. The outflowing dust around Eta Carinae. *A&A*, 268:283–293, Feb. 1993.

[263] A. Mehner, K. Davidson, J. C. Martin, R. M. Humphreys, K. Ishibashi, and G. J. Ferland. Critical Differences and Clues in Eta Car's 2009 Event. *ApJ*, 740:80, Oct. 2011. doi: 10.1088/0004-637X/740/2/80.

[264] D. L. Meier, R. I. Epstein, W. D. Arnett, and D. N. Schramm. Magnetohydrodynamic phenomena in collapsing stellar cores. *ApJ*, 204:869–878, Mar. 1976. doi: 10.1086/154235.

[265] W. P. S. Meikle, J. Spyromilio, G.-F. Varani, and D. A. Allen. Spectroscopy of supernova 1987A at 1-5 microns. I - The first year. *MNRAS*, 238:193–223, May 1989.

[266] W. P. S. Meikle, S. Mattila, A. Pastorello, C. L. Gerardy, R. Kotak, J. Sollerman, S. D. Van Dyk, D. Farrah, A. V. Filippenko, P. Höflich, P. Lundqvist, M. Pozzo, and J. C. Wheeler. A Spitzer Space Telescope Study of SN 2003gd: Still No Direct Evidence that Core-Collapse Supernovae are Major Dust Factories. *ApJ*, 665:608–617, Aug. 2007. doi: 10.1086/519733.

[267] D. Mihalas. *Stellar atmospheres /2nd edition/*. 1978.

[268] D. Mihalas and B. W. Mihalas. *Foundations of radiation hydrodynamics*. 1984.

[269] D. Mihalas, P. B. Kunasz, and D. G. Hummer. Solution of the comoving frame equation of transfer in spherically symmetric flows. I - Computational method for equivalent-two-level-atom source functions. *ApJ*, 202:465–489, Dec. 1975. doi: 10.1086/153996.

[270] D. Mihalas, P. B. Kunasz, and D. G. Hummer. Solution of the Comoving-Frame Equation of Transfer in Spherically Symmetric Flows. III. Effect of Aberration and Advection Terms. *ApJ*, 206:515–524, June 1976. doi: 10.1086/154407.

[271] D. Mihalas, P. B. Kunasz, and D. G. Hummer. Solution of the comoving-frame equation of transfer in spherically symmetric flows. IV - Frequency-dependent source functions for scattering by atoms and electrons. *ApJ*, 210:419–433, Dec. 1976. doi: 10.1086/154845.

[272] A. A. Miller, N. Smith, W. Li, J. S. Bloom, R. Chornock, A. V. Filippenko, and J. X. Prochaska. New Observations of the Very Luminous Supernova 2006gy: Evidence for Echoes. *AJ*, 139:2218–2229, June 2010. doi: 10.1088/0004-6256/139/6/2218.

[273] R. Minkowski. Spectra of Supernovae. *PASP*, 53:224–+, Aug. 1941. doi: 10.1086/125315.

[274] R. C. Mitchell, E. Baron, D. Branch, P. Lundqvist, S. Blinnikov, P. H. Hauschildt, and C. S. J. Pun. ^{56}Ni Mixing in the Outer Layers of SN 1987A. *ApJ*, 556:979–986, Aug. 2001. doi: 10.1086/321623.

[275] T. Morel, S. Hubrig, and M. Briquet. Nitrogen enrichment, boron depletion and magnetic fields in slowly-rotating B-type dwarfs. *A&A*, 481:453–463, Apr. 2008. doi: 10.1051/0004-6361:20078999.

[276] H. L. Morgan and M. G. Edmunds. Dust formation in early galaxies. *MNRAS*, 343:427–442, Aug. 2003. doi: 10.1046/j.1365-8711.2003.06681.x.

[277] J. A. Morse, K. Davidson, J. Bally, D. Ebbets, B. Balick, and A. Frank. Hubble Space Telescope Wide Field Planetary Camera 2 Observations of eta Carinae. *AJ*, 116:2443–2461, Nov. 1998. doi: 10.1086/300581.

[278] J. A. Morse, J. R. Kellogg, J. Bally, K. Davidson, B. Balick, and D. Ebbets. Hubble Space Telescope Proper-Motion Measurements of the η Carinae Nebula. *ApJL*, 548: L207–L211, Feb. 2001. doi: 10.1086/319092.

[279] D. C. Morton and T. F. Adams. Effective Temperatures and Bolometric Corrections of Early-Type Stars. *ApJ*, 151:611, Feb. 1968. doi: 10.1086/149461.

[280] E. Mueller, B. Fryxell, and D. Arnett. Instability and clumping in SN 1987A. *A&A*, 251:505–514, Nov. 1991.

[281] E. S. Myra and S. A. Bludman. Neutrino transport and the prompt mechanism for type II supernovae. *ApJ*, 340:384–395, May 1989. doi: 10.1086/167401.

[282] F. Najarro, R. P. Kudritzki, J. P. Cassinelli, O. Stahl, and D. J. Hillier. Stellar winds and the EUV continuum excess of early B-giants. *A&A*, 306:892, Feb. 1996.

[283] F. Najarro, D. J. Hillier, and O. Stahl. A spectroscopic investigation of P Cygni. I. H and HeI lines. *A&A*, 326:1117–1134, Oct. 1997.

[284] K. Nakazato, K. Sumiyoshi, H. Suzuki, and S. Yamada. Oscillation and future detection of failed supernova neutrinos from a black-hole-forming collapse. *Phys. Rev. D*, 78(8): 083014, Oct. 2008. doi: 10.1103/PhysRevD.78.083014.

[285] K. E. Nielsen, M. F. Corcoran, T. R. Gull, D. J. Hillier, K. Hamaguchi, S. Ivarsson, and D. J. Lindler. η Carinae across the 2003.5 Minimum: Spectroscopic Evidence for Massive Binary Interactions. *ApJ*, 660:669–686, May 2007. doi: 10.1086/513006.

[286] K. Nomoto. Accreting white dwarf models for type I supernovae. I - Presupernova evolution and triggering mechanisms. *ApJ*, 253:798–810, Feb. 1982. doi: 10.1086/159682.

[287] K. Nomoto. Accreting white dwarf models for type 1 supernovae. II - Off-center detonation supernovae. *ApJ*, 257:780–792, June 1982. doi: 10.1086/160031.

[288] K. Nomoto and D. Sugimoto. Rejuvenation of Helium White Dwarfs by Mass Accretion. *PASJ*, 29:765–780, 1977.

[289] K. Nomoto, S. Wanajo, Y. Kamiya, N. Tominaga, and H. Umeda. Chemical Yields from Supernovae and Hypernovae. In J. Andersen, J. Bland-Hawthorn, & B. Nordström, editor, *IAU Symposium*, volume 254 of *IAU Symposium*, pages 355–368, Mar. 2009. doi: 10.1017/S1743921308027816.

[290] T. Nozawa, T. Kozasa, H. Umeda, K. Maeda, and K. Nomoto. Dust in the Early Universe: Dust Formation in the Ejecta of Population III Supernovae. *ApJ*, 598:785–803, Dec. 2003. doi: 10.1086/379011.

[291] P. E. Nugent, M. Sullivan, S. B. Cenko, R. C. Thomas, D. Kasen, D. A. Howell, D. Bersier, J. S. Bloom, S. R. Kulkarni, M. T. Kandrashoff, A. V. Filippenko, J. M. Silverman, G. W. Marcy, A. W. Howard, H. T. Isaacson, K. Maguire, N. Suzuki, J. E. Tarlton, Y.-C. Pan, L. Bildsten, B. J. Fulton, J. T. Parrent, D. Sand, P. Podsiadlowski, F. B. Bianco, B. Dilday, M. L. Graham, J. Lyman, P. James, M. M. Kasliwal, N. M. Law, R. M. Quimby, I. M. Hook, E. S. Walker, P. Mazzali, E. Pian, E. O. Ofek, A. Gal-Yam, and D. Poznanski. Supernova SN 2011fe from an exploding carbon-oxygen white dwarf star. *Nature*, 480:344–347, Dec. 2011. doi: 10.1038/nature10644.

[292] M. Obergaulinger, M. A. Aloy, and E. Müller. Axisymmetric simulations of magneto-rotational core collapse: dynamics and gravitational wave signal. *A&A*, 450:1107–1134, May 2006. doi: 10.1051/0004-6361:20054306.

[293] E. O. Ofek, P. B. Cameron, M. M. Kasliwal, A. Gal-Yam, A. Rau, S. R. Kulkarni, D. A. Frail, P. Chandra, S. B. Cenko, A. M. Soderberg, and S. Immler. SN 2006gy: An Extremely Luminous Supernova in the Galaxy NGC 1260. *ApJL*, 659:L13–L16, Apr. 2007. doi: 10.1086/516749.

[294] A. T. Okazaki, S. P. Owocki, C. M. P. Russell, and M. F. Corcoran. Modelling the RXTE light curve of η Carinae from a 3D SPH simulation of its binary wind collision. *MNRAS*, 388:L39–L43, July 2008. doi: 10.1111/j.1745-3933.2008.00496.x.

[295] C. B. Opal, W. K. Peterson, and E. C. Beaty. Measurements of Secondary-Electron Spectra Produced by Electron Impact Ionization of a Number of Simple Gases. *JChPh*, 55:4100–4106, Oct. 1971. doi: 10.1063/1.1676707.

[296] D. E. Osterbrock. *Astrophysics of gaseous nebulae*. 1974.

[297] S. P. Owocki, S. R. Cranmer, and K. G. Gayley. Inhibition FO Wind Compressed Disk Formation by Nonradial Line-Forces in Rotating Hot-Star Winds. *ApJL*, 472:L115+, Dec. 1996. doi: 10.1086/310372.

[298] S. P. Owocki, K. G. Gayley, and S. R. Cranmer. Effects of Gravity Darkening on Radiatively Driven Mass Loss from Rapidly Rotating Stars. 131:237–+, 1998.

[299] N. Panagia. A Geometric Determination of the Distance to SN 1987A and the LMC. In J.-M. Marcaide & K. W. Weiler, editor, *IAU Colloq. 192: Cosmic Explosions, On the 10th Anniversary of SN1993J*, pages 585–+, 2005.

[300] A. Pastorello, E. Baron, D. Branch, L. Zampieri, M. Turatto, M. Ramina, S. Benetti, E. Cappellaro, M. Salvo, F. Patat, A. Piemonte, J. Sollerman, B. Leibundgut, and G. Altavilla. SN 1998A: explosion of a blue supergiant. *MNRAS*, 360:950–962, July 2005. doi: 10.1111/j.1365-2966.2005.09079.x.

[301] A. Pastorello, S. J. Smartt, S. Mattila, J. J. Eldridge, D. Young, K. Itagaki, H. Yamaoka, H. Navasardyan, S. Valenti, F. Patat, I. Agnoletto, T. Augusteijn, S. Benetti, E. Cappellaro, T. Boles, J.-M. Bonnet-Bidaud, M. T. Botticella, F. Bufano, C. Cao, J. Deng, M. Dennefeld, N. Elias-Rosa, A. Harutyunyan, F. P. Keenan, T. Iijima, V. Lorenzi, P. A. Mazzali, X. Meng, S. Nakano, T. B. Nielsen, J. V. Smoker, V. Stanishev, M. Turatto, D. Xu, and L. Zampieri. A giant outburst two years before the core-collapse of a massive star. *Nature*, 447:829–832, June 2007. doi: 10.1038/nature05825.

[302] A. Pauldrach, J. Puls, and R. P. Kudritzki. Radiation-driven winds of hot luminous stars - Improvements of the theory and first results. *A&A*, 164:86–100, Aug. 1986.

[303] J. Pelan and K. A. Berrington. Atomic data from the IRON Project. XXI. Electron excitation of fine-structure transitions involving the 3dˆ64sˆ2 ˆ5D ground state and the 3dˆ74s ^{5}F metastable state of Fe i. *A&APS*, 122:177–180, Apr. 1997. doi: 10.1051/aas:1997328.

[304] D. M. Peterson, C. A. Hummel, T. A. Pauls, J. T. Armstrong, J. A. Benson, G. C. Gilbreath, R. B. Hindsley, D. J. Hutter, K. J. Johnston, D. Mozurkewich, and H. R. Schmitt. Vega is a rapidly rotating star. *Nature*, 440:896–899, Apr. 2006. doi: 10.1038/nature04661.

[305] M. M. Phillips, S. R. Heathcote, M. Hamuy, and M. Navarrete. An optical spectrophotometric atlas of Supernova 1987A in the LMC. I - The first 130 days. *AJ*, 95:1087–1110, Apr. 1988. doi: 10.1086/114705.

[306] M. M. Phillips, M. Hamuy, S. R. Heathcote, N. B. Suntzeff, and S. Kirhakos. An optical spectrophotometric atlas of supernova 1987A in the LMC. II - CCD observations from day 198 to 805. *AJ*, 99:1133–1145, Apr. 1990. doi: 10.1086/115402.

[307] J. M. Pittard and M. F. Corcoran. In hot pursuit of the hidden companion of eta Carinae: An X-ray determination of the wind parameters. *A&A*, 383:636–647, Feb. 2002. doi: 10.1051/0004-6361:20020025.

[308] P. Podsiadlowski, P. C. Joss, and S. Rappaport. A merger model for SN 1987 A. *A&A*, 227:L9–L12, Jan. 1990.

[309] P. Podsiadlowski, A. C. Fabian, and I. R. Stevens. Origin of the Napoleon's hat nebula around SN1987A and implications for the progenitor. *Nature*, 354:43–46, Nov. 1991. doi: 10.1038/354043a0.

[310] R. Poeckert and J. M. Marlborough. Intrinsic linear polarization of Be stars as a function of V sini. *ApJ*, 206:182–195, May 1976. doi: 10.1086/154369.

[311] D. Pooley, W. H. G. Lewin, D. W. Fox, J. M. Miller, C. K. Lacey, S. D. Van Dyk, K. W. Weiler, R. A. Sramek, A. V. Filippenko, D. C. Leonard, S. Immler, R. A. Chevalier, A. C. Fabian, C. Fransson, and K. Nomoto. X-Ray, Optical, and Radio Observations

of the Type II Supernovae 1999em and 1998S. *ApJ*, 572:932–943, June 2002. doi: 10.1086/340346.

[312] M. Pozzo, W. P. S. Meikle, A. Fassia, T. Geballe, P. Lundqvist, N. N. Chugai, and J. Sollerman. On the source of the late-time infrared luminosity of SN 1998S and other Type II supernovae. *MNRAS*, 352:457–477, Aug. 2004. doi: 10.1111/j.1365-2966.2004.07951.x.

[313] M. Pozzo, W. P. S. Meikle, A. Fassia, T. Geballe, P. Lundqvist, N. N. Chugai, and J. Sollerman. Dust Signatures from Late-time Infrared and Optical Observations of SN 1998S. In M. Turatto, S. Benetti, L. Zampieri, & W. Shea, editor, *1604-2004: Supernovae as Cosmological Lighthouses*, volume 342 of *Astronomical Society of the Pacific Conference Series*, page 337, Dec. 2005.

[314] J. L. Prieto, K. Z. Stanek, and J. F. Beacom. Characterizing Supernova Progenitors via the Metallicities of their Host Galaxies, from Poor Dwarfs to Rich Spirals. *ApJ*, 673:999–1008, Feb. 2008. doi: 10.1086/524654.

[315] N. Przybilla and K. Butler. Non-LTE line formation for N: Abundances and stellar parameters. Model atom and first results on BA-type stars. *A&A*, 379:955–975, Dec. 2001. doi: 10.1051/0004-6361:20011393.

[316] N. Przybilla, K. Butler, and R. P. Kudritzki. Non-LTE line-formation for neutral and singly-ionized carbon. Model atom and first results on BA-type stars. *A&A*, 379:936–954, Dec. 2001. doi: 10.1051/0004-6361:20011384.

[317] C. A. Ramsbottom. Electron-impact excitation of Fe II: Effective collision strengths for optically allowed fine-structure transitions. *Atomic Data and Nuclear Data Tables*, 95:910–986, Nov. 2009. doi: 10.1016/j.adt.2009.08.002.

[318] C. A. Ramsbottom, C. E. Hudson, P. H. Norrington, and M. P. Scott. Electron-impact excitation of Fe II. Collision strengths and effective collision strengths for low-lying fine-structure forbidden transitions. *A&A*, 475:765–769, Nov. 2007. doi: 10.1051/0004-6361:20078640.

[319] B. C. Reed. Catalog of Galactic OB Stars. *AJ*, 125:2531–2533, May 2003. doi: 10.1086/374771.

[320] A. Rest, R. J. Foley, B. Sinnott, D. L. Welch, C. Badenes, A. V. Filippenko, M. Bergmann, W. A. Bhatti, S. Blondin, P. Challis, G. Damke, H. Finley, M. E. Huber, D. Kasen, R. P. Kirshner, T. Matheson, P. Mazzali, D. Minniti, R. Nakajima, G. Narayan, K. Olsen, D. Sauer, R. C. Smith, and N. B. Suntzeff. Direct Confirmation of the Asymmetry of the Cas A Supernova with Light Echoes. *ApJ*, 732:3, May 2011. doi: 10.1088/0004-637X/732/1/3.

[321] N. D. Richardson, D. R. Gies, T. J. Henry, E. Fernández-Lajús, and A. T. Okazaki. The Hα Variations of η Carinae During the 2009.0 Spectroscopic Event. *AJ*, 139: 1534–1541, Apr. 2010. doi: 10.1088/0004-6256/139/4/1534.

[322] A. G. Riess, A. V. Filippenko, W. Li, and B. P. Schmidt. Is there an Indication of Evolution of Type IA Supernovae from their Rise Times? *AJ*, 118:2668–2674, Dec. 1999. doi: 10.1086/301144.

[323] H. Sawai, K. Kotake, and S. Yamada. Core-Collapse Supernovae with Nonuniform Magnetic Fields. *ApJ*, 631:446–455, Sept. 2005. doi: 10.1086/432529.

[324] D. Schaerer and A. de Koter. Combined stellar structure and atmosphere models for massive stars. III. Spectral evolution and revised ionizing fluxes of O3-B0 stars. *A&A*, 322:598–614, June 1997.

[325] L. Scheck, K. Kifonidis, H.-T. Janka, and E. Müller. Multidimensional supernova simulations with approximative neutrino transport. I. Neutron star kicks and the anisotropy of neutrino-driven explosions in two spatial dimensions. *A&A*, 457:963–986, Oct. 2006. doi: 10.1051/0004-6361:20064855.

[326] E. M. Schlegel. A new subclass of Type II supernovae? *MNRAS*, 244:269–271, May 1990.

[327] E. M. Schlegel. X-Ray Detection of SN 1994W in NGC 4041? *ApJL*, 527:L85–L88, Dec. 1999. doi: 10.1086/312408.

[328] E. M. Schlegel and R. Petre. A Chandra ACIS Observation of the X-Ray-luminous SN 1988Z. *ApJ*, 646:378–384, July 2006. doi: 10.1086/504890.

[329] R. E. Schulte-Ladbeck, A. Pasquali, M. Clampin, A. Nota, D. J. Hillier, and O. L. Lupie. Hubble Space Telescope Imaging Polarimetry of eta Carinae. *AJ*, 118:1320–1337, Sept. 1999. doi: 10.1086/301000.

[330] M. B. Shah, D. S. Elliott, and H. B. Gilbody. Pulsed crossed-beam study of the ionisation of atomic hydrogen by electron impact. *Journal of Physics B: Atomic and Molecular Physics*, 20(14):3501, 1987. URL http://stacks.iop.org/0022-3700/20/i=14/a=022.

[331] T. Shigeyama and K. Nomoto. Theoretical light curve of SN 1987A and mixing of hydrogen and nickel in the ejecta. *ApJ*, 360:242–256, Sept. 1990. doi: 10.1086/169114.

[332] T. Shigeyama, K. Iwamoto, I. Hachisu, K. Nomoto, and H. Saio. Instabilities and Mixing in Type II-P and II-b Supernovae. In T. S. Kuhn, editor, *IAU Colloq. 145: Supernovae and Supernova Remnants*, pages 129–+, 1996.

[333] T. M. Shimizu, T. Ebisuzaki, K. Sato, and S. Yamada. Effect of Anisotropic Neutrino Radiation on Supernova Explosion Energy. *ApJ*, 552:756–781, May 2001. doi: 10.1086/320544.

[334] M. M. Sirk, J. V. Vallerga, D. S. Finley, P. Jelinsky, and R. F. Malina. Performance of the Extreme Ultraviolet Explorer Imaging Telescopes. *ApJS*, 110:347, June 1997. doi: 10.1086/313002.

[335] S.M. and Younger. Electron impact ionization cross sections and rates for highly ionized atoms. *Journal of Quantitative Spectroscopy and Radiative Transfer*, 26(4): 329 – 337, 1981. ISSN 0022-4073. doi: 10.1016/0022-4073(81)90127-8. URL http://www.sciencedirect.com/science/article/pii/0022407381901278.

[336] S. J. Smartt, J. J. Eldridge, R. M. Crockett, and J. R. Maund. The death of massive stars - I. Observational constraints on the progenitors of Type II-P supernovae. *MNRAS*, 395:1409–1437, May 2009. doi: 10.1111/j.1365-2966.2009.14506.x.

[337] N. Smith. The Structure of the Homunculus. I. Shape and Latitude Dependence from H_2 and $[FeII]$ Velocity Maps of η Carinae. *ApJ*, 644:1151–1163, June 2006. doi: 10.1086/503766.

[338] N. Smith. Episodic Mass Loss and Pre-SN Circumstellar Envelopes. In F. Bresolin, P. A. Crowther, & J. Puls, editor, *IAU Symposium*, volume 250 of *IAU Symposium*, pages 193–200, June 2008. doi: 10.1017/S1743921308020498.

[339] N. Smith. Episodic post-shock dust formation in the colliding winds of Eta Carinae. *MNRAS*, 402:145–151, Feb. 2010. doi: 10.1111/j.1365-2966.2009.15901.x.

[340] N. Smith and G. J. Ferland. The Structure of the Homunculus. II. Modeling the Physical Conditions in η Carinae's Molecular Shell. *ApJ*, 655:911–919, Feb. 2007. doi: 10.1086/510328.

[341] N. Smith and R. D. Gehrz. Proper Motions in the Ejecta of eta Carinae with a 50 Year Baseline. *AJ*, 116:823–828, Aug. 1998. doi: 10.1086/300447.

[342] N. Smith and R. McCray. Shell-shocked Diffusion Model for the Light Curve of SN 2006gy. *ApJL*, 671:L17–L20, Dec. 2007. doi: 10.1086/524681.

[343] N. Smith, R. D. Gehrz, and J. Krautter. The Infrared Morphology of eta Carinae. *AJ*, 116:1332–1345, Sept. 1998. doi: 10.1086/300501.

[344] N. Smith, K. Davidson, T. R. Gull, K. Ishibashi, and D. J. Hillier. Latitude-dependent Effects in the Stellar Wind of η Carinae. *ApJ*, 586:432–450, Mar. 2003. doi: 10.1086/367641.

[345] N. Smith, W. Li, R. J. Foley, J. C. Wheeler, D. Pooley, R. Chornock, A. V. Filippenko, J. M. Silverman, R. Quimby, J. S. Bloom, and C. Hansen. SN 2006gy: Discovery of the Most Luminous Supernova Ever Recorded, Powered by the Death of an Extremely Massive Star like η Carinae. *ApJ*, 666:1116–1128, Sept. 2007. doi: 10.1086/519949.

[346] N. Smith, R. Chornock, W. Li, M. Ganeshalingam, J. M. Silverman, R. J. Foley, A. V. Filippenko, and A. J. Barth. SN 2006tf: Precursor Eruptions and the Optically Thick

Regime of Extremely Luminous Type IIn Supernovae. *ApJ*, 686:467–484, Oct. 2008. doi: 10.1086/591021.

[347] N. Smith, R. J. Foley, J. S. Bloom, W. Li, A. V. Filippenko, R. Gavazzi, A. Ghez, Q. Konopacky, M. A. Malkan, P. J. Marshall, D. Pooley, T. Treu, and J.-H. Woo. Late-Time Observations of SN 2006gy: Still Going Strong. *ApJ*, 686:485–491, Oct. 2008. doi: 10.1086/590141.

[348] N. Smith, R. Chornock, J. M. Silverman, A. V. Filippenko, and R. J. Foley. Spectral Evolution of the Extraordinary Type IIn Supernova 2006gy. *ApJ*, 709:856–883, Feb. 2010. doi: 10.1088/0004-637X/709/2/856.

[349] N. Smith, W. Li, A. V. Filippenko, and R. Chornock. Observed fractions of core-collapse supernova types and initial masses of their single and binary progenitor stars. *MNRAS*, 412:1522–1538, Apr. 2011. doi: 10.1111/j.1365-2966.2011.17229.x.

[350] R. G. Smith. An infrared study of the stellar population in the direction of the Carina nebula - NGC 3372. *MNRAS*, 227:943–965, Aug. 1987.

[351] J. Sollerman, R. J. Cumming, and P. Lundqvist. A Very Low Mass of 56Ni in the Ejecta of SN 1994W. *ApJ*, 493:933, Jan. 1998. doi: 10.1086/305163.

[352] L. V. Spencer and U. Fano. Energy Spectrum Resulting from Electron Slowing Down. *Physical Review*, 93:1172–1181, Mar. 1954. doi: 10.1103/PhysRev.93.1172.

[353] O. Stahl, K. Weis, D. J. Bomans, K. Davidson, T. R. Gull, and R. M. Humphreys. A spectroscopic event of η Car viewed from different directions: The data and first results. *A&A*, 435:303–312, May 2005. doi: 10.1051/0004-6361:20042547.

[354] K. Z. Stanek, T. Matheson, P. M. Garnavich, P. Martini, P. Berlind, N. Caldwell, P. Challis, W. R. Brown, R. Schild, K. Krisciunas, M. L. Calkins, J. C. Lee, N. Hathi, R. A. Jansen, R. Windhorst, L. Echevarria, D. J. Eisenstein, B. Pindor, E. W. Olszewski, P. Harding, S. T. Holland, and D. Bersier. Spectroscopic Discovery of the Supernova 2003dh Associated with GRB 030329. *ApJL*, 591:L17–L20, July 2003. doi: 10.1086/376976.

[355] R. A. Stathakis and E. M. Sadler. What was supernova 1988Z? *MNRAS*, 250:786–795, June 1991.

[356] P. Stone, Y.-K. Kim, and J. Desclaux. Electron-impact cross sections for dipole-and spin-allowed excitations of hydrogen, helium, and lithium. *J. Res. Natl. Inst. Stand. Technol.*, 107:327, 2002.

[357] K. Sumiyoshi, S. Yamada, H. Suzuki, H. Shen, S. Chiba, and H. Toki. Postbounce Evolution of Core-Collapse Supernovae: Long-Term Effects of the Equation of State. *ApJ*, 629:922–932, Aug. 2005. doi: 10.1086/431788.

[358] N. B. Suntzeff and P. Bouchet. The bolometric light curve of SN 1987A. I - Results from ESO and CTIO U to Q0 photometry. *AJ*, 99:650–663, Feb. 1990. doi: 10.1086/115358.

[359] R. Sunyaev, A. Kaniovsky, V. Efremov, M. Gilfanov, E. Churazov, S. Grebenev, A. Kuznetsov, A. Melioranskiy, N. Yamburenko, S. Yunin, D. Stepanov, I. Chulkov, N. Pappe, M. Boyarskiy, E. Gavrilova, V. Loznikov, A. Prudkoglyad, V. Rodin, C. Reppin, W. Pietsch, J. Engelhauser, J. Truemper, W. Voges, E. Kendziorra, M. Bezler, R. Staubert, A. C. Brinkman, J. Heise, W. A. Mels, R. Jager, G. K. Skinner, O. Al-Emam, T. G. Patterson, A. P. Willmore, M. Gilfanov, and E. Churazov. Discovery of hard X-ray emission from supernova 1987A. *Nature*, 330:227–229, Nov. 1987. doi: 10.1038/330227a0.

[360] D. A. Swartz. Ionization by high-energy particles and the electron scattering opacity in supernovae. *ApJ*, 373:604–613, June 1991. doi: 10.1086/170079.

[361] D. A. Swartz, A. V. Filippenko, K. Nomoto, and J. C. Wheeler. Spectra of low-mass helium star models and the type IC supernova SN 1987M. *ApJ*, 411:313–322, July 1993. doi: 10.1086/172831.

[362] D. A. Swartz, P. G. Sutherland, and R. P. Harkness. Gamma-Ray Transfer and Energy Deposition in Supernovae. *ApJ*, 446:766–+, June 1995. doi: 10.1086/175834.

[363] M. Tapia, M. Roth, H. Marraco, and M. T. Ruiz. The interstellar extinction in the open clusters TR 14, TR 15, TR 16/Cr 232 and CR 228 in NGC 3372 - New near-infrared photometry. *MNRAS*, 232:661–681, June 1988.

[364] M. Teodoro, A. Damineli, R. G. Sharp, J. H. Groh, and C. L. Barbosa. Near-infrared integral field spectroscopy of the Homunculus nebula around η Carinae using Gemini/CIRPASS. *MNRAS*, pages 584–+, May 2008. doi: 10.1111/j.1365-2966.2008.13264.x.

[365] M. Teodoro, A. Damineli, J. I. Arias, F. X. de Araújo, R. H. Barbá, M. F. Corcoran, M. Borges Fernandes, E. Fernández-Lajús, L. Fraga, R. C. Gamen, J. F. González, J. H. Groh, J. L. Marshall, P. J. McGregor, N. Morrell, D. C. Nicholls, E. R. Parkin, C. B. Pereira, M. M. Phillips, G. R. Solivella, J. E. Steiner, M. Stritzinger, I. Thompson, C. A. O. Torres, M. A. P. Torres, and M. I. Zevallos Herencia. He II λ4686 in η Carinae: Collapse of the Wind-Wind Collision Region during Periastron Passage. *ApJ*, 746:73, Feb. 2012. doi: 10.1088/0004-637X/746/1/73.

[366] A. D. Thackeray. Polarization of eta Carinae. *The Observatory*, 76:154–155, Aug. 1956.

[367] A. D. Thackeray. Spectra of the polarized halo around eta Carinae. *The Observatory*, 81:99–102, June 1961.

[368] P. S. The and F. Graafland. The Extinction Law in the Carina Nebula (Invited Paper). In V. Niemela, N. Morrell, & A. Feinstein, editor, *Revista Mexicana de Astronomia*

y Astrofisica Conference Series, volume 2 of *Revista Mexicana de Astronomia y Astrofisica, vol. 27*, page 75, June 1995.

[369] T. A. Thompson, A. Burrows, and P. A. Pinto. Shock Breakout in Core-Collapse Supernovae and Its Neutrino Signature. *ApJ*, 592:434–456, July 2003. doi: 10.1086/375701.

[370] A. G. G. M. Tielens. Interstellar Depletions and the Life Cycle of Interstellar Dust. *ApJ*, 499:267–+, May 1998. doi: 10.1086/305640.

[371] D. Y. Tsvetkov. SN 1994W: Unprecedented Brightness Decline at Late Stage. *Information Bulletin on Variable Stars*, 4253:1, Sept. 1995.

[372] M. Turatto, E. Cappellaro, I. J. Danziger, S. Benetti, C. Gouiffes, and M. della Valle. The Type II supernova 1988Z in MCG + 03-28-022 - Increasing evidence of interaction of supernova ejecta with a circumstellar wind. *MNRAS*, 262:128–140, May 1993.

[373] A. ud-Doula and S. P. Owocki. Dynamical Simulations of Magnetically Channeled Line-driven Stellar Winds. I. Isothermal, Nonrotating, Radially Driven Flow. *ApJ*, 576:413–428, Sept. 2002. doi: 10.1086/341543.

[374] A. Uesugi and I. Fukuda. *Catalogue of stellar rotational velocities (revised)*. 1982.

[375] V. Utrobin. Hydrodynamic study of supernova 1987A - Near the peak luminosity. *A&A*, 270:249–258, Mar. 1993.

[376] V. P. Utrobin. The Light Curve of Supernova 1987A: The Structure of the Presupernova and Radioactive Nickel Mixing. *Astronomy Letters*, 30:293–308, May 2004. doi: 10.1134/1.1738152.

[377] V. P. Utrobin. An optimal hydrodynamic model for the normal type IIP supernova 1999em. *A&A*, 461:233–251, Jan. 2007. doi: 10.1051/0004-6361:20066078.

[378] V. P. Utrobin and N. N. Chugai. Ionization Freeze-out and Hydrogen Excitation in the SN IIP Atmosphere. *Astronomy Letters*, 28:386–392, June 2002. doi: 10.1134/1.1484138.

[379] V. P. Utrobin and N. N. Chugai. Strong effects of time-dependent ionization in early SN 1987A. *A&A*, 441:271–281, Oct. 2005. doi: 10.1051/0004-6361:20042599.

[380] J. V. Vallerga, P. W. Vedder, and B. Y. Welsh. Intense extreme ultraviolet emission from the B star Epsilon Canis Majoris. *ApJL*, 414:L65–L67, Sept. 1993. doi: 10.1086/186997.

[381] S. van den Bergh, W. Li, and A. V. Filippenko. Classifications of the Host Galaxies of Supernovae, Set III. *PASP*, 117:773–782, Aug. 2005. doi: 10.1086/431435.

[382] S. D. van Dyk, K. W. Weiler, R. A. Sramek, and N. Panagia. SN 1988Z: The Most Distant Radio Supernova. *ApJL*, 419:L69, Dec. 1993. doi: 10.1086/187139.

[383] M. H. van Kerkwijk, P. Chang, and S. Justham. Sub-Chandrasekhar White Dwarf Mergers as the Progenitors of Type Ia Supernovae. *ApJL*, 722:L157–L161, Oct. 2010. doi: 10.1088/2041-8205/722/2/L157.

[384] F. van Leeuwen. Validation of the new Hipparcos reduction. *A&A*, 474:653–664, Nov. 2007. doi: 10.1051/0004-6361:20078357.

[385] H. van Regemorter. Rate of Collisional Excitation in Stellar Atmospheres. *ApJ*, 136: 906–+, Nov. 1962. doi: 10.1086/147445.

[386] E. Verner, F. Bruhweiler, and T. Gull. The Binarity of η Carinae Revealed from Photoionization Modeling of the Spectral Variability of the Weigelt Blobs B and D. *ApJ*, 624:973–982, May 2005. doi: 10.1086/429400.

[387] R. Viotti, L. Rossi, A. Cassatella, A. Altamore, and G. B. Baratta. The ultraviolet spectrum of Eta Carinae. *ApJS*, 71:983–1009, Dec. 1989. doi: 10.1086/191405.

[388] N. Visvanathan. Polarization in η carinae. *MNRAS*, 135:275–+, 1967.

[389] H. von Zeipel. The radiative equilibrium of a rotating system of gaseous masses. *MNRAS*, 84:665–683, June 1924.

[390] J. R. Walsh and N. Ageorges. High resolution near-infrared polarimetry of eta Carinae and the Homunculus Nebula. *A&A*, 357:255–267, May 2000.

[391] B. Wang, X. Meng, X. Chen, and Z. Han. The helium star donor channel for the progenitors of Type Ia supernovae. *MNRAS*, 395:847–854, May 2009. doi: 10.1111/j.1365-2966.2009.14545.x.

[392] L. Wang and J. C. Wheeler. Spectropolarimetry of Supernovae. *ARA&A*, 46:433–474, Sept. 2008. doi: 10.1146/annurev.astro.46.060407.145139.

[393] L. Wang, D. Baade, P. Höflich, and J. C. Wheeler. Supernova polarimetry with the VLT: lessons from asymmetry. *The Messenger*, 109:47–51, Sept. 2002.

[394] L. Wang, J. C. Wheeler, P. Höflich, A. Khokhlov, D. Baade, D. Branch, P. Challis, A. V. Filippenko, C. Fransson, P. Garnavich, R. P. Kirshner, P. Lundqvist, R. McCray, N. Panagia, C. S. J. Pun, M. M. Phillips, G. Sonneborn, and N. B. Suntzeff. The Axisymmetric Ejecta of Supernova 1987A. *ApJ*, 579:671–677, Nov. 2002. doi: 10.1086/342824.

[395] R. F. Warren-Smith, S. M. Scarrott, P. Murdin, and R. G. Bingham. Optical polarization map of Eta Carinae and the nature of its outburst. *MNRAS*, 187:761–768, June 1979.

[396] L. B. F. M. Waters. Be/X ray binaries. In J. Hunt & B. Battrick, editor, *Two Topics in X-Ray Astronomy, Volume 1: X Ray Binaries. Volume 2: AGN and the X Ray Background*, volume 296 of *ESA Special Publication*, pages 25–30, Nov. 1989.

[397] L. B. F. M. Waters, E. P. J. van den Heuvel, A. R. Taylor, G. M. H. J. Habets, and P. Persi. Evidence for low-velocity winds in Be/X-ray binaries. *A&A*, 198:200–210, June 1988.

[398] T. A. Weaver, G. B. Zimmerman, and S. E. Woosley. Presupernova evolution of massive stars. *ApJ*, 225:1021–1029, Nov. 1978. doi: 10.1086/156569.

[399] R. F. Webbink. Double white dwarfs as progenitors of R Coronae Borealis stars and Type I supernovae. *ApJ*, 277:355–360, Feb. 1984. doi: 10.1086/161701.

[400] G. Weigelt and J. Ebersberger. Eta Carinae resolved by speckle interferometry. *A&A*, 163:L5+, July 1986.

[401] G. Weigelt, S. Kraus, T. Driebe, R. G. Petrov, K.-H. Hofmann, F. Millour, O. Chesneau, D. Schertl, F. Malbet, J. D. Hillier, T. Gull, K. Davidson, A. Domiciano de Souza, P. Antonelli, U. Beckmann, Y. Bresson, A. Chelli, M. Dugué, G. Duvert, S. Gennari, L. Glück, P. Kern, S. Lagarde, E. Le Coarer, F. Lisi, K. Perraut, P. Puget, F. Rantakyrö, S. Robbe-Dubois, A. Roussel, E. Tatulli, G. Zins, M. Accardo, B. Acke, K. Agabi, E. Altariba, B. Arezki, E. Aristidi, C. Baffa, J. Behrend, T. Blöcker, S. Bonhomme, S. Busoni, F. Cassaing, J.-M. Clausse, J. Colin, C. Connot, A. Delboulbé, P. Feautrier, D. Ferruzzi, T. Forveille, E. Fossat, R. Foy, D. Fraix-Burnet, A. Gallardo, E. Giani, C. Gil, A. Glentzlin, M. Heiden, M. Heininger, O. Hernandez Utrera, D. Kamm, M. Kiekebusch, D. Le Contel, J.-M. Le Contel, T. Lesourd, B. Lopez, M. Lopez, Y. Magnard, A. Marconi, G. Mars, G. Martinot-Lagarde, P. Mathias, P. Mège, J.-L. Monin, D. Mouillet, D. Mourard, E. Nussbaum, K. Ohnaka, J. Pacheco, C. Perrier, Y. Rabbia, S. Rebattu, F. Reynaud, A. Richichi, A. Robini, M. Sacchettini, M. Schöller, W. Solscheid, A. Spang, P. Stee, P. Stefanini, M. Tallon, I. Tallon-Bosc, D. Tasso, L. Testi, F. Vakili, O. von der Lühe, J.-C. Valtier, M. Vannier, N. Ventura, K. Weis, and M. Wittkowski. Near-infrared interferometry of ¡ASTROBJ¿η Carinae¡/ASTROBJ¿ with spectral resolutions of 1 500 and 12 000 using AMBER/VLTI. *A&A*, 464:87–106, Mar. 2007. doi: 10.1051/0004-6361:20065577.

[402] B. Y. Welsh. The interstellar tunnel of neutral-free gas toward Beta Canis Majoris. *ApJ*, 373:556–559, June 1991. doi: 10.1086/170074.

[403] J. C. Wheeler, D. L. Meier, and J. R. Wilson. Asymmetric Supernovae from Magnetocentrifugal Jets. *ApJ*, 568:807–819, Apr. 2002. doi: 10.1086/338953.

[404] J. Whelan and I. Iben, Jr. Binaries and Supernovae of Type I. *ApJ*, 186:1007–1014, Dec. 1973. doi: 10.1086/152565.

[405] S. M. White, R. A. Duncan, J. Lim, G. J. Nelson, S. A. Drake, and M. R. Kundu. The radio source around Eta Carinae. *ApJ*, 429:380–384, July 1994. doi: 10.1086/174327.

[406] P. A. Whitelock, M. W. Feast, F. Marang, and E. Breedt. The 2003 shell event in η Carinae. *MNRAS*, 352:447–456, Aug. 2004. doi: 10.1111/j.1365-2966.2004.07950.x.

[407] C. L. Williams, N. Panagia, S. D. Van Dyk, C. K. Lacey, K. W. Weiler, and R. A. Sramek. Radio Emission from SN 1988Z and Very Massive Star Evolution. *ApJ*, 581: 396–403, Dec. 2002. doi: 10.1086/344087.

[408] J. R. Wilson, R. Mayle, S. E. Woosley, and T. Weaver. Stellar core collapse and supernova. *Annals of the New York Academy of Sciences*, 470:267–293, 1986. doi: 10.1111/j.1749-6632.1986.tb47980.x.

[409] S. Woosley and T. Janka. The physics of core-collapse supernovae. *Nature Physics*, 1: 147–154, Dec. 2005. doi: 10.1038/nphys172.

[410] S. E. Woosley. SN 1987A - After the peak. *ApJ*, 330:218–253, July 1988. doi: 10.1086/166468.

[411] S. E. Woosley and R. G. Eastman. Type Ib and Ic supernovae: models and spectra. In P. Ruiz-Lapuente, R. Canal, & J. Isern, editor, *NATO ASIC Proc. 486: Thermonuclear Supernovae*, pages 821–+, 1997.

[412] S. E. Woosley and D. Kasen. Sub-Chandrasekhar Mass Models for Supernovae. *ApJ*, 734:38, June 2011. doi: 10.1088/0004-637X/734/1/38.

[413] S. E. Woosley and T. A. Weaver. Sub-Chandrasekhar mass models for Type IA supernovae. *ApJ*, 423:371–379, Mar. 1994. doi: 10.1086/173813.

[414] S. E. Woosley, S. Blinnikov, and A. Heger. Pulsational pair instability as an explanation for the most luminous supernovae. *Nature*, 450:390–392, Nov. 2007. doi: 10.1038/nature06333.

[415] Y. Xu and R. McCray. Energy degradation of fast electrons in hydrogen gas. *ApJ*, 375:190–201, July 1991. doi: 10.1086/170180.

[416] T. Yamasaki and S. Yamada. Effects of Rotation on the Revival of a Stalled Shock in Supernova Explosions. *ApJ*, 623:1000–1010, Apr. 2005. doi: 10.1086/428496.

[417] S.-C. Yoon and N. Langer. The first binary star evolution model producing a Chandrasekhar mass white dwarf. *A&A*, 412:L53–L56, Dec. 2003. doi: 10.1051/0004-6361:20034607.

[418] S. M. Younger. Electron impact ionization cross sections and rates for highly ionized atoms. *JQSRT*, 26:329–337, 1981. doi: 10.1016/0022-4073(81)90127-8.

[419] L. Yungelson and M. Livio. Type IA Supernovae: an Examination of Potential Progenitors and the Redshift Distribution. *ApJ*, 497:168, Apr. 1998. doi: 10.1086/305455.

[420] J. Zorec, L. Cidale, M. L. Arias, Y. Frémat, M. F. Muratore, A. F. Torres, and C. Martayan. Fundamental parameters of B supergiants from the BCD system. I. Calibration of the (λ_1, D) parameters into T_{eff}. *A&A*, 501:297–320, July 2009. doi: 10.1051/0004-6361/200811147.